Universidad de Oviedo

Departamento de Ingeniería Eléctrica, Electrónica,
de Computadores y Sistemas

Doctoral Dissertation

Novel XYZ scanner-based radiation and scattering measurement techniques for antenna diagnostics and imaging applications

Ana Arboleya Arboleya

Programa de Doctorado en Tecnologías de la Información y
Comunicaciones en Redes Móviles

2016

Directors:
Prof. Fernando Las-Heras Andrés, Universidad de Oviedo
Dr. Yuri Álvarez López, Universidad de Oviedo

Preliminary examiners:
Dr. Laurent Le Coq, IETR, University of Rennes
Prof. Cyril Luxey, University of Nice Sophia Antipolis

Examining board:
Prof. Marcos Rodríguez Pino, Universidad de Oviedo
Prof. Manuel Sierra Castañer, Universidad Politécinca de Madrid
Prof. Custodio Peixeiro, University of Lisbon

Tesis académica que, con el permiso de la Universidad de Oviedo, se presenta a escrutinio público para la obtención del título de Doctor con Mención Internacional. La defensa de la tesis tendrá lugar en la sala *Tecnologías de Radio Frecuencia*, en la Escuela Politécnica de Ingeniería de la Universidad de Oviedo, Gijón.

Resumen extendido

En la presente Tesis doctoral se presentan nuevos resultados experimentales en los campos de medida de antenas e imagen electromagnética. Los recientes avances en tecnologías de fabricación han contribuido enormemente al desarrollo de nuevos componentes y antenas para las bandas de longitudes de onda milimétricas y submilimétricas con la consecuente aparición de nuevas aplicaciones a nivel comercial para las que se demandan la simplificación y el desarrollo de nuevos dispositivos de coste reducido, y la creación de nuevas técnicas de post-procesado en tiempo real, que permitan desarrollar sistemas de imagen electromagnética competitivos en coste, tamaño y resolución. Por otra parte, se hace necesario el desarrollo de nuevos sistemas de medida de gran precisión, capaces de cumplir con las restricciones necesarias para la medida de antenas en estas bandas.

Las técnicas indirectas de holografía *off-axis* son técnicas interferométricas que permiten la caracterización de un campo electromagnético a partir de adquisiciones de sólo-amplitud. La recuperación del campo electromagnético, o de su fase, en caso de que su amplitud sea medida independientemente, se realiza mediante un sencillo proceso de filtrado del patrón de interferencia, conocido como holograma, en el dominio espectral, siempre que se disponga de la caracterización previa del campo empleado para crear la interferencia en amplitud y fase. La aplicación de estas técnicas resulta beneficiosa tanto en medida de antenas como en los sistemas de obtención de imagen electromagnética.

Las medidas de fase, particularmente en bandas de alta frecuencia, como son las bandas de longitudes de onda milimétricas y submilimétricas, resultan muy complicadas y demandan el uso de dispositivos de alto coste puesto que se requieren señales de referencia muy precisas. Dicha precisión hace necesario el uso de fuentes muy estables, condiciones constantes de temperatura y alta precisión en el posicionamiento. La deriva térmica que se produce en los dispositivos electrónicos y las variaciones que se introducen en los cables por su movimiento y cambio de curvatura, son dos grandes fuentes de error en la adquisición de fase en dichas bandas de frecuencia.

Puesto que las técnicas de holografía *off-axis* requieren únicamente del conocimiento de la amplitud, pueden ser empleadas para evitar el efecto de estos tipos de error y desarrollar sistemas de medida más robustos.

El reemplazo de los receptores heterodinos para la adquisición coherente de fase por sencillos detectores de amplitud, permite también la reducción de costes y simplificación y reducción de tamaño y complejidad de los sistemas de medida. Debido a lo anterior, el uso de holografía *off-axis* en sistemas de imagen resulta altamente adecuado. Además, tanto la recuperación coherente de fase como el proceso de enfoque de la imagen se realizan durante el post-procesado, permitiendo prescindir del uso de elementos ópticos para el enfoque como las lentes, que limitarían el rango de uso y el campo de visión de los sistemas.

Las técnicas de procesado empleadas durante la recuperación de fase del campo y el enfoque del objeto, son técnicas basadas en el uso de Transformadas de Fourier, lo que hace que resulten muy adecuadas para el desarrollo de sistemas de reconstrucción de imagen en tiempo real.

En el campo de diagnóstico y medida de antenas se han desarrollado tres técnicas de medida:

La primera de ellas [**I**] es una modificación del setup convencional en la que los desfases, generalmente introducidos mediante el uso de *phase-shifters*, son generados mediante desplazamientos mecánicos de la sonda, de modo que se evita el uso de dichos dispositivos, que en bandas de frecuencias de longitudes de onda milimétricas y submilimétricas pueden resultar complejos y caros.

La segunda técnica desarrollada [**II**] describe un método para incrementar, de forma artificial, la separación de los términos del holograma en el dominio espectral, permitiendo un filtrado mucho más efectivo. La técnica consiste en la multiplexación de dos hologramas que se forman con distintas posiciones de la antena de referencia de manera que se genera un cambio en la fase de la señal de referencia en el plano de adquisición. Esto permite obtener resultados similares a los que proporcionan las técnicas que emplean ondas de referencia sintetizadas, pero mediante el uso de ondas radiadas en las que, en el método convencional, la posición de la antena de referencia limita la separación espectral causando mayores solapamientos e incrementando el error en el proceso de recuperación de fase.

En ambas técnicas el filtrado se realiza en el dominio de la frecuencia espacial tras la adquisición completa del holograma en el dominio espacial y para una frecuencia de trabajo dada. Por este motivo, este tipo de técnicas mono-

cromáticas, no resultan eficientes para la caracterización de antenas de banda ancha en las que el proceso debe repetirse para cada una de las frecuencias de trabajo.

En la tercera técnica propuesta [**III**], el proceso de adquisición del holograma se modifica de manera que en cada punto del plano de adquisición el holograma se obtiene para una banda de frecuencias. El proceso de recuperación de fase, se va realizando punto a punto, simultáneamente para todas las frecuencias mediante filtrado en el dominio del tiempo de forma que dicho método resulta una forma eficiente de caracterización de antenas de banda ancha mediante medidas de sólo-amplitud. Una ventaja añadida es que en este método no es necesario implementar ningún tipo de desfase ni eléctrico ni mecánico, por lo que la complejidad del sistema se reduce al mínimo.

Paralelamente se han implementado técnicas de muestreo no redundante compatibles con esta última técnica [**IV**] que permiten reducir el número de muestras necesarias en gran medida, reduciendo drásticamente el tiempo de medida.

En lo relativo a las aplicaciones de imagen electromagnética se han desarrollado también tres técnicas con el fin de mejorar la calidad de los algoritmos convencionales y de reducir su complejidad en cuanto al número de elementos.

El uso de ondas de referencia sintetizadas presenta las siguientes ventajas: por una parte reduce el solapamiento espectral, y por otra parte, elimina la necesidad de caracterizar en amplitud y fase la señal de referencia, puesto que ésta se genera a partir de una muestra constante de la fuente y desfases introducidos de manera controlada mediante un *phase-shifter*. Sin embargo, el funcionamiento de estos dispositivos introduce cambios en la amplitud de la señal en función del desfase necesario, por lo que una caracterización adecuada permite una mejor recuperación de fase. En la primera de las técnicas desarrolladas se presenta un método para la estima de la señal de referencia a partir del estudio del comportamiento del holograma en un extremo del plano de adquisición [**V**].

En la segunda técnica [**VI**] se propone una implementación en la que se consigue sintetizar la señal de referencia sin la necesidad de emplear *phase-shifters* ni acopladores direccionales. La señal de referencia se inyecta directamente en el receptor mediante acoplo directo con el transmisor y los desfases se generan mediante desplazamientos mecánicos de la sonda. Al no emplear ningún com-

ponente a excepción de las antenas, la técnica puede emplearse fácilmente en cualquier banda de frecuencia. Su validación se ha realizado a 300 GHz.

Por último, la técnica presentada en [**VII**] y [**VIII**] sigue el mismo principio de funcionamiento que la técnica de medida de antenas en banda ancha descrita en [**III**], pero la formulación ha sido adaptada para sistemas radar de apertura sintética en configuración monostática de manera que es posible realizar la imagen electromagnética del objeto en tres dimensiones.

Las técnicas desarrolladas han sido validadas experimentalmente mediante ensayos en un rango de medida plano cuyas principales características se presentan en los Apéndices A y B, desarrollado también como parte de la tesis. Dicha validación se ha llevado a cabo principalmente en la banda correspondiente a longitudes de onda milimétricas, aunque algunas de las técnicas también han sido validadas en bandas inferiores del espectro de microondas y en la parte baja de la banda de longitudes de onda submilimétricas.

Conclusiones

El trabajo realizado en la presente tesis doctoral se centra en el desarrollo de nuevas técnicas de medida eficientes, a partir de adquisiciones de sólo-amplitud que permiten la reducción del coste y complejidad de los sistemas y que resultan adecuadas para su aplicación tanto en medida de antenas como en sistemas de imagen electromagnética. Por otra parte, se ha desarrollado un rango plano de medida en campo cercano que, entre otras cosas, ha permitido validar todas las técnicas desarrolladas experimentalmente.

La tesis se basa en el trabajo de investigación presentado en las publicaciones [**I**]-[**VIII**] y [A**I**], [B**I**] y [B**II**] y consiste en una revisión del estado del arte, un resumen de los fundamentos teóricos y la descripción del trabajo desarrollado (Capítulos 1-5). Se incluyen además dos apéndices que resumen las principales características técnicas del sistema de medida (Apéndice A) y su caracterización (Apéndice B).

Los métodos desarrollados consisten en modificaciones de la técnica indirecta de holografía *off-axis* centrándose en nuevas formas de síntesis del campo de referencia para la creación del holograma y nuevos métodos de filtrado para la recuperación de la fase del campo, de manera que se consiguen compensar las limitaciones de la técnica convencional, como pueden ser las altas tasas de muestreo requeridas, los problemas de solapamiento espectral o el número de dispositivos necesarios (*phase-shifters*, acopladores direccionales, combinadores de potencia, etc.) que pueden encarecer los sistemas.

Con el fin de compensar las altas tasas de muestreo se han empleado técnicas de muestreo no redundantes que permiten una reducción drástica del número de muestras y el tiempo de adquisición. También se han desarrollado nuevas técnicas holográficas que permiten la recuperación de la fase del campo punto a punto en el dominio de adquisición simultaneamente en una banda de frecuencias, lo que permite la caracterización eficiente de antenas de banda ancha y la implementación de técnicas radar de apertura sintética que permiten reconstrucciones tridimensionales de objetos.

También se han introducido modificaciones a la técnica convencional de holografía que permiten reducir el solapamiento en sistemas que emplean ondas de referencia radiadas, técnicas para la estimación del campo de referencia, y técnicas que permiten sustituir los saltos de fase eléctricos generados mediante el uso de *phase-shifters* por desplazamientos mecánicos.

En medida de antenas, todos los resultados obtenidos mediante los métodos propuestos se comparan con resultados obtenidos mediante los métodos convencionales de adquisición con amplitud y fase con muy alto grado de coincidencia.

Por el contrario, en las técnicas desarrolladas para aplicaciones de imagen, no se ha empleado ninguna métrica para la caracterización de los resultados puesto que la comparación con los objetos originales reconstruidos, permite evaluar directamente la calidad de los algoritmos presentados.

En cuanto al sistema de medida, además de la caracterización presentada en los apéndices de este trabajo y de su uso para la validación de los métodos presentados, cabe destacar que ha sido ampliamente empleado para la realización de otros trabajos (e.g. [i]-[xiii], [b]-[e], [g] o [i]) y como base para la implementación de varios demostradores dentro de proyectos europeos y nacionales realizados por el grupo de investigación TSC-UNIOVI.

Abstract

This thesis presents novel experimental results in the fields of antenna measurement and inverse scattering and electromagnetic imaging applications. Recent advances in fabrication technologies have contributed to the development of new components and antennas at millimeter- and submillimeter-wave bands which have led to the appearance of new applications at a commercial level that demand, on the one hand, a simplification and cost reduction in the design of the transceivers and availability of novel accurate and real-time post-processing techniques, and on the other hand, new measurement systems and techniques to cope with the strict requirements needed for the characterization of the antennas at those frequency bands.

Indirect off-axis holography is an interferometric technique that allows for amplitude-only characterization of an unknown field by means of a simple filtering process of the hologram or interference pattern in the spectral domain, providing that the reference field, employed to interfere the unknown field, is known in amplitude and phase. This technique is appropriate for its use in both of the herein studied applications: antenna measurement and inverse scattering and electromagnetic imaging.

Phase acquisition, specially at millimeter- and submillimeter-wave frequencies is an expensive and challenging task since the need of a steady phase reference demands not only a very stable source but steady temperature conditions and strong positioning requirements. Thus, thermal drift and cable flexing are two of the main error sources in these frequency bands. Indirect off-axis holography can be used to prevent the effect of these errors and develop new efficient and robust phaseless techniques while allowing for cost and complexity reduction of the measurement setup.

Indirect off-axis holography techniques for imaging systems are very useful since the bulky systems required for coherent detection in active imaging are replaced with direct detectors, drastically reducing costs, complexity and size of the array of transceivers. Furthermore coherent phase retrieval as well as

the focusing, are done in the post-processing stage by means of Fourier-based procedures suitable for real-time imaging.

Nevertheless, conventional off-axis holography exhibits some limitations such as high sampling rate requirements, spectral domain overlapping or number of required devices (phase-shifters, directional couplers, power combiners, etc.). The novel proposed methods have been developed in order to bypass these known limitations.

With the aim of reducing the sampling requirements, non-redundant sampling techniques have been adapted for its use with off-axis holography [**IV**], [**VII**]. New broadband holography techniques allowing for point-by-point phase retrieval that enables efficient broadband antenna characterization [**III**],[**IV**] and three-dimensional synthetic aperture radar applications [**VII**],[**VIII**] have also been developed. Other modifications of the conventional method in order to reduce overlapping in setups with radiated reference fields [**II**], provide accurate characterization of the reference field [**V**] or substituting the electrical phase-shifts with mechanical displacements [**I**],[**III**] have been proposed and successfully tested.

The presented techniques have been validated experimentally by means of a planar near field measurement system, whose main features are summarized in Appendices A and B, developed also as part of the research. Validation has been made mainly in the millimeter-wave band but also in lower bands of the microwave spectrum and in the lower submillimeter-wave band.

Dissertation

This thesis consists of an overview and of the following publications which are referred to in the text by their Roman numerals. A complete copy of all the publications is included in the final part of the dissertation. The publications do not appear in chronological order but grouped by topic:

[I] J. Laviada, **A. Arboleya-Arboleya**, Y. Álvarez-López, C. García-González, and F. Las-Heras, "Phaseless antenna diagnostics based on off-axis holography with synthetic reference wave," *IEEE Antennas and Wireless Propagation Letters,* vol. 13, pp. 43–46, 2014.

[II] **A. Arboleya**, J. Ala-Laurinaho, J. Laviada, Y. Álvarez, F. Las-Heras and A.V. Räisänen, "Millimeter-wave phaseless antenna measurement based on a modified off-axis holography setup," *Journal of Infrared, Millimeter, and Terahertz Waves,* vol. 37, no. 2, pp. 160–174, Feb. 2016.

[III] **A. Arboleya**, J. Laviada, J. Ala-Laurinaho, Y. Álvarez, F. Las-Heras and A.V. Räisänen, "Phaseless characterization of broadband antennas," *IEEE Transactions on Antennas and Propagation,* vol. 64, no. 2, pp. 484–495, Feb. 2016.

[IV] **A. Arboleya**, J. Laviada, J. Ala-Laurinaho, Y. Álvarez, F. Las-Heras and A.V. Räisänen, "Reduced set of points in phaseless broadband near-field antenna measurement: effects of noise and mechanical errors," in *10th European Conference on Antennas and Propagation (EUCAP'16),* pp. 1–5 (Convened sessions), Davos (Switzerland), 10–15 Apr. 2016.

[V] **A. Arboleya**, J. Laviada, Y. Álvarez-López and F. Las-Heras, "Versatile measurement system for imaging setups prototyping," *9th European Conference on Antennas and Propagation (EUCAP'15),* pp. 1–5 (Convened sessions), Lisbon (Portugal), 12–17 Apr. 2015.

[VI] J. Laviada, Y. Álvarez-López, **A. Arboleya-Arboleya**, C. García-González, and F. Las-Heras, "A modified phaseless inverse scattering setup based on indirect holography implemented at submillimeter-wave band," *IEEE Transactions on Antennas and Propagation,* vol. 61, no. 9, pp. 4876–4881, Sept. 2013.

[**VII**] J. Laviada, **A. Arboleya-Arboleya**, Y. Álvarez-López, C. García-González, and F. Las-Heras, "Phaseless synthetic aperture radar with efficient sampling for broadband near-field imaging: theory and validation," *IEEE Transactions on Antennas and Propagation,* vol. 62, no. 2, pp. 573–584, Feb. 2015.

[**VIII**] J. Laviada, **A. Arboleya**, F. López-Gayarre and F. Las-Heras, "Broadband synthetic aperture scanning system for three-dimensional through-the-wall inspection," *IEEE Geoscience and Remote Sensing Letters,* vol. 13, no. 1, pp. 97–101, Jan. 2016.

[A**I**] **A. Arboleya Arboleya**, C. García González, Y. Álvarez López, J. Laviada Martínez, and F. Las-Heras Andrés, "Millimeter and submillimeter planar measurement setup," in *IEEE international Symposium on Antennas and Propagation and USNC-URSI National Radio Science Meeting (APS / USNC-URSI),* Florida (USA), pp. 1–2, 7–13 Jul. 2013.

[B**I**] **A. Arboleya**, J. Laviada, Y. Álvarez-López, and F. Las-Heras, "Error characterization tool for planar near-field antenna measurement and diagnostics applications," *1st Conference on Antenna Measurements and Applications (2014 IEEE CAMA),* Antibes (France), 26–29 Nov. 2014.

[B**II**] **A. Arboleya**, J. Laviada, Y. Álvarez-López, and F. Las-Heras, "Study of the influence of mechanical errors in diagnostics applications by means of statistical analysis," in *9th European Conference on Antennas and Propagation (EUCAP'15),* pp. 1–5 (Convened sessions), Lisbon (Portugal), 12–17 Apr. 2015.

Other publications and works related to the topics of the thesis but not included as part of the dissertation

In addition to the above-mentioned references, the following publications also related to the topic of the thesis have also been authored or coauthored by Ana Arboleya during her time as a doctoral candidate in Universidad de Oviedo:

International journals

[i] J. Laviada, Y. Álvarez-López, **A. Arboleya Arboleya**, C. García González, and F. Las-Heras, "Inverse scattering with phase retrieval based on indirect holography via synthesized plane-waves," *IET Microwaves, Antennas and Propagation,* vol. 6, no. 12, pp. 1389–1398, Sept. 2012.

[ii] Y. Álvarez, R. Camblor, C. García, J. Laviada, C. Vázquez, S. Ver-Hoeye, G. Hotopan, M. Fernández, A. Hadarig, **A. Arboleya** and F. Las-Heras, "Sub-millimeter wave frequency scanning system for imaging applications," *IEEE Transactions on Antennas and Propagation,* vol. 61, no. 11, pp. 5689–5696, Nov. 2013.

[iii] J. Laviada, Y. Álvarez-López, **A. Arboleya-Arboleya**, C. García-González, and F. Las-Heras, "Interferometric technique with non-redundant sampling for phaseless inverse scattering," *IEEE Transactions on Antennas and Propagation,* vol. 62, no. 2, pp. 739–746, Feb. 2014.

[iv] J. Laviada, Y. Álvarez-López, R. Camblor-Diaz, C. García-González, C. Vázquez-Antuña, **A. Arboleya-Arboleya**, M. Fernández-García, G. Hotopan, S. Ver-Hoeye and F. Las-Heras, "Phase retrieval technique for sub-millimeter-wave frequency scanning-based radar system," *IET Microwaves, Antennas and Propagation,* vol. 8, no. 14, pp. 1170–1178, Nov. 2014.

[v] B. González-Valdés, Y. Álvarez, Y. Rodriguez-Vaqueiro, **A. Arboleya-Arboleya**, A. García-Pino, C.M. Rappaport, F. Las-Heras, and J.A. Martínez-Lorenzo, "Millimeter wave imaging architecture for on-the-move whole body imaging," *IEEE Transactions on Antennas and Propagation,* vol. 64, no. 6, pp. 2328–2338, March. 2016.

International conferences and workshops

[vi] J. Laviada, Y. Álvarez-López, **A. Arboleya-Arboleya**, C. García-González and F. Las-Heras, "Phaseless antenna diagnostics based on a novel antenna measurement setup," in *7th European Conference on Antennas and Propagation (EUCAP'13),* pp. 1–2 (Convened sessions), Gothenburg (Sweden), 8–12 Apr. 2013.

[vii] J. Laviada, Y. Álvarez-López, **A. Arboleya-Arboleya**, C. García-González and F. Las-Heras, "Microwave phaseless inverse scattering setup based on indirect holography," in *7th European Conference on Antennas and Propagation (EUCAP'13),* pp. 1–2 (Convened sessions), Gothenburg (Sweden), 8–12 Apr. 2013.

[viii] J.Laviada, **A. Arboleya-Arboleya**, Y. Álvarez-López, C. García-González and F. Las-Heras, "Indirect holography setup for efficient phaseless cylindrical acquisition for antenna measuement," in *8th European Conference on Antennas and Propagation (EUCAP'14),* pp. 1–2, The Hague (The Netherlands), 6–11 Apr. 2014.

[ix] **A. Arboleya**, J. Laviada, Y. Álvarez and F. Las-Heras, "Statistical analysis of the influence of mechanical errors in diagnostics applications," *7th WG Meeting and Technical Workshop, COST IC1102,* Madrid (Spain), Oct. 22–24, 2014.

[x] **A. Arboleya**, J. Laviada, J. Ala-Laurinaho, Y. Álvarez, F. Las-Heras and A.V. Räisänen, "Broadband antenna characterization based on a novel off-axis holography setup," *8th WG Meeting and Technical Workshop, COST IC1102,* Sofia (Bulgaria), May 18–22, 2015.

National conferences

[xi] **A. Arboleya Arboleya**, C. García González, Y. Álvarez López, J. Laviada and F. Las-Heras, "Millimeter and submillimeter-wave measurement system implementation," *XXXVII Simposium Nacional de la Unión Científica de Radio (URSI'12),* pp. 1–4, Elche (España), 12–14 Sept. 2012.

[xii] C. García González, **A. Arboleya Arboleya**, Y. Álvarez López, J. Laviada and F. Las-Heras, "Measurement setup for profile reconstruction at 90 GHz," *XXXVII Simposium Nacional de la Unión Científica de Radio (URSI'12),* pp. 1–4, Elche (España), 12–14 Sept. 2012.

[xiii] **A. Arboleya**, J. Laviada, J. Ala-Laurinaho, Y. Álvarez, F. Las-Heras and A.V. Räisänen, "Extrapolation of conventional off-axis holography method for broadband antenna characterization," *XXX Simposium Nacional de la Unión Científica de Radio (URSI'15),* pp. 1–4, Navarra (España), 2–4 Sept. 2015.

Book chapters

[xiv] **A. Arboleya**, J. Laviada, J. Ala-Laurinaho, Y. Álvarez, F. Las-Heras and A.V. Räisänen, "Indirect off-axis holography for antenna metrology," in *Holography,* Izabela Naydenova, Ed. Intech, ISBN 978-953-51-5033-6 (Estimated date of publication: Jan. 2017).

Other publications and works

The following publications, related to teaching activities or other collaborations have also been authored and coauthored by the author during her time as doctoral candidate in Universidad de Oviedo:

International journals

[a] J. Laviada, C. Vázquez-Antuña, R. Camblor, M. Fernández-García, **A. Arboleya-Arboleya** and F. Las-Heras, "Antenna manufacturing at VHF frequencies applied to weather-satellite data reception," *IEEE Antennas and Propagation Magazine,* vol.55, no. 3, pp. 201–211, Jun. 2013.

[b] J. Álvarez, R.G. Ayestarán, G. León, L.F. Herrán, **A. Arboleya**, J.A. López-Fernández and F. Las-Heras, "Near field multifocusing on antenna arrays via non-convex optimization," *IET Microwaves, Antennas and Propagation,* vol.8, no. 10, pp. 754–764, Jul. 2014.

International conferences and workshops

[c] C. García González, **A. Arboleya Arboleya**, Y. Álvarez López and F. Las-Heras, "Measurement setup for profile reconstruction on the 90 GHz frequency band," *IEEE International Symposium on Antennas and Propagation and USNC / URSI National Radio Science Meeting (AP-S / USNC-URSI),* Florida (USA), 7–13 Jul. 2013.

[d] C. García-González, Y. Álvarez-López, F. Las-Heras, J. Laviada, **A. Arboleya-Arboleya**, P. Rocca, G. Oliveri and A. Massa, "Inverse scattering problem of homogeneous dielectrics using genetic algorithms," in *8th European Conference on Antennas and Propagation (EUCAP'14),* pp. 1–2, The Hague (The Netherlands), 6–11 Apr. 2014.

[e] Y. Álvarez, A. Bisognin, J. Laviada, **A. Arboleya**, F. Gianesello, R. Pilard, D. Titz, F. Las-Heras, J.R. Costa, C.A. Fernandes, F. Devillers and C. Luxey, "Phaseless techniques for probe-fed 140 GHz 3D printed lens antennas NF-FF transformation," *9th WG Meeting and Technical Workshops, COST IC1102,* Villefranche-sur-Mer, France, Oct. 21-23, 2015.

National conferences

[f] **A. Arboleya Arboleya**, J. Álvarez Muñiz and F. Las-Heras, "Plataforma de difusión y demostración de la observación terrestre para aplicaciones medioambientales," *VII Congreso Nacional de Evaluación de Impacto Ambiental (CONEIA 2013),* Oviedo (Spain), 13–15 Mar. 2013.

[g] J. Romeu, A. Broquetas, L. Jofre, M. Alonso, J. Abril, E. Nova, D.S. Escuderos, M.F. Bataller, A. Berenguer, F.L.-H. Andrés, J. Laviada, Y. Álvarez López, C.G. González, **A. Arboleya**, L. E. García, and D. Segovia, "Terasense: Thz tomographic biospectrometer," *XXVIII Simposium Nacional de la Unión Científica Internacional de Radio, (URSI'13),* Santiago de Compostela, Spain, 11–13 Sep. 2013.

[h] **A. Arboleya** and F. Las-Heras, "Improving independent learning and communication skills of students in last year of engineering degrees through the use of project-based learning methodologies," *Tecnologías, Aprendizaje y Enseñanza de la Electrónica (TAEE 2014),* Bilbao (Spain), 11-13 Jun. 2014.

[i] J. Romeu, A. Broquetas, L. Jofre, D. Sánchez-Escuderos, M.A. Berenguer, M. Baquero-Escudero, J. Laviada, Y. Alvarez, R. Camblor, S. Ver-Hoeye, F. Las-Heras, C. García, C. Vázquez-Antuña, **A. Arboleya**, M. Fernández, G. Hotopan, L. E. García, D. Segovia and J. Montero de Paz, "TeraSense: THz Tomographic Biospectrometer," *XXiX Simposium Nacional de la Unión Científica Internacional de Radio, (URSI'14),* Valencia (Spain), 3–5 Sept. 2014.

International research stays and short visits

During the development of this doctoral thesis the author carried out a research stay and a short visit in the Radio Science and Engineering Department and Millilab, at Aalto University. The developed work in collaboration with part of the research team of the host University originated publications [**II**]-[**IV**], [x] [xiii] and [xiv].

1. Radio Science and Engineering Department and MilliLab, Aalto University, Finland.
    - Stay under supervision of Professor Antti V. Räisänen .
    - Duration: From September 15th, 2014 to December 15th, 2014.
    - Fundings: Ayudas económicas de movilidad de excelencia para docentes e investigadores de la Universidad de Oviedo.
2. Radio Science and Engineering Department and MilliLab, Aalto University, Finland.
    - Short visist under supervision of Dr. Juha Ala-Laurinaho.
    - Duration: From 13 to 25 March, 2015.
    - Fundings: European Science Foundation. New Focus Programme (New Frontiers in Millimetre / Submillimetre Waves Integrated Dielectric Focusing Systems).

Research projects and funding

The doctoral thesis has been developed in the framework of several national funded research projects in which the candidate has actively participated:

1. iScat, *Inverse scattering techniques for imaging: new approaches and measurement techniques*, TEC2011-24492. Ministerio de Ciencia e Innovación. Programa Nacional de Proyectos de Investigación Fundamental, VI Plan Nacional de Investigación Científica, Desarrollo e Innovación Tecnológica, 2011–2014.
2. PortEMVision, *New Generation of Portable Electromagnetic Scanners Based on Computer Vision*, TEC2014-55290-JIN. Ministerio de Economía y Competitividad. Proyectos de I+D+I para jóvenes investigadores sin vinculación o con vinculación temporal correspondientes al Programa Estatal de Investigación, Desarrollo e Innovación Orientada a los Retos de la Sociedad. Plan Estatal de Investigación Científica y Téncica y de Innovación, 2015–2017.
3. MIRIIEM, *Multiple Information Resources for Improving Inverse EM techniques for reflectometry and imaging applications*, TEC2014-54005-P. Ministerio de Economía y Competitividad. Proyectos de I+D "EXCELENCIA" y Proyectos de I+D+I "RETOS INVESTIGACIÓN", 2015–2017.
4. Grant LINE-525-002. Universidad de Oviedo, 2015-2016.
5. Grant FC-15-GRUPIN14-114. Fondos FEDER, Plan Regional. Grupos de investigación Principado de Asturias, 2016.

Furthermore, the developed measurement system has also been employed for exhaustive measurement campaigns, within the framework of other National and European funded research projects in which other members of the TSC-Uniovi research group where involved:

1. TERASENSE, *Terahertz Technology for Electromagnetic Sensing Applications*, CONSOLIDER- CSD2008-00068. Ministerio de Ciencia e Innovación, 2009–2013.
2. INSIDDE, *INtegration of technological Solutions for Imaging, Detection, and, Digitisation of hidden Elements in artworks*, Grant agreement no. 600849. FP7 - THEME [ICT-2011.8.2] ICT for access to cultural resources, 2013–2015.

Patents

Patent application no. P201600073 from 21/01/2016. *Sistema aerotransportado y métodos para la detección, localización y obtención de imágenes de objetos enterrados y la caracterización de la composición del subsuelo.* Admitida a trámite.

Awards and recognition

The developed work of the author as a PhD candidate has been recognized by two awards one at a national level, given by the *Ministry of Education of Spain* and the other one given by the *Society of Partners* of the University of Oviedo:

1. *XI Arquímedes Contest: Initiation to Scientific Research*; Government of Spain, Education, Culture and Sports Department, November 2012.

    - Special price of the jury to the research work *XYZ scanner for radiation and scattering measurements with applications in the security and medical imaging fields*.

2. *II awards of the Society of partners of the Technical School of Engineering of University of Oviedo*, March 2013.

    - Award given by the partner *BIC Asturias* (European Business and Innovation Centre) to the work *XYZ scanner for radiation and scattering measurements*.

Author's contribution

This section states the stance of the author and the coauthors for each of the publications that compose this dissertation.

- **Publication [I] "Phaseless antenna diagnostics based on off-axis holography with synthetic reference wave"**
  This publication is the result of a collaborative work with Dr. Jaime Laviada, who was the main author. The candidate was in charge of the the design and preparation of the measurement setup and performed the measurements. She also assisted in the data processing and writing of the manuscript.

- **Publication [II] "Millimeter-wave phaseless antenna measurement based on a modified off-axis holography setup"**
  This publication was mainly done by the author. The main idea came up after some discussion of her previous works with Dr. Juha Ala-Laurinaho during her stay in Aalto University. The candidate formulated the methods in detail, performed numerical simulations for their validation and carried out the measurements and post-processing of the data. She was also responsible for writing the publication. The measurements and post-processing of the data were performed at MilliLab, under supervision of Dr. Juha Ala-Laurinaho. The rest of the coauthors supervised the work.

- **Publication [III] "Phaseless characterization of broadband antennas"**
  The author has provided the main contribution to this publication. The author formulated the idea jointly with Dr. Jaime Laviada and developed the algorithms and the numerical simulations. She also designed the measurement setup and carried out the measurements, post-processing and writing of the publication. Part of the measurements, carried out at MilliLab, were supervised by Dr.Juha Ala-Laurinaho. The rest of the coauthors supervised the work.

- **Publication [IV] "Reduced set of points in phaseless broadband near-field antenna measurement: effects of noise and mechanical errors"**
  This work was mainly done by the author. Dr. Jaime Laviada assisted in the calculation of the reduced set of points. The author designed the measurement setup and carried out the measurements and post-processing and also developed the Monte Carlo method for the error analysis. The writing of the paper was done by the author and supervised by the rest of coauthors.

- **Publication [V] "Versatile measurement system for imaging setups prototyping"**
  This is a result of a collaborative work. The author design the measurement setups and performed the measurements and the post-processing of the data. Dr. Jaime Laviada assisted in the development of the post-processing algorithms. The contribution was written and presented by the author and supervised by the rest of the coauthors.

- **Publication [VI] "A modified phaseless inverse scattering setup based on indirect holography implemented at submillimeter-wave band"**
  This is the result of a collaborative work. Dr. Jaime Laviada had the main responsibility for formulating the method, the data processing and the writing of the paper. Dr. Yuri Álvarez participated in the data processing and the author was in charge of the design and preparation of the measurements setup, performed the measurements and assisted in the preparation of the manuscript.

- **Publication [VII] "Phaseless synthetic aperture radar with efficient sampling for broadband near-field imaging: theory and validation"**
  This publication is the result of a collaborative work with Dr. Jaime Laviada. The author designed the measurement setup and performed the measurements. She also collaborated in the analysis and post-processing of the data and in the writing and preparation of the manuscript. Dr. Yuri Álvarez and Cebrián García collaborated in the object reconstruction tasks and Prof. Fernando Las-Heras supervised the work.

- **Publication [VIII] "Broadband synthetic aperture scanning system for three-dimensional through-the-wall inspection"**
  This publication is the result of a collaborative work with Dr. Jaime Laviada, who was the main author. The candidate was in charge of the design and preparation of the measurement setups and performed the measurements. She also assisted in the data post-processing and the preparation of the manuscripts. Dr. Fernando López-Gayarre provided the construction materials employed in the setups and Prof. Fernando Las-Heras supervised the work.

- **Publication [AI] "Millimeter and submillimeter planar measurement setup"**
  This work was mainly contributed by the author who designed and implemented the measurement system and setup and wrote and presented the contribution. Dr. Yuri Álvarez and Prof. Fernando Las-Heras supervised the work.

- **Publication [BI] "Error characterization tool for planar near-field antenna measurement and diagnostics applications"**
  This work was mainly contributed by the author who designed and implemented the tool and performed the measurements. The rest of coauthors supervised the work. The contribution was written and presented by the author.

- **Publication [BII] "Study of the influence of mechanical errors in diagnostics applications by means of statistical analysis"**
  This work was mainly contributed by the author who designed and implemented the measurement setup, performed the measurements and developed the Monte Carlo method for the statistical analysis. Preparation and presentation of the manuscript were also done by the author. The rest of coauthors supervised the work.

List of acronyms

2D	Bi-Dimensional.
3D	Three-Dimensional.
ACE	Antenna Centre of Excellence.
APS	Antennas and Propagation Society.
AUT	Antenna Under Test.
AWPL	Antenna and Wireless Propagation Letters.
CAMA	Conference on Antenna Measurements and Applications.
CNEAI	National Commission for the Evaluation of Research Activity.
ESF	Edge Spread Function.
ESS	Equivalent Stray Signal.
EuCAP	European Conference on Antennas and Propagation.
FD	Frequency Domain.
FF	Far-Field.
FMM	Fast Multipole Method.
FoV	Field of View.
FPA	Focal Plane Array.
FT	Fourier Transform.
GHz	GigaHertz.
GPIB	General-Purpose Interface Bus.
GPR	Ground Penetrating Radar.
GPU	Graphics Processing Units.
GRSL	Geoscience and Remote Sensing Letters.
IEEE	Institute of Electrical and Electronics Engineers.
IF	Impact Factor.
iFMM	inverse Fast Multipole Method.
ISBN	International Standard Book Number.
ISSN	International Standard Serial Number.
ITU-R	Radiocommunication sector of the International Telecommunication Union.

JCR	Journal Citation Reports.
JIMTW	Journal of Infrared Millimeter and Terahertz Waves.
NF	Near-Field.
NIST	National Institute of Standards and Technology.
OEWG	Open-Ended Wave Guide.
OSI	Optimal Sampling Interpolation.
OUT	Object Under Test.
PNF	Planar Near-Field.
PSF	Point Spread Function.
PWE	Planar Wave Expansion.
PWS	Planar Wave Spectrum.
RAM	Radar Absorbing Material.
RCS	Radar Cross Section.
RF	Radio Frequency.
RMS	Root Mean Square.
RSS	Root of Sum of Squares.
RX	Receiver.
SAR	Synthetic Aperture Radar.
SCI	Science Citation Index.
SCPI	Standard Commands for Programmable Instruments.
SGH	Standard Gain Horn.
SLL	Secondary Lobe Level.
TAP	Transactions on Antennas and Propagation.
TD	Time Domain.
THz	TeraHertz.
TX	Transmitter.
URSI	International Union for Radio Science.
UWB	Ultra Wide Band.
VNA	Vector Network Analyzer.

Notation

A	Amplitude of a plane wave.
a_0	Input power to the AUT.
$arg\{\cdot\}$	Argument of a complex number.
b'_0	Measured electric field in the probe.
B	Frequency bandwidth.
C	Constant reference signal.
c	Speed of light.
$(\cdot)^*$	Complex conjugate.
$\otimes$	Convolution operator.
D	Distance from the antennas to the AUT in the z-axis.
D_1, D_2	Coupling equation for two orthogonal probe polarizations.
D_{aut}	Diameter of the AUT.
d_{error}	Positioning accuracy.
$\vec{d}$	Mechanical displacement.
d_m	Distance from the aperture of the reference antenna to the mirror.
d_{min}	Minimum distance between the OUT and the antennas in a monostatic setup.
d_{out}	Distance from the aperture of the RX and TX antennas to the OUT.
$d\vec{r}$	Differential of $\vec{r}$.
$\vec{E}$	Electric field vector in the spatial domain.
E_{aut}	Electric field component of the AUT in the spatial domain.
e_{aut}	Electric field component of the AUT in the spectral domain.
e_b	Error due to the monostatic approximation.
E_{FF}	Electric field component in the far-field region.
E_r	Electric field component of the reference source in the spatial domain.
e_r	Electric field component of the reference source in the spectral domain.
E_s	Electric field component scattered by the OUT in the spatial domain.
e_s	Electric field component scattered by the OUT in the spectral domain.
E_T	Tangential components of the Electric field.
E_y	Electric field y component of the retrieved field in the spatial domain.

f	Frequency.
f_c	Central frequency of the band.
FT^{-1}	Inverse Fourier transform.
$f\#$	Ratio of the diameter and focal length of a focusing element.
G_φ	Interpolation function for a closed curve.
G_{RX}	Gain of the receiver antenna.
G_{TX}	Gain of the transmitter antenna.
G_ξ	Interpolation function for an open curve.
H	Component of the hologram in the spatial domain.
h	Component of the hologram in the spectral domain.
$H_{filtered}$	Filtered term of the hologram in the spatial domain.
$h_{filtered}$	Filtered term of the hologram in the spectral domain.
H_m	Component of the *modified* hologram in the spatial domain.
h_m	Component of the *modified* hologram in the spectral domain.
H_n	Indexed hologram.
H_{op}	Component of the *opposite phase* hologram in the spatial domain.
$Im\{\cdot\}$	Imaginary part of a complex number.
I_n	Indexed difference hologram.
k	Spatial frequency domain, k-space, spectral domain.
k_0	Free-space wave number.
Ka	Frequency band from 26.5 to 40 GHz.
k_c	Free-space wave number for the central frequency of the band.
$(k_{r,x}, k_{r,y}, k_{r,z})$	Image term center for an off-axis angle in the x-, y- and z-axes.
$k_{r,x\,max}$	Image term center for the maximum off-axis angle in the x-axis.
$k_{r,x\,min}$	Image term center of the hologram for avoiding overlapping with synthesized reference waves.
k_s	Extension of the k-space.
Ku	Frequency band from 12 to 18 GHz.
(k_x, k_y, k_z)	x, y and z components of the wave vector.
K_{xx}	Factor for the expanded uncertainty calculation.
L	Length of the acquisition plane.
L_{eff}	Effective length of the transmission line connecting the reference antenna and the source.
mm-	Millimeter wave frequency band from 30 to 300 GHz.
n	Index.

$\|\cdot\|_2$	*Euclidean* distance.
N_ϕ	Number of phase shifts.
O	Origin of coordinates.
p	Distance from the origin of coordinates to the antennas.
P_r	Power coupled between transmitter and receiver antennas.
P_{TX}	Power transmitted by the transmitter antenna.
q	Index.
$\vec{R}$	Vector from the antennas to the center of the OUT.
$Re\{\cdot\}$	Real part of a complex number.
r_{FF}	Far-field distance.
R_{max0}	Maximum OUT range.
$\vec{R}'$	Vector from the antennas to the center of the OUT in the modified points.
$\vec{r}_{rx}$	Position vector of the receiver antenna.
$\vec{r}_{tx}$	Position vector of the transmitter antenna.
$\hat{R}$	Unitary vector of R.
$\vec{r}$	Position vector.
s	Index.
S	Spectrum of the scattered electric field in the spectral domain.
submm-	Submillimeter wave frequency band from 0.3 to 3 THz.
T_{PWS}	FT of the Electric field with respect to its tangential components.
T	Plane Wave Spectrum.
T_{TD}	Duration of the signal in the time domain.
t	Time.
t_{aut}	Starting time of the signal coming from the AUT.
t_d	Delay introduced in the reference branch of the setup for broadband phaseless SAR.
t_{min}	Starting time of the scattered field in a monostatic setup.
T'	Plane wave spectrum of the probe antenna.
t_r	Starting time of the signal coming from the reference source.
T_T	Tangential components of the PWS.
U_c	Combined uncertainty.
u_i	Uncertainty contribution of an individual term i.
U_k	Expanded uncertainty.
$\hat{a}, \hat{b}, \hat{c}...$	Unitary vector notation.
(u, v, w)	Direction cosines coordinate system.

$\vec{a}, \vec{b}, \vec{c}$	Vector field notation.
W	Frequency band from 75 to 110 GHz.
ω	Angular frequency.
W_k	Bandwidth of the spectral terms of the hologram.
X	Frequency band from 8 to 12 GHz.
(x, y, z)	Cartesian coordinates X,Y,Z.
(x', y', z')	Modified Cartesian coordinates of the acquisition plane in holography formulation with mechanical displacements, or position of the sources in Fourier-based imaging techniques.
xx	Confidence level of the expanded uncertainty.
z_0	Constant z coordinate of the acquisition plane.
α	Tilt angle with respect to the maximum radiation direction.
β	Complementary angle of α.
∂/∂	First order partial derivative.
∂/∂^2	Second order partial derivative.
δx, δy	Spatial sampling resolution in the x- and y-axes.
Δf	Frequency sampling step.
$\Delta\phi$	Phase step of the reference field in the acquisition plane.
$\Delta x, \Delta y$	Spatial sampling step in the x- and y-axes.
$\Delta\tau$	Spread of the image terms in the time domain.
$\Delta\varphi$	Sampling step of the azimuthal coordinate in the reduced set of points.
$\nabla\cdot$	Divergence operator.
∇^2	Laplacian operator.
γ	Phase factor.
λ	Free-space wavelength.
λ_c	Free-space wavelength for the central frequency of the band.
ϕ	Spherical coordinate.
φ	Azimuthal coordinate for the reduced set of points and plane-polar domains.
φ_b	Phase error due to the monostatic approximation.
φ_f	Phase error due to the multi frequency acquisition.
φ_p	Phase error due to the positioning error.
$\Pi(\cdot)$	Rectangular window in the spectral domain.
π	Ratio of a circle's circumference to its diameter.
ψ	Reflectivity of a target in the spatial domain.
Ψ	Reflectivity of a target in the spectral domain.
ρ	Radial coordinate for the plane-polar domain.

Γ_p	Reflection coefficient towards the probe.
Γ_r	Reflection coefficient towards the receiver.
τ_n	Indexed phase-shifts.
θ	Spherical coordinate.
θ_a	Angle of the aperture edge of the AUT and the center of the acquisition plane.
θ_b	Coverage angle in monostatic radar setups.
θ_m	Off-axis angle of the mirror and the acquisition plane.
θ_r	Off-axis angle of the reference antenna and the acquisition plane.
θ_v	Valid angular margin of the NF-FF transformation.
ξ	Radial coordinate for the reduced set of points domain.
ξ_n	Indexed radial coordinate for the reduced set of points domain.

Table of contents

CHAPTER

1

Introduction

1.1 Introduction

New approaches in antenna measurement techniques are constantly emerging to cope with the rapid development of fabrication technologies and to provide accurate characterization for different types of antennas (broadband, electrically large, on-wafer, smart antennas, etc.). Multiple efforts are being made in

developing post-processing techniques to improve performance of conventional measurement ranges [1]. In addition new advanced measurement ranges such as multiprobe systems [2], configurable robotic scanners [3] or probe-fed antenna measurement systems [4] have also appeared.

Furthermore antenna diagnostics gives a non-invasive way of quickly finding design or fabrication failures from the analysis of their extremely near field or their equivalent currents on the antenna surface and fast and accurate methods to this end have spread fast [5–8],[**I**].

Inverse scattering and electromagnetic imaging techniques have also received great interest, specially at mm- (millimeter-) and submm- (submillimeter) wave bands (see Section 1.4 for definition) in which great research effort has been made during the last decades. These techniques are very useful for a wide variety of applications in fields such as surveillance [9], security [10], medicine [11], or detection of buried objects [12], due to its non-destructive nature and the capabilities to retrieve high resolution images.

The aforementioned techniques for both, antenna measurement and diagnostics and inverse scattering and electromagnetic imaging applications, can be divided into two main families: Frequency Domain (FD) and Time Domain (TD) techniques, each of them presenting several advantages and disadvantages.

The general approach for the implementation of TD measurement or imaging systems typically consists of a pulse generator and a oscilloscope [13–15] or a network analyzer with TD modules [11, 16, 17]. The main advantage of these systems is their higher measurement speed compared to FD systems in which the frequency sweep of the working frequency band requires more time than the generation of a short wave pulse [18, 19]. However, TD systems exhibit lower dynamic range and are likely to have poorer performance, particularly when used in complex scenarios [11].

Regarding antenna measurement and diagnostics applications these TD systems are specially appropriate for broadband characterization [16, 17], moreover, specific Near-Field (NF) formulation has been developed to solve the poor dynamic range issue [20]. In the imaging field, TD systems have been widely employed in biomedical, Ground Penetrating Radar (GPR) or long-range radar detection applications in the microwave bands or for development of short-range radar for example for automotive applications in the mm-wave band.

On the other hand, basic instrumentation for a FD acquisition system consists of a frequency synthesizer and a receiver that is usually phase locked to the frequency sythesizer to enable phase acquisition. In general, the described setup is implemented by means of a Vector Network Analyzer (VNA) operating in the FD [21]. Main advantages of FD systems are their high accuracy and the out-

standing number of available techniques in NF and in Far-Field (FF) that can be applied to many different acquisition geometries for both antenna measurement and imaging systems.

Nevertheless, those conventional techniques for antenna characterization and diagnostics as well as for inverse scattering require, in general, the knowledge of the amplitude and phase of the field. Phase acquisition is a challenging matter that requires complex and expensive equipment, specially at mm- and submm-wave bands due to the high thermal stability requirements and the effect of the errors [22, 23], mostly resulting from thermal drift (Figure 1.1(a)) in the acquisition system and cable flexing (Figure 1.1(b)).

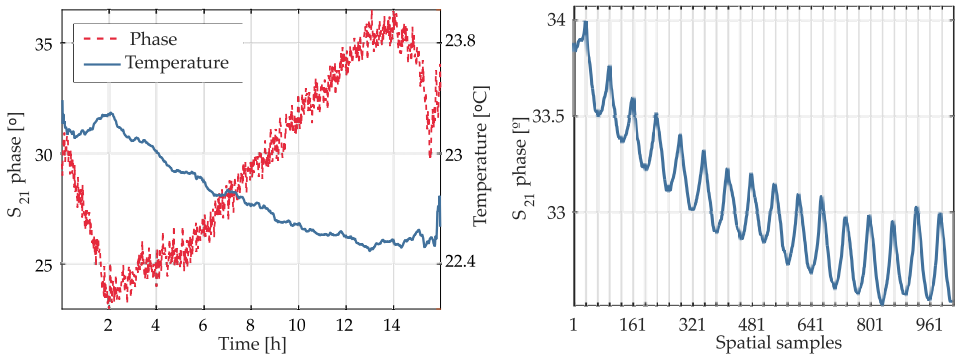

(a) (b)

Figure 1.1: Phase errors in a Planar Near-Field (PNF) measurement range. (a) Phase and temperature variation of the S_{21} parameter with stationary Antenna Under Test (AUT) and probe at 275 GHz along 16 hours with no room temperature control. (b) Cable flexing errors in the S_{21} phase for an antenna acquisition setup at 20 GHz. x axis ticks are coincident with direction changes of the probe in the sweept axis [24].

For the previous reasons many authors have focused in the development of the so called *phaseless techniques* capable of retrieving the phase of the fields from amplitude-only measurements, with the consequent reduction in complexity and cost of the systems [25, 26]. These techniques, can indistinctly be applied to both, antenna measurement and diagnostics, and imaging setups, and can be divided into two main groups depending on the implementation approach: iterative and interferometric techniques.

Most of iterative techniques are based on the acquisition of the amplitude of the unknown field in two or more surfaces [5, 27, 28]. Then the phase is retrieved through an iterative process that propagates the field back and forward from one surface to another until a condition for the phase is satisfied from both

of the surfaces. These techniques are very popular because they involve minor changes in conventional setups, nevertheless they can suffer from stagnation and its convergence is strongly related to the initial imposed conditions or first guess solution. Some authors have proposed the use of two probes [29], avoiding the need of performing two different spatial acquisitions.

Hybrid approaches based on a modified probe composed of two antennas interfering each other [30] have also been developed. The phase is retrieved after an iterative procedure for the minimization of the phase difference between both probes.

On the other hand, most of interferometric approaches, such as indirect off-axis holography, rely on the use of a reference field, known in amplitude and phase, that is combined with the unknown field creating an interference pattern and making possible to retrieve the unknown phase by means of a filtering process and iteration-free from the direct acquisition of the amplitude hologram [31–33]. Different techniques to avoid phase measurement of the reference field have been developed; also wide research has been made to develop new filtering techniques and to lower sampling requirements as it will be addressed in Chapter 2.

Indirect off-axis holography is the selected approach for the developing of new measurement techniques for antenna measurement and imaging applications in this thesis.

1.2 Motivation and scope

As previously mentioned, a wide variety of applications related specially to communication systems, imaging or remote sensing, mainly in the mm- and submm-wave bands are being developed thanks to the novel antenna and microwave devices design and manufacturing techniques. Despite of all the advances in mm- and submm-wave technologies, most of the applications are not yet at an affordable level in terms of cost, compactness or complexity.

This thesis is devoted to the achievement of two main goals; on the one hand, the design and development of a versatile measurement range that allows for the implementation of antenna measurement setups along with validation tests for different imaging setups and, on the other hand, the need to find cost effective solutions in measurement systems and techniques for antenna characterization and electromagnetic imaging.

The expected cost-effectiveness is based on minimizing the complexity of the systems, reducing the measurement time and developing robust algorithms not

easily affected by errors such as mechanical and electrical. Novel phaseless algorithms based on indirect off-axis holography, for antenna measurement and diagnostics and for imaging applications have been developed focusing on efficient sampling, reducing the number of components or extending the methods to be efficiently employed with broadband systems.

1.3 State of the art

1.3.1 Antenna measurement and diagnostics

NF ranges emerged with the need of accurate characterization of antennas such as electrically large or low-sidelobe antennas, specially at mm- and submm-wave frequency bands that are not suitable for conventional FF characterization, mainly for the large size, costs and lack of accuracy of the measurement ranges needed for housing that type of setups [34].

In NF ranges, the field acquisition is performed in the radiating region, which spans from a distance from λ of the aperture of the AUT to the FF border, defined by $r_{FF} = 2D_{aut}^2/\lambda$ (with $r_{FF} >>> \lambda$) as shown in Figure 1.2.

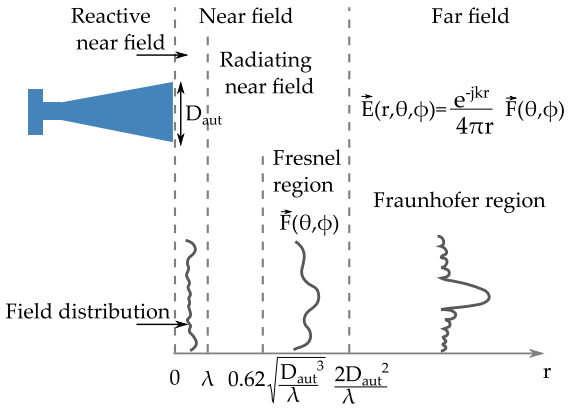

Figure 1.2: Electromagnetic field regions fo antenna measurement.

Since NF scanners appeared in 1950 [34], research has focused in the formulation of accurate techniques for the computation of the antenna FF pattern [35] and main parameters such as gain, directivity or polarization. Nowadays NF-FF transformation is one of the most extended approaches for antenna characterization.

1.3.1.1 Planar near-field measurement systems

In particular, PNF measurement ranges, as the one developed in this work, are well suited for testing high gain antennas at high frequency bands [36] providing excellent results for the characterization of gain, axial ratio, close sidelobes (up to -55 to -60 dB relative to the main lobe level [37]).

PNF measurement ranges also provide a good environment for zero G effects, when the layouts are set in horizontal mode and the capability of mechanical surface measurements with relative low complexity and moderate implementation and operation costs [36].

Other important features of this type of systems are the excellent acquisition speed for complete antenna pattern characterization, easy alignment procedures and excellent antenna access.

Instrumentation of the Radio Frequency (RF) subsystem can slightly vary depending on the system but generally a VNA is employed as RF source and receiver. Frequency extension modules can be added to the subsystem depending on the working frequency. The AUT is connected to the VNA output port and the probe antenna is connected to the input. Normally a reference signal from the source is conveyed to the receiver end by means of a directional coupler. Independent RF sources and receivers can be used instead of the VNA and in case of phaseless acquisitions, the receiver can be implemented with a simple power detector, lowering the costs and the complexity of the RF subsystem.

Synchronization of the RF and mechanical subsystem is usually made from a control interface on a dedicated computer that can also be employed for data representation and mathematical transformation of the acquired data. Connection between the different elements is usually made through General-Purpose Interface Bus (GPIB) or ethernet buses.

Two different approaches can be followed for the implementation of NF-FF transformation software [35]. The first one is based on the computation of the equivalent currents of the source by means of a backpropagation of the acquired data and then, calculation of the FF pattern is made employing integral equations [38]. The other approach is based on the expansion of the radiated fields in terms of planar wave functions, then the NF acquisitions are used as the coefficients of that expansion to obtain the FF pattern [39].

NF probes need to comply with several requirements. Generally the antennas used as probes for a PNF are required to have no pattern nulls in the forward hemisphere which implies low directivity and physically and electrically small antennas. Besides wideband antennas with a small return loss and time invariant gain are required. Other important features are good polarization purity and good front to back ratio [22].

Typical antennas used as NF probes are rectangular and cylindrical waveguides and pyramidal and corrugated horns. Their pattern have to be characterized in order to apply probe correction algorithms during the NF-FF transformation.

Different system layouts can be employed in the implementation of a planar measurement range being the most common the vertical (tower or T-scanner) and horizontal (box or frame scanner) rectangular configurations shown in Figure 1.3. Planar setups using polar or bipolar acquisition surfaces are also very extended [40, 41]. Dimensions of the scanners can vary from a meter or less, as for the system developed in this work (see Appendix A), to several meters to test very big antennas or for Radar Cross Section (RCS) measurements [42].

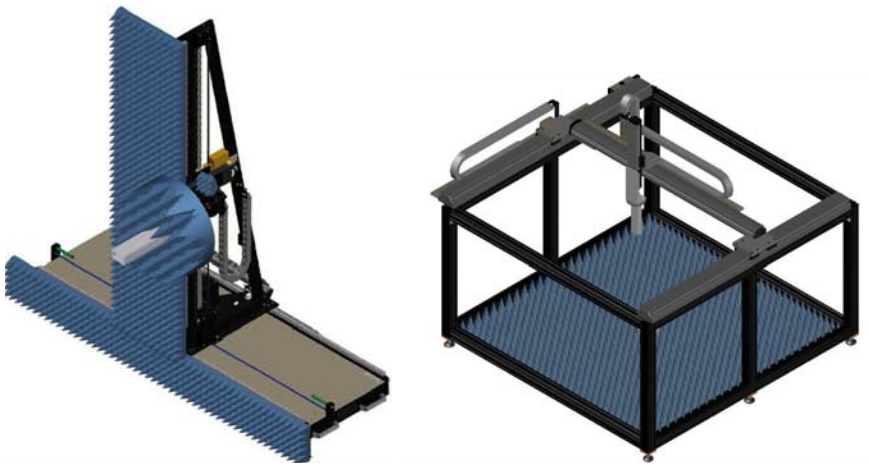

(a) (b)

Figure 1.3: Most common layouts in planar measurement range. (a) Vertical and rectangular [36], and (b) horizontal and rectangular.

Both types of scanners consist on, at least, two orthogonal carriages, supported on a rigid framework to create planar scanning surfaces. Manual micropositioners for fine adjustments of the probe and alignment are usually included. Modern implementations, as the one from the schematic shown in Figure 1.3(b), are based on four axis linear stages (one of them duplicated and working as master/slave), allowing for Three-Dimensional (3D) arbitrary acquisitions [A**I**].

Frame scanners offer improved rigidity and better positioning accuracy over T-scanners although the metallic frame act as a scattering source. Frame scanners also offer a good environment for testing big antennas with zero-G effects and uniform gravitational pull. On the other hand, some of the advantages of the T-scanners are the reduced multipath effects and the easy access to the AUT. However, mechanical vibrations are non uniform in T-scanners having larger effects in

the upper side of the scanner. Also thermal stratification can pose a problem for large T-scanners [22].

Frequency of operation ranges from microwaves to submm-wave bands and is limited for the mechanical accuracy of the positioners (and for the RF instrumentation) [43]. Normally a tolerance of $\lambda/50$ is required. Positioning error has to be calibrated, commonly by means of laser trackers. Then positioning errors can be compensated during post-processing, as it will be addressed later in this section.

In order to reduce the acquisition time and the effect of vibrations, acquisitions are usually performed *on the fly*, that is, without stopping the probe at each point. However, some commercial tracking devices cannot provide the required accuracy if the probe is in motion [22, 43]. Special attention has to be given to the configuration of the measurement device, since large number of averages or narrow intermediate frequency filter bandwidth can slow the acquisition time introducing errors in the measurements. It is possible, though, to perform *step by step* acquisitions and stop the probe at each acquisition point. In this case, more accurate acquisition are performed, but at the expense of increasing the acquisition time. Besides, frequency sweeps can be made when the measurements are taken step-by-step, minimizing the impact of continuous sweep positioning errors, and enabling broadband acquisitions in the frequency domain [**III**]-[**IV**].

1.3.1.2 **Main error sources and post-processing techniques**

Error analysis is essential for NF techniques, which involve complex mathematical developments in the computation of the FF pattern (see Section 2.1) that requires very precise data [34]. Accuracy requirements in the FF will determine the maximum tolerances and allowed truncation and sampling requirements in the NF acquisition [44].

Main sources of error in PNF measurements were identified and analyzed in [45–48]. Since then NF measurement techniques have been developed to increase accuracy, throughput and lower costs.

Accuracy is mainly related to the data acquisition process: probe characterization and errors in the Planar Wave Spectrum (PWS) arising from measurement data contaminated with truncation, aliasing, random or other type of errors [34, 46], as it will be addressed next.

The effect of the probe has to be removed from the computed FF data. Thus several correction techniques focusing on the probe pattern [34, 49, 50], gain [51], polarization [52] and alignment [53] in the measurement setup have been developed.

Errors regarding the measurement data are primarily systematic errors [46] that can be compensated when correctly characterized. These errors are mainly related to the acquisition process, i.e. aliasing or truncation of the measurement surface, to the mechanical subsystem, as alignment between antennas, to the measurement subsystem, i.e. receiver non linearities, cable flexing, dynamic range and leakage error sources, or to the measurement facility as multiple reflections, or room scattering [54].

Aliasing issues, which are related to the sampling of the acquisition plane [34, 48], are a main concern in off-axis holography [31, 55]. Sampling requirements for conventional Planar Wave Expansion (PWE) NF-FF transformation will be addressed in Section 2.1 and particularized for indirect off-axis holography in Section 2.4.

In short, for a field with band-limited spectrum, aliasing can be avoided if the *Nyquist* sampling criteria is satisfied [46]. However, sampling rate can be reduced if only a small FF angular margin is needed; or increased if evanescent modes are being considered. Relationships between sampling and valid angular marging are given in [56] for the case of considering an aperture antenna.

Truncation of the acquisition plane defines the valid angular margin of the FF pattern [34]. This margin depends on the size of the acquisition plane and its distance to the AUT, thus the lower limit is established by the physical size of the AUT [46]. Although small distances will maximize the angular margin for a given scan plane size, the effect of other types of error such as multiple reflections will influence the acquisition. Besides sampling requirements are more demanding if the scan plane distance is shortened and the evanescent portion of the field has to be taken into account [47]. Thus, a trade off between either maximizing angular coverage along with reduced truncation or minimizing multiple reflection and relaxing the sampling rate has to be made.

Techniques for reducing the effect of truncation errors are based on different methodologies. First group attempts to mitigate the erroneous ripples that appear inside the valid angular region by means of the use of smooth tappered windows for the NF data [57], while second group is based on extrapolating the known NF data outside the valid angular region [58, 59]. Other techniques such as adaptative truncation by optimization of the scan plane limits based on constant field intensity contours [60], have also been probed successful. The use of the so-called *poliplanar* acquisitions [22] in PNF systems also mitigates the effect of the finite scan plane and helps widening the valid angular margin of the FF pattern.

Errors introduced by the mechanical subsystem can be divided into alignment and positioning errors. Alignment errors include orthogonality errors of the scanner and aligment of the AUT and the probe [61]. Well defined methods employing

laser trackers or theodolites are used for a correct alignment, furthermore electrical procedures can also be employed for the alignment of the AUT, minimizing pointing and polarization errors [23].

Along with the aforementioned error sources the effect of positioning inaccuracies during the acquisition process have been one of the most studied types of error [31, 62, 63] leading to several correction techniques [64–68] and to transformation techniques directly from arbitrary and non-regular acquisition points [69, 70]. Precision devices such are laser-trackers are needed to accurately know the exact probe position in these techniques.

Errors associated to probe positioning have different effect in the FF; periodic positioning error concentrates its effect in a certain area of the FF pattern while the effect of random errors spread in all the angular directions [23]. Tolerances in the mechanical subsystem are defined by the accuracy requirements of the FF pattern. Accuracy of a fraction of wavelength is required for precise side lobe measurements. It is worth noting that opposite to amplitude and phase techniques, phaseless techniques are less sensitive to scan planarity or z-axis errors, which are usually the largest errors regarding probe positioning, as it has been proven in [63] for iterative techniques and in [31], [**IV**] for off-axis holography.

Multiple reflections between the AUT and the probe introduce undesirable effects in the FF such as ripple. Their effect can be reduced by means of different methods; in the classical approach the field acquired at several surfaces at distances of $\lambda/8$ is averaged [23]. Nevertheless this approach is very time consuming and more efficient techniques have been developed.

Multiple reflections as well as multipath and room scattering effects can be mitigated with the use of time gating techniques [71] which have also been proven effective for the leakage and cable flexing reduction [23]. More recent approaches are based on a spatial filtering of the aperture fields before obtaining the FF [72]. Adaptation of the spatial filtering techniques to compensate also leakage effects [73] or even to improve the dynamic range of the systems [74] have also been made.

Other type of errors related to the electrical system such as drift, non linearities, crosstalk, noise, impedance mismatch or random errors have also to be minimized to mitigate its contribution to the FF pattern [23].

Throughput can be improved in many ways such as with the use of non-redundant sampling techniques which reduce the required high volume of data [33, 69, 75, 76] or with the use of more efficient scanning surfaces rather than conventional rectangular grids i.e. plane-polar grids [76], spiral grids [77] or non conventional rectangular grids [78]. The use of dual polarized probes or multiple probes such as the ones employed in phaseless setups [29, 30] also increase effi-

ciency since the acquisition time is reduced, but at the expenses of increasing the complexity of the setup.

Finally, the techniques focused on lowering the costs are those that reduce the number of elements or the setup complexity. For example phaseless techniques presented in this work which promote simplified setups [**I**]-[**IV**].

1.3.1.3 **Uncertainty analysis**

The aforementioned error sources will introduce uncertainty in the computation of the FF pattern that can vary depending on the AUT, frequency or measurement facility. Therefore, an estimate of the total introduced uncertainty is advisable to complete every antenna measurement and absolutely mandatory in the case of high accuracy antenna measurements.

As previously mentioned, exhaustive studies have been made in order to characterize antenna measurement systems [47, 48, 79, 80] being the *NIST 18 terms* [46] one of the most employed methodologies. The need of standard procedures has motivated the work of different networks such as the Antenna Centre of Excellence (ACE) towards a unified methodology [54, 81] while the Institute of Electrical and Electronics Engineers (IEEE) standards association has published the Recommended Practice for NF Antenna Measurements [23].

A comprehensive error analysis is based on a four-step approach [46]: 1) identification of all the sources of error. 2) Measurement or estimate of the NF error sources. 3) Determination of relationships between the NF measurement errors and their effect in the FF parameters (pattern, gain, Secondary Lobe Level (SLL), beamwidth, etc.). 4) Overall uncertainty estimate by combination of the individual estimated uncertainties due to each of the studied error terms.

Error terms can be evaluated by means of three different methods [46]: mathematical analysis, self-comparison measurements, and/or computer simulations. The most appropriate way of characterization for each term is described in [23].

Mathematical analysis makes use of analytical expressions derived from general assumptions. Althought this approach is more successful for planar geometries [23], it is mainly devoted to set the upper bounds of the error [45] and usually represents the worst case scenario, with large estimate of errors [82, 83].

Self-comparison measurements procedures consist on the study of the differences in the analyzed parameters after introducing a change in the setup. These modifications are carefully selected in order to try to emphasize and isolate the effect of an individual error each time [79]. This approach is very time consuming and presents some disadvantages: i) the isolation of individual error sources is

very difficult and ii) the error characterization is only valid for an specific probe-AUT-facility combination. Furthermore, this method does not allow to perform an statistical analysis based on a large number of acquisitions [82] although effective methods have already been developed to obtain statistical evaluations from measurement comparisons [80].

Computer simulations assume a numerical form of the error and can obtain the statistical variation caused by that error in the studied FF parameters. Generally, statistical modeling of the uncertainty is computed by means of Monte Carlo analyses [79, 84]. Quality of the error estimate depends on the validity of the assumed error.

Uncertainty terms can also be categorized as either *Type A*, when the estimate is made from statistical analysis, or *Type B* if the estimate is made from available information (i.e. calibration tables, manufacturer data, etc.) and previous experience [85].

The estimated individual uncertainty from each analysis u_i can be given in terms of the change in the FF parameter expressed in dB or percent or by means of the ratio of an Equivalent Stray Signal (ESS) to the signal of the FF parameter [23].

The *combined uncertainty* U_c is obtained by means of the Root of Sum of Squares (RSS) from all the independent terms u_i, and it is normally multiplied by a constant factor K_{xx}, usually 2 or 3, to obtain the *expanded uncertainty* U_k at a confidence level of $xx\%$, which is valid because one of the main assumptions is that U_c follows a Normal distribution with an associated standard deviation [54].

Due to the subjective component in the antenna measurement uncertainty analysis, intercomparison campaigns [81, 86, 87] are an effective way of checking the validity of the adopted procedures and have helped to establish common procedures for the NF measurement ranges [23].

Although no comprehensive uncertainty analysis have been performed as part of the present thesis, the study of the effect of mechanical and electrical error terms have been made by means of an error simulation tool for the developed PNF measurement system for antenna measurement [B**I**] and diagnostics applications [B**II**]. Influence of errors in some of the proposed techniques have also been addressed in [**IV**] and [**VI**]. Main results are gathered in Appendix B.

1.3.2 **Electromagnetic imaging**

Electromagnetic imaging is a very useful tool for scenarios in which other techniques such as X-ray, infrared or visible light imaging techniques are inconvenient, unsafe or ineffective [88].

Since the first works were presented in 1930, wide research has been made to improve results and extend the working range of electromagnetic imaging applications [9, 89]. Nowadays, microwave imaging under 30 GigaHertz (GHz) is a very mature technology. Due to the excellent penetration properties in the atmosphere (see Figure 1.4) and other obscurants, imaging systems under 30 GHz have been extensivelly employed for applications such as personnel screening [v], GPR, medical imaging or surveillance radars with standoff ranges of hundreds of kilometers [9].

Above 30 GHz, atmospheric attenuation, mainly governed by the absorption properties of molecular oxygen and water, has great variability, as shown in Figure 1.4, reducing the link budget and limiting the operation range of systems in the mm- and submm- wave bands. Nevertheless, transparency of dielectric materials such as cloth and polymers, high reflectivity of skin and metalic materials and the high resolution limits at these frequency bands have attracted the interest of many researchers [89–93] despite propagation and technology limitations.

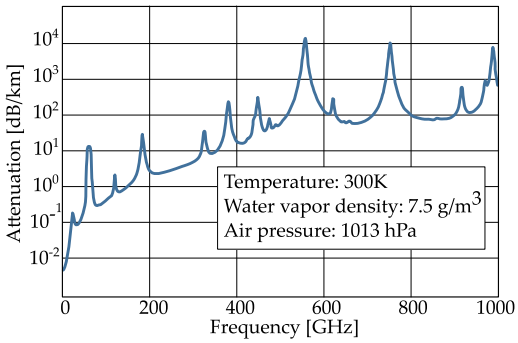

Figure 1.4: Atmospheric attenuation with frequency [94].

1.3.2.1 **Fundamentals**

Imagery can be generated in two ways, passively or actively, depending on the illumination of the scene. In passive imaging systems only natural radiation emitted and reflected from the scene is employed to retrieve the image while in active imaging systems a coherent source is employed to illuminate the scene and then the reflected field is collected.

In active imaging or simply *radar*, the signature of the Object Under Test (OUT) is therefore dominated by the reflected field. The dynamic range is increased due to the artificial illumination source, but the effects of multipath, speckle and shadowing can degrade the image quality [93]. The atmosphere attenuation windows

(see Figure 1.4) are generally chosen for the implementation of these systems, to avoid extremely large attenuation values.

On the other hand, the signature of the OUT in passive imaging depends on the brightness temperature of the scene and the emissivity of the target [9]. These systems need to be broadband in order to collect the maximum amount of radiation, specially in poor contrast scenes and in submm-wave bands due to the lack of sensitive detectors. Nevertheless contrast in mm- and submm-wave band imaging systems is strongly dependent on the working frequency [93] and image quality can be degraded in these cases due to the effect of thermal noise. Narrower bandwidth receivers and illumination of the scene make coherent active systems much less sensitive to thermal noise.

Coherent active imaging in the mm-wave band has been extensively used in the last decades to the detriment of passive systems motivating the development of many commercial systems for security [10], poor weather navigation [95] and automotive applications [96] or cracks and failure detection in civil structures [91]. But lately, development of low noise receivers using semiconductors such as gallium arsenide has given rise to systems with good thermal sensitivity [9] encouraging the development of passive imaging systems for the same kind of applications [97, 98].

On the other hand, until recently, it has been very difficult to develop high power sources and sensitive detectors for the submm-wave bands. First imaging system in this band was reported in [99]. Since then, and despite the atmosphere is strongly absorbing in this region, different systems for short range security applications or medical imaging have been reported [100].

1.3.2.2 **Imaging setups and arrangements**

Focusing in imaging setups can be accomplished by means of focusing devices such as mirrors and lenses, or during the post-processing stage.

Focused arrays can be formed by a single Receiver (RX)-Transmitter (TX) pair and a focusing element; in this type of setups the image is obtained by mechanically changing the position of the focusing element or the OUT as in [99]. Other option which have been widely employed for passive mm-wave band systems is the use of the so-called Focal Plane Arrays (FPAs) in which the position of the focusing element is fixed and the receivers correspond to the image pixels, analogous to conventional cameras [101]. Implementation of FPA systems in the submm-wave bands is often combined with mechanical scanning in order to reduce the number of elements of the array of RXs [102].

FPAs are limited to a working spatial range in which the focusing element can provide good focused images; The *f-number* or *f#*, defined as the ratio of the diameter and the focal length of the focusing element is used to determine this range. Strict spacing requirements of the elements of the array and complex circuitry are also limiting factors.

Focusing elements with small f# produce compact systems in which each element of the array can have wide beamwidth. Therefore, those systems can be implemented with small detectors closely packed [93]. Nevertheless those systems are associated to limited Field of View (FoV) due to degradation of the beam far from boresight directions. On the other hand, systems with large f# need to employ more directive elements in the array yielding larger spacing between elements and larger detector sizes that can be impracticable for some submm-wave band applications [93].

Opposite to the previous systems, non-focused arrays prescind from the focusing element performing this operation during the post-processing stage and bypassing all the aforementioned limitations regarding the FoV or the strict spacing requirements. Those systems can be implemented by means of several arrangements of the available TXs and RXs.

The most general setup, which consider arbitrary positions of the TXs and RXs, is known as *multistatic*. *Bistatic* setups can be seen as a particularization of multistatic setups in which the number of TXs is reduced to one; nevertheless, if the TX is moved to different positions, the bistatic setups can be reformulated as multistatic [**VII**].

Spatial diversity in those types of setups allows for different aspects of a target to be detected simultaneously [103] and therefore multistatic and bistatic systems are better suited for imaging targets with sudden profile variations [104], i.e. the so-called *stealth* targets, designed to minimize its return to monostatic systems in military radar applications.

Despite first radar systems in World War II had bistatic and multistatic arrangements [105, 106], the concept of monostatic radar, that will be explained next, prevailed due to several advantages such as TX-RX coherence and synchronization and better exploitation of the received power [106]. Nevertheless, multistatic and bistatic systems reappeared again with the advances in communications and navigation by taking advantage of the spatial diversity offered by the multiple earth observation and communication satellites [107]. Since then, these arrangements have been adapted for its use in microwave, mm- and submm-wave bands imaging systems mainly for security and medical applications [105, 108**?**],[v].

On the other hand, *monostatic setups* are formed by a single element acting as TX and RX. Two independent TX and RX closely placed can also be employed to implement this type of arrangement in the so-called *quasi-monostatic* configuration. When several monostatic (or quasi-monostatic) units are distributed on an array the arrangement is known as *multi-monostatic*. An equivalent implementation of multi-monostatic setups is the use of a single TX-RX unit with a raster scan in which is sometimes known as *simultaneous source-receiver scanner* [88]. This latter approach is clearly equivalent to a Synthetic Aperture Radar (SAR) [**VII**].

Multi-monostatic arrangements are simpler than multistatic or bistatic arrangements and yet, they can provide high quality results. The high angular diversity given by the different illumination of the scene with respect to monostatic setups avoid shadowing due to high specular reflections and reduce the speckle [10]. Furthermore, the apparent phase shift in the synthetic aperture is doubled (2.63) yielding twice the spatial resolution of a conventional system implemented with a stationary source [88]. Multiple SAR setups have been implemented at microwave [12, 109], mm- [10, 96, 98, 108, 110] and submm-wave bands [93],[**VI**],[ii],[iv].

1.3.2.3 **Image processing techniques**

Focusing algorithms for the retrieval of the OUT parameters are implemented either with Fourier techniques, based on plane-to-plane transformations [88, 108, 111], or by means of the tomographic approach, that make use of inverse scattering methods [11, 112],[d]. As mentioned in Section 1.1, these techniques have been adapted to their use either in the TD [11] or the FD [9, 10] and for systems operating in the NF [10, 92] or the FF [90, 95] of the OUT.

When tomographic techniques are employed, constitutive parameters of the OUT can be retrieved. Nevertheless, these techniques are generally computationally expensive and time consuming. Hence, Fourier-based methods are preferred in real-time imaging applications [10, 93, 104].

In principle, post-processing techniques need amplitude and phase information. Some techniques such as the *blind deconvolution* [113] or those based in the *Rytov* approximations [114] have been used to successfully deblurring images with no phase information in favorable cases such as imaging of weak scatterers [**VI**]. On the other hand phase retrieval techniques such as the ones enumerated in Section 1.1, based on iterative [5, 28] or interferometric [32],[**VI**]-[**VIII**] approaches, can be applied to retrieve the phase of the field in more general scenarios before applying the post-processing focusing algorithms with substantial quality improvement. An exhaustive revision of the main features of several phaseless methods can be found in [**VII**] and summarized in Table I of [**VII**].

Image resolution is related to the working frequency and the post-processing technique. When single frequency acquisitions are employed a trade-off between resolution and penetration depth must be made when the working frequency is selected. Nevertheless TD techniques or broadband frequency acquisitions increase spectral information and allow for 3D OUT retrieval with a range resolution up to $c/2B$, being c the speed of light in vacuum and B the frequency working range or bandwidth of the system.

In an ideal scenario, for optimal cross-range resolution, an imaging system should have as many detectors as the number of pixels of the image, specially for active imaging [93]. Nevertheless low feasibility of such large arrays due to bulky coherent RXs and low integration level of the systems, specially at submm-wave bands, has motivated the research in different types of layouts and post-processing techniques that allow for high resolution image retrieval from sparse arrays, lowering complexity, size and cost of the imaging systems.

Therefore, phaseless methods based on Fourier techniques applied to multi-frequency acquisitions, combined with the use of sparse sampling approaches are very powerful tools for helping in the developing of real-time, cost-efficient and high quality imaging systems. The works presented in **[VI]**-**[VIII]** contribute to that development since they are focused in creating new phaseless techniques for multi-monostatic and multi-frequency SAR based on off-axis holography and Fourier imaging, yielding less complex setups. Also sparse sampling techniques have been implemented in **[VI]** and **[VII]** in order to further simplify the systems and highly reduce the acquisition time.

1.4 Scientific contributions

This thesis contributes to experimental work in the fields of antenna measurement and diagnostics techniques and imaging applications ranging from the microwave to the submm-wave frequency bands. Main scientific and experimental achievements are listed below:

- Design and development of a cost-effective PNF measurement range for quick prototyping and validation of novel radiation and scattering measurement techniques for antenna diagnostics and characterization, and imaging applications. Feasibility of the developed measurement range, an XYZ scanner, has been demonstrated at a wide range of frequencies and for many different uses. Table 1.1 summarizes the publications that conform this dissertation grouped by topic and frequency band, **[I]**-**[VIII]**, [A**I**], [B**I**] and [B**II**].

In addition to the publications that conform this thesis, the works developed in publications [i]-[xiii], [b]-[d], [g] and [i], authored or coauthored by the candidate, have also made extensive use of the developed XYZ scanner.

- Formulation, numerical and experimental validation of a novel phaseless technique, based on indirect off-axis holography, for efficient characterization of broadband antennas, [**III**]. Non redundant sampling techniques have also been applied to the developed technique to reduce the measurement time in [**VI**].

- Modification of conventional off-axis holography antenna measurement techniques for reduced complexity with the use of: a) synthesized plane reference wave and mechanical phase shifts, [**I**], and b) radiated spherical reference wave and artificial expansion of the spectral domain for the characterization of low directivity antennas, [**II**].

- Development of a new imaging setup based on indirect off-axis holography with partial characterization of the reference signal, [**V**].

- Development of a new imaging setup based on indirect off-axis holography validated at the submm-wave band with reduced number of components, [**VI**]. The reference signal is obtained by means of direct coupling between the transmitting and receiving antennas, and the phase shifts are implemented by means of mechanical displacements, avoiding the use of a reference antenna, a directional coupler and a phase-shifter.

- Design and experimental validation of a new monostatic element for broadband and phaseless SAR applications with efficient sampling, [**VII**], and its application to through-the-wall imaging techniques, [**VIII**], which has been validated in the microwave and mm-wave bands.

- Implementation of an error analysis tool for the developed measurement range [B**I**] for the study of the impact of mechanical and electrical errors in the NF acquisition system in the final FF results [**IV**], [B**I**], and in antenna diagnostics applications, [B**II**]. Error analysis has also been done for the developed technique presented in [**VI**].

As shown in Table 1.1 the measurement system has been fully validated, together with the developed techniques, in the upper part of the microwave spectrum for the *X*- and *Ku*-bands and for the mm-wave bands *Ka*- and *W*-bands. The holographic method has also been tested at 300 GHz in the limit between mm- and submm-wave bands.

Table 1.1: Publications grouped by topic and frequency band.

	Antenna measurements			Electromagnetic imaging			
Frequency band	*X*	*Ka*	*W*	*Ku*	*Ka*	*W*	300 GHz
System validation	[A**I**]					[**V**]	
Technique validation		[**I**], [**III**], [**IV**]	[**II**], [**III**]	[**V**], [**VIII**]	[**VII**], [**VIII**]		[**VI**]
Error analysis	[B**I**]	[**IV**]	[B**II**]				[**VI**]

The aforementioned microwave bands are defined according to the *IEEE Standard 521-2002* which is a review of the standard published in 1984 [115]. The X-band ranges from 8 to 12 GHz. The *Ku*-band is defined from 12 to 18 GHz. The *Ka* and *W*- bands, respectively defined from 27 to 40 GHz and from 75 to 110 GHz, were considered as part of the mm-wave band in the 1984 standard. Nevertheless, in the 2002 standard revision, the mm-wave band is defined from 110 to 300 GHz. Despite this definition, is commonly accepted to refer to the *Ka* and W-bands also as mm-wave bands [115].

Frequency bands above 300 GHz are not included in the standard. The submm-wave band corresponds, depending on the author, to the fraction of the spectrum from 300 GHz to either 3 or 10 TeraHertz (THz) in the lower limit of the far-infrared spectrum.

1.5 Outline of the thesis

The following chapters of this thesis are organized as follows:

Chapter 2 reviews the theoretical background of the thesis, focusing in the methods used as a tool during the thesis development such as NF-FF transformation techniques, efficient sampling or the signal processing methods employed in the presented electromagnetic imaging applications.

Chapter 3 is an overview of the novel techniques developed for antenna measurement and diagnostics applications described and validated in publications [**I**]-[**IV**] while Chapter 4 is devoted to the novel indirect off-axis techniques developed regarding imaging systems and applications reported in publications [**V**]-[**VIII**].

Chapter 5 remarks the main conclusions of the work and outline the future research lines.

Finally, the main features of the designed PNF measurement range, described in publications [A**I**] and [**IV**] are presented in Appendix A. Appendix B contains several error analysis tests, described in publications [B**I**] and [B**II**], carried out in order to characterize the measurement system performance, mainly for antenna measurement and diagnostics applications.

CHAPTER

2

Theoretical background

The objective of this chapter is to introduce the different techniques used through the dissertation such as the NF-FF transformation (Section 2.1), Fourier-based imaging post-processing methods (Section 2.2) and efficient sampling techniques (Section 2.3), as a tool for developing and validate the novel proposed techniques based on indirect off-axis holography, whose basis is introduced in the final part of the chapter (Section 2.4).

The numerical tools employed for developing the mentioned methods are MATLAB [116] and Feko [117].

2.1 Planar NF-FF transformation in antenna measurement

The PWE is one of the most extended methods to perform the NF-FF transformation due to the close relationship between the asymptotic representation of the FF of an antenna and the PWS representation of its radiated field.

2.1.1 Angular spectrum of plane waves

The angular spectrum of plane waves, or simply the PWS, describes the decomposition of an electromagnetic field $\vec{E}(x,y,z)$, in a homogeneous, isotropic, linear and source-free medium, in an infinite number of plane modes traveling in different directions described by the wave vector $\vec{k_0} = k_x\hat{x} + k_y\hat{y} + k_z\hat{z}$.

The modes, or expansion coefficients, are the solutions of the Helmholtz equation

$$(\nabla^2 + k_0^2)\vec{E}(x,y,z) = \left(\frac{\partial^2}{\partial x^2} + \frac{\partial^2}{\partial y^2} + \frac{\partial^2}{\partial z^2} + k_0^2\right)\vec{E}(x,y,z) = 0 \tag{2.1}$$

being k_0 the magnitude of the wave vector, usually known as the wave number, defined as $k_0 = 2\pi/\lambda = \sqrt{k_x^2 + k_y^2 + k_z^2}$, and λ the wavelength of the studied field.

If the Fourier Transform (FT)[1] with respect to x and y is applied to (2.1) the following is obtained:

$$\left(\frac{\partial^2}{\partial z^2} + k_z^2\right)\vec{T}_{PWS}(k_x,k_y;z) = 0, \tag{2.2}$$

where $k_z^2 = k_0^2 - k_x^2 - k_y^2$ and $\vec{T}_{PWS}(k_x,k_y;z)$ is the FT of $\vec{E}(x,y,z)$.

[1]The FT of a function $f(x,y)$ is defined as $F(\omega_x,\omega_y) = \iint_{-\infty}^{\infty} f(x,y)e^{-j(\omega_x x+\omega_y y)}dydx$ while the inverse FT is defined as $f(x,y) = \frac{1}{4\pi^2}\iint_{-\infty}^{\infty} F(\omega_x,\omega_y)e^{j(\omega_x x+\omega_y y)}d\omega_x d\omega_y$. Note that both normalization factors $(1/2\pi)$ are grouped together in the inverse FT.

Equation (2.2) can be rewritten in terms of the components of $\vec{T}_{PWS}(k_x, k_y; z)$ as

$$k_x T_{PWS,x}(k_x, k_y; z) + k_y T_{PWS,y}(k_x, k_y; z) - j\frac{\partial T_{PWS,z}(k_x, k_y; z)}{\partial z} = 0, \quad (2.3)$$

with two solutions proportional to $e^{\pm jk_z z}$, representing elementary plane waves traveling in opposite directions. The solution associated to the positive sign of the exponent represents a PWS traveling in the z direction whereas the one with the negative sign corresponds to a PWS traveling in $-z$.

Despite both solutions are valid, the convention in the classical electrodynamics approach is to consider that the source is located in the region with $z \leq 0$ and radiates into the positive half-space and hence, the waves travel in the $+z$ direction [22]. Thus, only the solution associated to $e^{jk_z z}$ is taken into account, yielding the following PWS:

$$\vec{T}_{PWS}(k_x, k_y; z) = \vec{T}(k_x, k_y) e^{jk_z z}, \quad (2.4)$$

where $\vec{T}(k_x, k_y)$ is unknown.

The propagation constant k_z can be computed from k_0 and the tangential components k_x and k_y, and its value defines the nature of the field.

$$k_z = \begin{cases} \sqrt{k_0^2 - k_x^2 - k_y^2}, & if \quad k_x^2 + k_y^2 \leq k_0 \\ -j\sqrt{k_0^2 - k_x^2 - k_y^2}, & otherwise. \end{cases} \quad (2.5)$$

Positive real values of k_z correspond to propagating waves and are defined inside the circumference of radius k_0 in the k-space (see Figure 2.2), whereas negative complex values of k_z define the evanescent waves.

Finally, the electric field can be computed at any point in the positive half-space if the inverse FT is applied to the PWS.

$$\vec{E}(x, y, z) = FT^{-1}\{\vec{T}_{PWS}(k_x, k_y; z)\} = \frac{e^{jk_z z}}{4\pi^2} \iint_{-\infty}^{\infty} \vec{T}(k_x, k_y) e^{j(k_x x + k_y y)} dk_x dk_y, \quad (2.6)$$

where, applying the FT on both sides of (2.6) and rearranging,

$$\vec{T}(k_x, k_y) = FT\{\vec{E}(x, y, z)\} = \iint_{-\infty}^{\infty} \vec{E}(x, y, z) e^{-jk_z z} e^{-j(k_x x + k_y y)} dx dy. \quad (2.7)$$

Therefore, the field acquired over a plane ($z = z_0$), can be employed to calculate the field over any other plane in the positive half-space at a distance z from the acquisition surface by the application of a differential phase change [22] to the PWS in which is commonly known as *plane-to-plane* transformation, a fundamen-

tal technique for antenna diagnostics or focusing in imaging applications:

$$\vec{E}(x,y,z) = FT^{-1}\{FT\{\vec{E}(x,y,z_0)\}e^{-jk_z(z-z_0)}\}. \tag{2.8}$$

On the other hand, if the solenoidal field condition ($\nabla \cdot \vec{E} = 0$) is applied to (2.6), after differentiating and rearranging terms [118]:

$$\vec{T}(k_x,k_y)\cdot\vec{k} = T_x(k_x,k_y)k_x + T_y(k_x,k_y)k_y + T_z(k_x,k_y)k_z = 0. \tag{2.9}$$

As it can be clearly seen, only two components of the PWS can vary independently. Hence, the longitudinal component $T_z(k_x,k_y)$ can be obtained from the knowledge of the tangential components $T_x(k_x,k_y)$ and $T_y(k_x,k_y)$ as

$$T_z(k_x,k_y) = -\frac{T_x(k_x,k_y)k_x + T_y(k_x,k_y)k_y}{k_z}, \tag{2.10}$$

and the complete PWS can be obtained, only from the tangential components of the electric field, as

$$\vec{T}(k_x,k_y) = \vec{T}_T(k_x,k_y) + T_z(k_x,k_y)\hat{k}_z. \tag{2.11}$$

2.1.2 Far-field antenna radiation patterns

In PNF antenna measurement, the two tangential components of the electric field E_x and E_y are acquired over a planar surface at a distance $z = z_0$ of the aperture of the antenna in the NF radiating region (see Figure 1.2) as depicted in Figure 2.1.

$$\vec{E}_T(x,y,z_0) = E_x(x,y,z_0)\hat{x} + E_y(x,y,z_0)\hat{y}. \tag{2.12}$$

The PWS of the tangential components is obtained directly from the previous expression as

$$\vec{T}_T(k_x,k_y) = FT\{\vec{E}_T(x,y)\} = T_x(k_x,k_y)\hat{k}_x + T_y(k_x,k_y)\hat{k}_y. \tag{2.13}$$

The vector PWS can be obtained as in (2.11), after computing the longitudinal component from (2.10), allowing to obtain the electrical field as defined in (2.6).

To compute the FF pattern of the AUT, (2.6) has to be evaluated in the limit of the observation point $\vec{r}$ (with $\vec{r} = x\hat{x} + y\hat{y} + z\hat{z}$), that is, $\vec{E}_{FF}(\vec{r}) = \lim_{r\to\infty}\vec{E}(\vec{r})$. Evaluation of that expression is a difficult process and the method of stationary phase [22] is employed for the asymptotically evaluation of (2.6), reducing the

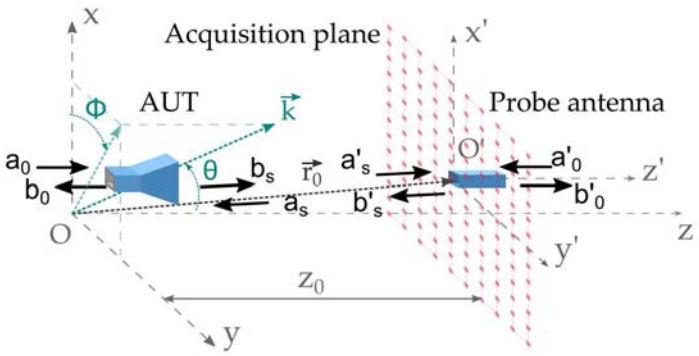

Figure 2.1: Typical coordinate system for PNF measurement ranges and main parameters for the scattering matrix antenna representation (a_0, b_0, a_s, b_s, a'_0, b'_0, a'_s, b'_s).

process to a multiplication with a trigonometric function:

$$\vec{E}_{FF}(ru, rv, rw) \approx j\frac{e^{-jkr}}{\lambda r}\frac{k_z}{k_0}\vec{T}(k_x, k_y). \tag{2.14}$$

where the factors (u, v, w), multiplying the position vector, are the cosine directors.

The FF is obtained over a hemisphere defined as

$$x = r\sin(\theta)\cos(\phi) = ru, \quad y = r\sin(\theta)\sin(\phi) = rv, \quad z = r\cos(\theta) = rw; \tag{2.15}$$

the wave vector is defined over the same surface as

$$k_x = k_0\sin(\theta)\cos(\phi), \quad k_y = k_0\sin(\theta)\sin(\phi), \quad k_z = k_0\cos(\theta), \tag{2.16}$$

where θ and ϕ are defined in Figure 2.1.

In practice the field is measured in a series of discrete points and the continuous FT is replaced by the discrete FT. Multiple copies of the spectrum appear, as shown in Figure 2.2, and special attention must be given to the sampling criteria in order to avoid aliasing.

As defined in (2.5) propagating waves are confined inside the circumference of radius k_0 also known as the *visible region* whereas the spectrum outside the circumference in the so-called *invisible region*, corresponds to the evanescent waves. The level of the spectrum in the invisible region is almost zero, and in real systems is below the noise floor for scan distances larger than λ [48]. Therefore, the

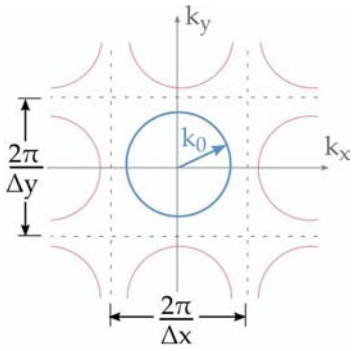

Figure 2.2: Distribution of the spectrum for discrete sampling. In red, the copies of the original spectrum, which is represented in blue.

PWS can be seen as a band-limited function, i.e., $\vec{T}_T(k_x, k_y) = 0$ for $|k_x| \geq k_0$ and $|k_y| \geq k_0$.

The maximum sample spacing for each axis can be determined then by

$$\Delta x = \frac{\pi}{k_0} = \frac{\lambda}{2}, \quad \Delta y = \frac{\pi}{k_0} = \frac{\lambda}{2}. \tag{2.17}$$

If the required angular valid margin θ_v, which will be defined next, is smaller than $\pm 90°$, larger values of Δx and Δy can be taken [119]:

$$\Delta x = \Delta y = \frac{\lambda}{1 + \sin(\theta_v)}. \tag{2.18}$$

However, if the sample spacing is chosen larger than $\lambda/2$ or the AUT radiates significant power outside the scan plane, aliasing will occur.

If the measurement distance z_0 is less than λ, evanescent waves are present and the spectrum will be wider, thus sampling space must be chosen smaller [34]:

$$\Delta x = \Delta y = \frac{\lambda}{\sqrt{1 + (\lambda/z_0)^2}}. \tag{2.19}$$

Finite size of the acquisition plane introduces an error in the entire FF [22]. Nevertheless, the effect of truncation errors is more noticeable in the pattern broadsides and a valid margin in which the NF-FF transformation is reliable can be defined from a geometric optics perspective as shown in Figure 2.3.

The valid margin depends on the size of the acquisition plane (L) the AUT diameter (D_{aut}) and the distance of the acquisition plane (z_0), and is defined as

$$\theta_v = \arctan\left(\frac{L - D_{aut}}{2z_0}\right). \tag{2.20}$$

The angular margin of the FF pattern can be maximized for a given scan plane size if the distance between the AUT and the acquisition plane is reduced. Nevertheless depending on the type of antennas, this could increase the effect of multiple reflections between the probe and the AUT [48].

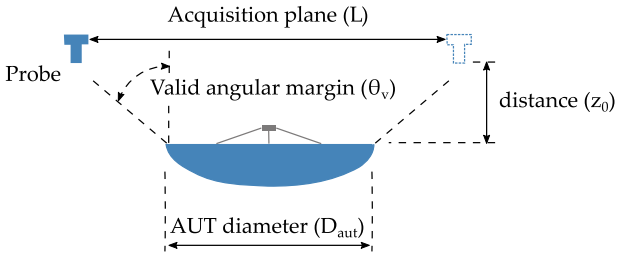

Figure 2.3: Angular margin for the NF-FF transformation in a PNF measurement.

2.1.2.1 **Probe correction**

Due to the non ideal response of the probe, correction techniques have to be applied in order to obtain accurate results outside of the main beam region of the probe [34]. Despite Open-Ended Wave Guide (OEWG) probes are recommended for PNF, their fields differ appreciably from those of elementary electric dipoles. Furthermore in PNF measurement ranges the probe remains oriented always in the same direction and the sidelobes of the AUT, in the outer area of the acquisition plane, are sampled at an angle of the boresight direction of the probe, making necessary to compensate for the radiation pattern of the probe.

The most extended approach employs the scattering matrix antenna representation, whose main parameters are shown in Figure 2.1, to obtain the coupling equation (2.21) between the probe antenna and the AUT [39] from the reformulation of (2.7).

$$D(k_x, k_y) = \vec{T}'(k_x, -k_y) \cdot \vec{T}(k_x, k_y) = \frac{(1 - \Gamma_p \Gamma_r) e^{jk_z z_0}}{a_0} \iint_{-\infty}^{\infty} b_0{}'(\vec{r}) e^{j(k_x x + k_y y)} dx dy, \tag{2.21}$$

where the parameters $\vec{T}'(k_x, -k_y)$, $\vec{T}(k_x, k_y)$, Γ_p, Γ_r and a_0, representing the probe coefficients, the AUT coefficients, the reflection coefficients in the probe and the

load and the input wave respectively, are known parameters and $b_0{}'(\vec{r})$ while the measured values [40].

In PNF measurements the tangential field components are acquired from two measurements with the probe rotated 90°. Thus, a set of equations for $D_{1,2}(k_x, k_y)$, where the numerical subindex denote different acquisitions with orthogonal polarizations of the probe, is obtained:

$$\begin{cases} D_1(k_x, k_y) = \vec{T}'_1(k_x, -k_y) \cdot \vec{T}(k_x, k_y) \\ D_2(k_x, k_y) = \vec{T}'_2(k_x, -k_y) \cdot \vec{T}(k_x, k_y). \end{cases} \tag{2.22}$$

Solution of the equation set gives both tangential components of $\vec{T}(k_x, k_y)$ without the effect of the probe.

$$T_x(k_x, k_y) = \frac{D_1(k_x, k_y) T'_{y,2}(k_x, -k_y) - D_2(k_x, k_y) T'_{y,1}(k_x, -k_y)}{T'_{x,1}(k_x, -k_y) T'_{y,2}(k_x, -k_y) - T'_{x,2}(k_x, k_y) T'_{y,1}(k_x, -k_y)}, \tag{2.23}$$

$$T_y(k_x, k_y) = \frac{D_2(k_x, k_y) T'_{x,1}(k_x, -k_y) - D_1(k_x, k_y) T'_{x,2}(k_x, -k_y)}{T'_{x,1}(k_x, -k_y) T'_{y,2}(k_x, -k_y) - T'_{x,2}(k_x, k_y) T'_{y,1}(k_x, -k_y)}. \tag{2.24}$$

2.1.3 **Antenna diagnostics**

The plane-to-plane transformation technique is usually employed in diagnostics applications to obtain the tangential field in the antenna aperture, which for the scenario considered in Figure 2.1 is:

$$\vec{E}(x, y, 0) = FT^{-1}\{FT\{\vec{E}_T(x, y, z_0)\} e^{jk_z z_0}\}. \tag{2.25}$$

It is worth noting that if the field has been acquired in the radiating NF region, the aperture field can be reconstructed with a resolution of $\lambda/2$ at the best [22, 48], since only propagating fields are taken into account. To improve the resolution, the field should be sampled closer to the aperture and with a denser grid, to register part of the evanescent waves [120, 121]. Zero-padding techniques in the spatial domain can be also employed to improve the sharpness and definition of the image of the aperture [59, 122].

2.2 Fourier-based imaging techniques

The plane-to-plane technique is the preferred approach for image reconstruction due to its simplicity and computational efficiency. In this approach, the reflectivity, defined as the ratio of the scattered into the incident fields, is backpropagated to the object plane where a focused image is obtained. Same resolution limitations than for antenna diagnostics apply.

Nevertheless, the PWS method is limited to bistatic setups in which the incident field is the same for different positions of the receivers such as in [104, 108, 110].

The setups implemented in this thesis are planar multi-monostatic configurations, and therefore the plane-to-plane transformation cannot be applied as it is. Planar multi-monostatic imaging can be accomplished by means of efficient Fourier-based monostatic SAR techniques.

As it will be described next, formulation for Fourier-based monostatic SAR imaging, is nearly identical to the PWS method. Nevertheless a factor of 2 must be considered in the phase of the plane waves due to the roundtrip propagation of the wave from the antennas to the OUT.

2.2.1 Synthetic aperture radar for monostatic setups

The employed technique is described in [10]. This approach makes an extension of the classical Bi-Dimensional (2D) SAR formulation for a linear aperture [123] to a planar aperture and wideband data so that a 3D reconstruction of the OUT can be computed from data gathered over a 2D aperture.

This method allows for NF imaging with wide beam antenna patterns, opposite to other systems in which the large size of the synthetic aperture causes small depth-focus for close range objects [10]. Thus, it can be employed for imaging of large objects within short range distances.

The typical setup for monostatic SAR is shown in Figure 2.4 with a reference system in which unprimed Cartesian coordinates are employed to refer to the points in the scanned aperture and the primed ones define the position of each point of the OUT.

The main component of the measured field over a plane with $z = z_0$ is the superposition of the reflectivity at each point of the OUT $\psi(x', y', z')$ times the roundtrip phase to the target (the amplitude decay with range is not considered due to its small impact in the focusing process), defined as follows:

$$E_s(x, y, k) = \iiint_{-\infty}^{\infty} \psi(x', y', z') e^{-2jk\sqrt{(x'-x)^2+(y'-y)^2+(z_0-z)^2}} dx' dy' dz' \qquad (2.26)$$

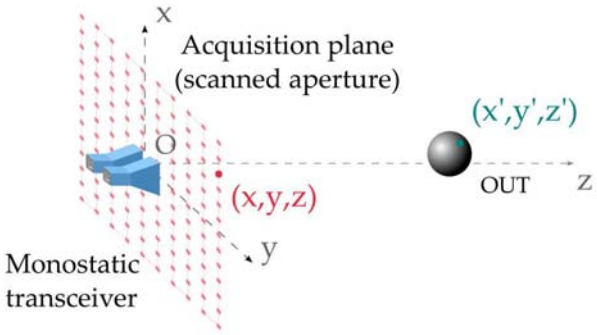

Figure 2.4: Typical setup for monostatic SAR imaging.

On the other hand, the phase term defines an spherical wave that can be expressed as an infinite superposition of plane waves as

$$e^{-2jk\sqrt{(x'-x)^2+(y'-y)^2+(z_0-z)^2}} = \iint_{-\infty}^{\infty} e^{-jk_x(x'-x)-jk_y(y'-y)-jk_z(z'-z_0)}dk_x dk_y \quad (2.27)$$

where k_z can be expressed as a function of the tangential components of the wave vector and the frequency as

$$k_z = \sqrt{(2k_0)^2 - k_x^2 - k_y^2}. \quad (2.28)$$

Inserting (2.27) into (2.26) and rearranging yields

$$E_s(x,y,\omega) = \iint_{-\infty}^{\infty}\left[\iiint_{-\infty}^{\infty}\psi(x',y',z')e^{-j(k_x x'+k_y y'+k_z z')}dx'dy'dz'\right] e^{j(k_x x+k_y y+k_z z_0)}dk_x dk_y. \quad (2.29)$$

The expression inside the square brackets is the 3D FT of the reflectivity function while the rest of the equation defines an inverse 2D FT allowing to express (2.29) in a compact manner as

$$E_s(x,y,\omega) = FT_{2D}^{-1}\{FT_{3D}\{\psi(x',y',z')\}e^{jk_z z_0}\} \quad (2.30)$$

Taking the 2D FT of both sides of (2.30) and dropping the distinction between the coordinates of the aperture and the OUT

$$S(k_x,k_y,k) = \Psi(k_x,k_y,k_z)e^{jk_z z_0}, \quad (2.31)$$

being $S(k_x, k_y, k)$ and $\Psi(k_x, k_y, k_z)$ the 2D and 3D FTs of the scattered field and reflectivity of the OUT respectively.

Finally, it is possible to obtain the reflectivity of the OUT in the spatial domain as

$$\psi(x, y, z) = FT_{3D}^{-1}\{FT_{2D}\{E_s(x, y, \omega)\}e^{-jk_z z_0}\}. \tag{2.32}$$

For additional details, this demonstration is also described in Section III.A of [10].

The field is acquired over a rectangular aperture uniformly sampled in the x and y directions (see Figure 2.4) for an equally spaced set of frequencies. Thus, the 2D FT can be directly applied to obtain $S(k_x, k_y, k)$ in discrete points of the spatial frequency domain. However, as shown in (2.31), $S(k_x, k_y, k)$ is defined as a function of $\Psi(k_x, k_y, k_z)$ and therefore the 3D FT cannot be directly applied due to the non-uniform distribution of the samples in k_z for a monostatic setup (see (2.28)). It is necessary to resort to linear sampling interpolation techniques to compute the spectrum of the reflectivity over a set of uniformly distributed points.

Figure 2.5 shows the spatial coverage in the range (longitudinal) and cross-range (tangential) direction. The required sampling depends on several factors such as the frequency, the size of the scanned aperture, and the size and distance to the target.

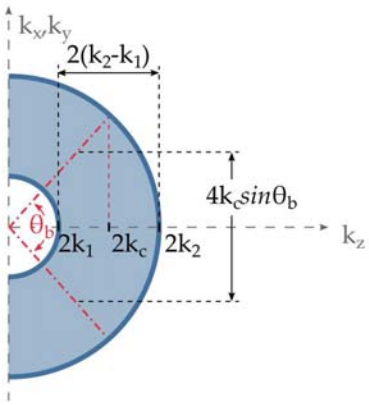

Figure 2.5: Spatial frequency coverage [10].

The maximum sampling space in the x and y axes is defined by

$$\Delta x = \Delta y = \frac{\pi}{2k_0} = \frac{\lambda}{4}. \tag{2.33}$$

Note that the larger extension of the spectrum due to the factor 2 in the phase term (see (2.26) and (2.28)) yields sampling requirements twice as dense as for the case of antenna measurement, and as it will be addressed in Section 2.4 and in **[V]** and **[VI]**, sampling requirements will be more demanding in case of working with phaseless techniques [124]. Nevertheless, the spatial sampling can often being relaxed according to the antenna beamwidth, which is usually less than 180° (see Figure 2.4).

The frequency sampling is determined in a similar way considering than a change Δk produces a phase shift of $2\Delta k R_{max}$, being R_{max} the maximum OUT range. Limiting this phase change to π yields

$$\Delta k < \frac{\pi}{2R_{max}} \quad \longrightarrow \quad \Delta f < \frac{c}{4R_{max}}. \tag{2.34}$$

The cross-range resolution of the image can be obtained if the polar coverage (shaded area in Figure 2.5) is approximated to a rectangular window of width $4k_c \sin\theta_b$ where k_c is the wave number of the central frequency and θ_b is selected as the minimum between the beamwidth of the antennas or their subtended angle, as

$$\delta_x \approx \frac{\lambda_c}{4k_c \sin\theta_b}. \tag{2.35}$$

where λ_c is the wavelenght of the central frequency.

The same approach can be followed for the determination of δ_y except that θ_b can have a different value.

Range resolution is typically defined as $\delta z = c/2B$, where B describes the frequency bandwidth, and can be expressed as

$$\delta_z = \frac{2\pi}{2(k_2 - k_1)}, \tag{2.36}$$

as a function of the wave numbers, being k_1 and k_2 the wave numbers corresponding to the lower and upper frequencies of the band.

2.2.1.1 **Other processing techniques**

Application of Fourier-based post-processing techniques is limited to the use of canonical domains, planar (described in Section 2.2.1), cylindrical or spherical, for the definition of both, the reconstruction (object) and the observation (acquisition) domains. When reconstruction or observation domains, other than canonical, are used, it is necessary to resort to post-processing techniques based on the inverse source problem [11, 112, 125], [ii],[d].

These techniques are not as efficient as Fourier-based techniques in terms of computing time and complexity, mainly for the electrically large scenarios studied in mm- and submm-wave bands. Nevertheless the use of acceleration techniques such as the Fast Multipole Method (FMM) or Graphics Processing Units (GPU) implementation contribute to alleviate this problem.

The Inverse FMM method for monostatic SAR applications described in [125] has been employed in [**VI**] and [**VII**]. The technique is a multipolar expansion optimization of the inverse source formulation in [126]. It is based on solving the inverse problem after dividing the observation and reconstruction domains in smaller subdomains. The final solution is computed by means of the well-known aggregation, translation, and disaggregation operations from the solutions in the subdomains.

2.3 Non-redundant sampling techniques

The band-limitation properties of the fields can be exploited to effectively reduce the amount of samples needed to unequivocally characterize those fields. In this work, the non-redundant sampling techniques presented in [127] are employed and adapted for the specific studied applications.

In non-redundant sampling techniques a reduced set of points is distributed in a plane-polar grid and therefore, the observation curves can be parametrized by a radial coordinate ξ and an azimuthal coordinate φ [127]. Points in the so-called *reduced grid* are equally spaced in a transformed coordinate system, with the aim of reducing the bandwidth of the signal to a minimum; however those points are not equally spaced in the Cartesian coordinate system employed for NF-FF transformation. Thus, an Optimal Sampling Interpolation (OSI) technique is considered to compute the field in a regular rectangular grid after the field acquisition.

OSI is based on a two-step scheme. First, the reduced set of points is obtained [76] and the field which exhibits minimum bandwidth in the transformed domain, hereafter the *reduced field*, is computed by multiplying the measured field over the reduced set of points $E(\xi, \varphi)$, by a phase factor γ [76]:

$$F(\xi, \varphi) = e^{j\gamma(\xi)} E(\xi, \varphi) . \tag{2.37}$$

Then, two OSI are required in order to retrieve the field at a given coordinate (ρ, φ) of the regular grid. For the sake of simplicity the coordinates of the regular grid are expressed also in plane-polar notation (being φ common to both

coordinate systems) and, therefore:

$$x = \rho\cos(\varphi),\ y = \rho\sin(\varphi). \tag{2.38}$$

The first interpolation retrieves the field at all the rings for the requested azimuth angle:

$$F(\xi_n, \varphi) = \sum_{m=m_0-q+1}^{q+1} F(\xi_n, \varphi_m)\, G_\varphi(\varphi - \varphi_m), \tag{2.39}$$

where G_φ is the interpolation function for a closed curve that can be expressed as a product of the Dirichlet function and a Tschebyscheff polynomial [76], $m_0 = \lfloor \varphi/\Delta\varphi \rfloor$ being $\Delta\varphi$ the sampling step along the φ coordinate and $2q$ is the number of samples used to calculate each point.

The second interpolation retrieves the reduced field along the radial coordinate and removes the phase factor:

$$E(\xi(\rho), \varphi) = e^{-j\gamma(\xi)} \sum_{n=n_0-s+1}^{s+1} F(\xi_n, \varphi)\, G_\xi(\xi(\rho) - \xi_0). \tag{2.40}$$

In this case, the interpolation function is related to an open curve and, consequently, it is expressed as a function of a prolate spheroidal function and cardinal sine function and the remaining parameters are defined analogous to the azimuthal interpolation case.

This formulation can be directly applied in full antenna measurements and bistatic imaging setups, and also with holographic techniques capable of retrieving the phase point-by-point in the sampling domain, such is the case of the broadband phaseless technique based on indirect holography presented in [**III**] and and [**IV**].

However, the technique has to be slightly modified in case of performing phaseless antenna measurements or phaseless bistatic imaging, since the acquisitions are usually performed by means of power meters which return a signal proportional to the squared field amplitude, doubling its bandwidth. In case of interferometric schemes, combination of signals result in even larger bandwidths. Due to this fact, the phase factor in (2.37) has to be increased resulting in denser reduced grids as shown in [33, 128] for phaseless plane-to-plane and interferometric approaches respectively.

For the case of monostatic setups further modifications are required since it is necessary to consider that the position of the sources changes for each position of the acquisition plane. The particularization for a monostatic setup based on indirect off-axis holography is shown in [**VI**].

2.4 Indirect off-axis holography

Indirect off-axis holography is one of the most extended approaches among phaseless methods for antenna measurement and diagnostics. The word *holography* comes from the Greek words *hólos* (whole) and *gráphō* (written or represented) and was coined by Gabor in 1948 to define a new technique for recording and reconstructing the amplitude and phase distributions of a coherent wave disturbance in the optics field [129], and later adapted to use an off-axis reference by Leith and Upatnieks [130].

The off-axis technique was then adapted to the microwave and acoustic bands and referred to as *long wave holography* and employed in microwave imaging applications [131–133]. These techniques were first used for antenna metrology by Napier [134, 135] and Bennett [136].

Subsequently, the term *holography* has been employed, in the context of antennas and electromagnetic imaging, to describe methods involving the use of plane-to-plane transformations with PWEs but where the phase information is directly acquired (direct holography), and a cable reference is used [137, 138]. Therefore, to avoid confusion, the phaseless holographic methods described in this chapter are referred to as *off-axis indirect holography* or *Leith-Upatnieks holography*.

The employed notation in this section is particularized for an antenna measurement context. Nevertheless extrapolation of the concepts for the application of off-axis indirect holography in imaging setups can be directly done. Furthermore, particularization regarding the use of this techniques for imaging applications will be given at the end of this chapter.

Off-axis indirect holography techniques for antenna measurement and diagnostics are two step techniques based on: 1) recording the intensity pattern formed by the AUT and a reference field, known in amplitude and phase, and 2) performing the phase retrieval of the field radiated by the AUT, by post-processing of the recorded pattern, also known as *hologram*. Phase retrieval techniques can be done by means of different approaches comprising different filtering techniques in the time domain, the spatial domain, etc. Nevertheless, conventional technique implies filtering in the spatial frequency domain or k-space.

Conventional setup is usually implemented as shown in Figure 2.6(a) using a radiated reference field [31, 135–137, 139]. Nevertheless there are most recent approaches that substitute the radiated reference field with a synthesized reference wave generated through the use of a phase-shifter [32, 33, 124, 140, 141] as illustrated in Figure 2.6(b). Advantages and limitations of each setup will be discussed later on this section. In both cases, the hologram, $H(\vec{r})$, is recorded at every point of the acquisition plane, and is defined as the squared sum of the AUT and the

reference fields (2.4):

$$H(\vec{r}) = |E_{aut}(\vec{r}) + E_r(\vec{r})|^2 \tag{2.41}$$

where $\vec{r}$ is the position vector defining the position of the probe antenna in the acquisition plane, $E_{aut}(\vec{r})$ is the field radiated by the AUT and $E_r(\vec{r})$ is the reference field. Both E_{aut} and E_r refer to the field component received by the probe antenna. The acquisition process can be repeated for the other field component just by turning the AUT 90° and repeating the process **[III]**.

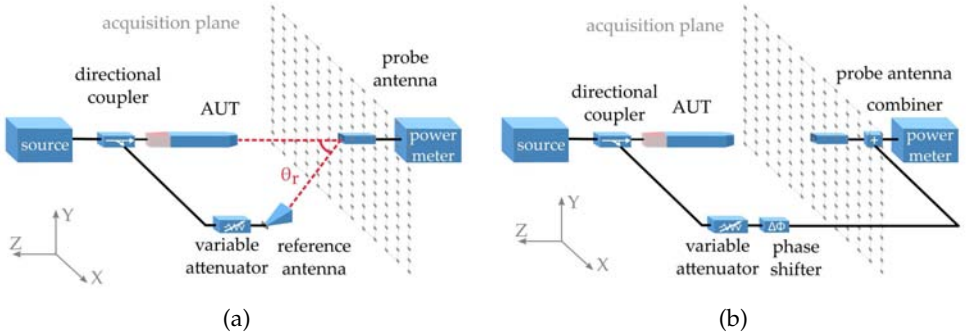

Figure 2.6: Off-axis indirect holography schemes for a PNF measurement range. (a) Radiated reference wave and, (b) synthesized reference wave.

2.4.1 Conventional Leith-Upatnieks technique

In conventional Leith-Upatnieks holography the phase retrieval is done by filtering the spectrum of the hologram in the spatial frequency domain or k-space. The expression in (2.4) can be further developed into (2.42):

$$H(\vec{r}) = |E_{aut}(\vec{r})|^2 + |E_r(\vec{r})|^2 + E_{aut}(\vec{r})E_r^*(\vec{r}) + E_{aut}^*(\vec{r})E_r(\vec{r}), \tag{2.42}$$

where the asterisk indicates complex conjugate. Since the reference signal is previously known, the $|E_r(\vec{r})|^2$ term, can be subtracted from the hologram to avoid its interference effects in the k-space [139].

After *Fourier* transforming to the k-space, the hologram can be expressed as

$$h(\vec{k}) = |e_{aut}(\vec{k})|^2 + |e_r(\vec{k})|^2 + e_{aut}(\vec{k}) \otimes e_r^*(-\vec{k}) + e_{aut}^*(-\vec{k}) \otimes e_r(\vec{k}), \tag{2.43}$$

being $e_{aut}(\vec{k})$ and $e_r(\vec{k})$ the FT of $E_{aut}(\vec{r})$ and $E_r(\vec{r})$ respectively, and $\otimes$ the convolution operator.

The first two terms are called the auto-correlation terms and give two zero-frequency harmonics in the k-space, whereas the following two terms, known as cross-correlation or image terms, contain shifted and distorted information about the amplitude and phase of the AUT [25].

Figure 2.7 shows an schematic representation of the spectrum of the hologram. Bandwidth[1] of the autocorrelation terms, $2W_k$, is twice the bandwidth of the cross-correlation terms, W_k, as they represent the spectrum of the squared intensity of the signals [142].

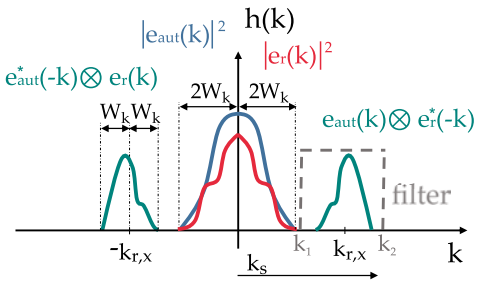

Figure 2.7: Spectrum of the acquired hologram.

Providing there is no overlap with the autocorrelation terms the cross-correlation term corresponding to $E_{aut}(\vec{r})E_r^*(\vec{r})$ can be band-pass filtered as

$$h_{filtered}(\vec{k}) = \{e_{aut}(\vec{k}) \otimes e_r^*(-\vec{k})\}\Pi(k_1, k_2), \tag{2.44}$$

being Π a window defined between the values k_1 and k_2 of the spectrum.

Finally, the complex magnitude of the AUT can be retrieved back in the spatial domain, after performing an inverse FT and dividing by the complex conjugate of the reference field.

$$E_{aut}(\vec{r}) = \frac{FT^{-1}\{h_{filtered}(\vec{k})\}}{E_r^*(\vec{r})}. \tag{2.45}$$

Quality of phase retrieval will depend mostly on the overlapping of the cross-correlation terms, related to the sampling and reference source position [31], as it will be addressed next, but also of other parameters such as the precise characterization of the reference field, the size of the setup [31], the accuracy of the probe positioning [31, 55], periodic errors [143], etc.

[1]Bandwidth is defined for $k > 0$ as shown in Figure 2.7. As the PWS of the hologram is symmetric, the total bandwidth is twice the described bandwidth.

2.4.1.1 Radiated versus synthesized reference waves

Initial approaches made use of radiated reference fields [136, 137, 139], and therefore, position of the image terms was related to the physical position of the reference antenna, leading generally to large separations between the reference antenna and the AUT and the acquisition plane, increasing the size of the setup and its sensibility to scanning and measurement errors [31].

Main differences between optical and microwave holography are stated in the work presented in [144]. The most important difference is that at microwave frequencies the hologram can be coherently recorded by scanning a probe through the acquisition plane, meaning that the reference field has not necessarily to be a radiated one but can be added electronically to the field measured at the hologram plane in which is called synthesized reference wave setup.

With the use of synthesized reference waves [32, 124, 140, 141, 144] it is possible to increase the separation of the image terms by controlling the phase shifts of the reference signal in the acquisition plane at the expenses of denser sampling to expand the spectrum limits. It is worth mentioning that synthesized reference fields were first employed in monostatic imaging setups due to the difficulty that supposed the need of a physical link between opposite ends of the antenna range in antenna measurement applications [134].

In [134, 135], an hybrid approach denominated *point reference source off-axis holography* between synthesized and radiated reference waves is introduced for a cylindrical setup. In these works the AUT is off-axis mounted on a turntable while the reference antenna is a small source with a fixed position. A phase shifter controlled by the movement of the turntable was employed to control the spectral position of the image terms of the hologram.

The basis of each of the approaches are presented next. Despite some of the mentioned works are done for cylindrical and spherical ranges [135–137, 139], the formulation presented here is particularized for planar measurement ranges, although easily adapted to other geometries.

Radiated reference signals

When using a radiated reference wave, separation of the image terms in the k-space can be controlled with the off-axis angle of the reference antenna with the acquisition plane, θ_r, see Figure 2.6(a). Particularly, the center of the image terms, $k_{r,x}$, as shown in Figure 2.7 can be calculated as

$$k_{r,x} = \pm k_0 \sin\theta_r, \tag{2.46}$$

considering that the reference antenna is placed at $y = 0$ and with an offset in the x-axis [145]. In planar measurement setups the offset can be introduced in the x or y axes, or in a combination of both. Here, for the sake of simplicity, an offset only in the x-axis is adopted without loss of generality.

According to [34], the maximum spatial bandwidth of a radiated field in a planar acquisition can be considered as $W_k = k_0$. Hence, as it can be seen in the schematic representation of the spectrum of the hologram, Figure 2.7, the non-overlapping condition is given by

$$k_{r,x} \geq 3k_0. \tag{2.47}$$

However, the maximum offset angle when a radiated reference wave is used, is limited to 90°, which yields a value of $k_{r,x\,max} = k_0$ after substituting in (2.46). This separation may not be enough to avoid overlapping between the spectral components, specially when working with the PWS of medium and low gain antennas [**II**], [140], which have wider spectra. Overlapping can be reduced if the PWS of the hologram is backpropagated to the aperture plane of the AUT [146] since the terms of the hologram become narrower, or by using the so called *modified hologram* technique [31], defined later in this section.

The representation of the spectrum of the hologram for this scenario is shown in Figure 2.8(a). Sampling requirements in the spatial domain can be obtained from further analysis of this scheme knowing that the extension of the k-space can be determined according to the *Nyquist* theorem [48] as a function of the sampling step, Δx, as

$$k_s = \pi/\Delta x. \tag{2.48}$$

As previously mentioned, the image terms, with a width of $W_k = k_0$, are centered around $\pm k_0$ (see Figure 2.8(a)), hence the maximum extension of the spectrum for the case of using a conventional indirect off-axis setup with radiated reference waves is $k_s = 2k_0$, yielding the following sample step that can be calculated from (2.48):

$$\Delta x = \frac{\pi}{k_s} = \frac{\pi}{2k_0} = \frac{\lambda}{4}. \tag{2.49}$$

Nonetheless, it is worth noting than $\theta_r = 90°$ is a theoretical limit and in practical implementations, offset angles are smaller than 90° and the sampling rate can be slightly relaxed. Furthermore although the autocorrelation terms have a bandwidth of $2k_0$, in practice the spectrum decays in a quite abrupt way due to the fact that it is calculated from the convolution of two spectra expected to vanish at k_0, hence overlapping can be tolerated up to a certain value without significantly degrading the performance of the technique [**I**] and the indirect holog-

raphy technique with radiated reference waves gives quite good results despite the overlapping (Figure 2.8(a)).

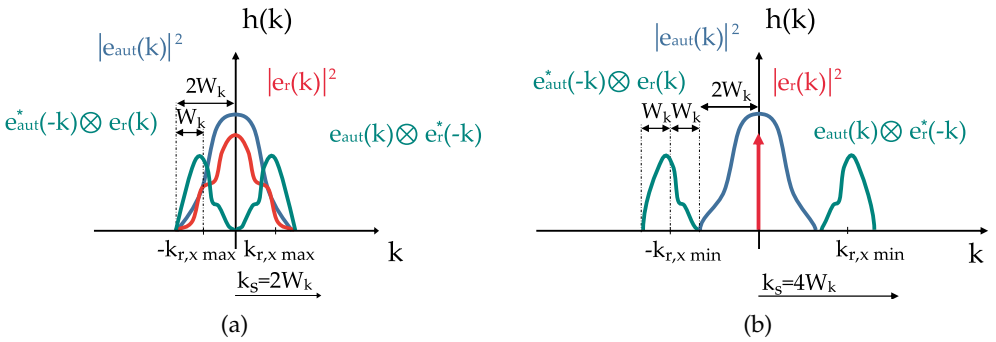

Figure 2.8: Spectum of the aquired hologram for different reference fields. (a) Radiated reference wave and $\theta_r = 90°$, maximum allowed separation of the hologram terms and (b) synthesized reference wave, minimum separation of the hologram terms to avoid overlapping.

Synthesized reference signals

In this case, see Figure 2.4(b), plane reference waves are generated from a sample of the source by means of a phase-shifter. The position of the image terms is no more dependent on the position of the reference antenna but on the phase step of the reference field, $\Delta\phi$, in the acquisition plane [140]

$$k_{r,x} = \pm\frac{\Delta\phi}{\Delta x}. \tag{2.50}$$

The use of synthesized reference waves removes the offset angle limitation and makes possible to displace the image terms to the non-visible part of the k-space ($|k| > k_0$). Therefore, overlapping can be controlled with a certain value of the phase shifts at the expenses of a more dense spatial sampling to increase the extension of the k-space.

Considering a a sampling step of $\Delta x = \lambda/8$ that yields an extension the k-space of $k_s = \pm 4k_0$, the required phase-shifts between consecutive points in the acquisition plane for the minimum separation fulfilling the non overlapping condition in (2.47) are

$$\Delta\phi = \Delta x\, k_{r,xmin} = \frac{\lambda 3k_0}{8} = \frac{3\pi}{4} = 135°. \tag{2.51}$$

As in the case of using a radiated reference field, the autocorrelation term corresponding to the field of the AUT is expected to vanish before $\pm 2k_0$ and therefore, the sampling rate could be relaxed.

It is worth noting than for this case, as the reference field is a synthesized plane wave, its autocorrelation term is a *Dirac delta function*.Thus, the image terms are proportional to its amplitude and not distorted by the convolution with the spectrum of the reference field, as it happens when a radiated spherical reference field is employed.

Another advantage of the use of synthesized reference waves is that, depending on the required accuracy and considering the amplitude of the reference field remains unchanged [139], it is not necessary to characterize the reference antenna since the reference field can be analytically computed from just one sample of the reference signal. Nevertheless, the directional coupler and phase shifter introduce variations in the amplitude of the reference field that should be taken into account for an accurate modeling of the reference field [**V**].

2.4.1.2 **The modified hologram technique**

This technique was first employed by Napier [134] and Junkin [31] for setups with radiated reference waves, and subsequently adapted for its use with synthesized reference waves in [33].

The squared reference and AUT field intensities are removed from the hologram leading to the following expression:

$$H_m(\vec{r}) = H(\vec{r}) - |E_{aut}(\vec{r})|^2 - |E_r(\vec{r})|^2 = E_{aut}(\vec{r})E_r^*(\vec{r}) + E_{aut}^*(\vec{r})E_r(\vec{r}), \tag{2.52}$$

and therefore, the spectrum of the modified hologram is composed only by the two image terms only (Figure 2.9), easing the filtering process:

$$h(\vec{k}) = e_{aut}(\vec{k}) \otimes e_r^*(-\vec{k}) + e_{aut}^*(-\vec{k}) \otimes e_r(\vec{k}). \tag{2.53}$$

As there are no autocorrelation terms, separation between image terms can be reduced, offering multiple advantages:

- The overlapping is reduced and so the error introduced during the filtering process.
- The extension of the k-space, defined in (2.48), can be reduced yielding bigger sampling steps.

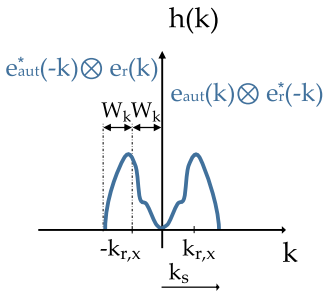

Figure 2.9: Diagrammatic representation of the spectrum of the modified hologram.

- The reference antenna can be placed closer to the AUT (for radiated reference waves), meaning that he size of the setup can be reduced; AUT and reference antenna paths are similar, leading to less sensitive setups to scanning errors and reducing phase errors due to source instability [31].

As a counterpart, an extra measurement is needed for the characterization of $|E_{aut}(\vec{r})|^2$ and therefore, it is advisable to develop switching subsystems that allow for simultaneously reception of the three measurements: hologram, AUT and reference fields, avoiding drift and/or inaccuracies in the acquisition of the fields at the same spatial point. Nevertheless, it has been demonstrated than values of drift below 1% produce insignificant errors in the FF pattern of the AUT [31].

2.4.1.3 **Characterization of the reference field**

Precise knowledge of the reference field is required during post-processing to compensate its effect and retrieve the AUT field without error as shown in (2.45). Characterization of the reference field intensity can be made directly using the proposed measurement schemes in Figure 2.6; nevertheless, special attention must be given to the reference phase, being possible to employ different techniques for its characterization.

When using radiated reference fields, the reference antenna is usually a well known antenna, e.g. Standard Gain Horn (SGH) or OEWG antennas, whose behavior in the acquisition plane can be obtained by correctly modeling the source and its position or even directly measured in a different measurement range. Another option is to employ an spherical wavefront to approximate the phase of the reference antenna in the acquisition plane [31, 108, 146]; strong precision requirements are demanded for all the cases in order to obtain the correct position to

the reference antenna in the measurement setup. In [108] an iterative process is included to refine the reference antenna position within a small area, searching for the position that produces the best focused image.

The reference antenna should be chosen smaller than the AUT to ensure that $E_r(\vec{r})$ does not have nulls in the angular margin in which $H(\vec{r})$ is significant [134]. This requirement has to be fulfilled specially in NF measurements in order to obtain the true FF pattern of the AUT without distortion. Conventional probe correction techniques can be applied [22, 34] to remove the effect of the probe antenna.

The process is simplified for the case of using synthesized reference waves since they are generally modeled as plane waves whose phase shifts can be analitically computed and whose intensity can be easily measured [32, 140, 141, 147, 148] as previously mentioned.

However, phase-shifters do not have an ideal behavior and the amplitude of the signal can be modified depending on the phase-shift applied at each moment. For this reason, some authors have chosen to independently characterize the synthesized reference signal [124, 149]. A more efficient technique for the characterization of the reference field is described in [**V**] in which the reference field is reconstructed from a few spatial acquisitions, avoiding the need of a complete spatial acquisition. Although particularized for imaging applications, the technique can be also applied to antenna measurements.

In [110] a detector for indirect holography applications with internal reference signal detection is designed and tested.

Finally, a characterization method from scalar measurements has been presented in [150] for its use in broadband SAR applications implemented through off-axis holography schemes.

2.4.1.4 **Accuracy and influence of errors**

A thorough analysis on the influence of several type of errors such as truncation, sampling rate, electrical and mechanical errors, position of the antennas or scan geometry is available in the literature [31, 55, 134, 136, 139, 143]. The mentioned types of error have similar effects for indirect holography using both types of reference fields: radiated and synthesized [55].

One of the early limitations of indirect holography was the poor dynamic range due to the quantization errors of the employed power detectors [31]. This issue has been solved with the use of modern heterodyne instrumentation, featuring both, high dynamic range and good sensitivity. An extense study on the effect of the noise in the hologram recording process can be found in [134].

Nevertheless it is advisable to include an amplifier or a variable attenuator in the AUT or the reference branch to help leveling the power between both branches and improve the dynamic range of the hologram. The variable attenuator can also be used as the switching element to cancel the corresponding branch during the acquisition process [**VI**].

Phase retrieval accuracy is highly dependent on scan geometry and the AUT [31, 134, 139]. Position of the reference antenna, when working with radiated reference fields, or adequate selection of the phase shifts in case of using synthesized reference waves, also play a very important role in achieving good results in the phase retrieval process.

Error due to the differences between the measured and modeled reference positions is addressed in [93] for an imaging application for the case of using the measured reference amplitude and a numerically modeled phase corresponding to an spherical waveform. It is demonstrated that errors in the model of the reference phase yield to shifts in the position of the source of the retrieved field that can be compensated, thus the former characterization method of the reference source is robust against misalignment errors of the reference source.

Sampling requirements are also strongly related to the position of the antennas and the scan geometry; the position of the reference antenna (or the phase shifts in case of using a synthesized reference wave), defined by θ_r (or $\Delta\phi$), shown in Figure 2.10, determines the center of the image terms in the spatial frequency domain as indicated in (2.46), while the width of the spectrum, related to the angle θ_a, depends on the aperture size of the AUT and the scan plane distance. Lower values of θ_a correspond to less directive antennas for the same scan distance, leading to wider spectra [141]. Hence, position of the antennas and distance to the scan plane, have to be carefully chosen, along with the sampling rate (2.49) to avoid truncation and overlapping of the image terms in the k-space [134].

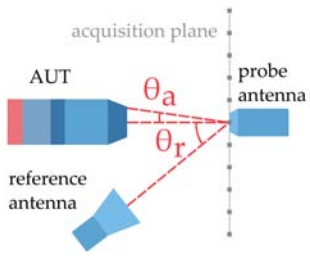

Figure 2.10: Detail of the position of the antennas in an indirect off-axis holography setup.

Sensitivity to probe positioning errors is another important source of inaccuracies in indirect holography setups. An exhaustive mathematical analysis of the effect of scanning errors during the data registration process has been developed in [31] proving that errors in the probe positioning system add supplementary convolution terms to the hologram spectrum, which are proportional to each of the components of the wavenumber, k.

Opposite to what happens with NF complex acquisitions [22], planarity errors in the probe positioning system have very low impact in the calculation of the FF pattern of the AUT, as k_z has a very low variation for small angles and tends to zero for $k_x^2 + k_y^2 = k_0^2$ [31]. However, this effect could be noticeable when wide valid angular margins of the FF pattern are required, and the size of the acquisition plane has to be increased. Nevertheless, the effect of planarity errors during the acquisition process become in errors in the sidelobes of the FF pattern after the NF-FF transformation [55], being its effect less critical in the main beam direction.

On the other hand errors in the x- and y- axes tend to make the image terms spread out [31]. The effect of this type of error is increased during the post-procesing stage if the reference signal is calculated on a perfect grid, different from the acquisition grid, and can be reduced if the exact acquisition points are precisely known.

The effect of random and periodic errors in the registration process, has also been statistically characterized through the use of mathematical models with correlation intervals in [55, 143] and by means of Monte Carlo analyses and empirically in the *Ka*-band considering a reduced set of acquisition points in [**IV**].

As indirect holography setups are more sensitive to x- and y- axes acquisition errors, special attention has to be given to the smearing effects caused by the acquisition speed and Doppler frequency shift. For multi-frequency acquisitions is recommended to employ point by point acquisition systems that allow the source and receiver to perform frequency sweeps statically at every acquisition point, leading to slightly higher scan time.

2.4.2 **Other phase retrieval techniques**

There are other phase retrieval techniques based on indirect off-axis holography that employ different acquisition and post-processing techniques.

2.4.2.1 **Spatial domain technique**

With this technique the phase retrieval is done directly in the spatial domain from the expression of the modified hologram, H_m, requiring an extra measurement for the characterization of the power density of the unknown antenna field, $|E_{aut}|^2$. Hence, magnitudes of the modified hologram and the power density of the AUT and magnitude and phase of the reference field are known, while the amplitude and phase of the AUT field are the unknowns of the problem.

The expression of the modified hologram can be rewritten as

$$\begin{aligned} H_m(\vec{r}) = E_{aut}(\vec{r})E_r^*(\vec{r}) + E_{aut}^*(\vec{r})E_r(\vec{r}) = \\ 2\left(Re\{E_{aut}(\vec{r})\}Re\{E_r(\vec{r})\} + Im\{E_{aut}(\vec{r})\}Im\{E_r(\vec{r})\}\right) \end{aligned} \tag{2.54}$$

being $Re\{\cdot\}$ and $Im\{\cdot\}$ the real and imaginary parts of the fields respectively.

On the other hand, the measured power density of the AUT can be expressed in function of its real and imaginary parts as

$$|E_{aut}(\vec{r})|^2 = Re\{E_{aut}(\vec{r})\}^2 + Im\{E_{aut}(\vec{r})\}^2 \tag{2.55}$$

and consequently, the real part of the antenna field can be computed as

$$Re\{E_{aut}(\vec{r})\} = \pm\sqrt{|E_{aut}(\vec{r})|^2 - Im\{E_{aut}(\vec{r})\}^2}. \tag{2.56}$$

If (2.56) is inserted in (2.54) the modified hologram expression can be rewritten as

$$H_m(\vec{r}) = \pm 2Re\{E_r(\vec{r})\}\sqrt{|E_{aut}(\vec{r})|^2 - 2Im\{E_{aut}(\vec{r})\}Im\{E_r(\vec{r})\}}, \tag{2.57}$$

and the imaginary part of the unknown field can be calculated as

$$Im\{E_{aut}(\vec{r})\} = \frac{H_m(\vec{r}) \mp 2Re\{E_r(\vec{r})\}\sqrt{|E_{aut}(\vec{r})|^2}}{2Im\{E_r(\vec{r})\}}. \tag{2.58}$$

The main advantage of this method is that there is no need of controlling the overlapping of the image terms in the spatial frequency domain since the field retrieval is done directly in the spatial domain. In consequence there are no limitations regarding the reference source position nor the sampling requirements that can be relaxed to $\lambda/2$ in order to obtain the FF of the AUT in the case of antenna measurement setups or to retrieve the OUT profile in imaging applications.

The method has been presented in [93, 151] for its use in bistatic imaging setups, although formulation and notation employed here are adapted for an antenna measurement setup.

2.4.2.2 **Opposite-phase holography**

This technique, employed in [141, 147, 148] for antenna measurement setups and in [110] for a bistatic imaging setup, achieves similar results than the *modified hologram* technique as it aims for the removal of the effect of the autocorrelation terms of the hologram. In order to do that, two different holograms are acquired introducing a 180° phase shift in the reference field of the second one. The final hologram is computed by subtracting the initial hologram with the one with opposite phase

$$\begin{aligned} H_{op} = |E_{aut}(\vec{r}) + E_r(\vec{r})|^2 - |E_{aut}(\vec{r}) - E_r(\vec{r})|^2 = \\ 2(E_{aut}(\vec{r})E_r^*(\vec{r}) + E_{aut}^*(\vec{r})E_r(\vec{r})). \end{aligned} \tag{2.59}$$

The rest of the field retrieval process is done in the same way as in the *modified hologram* technique although a small variation is introduced in [141, 147]. In that cases, the filtered image term is displaced to the center of the spectrum compensating the displacement introduced by the convolution of the unknown field with the reference field, which is a synthesized plane wave. Then, it is only necessary to divide the field back in the spatial domain by the amplitude of the reference field.

Nevertheless, this technique does not introduce any advantages with respect to the *modified hologram* technique, since it requires the same number of acquisitions. In fact the *modified hologram* technique gives better results since the amplitude of the unknown field can be obtained directly from the acquisition of $|E_{aut}(\vec{r})|^2$ and only the phase has to be retrieved from the hologram, with the consequent error reduction.

2.4.2.3 **Phase shifting indirect holography**

This technique is derived from digital in-line optical microscopy methodhs [152] and requires three intensity measurements to retrieve the phase of the AUT: the intensity of the AUT and two different acquisitions of the hologram with the reference field in quadrature phase states. Nevertheless, this approach presents several disavantages when applying it to the antenna measurement process, being its main limitation the spurious FF grating effects due to the sensivity of the system to the phase-step calibration [153].

The phase shifting technique has been adapted for antenna measurement in [153, 154]. In the referenced works, only three measurements of the hologram with equiangular phase shifts of 0°, 120° and 240° are employed. Hence, the existent symmetry in the complex plane, reduces the system sensitivity to the phase step accuracy.

Three different holograms are measured at each point of the acquisition grid considering the phase shifts described by $arg\{\tau_n\}$:

$$H_n = |E_{aut} + \tau_n E_r|^2; \qquad n = 1, 2, 3. \tag{2.60}$$

After the acquisition of the holograms, the following term is defined:

$$I_0 = |E_{aut}|^2 + |E_r|^2. \tag{2.61}$$

The difference holograms are calculated as

$$I_n = H_n - (I_0 + |E_r|^2(|\tau_n|^2 - 1)), \tag{2.62}$$

combined in pairs of two, that is $(I1, I2)$, $(I1, I3)$ and $(I2, I3)$, with a weighting factor, and divided into real and imaginary parts. This last step leads to a set of 6 different equations which give the same solution for 3 of the cases when considering noiseless environments. Final solution is obtained by averaging the three valid solutions in case of considering measurements affected by noise.

The phase retrieval is done point by point as previously shown and, therefore, *Nyquist* sampling rates can be applied, furthermore the method is a good option to employ in antenna alingment procedures [153]. The reference field does not have to be switched off during the acquisition process, and in consequence the scan time is reduced.

2.4.2.4 **Infrared holography**

Infrared holography is based on the same principles as Leith-Upatnieks holography. The main difference can be found in the acquisition process. In infrared holography, the fields are detected by a resistive screen that absorbs part of the incident energy of the fields and heats as a function of the electric field intensity distribution. Then an infrared camera is employed to record the temperature distribution of the hologram in the screen. Several new recording materials and optoelectronic sensors have been devised for recording the intensity distributions, increasing the quality of the recorded holograms and therefore, the phase retrieval quality [155].

Since the acquisitions of the hologram, the reference field and the AUT intensity can be done in real-time, the main advantage of this approach is the high reduction of the scan time [156]. Although several advances have been made in the development of infrared sensors and cameras, major drawbacks are the poor dynamic range and the impracticably high power levels for submm-wave applications. Nowadays, the technique is more employed for imaging applications than for antenna measurement and diagnostics.

2.4.3 **Particularization for imaging applications**

When off-axis holography techniques are applied to imaging, the unknown field of which the phase (or amplitude and phase) has to be retrieved becomes the scattered field from the OUT, $E_s(\vec{r})$.

Setups based on bistatic configurations involve minor changes in the setup with respect to the antenna measurement setup, specially when the OUT is placed between the TX and RX antennas and the imaging of the transmittance parameters is performed (see Figure 2.11(a)). Such is the case of the experimental setups presented in [110, 133]. In bistatic setups, the TX and RX antennas can also be placed at the same side of OUT [108] as shown in Figure 2.11(b). For this layout, the hologram for the imaging of reflectance parameters is acquired.

Sampling requirements for this case are the same as the ones defined for antenna measurement setups [34]. Also same restrictions regarding the reference antenna position can be directly applied. These type of setups generally employ radiated reference fields specially at mm- and sub-mm wave bands in where the direct link to convey the reference field from the directional coupler, on the source side, to the power detector, on the RX side, should be made with waveguide components in the case of synthesized reference waves.

Most of the off-axis holography setups for imaging applications have been implemented employing monostatic [144] or quasi-monostatic setups [32, 124, 157–159],**[VI]**-**[VIII]**. These setups are suitable for using synthesized reference waves due to the position of the TX and RX antennas (see Figure 2.11(c)), avoiding the need of a full characterization of the reference field. Quasi-monostatic setups with radiated reference waves have also been successfully validated **[VI]**.

Nevertheless these type of setups involve some modifications: (a) sampling rate has to be increased with respect to bistatic or antenna measurement setups according to the guidelines given in [160]. In practical, sampling rate can be relaxed as it happened for antenna measurement setups depending on the position and width of the image terms of the hologram and the allowed overlapping degree. (b) A correction in the phase term of the reference field has to be made to

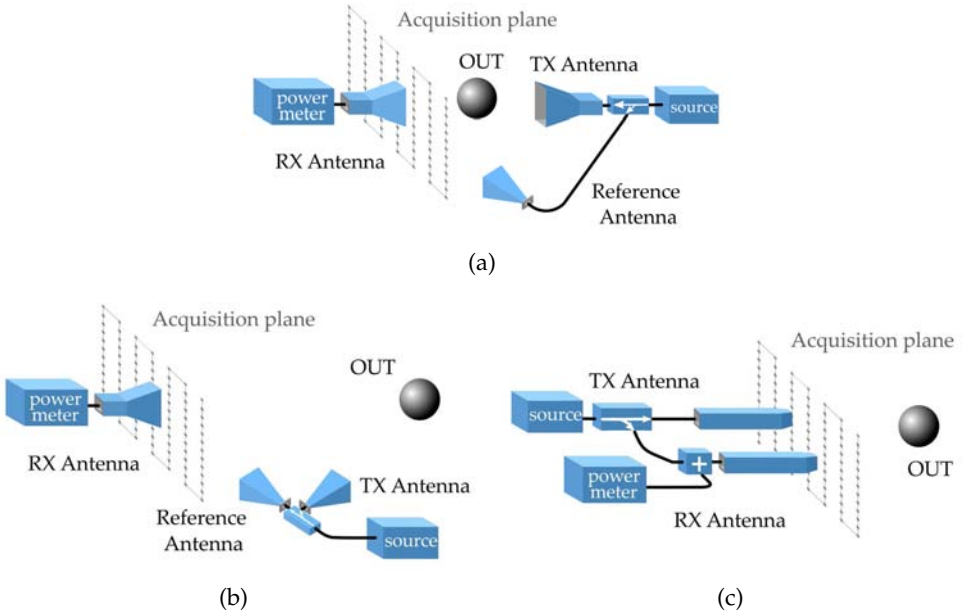

Figure 2.11: Typical layouts for imaging setups. (a) bistatic setup with radiated reference wave, *transmitted hologram*, (b) bistatic setup with radiated reference wave, *reflected hologram* and (c), multi-monostatic setup with synthesized reference wave.

take into account the distance increment expressing the reference field as

$$E_r(\vec{r}) = Ae^{-jk2d_{out}}, \tag{2.63}$$

being A the amplitude of the reference field and d_{out} the distance from the antennas to the OUT (see Section 2.2).

Sampling requirements are determined by the offset angle of the reference field (for radiated reference fields). Certain extent of aliasing can be allowed depending on the accuracy requirements and coarse sampling techniques can be applied allowing a reduction in the number of receivers or scan points. A brief compilation of coarse sampling techniques for on-axis and off-axis holography can be found in [93]. Adaptations of conventional non-redundant sampling techniques [76] to reduce the number of acquisition points can also be found in [149] for conventional off-axis approach and in [**VII**] for phaseless 3D SAR applications.

The use of retrieval schemes such as the spatial domain technique introduced in the Section 2.4.2 bypasses the sampling requirements of conventional off-axis techniques, allowing sampling according to the maximum extent of the OUT [151].

Assessment of image quality is done by subjective analysis of the obtained image focusing on the fine details and the overall profile for most of the available methods in the literature. Nevertheless, some authors have adopted a quantitative approach in which parameters such as the Point Spread Function (PSF) [93] or the Edge Spread Function (ESF) [110] are employed in order to characterize the spatial resolution of the imaging system.

In [161] the maximum resolution achievable for a bistatic setup with radiated reference field is calculated to be approximately 2.8λ. This reduction in the resolution with respect to the resolution limit for conventional imaging setups is due to the bandwidth of the spectral components of the hologram that is filtered out and do not contribute to the retrieval of the object. Fortunately, this resolution can be highly improved when synthesized reference waves are employed or if SAR techniques are implemented.

2.4.4 **Drawbacks and limitations**

Phase acquisition, specially at *mm-* and *submm*-wave bands is a challenging and very expensive process. The need of having a very stable phase reference demands very stable sources, steady temperature conditions and extremely accurate positioning systems.

Measurement system complexity and cost reduction are therefore, two of the main advantages offered by indirect off-axis holography techniques together with reduction of errors due to cable flexing and phase drift. Another advantage of indirect holography is that the phase is retrieved directly without the need of making use of iterative schemes that can suffer from stagnation, which is the main limitation of phaseless iterative approaches (as well as the higher calculation time).

Nevertheless indirect holography exhibits some limitations, discussed below, that make necessary further development of the technique.

In order to correctly remove the effect of the reference antenna interference during the phase retrieval process, it has to be accurately characterized both in amplitude and phase. This problem has been overcome by using well known antennas, whose phase can be accurately modeled by means of virtual sources [108] or synthesized plane waves.

The use of synthesized reference waves have also alleviated the overlapping problem in the spatial frequency domain, allowing to displace the image terms to the non-visible part of the spectrum. However, the use of synthesized reference waves has two main drawbacks. The first one is associated to the need of

extending the limits of the spatial frequency domain, which leads to denser spatial sampling. The other disadvantage is related to the use of phase shifters to synthesize the reference field. Implementation of these devices becomes difficult at high frequency bands, increasing the cost and complexity of the measurement setups. Furthermore, although possible for imaging applications, implementation of these kind of setups in mm- and submm-wave bands may not be possible as the connection between the moving probe antenna and the phase-shifter (see Figure 2.6(b)) should be done with waveguide components. In fact, this setup has only been validated in the X-band [32, 140, 141].

An alternative way of implementing synthesized reference wave setups for antenna measurement at high frequency bands is to convey a low frequency signal as a reference by means of a flexible cable and resort to a frequency multiplier at the end of the cable. Nevertheless, this approach can suffer from phase inaccuracies due to cable-flexing and temperature drift; The cost of the system is also increased by the use of a frequency multiplier.

Sampling rate can be reduced in case of using *modified holograms*; in exchange, the amplitude of the AUT has to be independently characterized. Nevertheless, a trade off between sampling rate reduction and the use of the complete hologram can be occasionally achieved [**I**]. This is possible because although the spectra of the autocorrelation terms are expected to have a wide of $2k_0$, they decay very quickly between k_0 and $2k_0$ since they are calculated as a convolution of two spectral terms expected to vanish at k_0. Therefore, a certain degree of overlapping may not have a significant impact on the final result.

For radiated reference fields, the size of the setup tends to be slightly higher than for complex acquisitions [31], specially when planar waves are required as reference fields; this yields to higher sensitivity to scan axis errors and denser sampling.

Finally, it is worth mentioning that conventional indirect off-axis holography, as the rest of techniques in the frequency domain, is not an efficient technique for the characterization of broadband antennas.

Table 2.1 summarizes the main advantages and disadvantages of the main available methods for indirect off-axis holography.

Table 2.1: Advantages and disadvantages of the main indirect off-axis holography methods.

Method	Advantages	Disadvantages
Modified [31, 33, 134][i][iii]	No autocorrelation terms Less dense sampling Overlapping reduction Only phase need to be retrieved ($\|E_{aut}(\vec{r})\|^2$ is measured)	Extra acquisition: $\|E_{aut}(\vec{r})\|^2$
Synthesized [55, 124, 139–141, 149][i]	Image terms: non-visible region Overlapping reduction No need of characterizing $E_{ref}(\vec{r})$ (scalar acquisition)	More dense sampling
Spatial domain [93, 151]	Field retrieval: spatial domain Reference source position: no limitations $\lambda/2$ sampling	Extra acquisition: $\|E_{aut}(\vec{r})\|^2$
Opposite phase [141, 147, 148]	No autocorrelation terms Less dense sampling Overlapping reduction (similar to modified hologram)	Acquisition of two holograms No acquisition of $\|E_{aut}(\vec{r})\|^2$ Amplitude and phase retrieval are needed
Phase shifting [110, 152–154]	Point-by-point field retrieval Spatial domain No reference position limitations $\lambda/2$ sampling	Requires 3 intensity measurements
Infrared [155, 156]	Drastic reduction of acquisition time	Poor dynamic range Required high power level

CHAPTER

3

Novel off-axis indirect holography techniques for antenna measurement and diagnostics

The work presented as part of this dissertation has been devoted to the development of new techniques, based on indirect holography, capable of overcame part of the limitations for phaseless antenna diagnostics and characterization mentioned in the State of the art chapter of this thesis. Thus, new techniques that avoid the use of phase-shifters (Section 3.1), artificially increase the separation of the image terms when using radiated reference fields (Section 3.2) or allow for efficient characterization of broadband antennas and reduction of the acquisition points (Section 3.3), have been developed and are gathered in publications **[I]**-**[IV]**.

For the sake of clarity part of the developed formulation included in the published works is repeated here.

3.1 Phase shifter substitution with mechanical shifts

As mentioned before, the use of a phase-shifter to synthesize a reference plane wave offers several advantages in the phase retrieval process as it allows to control the position of the image terms and displace them to the non-visible part of the spectrum, leading to an easier filtering process [162]. Nevertheless, phase shifters, can increase the overall cost of the setup at mm- and submm-wave bands or not being available.

When the reference field is a plane wave, $E_r(\vec{r}) = Ae^{-jk_0 r}$, the general expression of the hologram in (2.42) can be rewritten as

$$H(\vec{r}) = |E_{aut}(\vec{r})|^2 + A^2 + A\,E_{aut}(\vec{r})^* e^{-jk_0 r} + A\,E_{aut}(\vec{r}) e^{+jk_0 r}. \tag{3.1}$$

Furthermore, if only a variable attenuator, to level the power between both branches, and no phase shifter is included for the setup implementation, the recorded hologram can be further simplified as

$$H'(\vec{r}) = |E_{aut}(\vec{r}) + C|^2, \tag{3.2}$$

being C the constant reference signal injected through the variable attenuator. If a small three dimensional displacement is added to the sampling process such as the probe is displaced a distance $\vec{d} = d\vec{r}/||\vec{r}||_2$ as shown in Figure 3.1, the field at the modified sampling point, $\vec{r} + \vec{d}$, and disregarding the small amplitude variation, is given by

$$E_{aut}(\vec{r} + \vec{d}) \simeq E_{aut}(\vec{r}) e^{-jk_0 d}. \tag{3.3}$$

In that case, substituting (3.3) in (3.2), the acquired field can be expressed as

$$H'(\vec{r}+\vec{d}) = |E_{aut}(\vec{r}+\vec{d}) + C|^2 \simeq \\ |E_{aut}(\vec{r})|^2 + C^2 + C\,E_{aut}(\vec{r})^* e^{+jk_0 d} + C\,E_{aut}(\vec{r}) e^{-jk_0 d}, \tag{3.4}$$

and therefore, if the appropriate displacement is chosen for each acquisition point, sampling in the modified three dimensional grid results in the same hologram obtained in case of using conventional sampling and a phase-shifter.

As a consequence, the phase-shifter can be substituted with mechanical displacements that can be implemented by means of a micropositioner or directly if the measurement systems allows for this type of sampling [**AI**]. The acquisition grid can be seen as a regular grid in which some of the points are modified in order to introduce the mechanical phase shift. The grid creation process will be detailed next together with the experimental validation of the method.

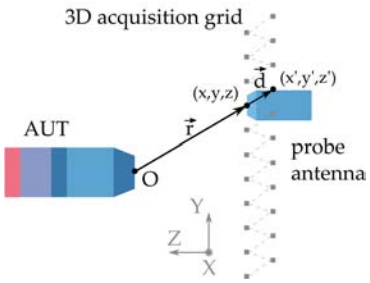

Figure 3.1: Displacement for the implementation of the three-dimensional grid.

The filtering process of the spectrum of the hologram is identical to the one used in conventional off-axis holography techniques. After transforming the filtered hologram back to the spatial domain, the field is retrieved by removing the effect of the reference field (see (2.45)). To be able to retrieve the field over a regular 2D grid, it is necessary to introduce a correction factor to compensate for the phase shift introduced in the modified points. The phase retrieval can be also done directly just by selecting the field in the original rectangular grid (see Figure 3.2) and discarding the field in the modified points, yielding to worse resolution.

It is worth noting that the approximation made in (3.3) is only valid in the case that the probe antenna is in the FF of the AUT. Nevertheless, the maximum introduced displacement is $\lambda/2$ which produces a shift of 180° in the received phase while the amplitude remains almost unchanged, and therefore, as it can be seen in the presented results [**I**], the method still provides accurate results even when the FF conditions are not strictly fulfilled.

3.1.1 Experimental validation

The method is validated for antenna diagnostics applications in [**I**] wherein an element failure in a two dimensional planar array is detected in a numerical example, and the shape of an object blocking the aperture of a *Ka*-band antenna is reconstructed from measurements.

To further explain the grid creation process and the equivalence of the new proposed hologram with the holograms obtained with conventional off-axis techniques, the main NF component of a small 15 dB SGH is characterized at 30 GHz. The initial acquisition grid, placed 20 cm away from the antenna aperture, is a rectangular grid of 340 mm x 400 mm with $\lambda/2$ sampling at 30 GHz, that is 5 mm, in the x-axis and $\lambda/8$ in the y-axis.

The sweep direction is coincident with the y-axis, and thus, the shift of the image terms of the spectrum of the hologram will be introduced in the k_y-axis. The mechanical displacements are selected to be 90°, meaning that four different phase values ($N_\phi = 4$) will be cyclically repeated. Different mechanical displacements are, therefore, applied to 3 of every 4 points in the y-axis of the original grid, leading to a layered acquisition grid as the one depicted in 3.2(a). The acquisition grid will have N_ϕ layers being the upper layer a lattice with regular sampling, $\lambda/2$ for the current example.

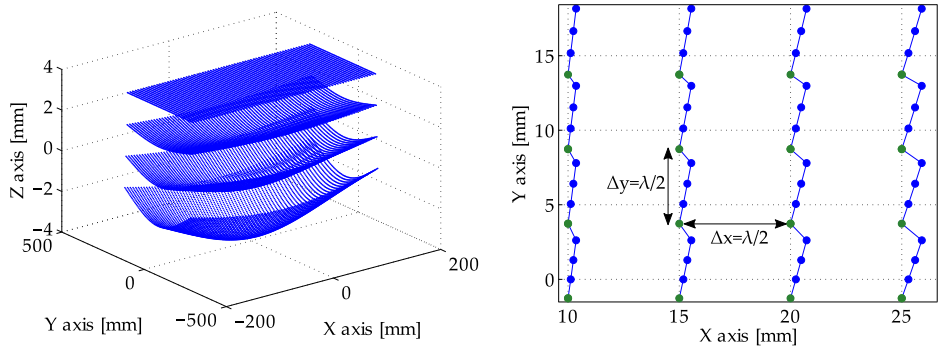

Figure 3.2: Acquisition grid for the mechanical phase-shifts. (a) Complete three dimensional grid; note the different scale for the z-axis, and (b) top view of a zoomed area; the green dots correspond to the upper layer of the grid forming the uniform rectangular lattice with $\lambda/2$ sampling and the blue points correspond to the modified points with the displacements in the x-, y- and z-axes that introduce the phase-shifts.

Figure 3.2(b) shows a zoomed top view of a small area of the grid. In this representation, the displacements in the x- and y-axes, cyclically repeated every four points, can be easily observed. It is worth noting that the displacements are individually calculated for each point due to the different distance from the AUT to each point of the acquisition grid.

The acquired field is shown in Figure 3.3(a). The interference pattern due to the mechanical displacements is equivalent to an hologram. The acquisition grid is swept in the y-axis direction, and therefore, the image terms of the spectrum of the hologram will be shifted in the k_y-axis in this occasion [163]. Its central position, knowing the sampling rate and the equivalent phase shifts can be obtained with (2.50) as

$$k_{r,y} = \pm\frac{\pi/2}{\lambda/8} = 2k_0. \tag{3.5}$$

The spectrum of the hologram is shown in Figure 3.3(b). The abrupt decay of the autocorrelation terms **[I]** makes possible to filter the image term between $0.5k_0 \leq k_{r,y} \leq 1.5k_0$.

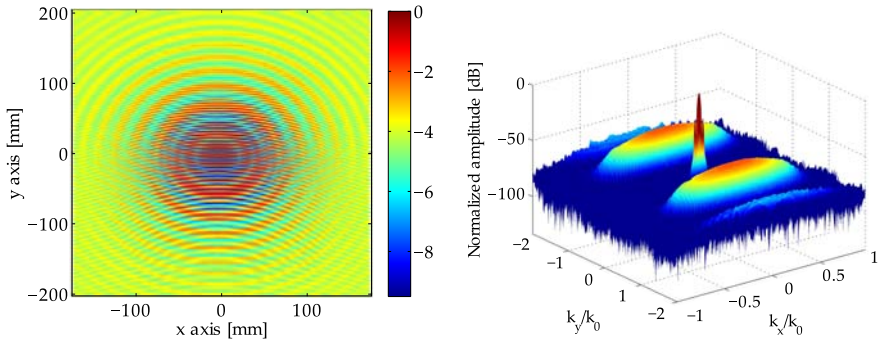

(a) (b)

Figure 3.3: Acquisition data; normalized patterns in dB. (a) Interferometric pattern in the acquisition plane and (b) three dimensional representation of the spectrum of the hologram.

The retrieved AUT amplitude and phase, shown respectively in Figure 3.4(a) and Figure 3.4(b), have been directly obtained once the filtered spectrum is transformed back to the spatial domain (2.45), just by selecting the field in the rectangular lattice (upper layer in Figure 3.2(a)). As mentioned before, another option is to consider the complete acquisition plane and correct the phase variation introduced by each of the mechanical displacements **[I]**, **[VI]** achieving higher resolution.

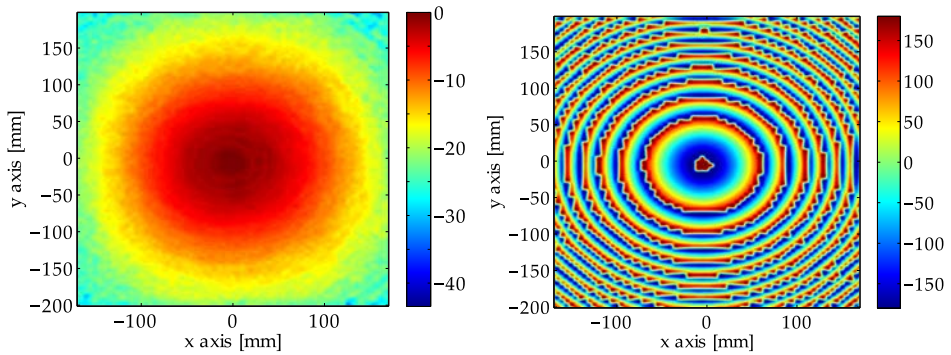

Figure 3.4: Retrieved fields in the NF rectangular uniform grid. (a) Retrieved normalized amplitude in dB, and (b) retrieved phase in degrees.

The amplitude of the reference signal is constant and only needs to be characterized at one point, at the beginning of the measurement. In this case, a variable attenuator has been introduced in the reference branch to adjust the constant level of the reference field to the maximum of the AUT level.

3.2 Multiplexed holograms for overlapping reduction

The previous scheme with three dimensional sampling cannot always be implemented in conventional planar measurement ranges since they can be limited to planar acquisitions. Moreover, at higher frequency bands the small displacements can be close to the accuracy limit of the positioners, increasing the effect of probe positioning error [31, 55] and if the setups are implemented by means of waveguides the reference wave might not be conveyed from the transmitter to the receiver's end. Additionally, the mechanical shifts technique cannot be applied in case of using radiated reference waves since the displacements of the probe antenna will introduce shifts in both, the AUT and the reference fields, leading to an erroneous approach to the off-axis holography technique.

A new method suitable for high frequency bands and radiated reference waves that avoids the use of phase shifters and three-dimensional sweeps has been developed. With the proposed method it is possible to artificially increase the image terms separation with respect to the autocorrelation terms, thus computation of the modified hologram [147] is not required and there is no need of the extra characterization of the squared amplitude of the AUT.

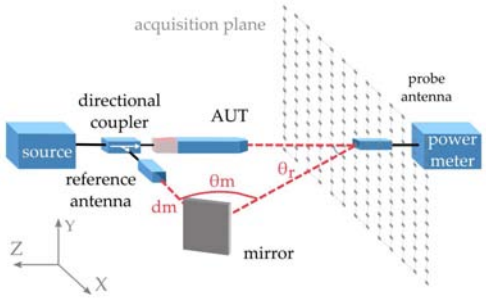

Figure 3.5: Proposed setup scheme for a PNF measurement range.

The method consists in spatially multiplexing two subsampled holograms obtained with two 180° phase-shifted reference waves. The phase-shift is achieved introducing a small displacement of $\lambda/2$ in the reference antenna towards the acquisition plane, although a phase shifter could alternatively been employed. The mechanical displacement has to be made only once, after acquiring the first subsampled hologram.

Combination of both subsampled holograms produce replicas of the image terms at half a period distance of the original image terms, whose amplitude is highly reduced, easing the filtering process of the desired replica. The replicas of the image terms appear in the non-visible part of the spectrum, as it happens when synthesized reference waves are used, and therefore, appropriate sampling must be selected to extend the limits of the spectrum and avoid truncation [34].

The setup, shown in Figure 3.5, is identical to the setup in conventional off-axis holography, although in this case, mirror reflection of the reference field is used to increase the path of the signal and obtain a quasi-plane reference field at the acquisition plane, which helps to reduce the amplitude of the original image terms (See Appendix in [**II**]).

With this technique, overlapping can be reduced without the need of physically increase the separation between the AUT and the reference antenna, reducing system sensitivity to scan errors [31]. As the separation of the image terms is larger than the separation achieved in conventional setups, this technique can be employed for the characterization of low and medium directivity antennas with wider PWS spatial bandwidth [140]. Furthermore, as it is shown in [**II**] better results are obtained also in the case of directive antennas characterization, where the difference between the power level of the AUT and the reference antenna can favor overlapping due to the low level of the image terms in the spectrum of the hologram.

3.2.1 Considerations

The theoretical basis of the proposed method together with numerical examples and experimental validation in the *W*-band for the NF characterization of three different antennas is presented in [**II**]. Therefore only a brief explanation about hologram formation, artificial modification of the phase shifts and the position of the replicas of the image terms in the spectrum of the hologram, as well as the necessary corrections that have to be applied during the phase retrieval process, will be given here.

3.2.1.1 Hologram formation

Figure 3.6 shows the hologram acquisition process. First subsampled hologram is acquired for the initial position of the mirror considering a grid with sampling steps of $2\Delta x$ and Δy. The acquired samples are stored in the odd columns of the final hologram. Then a displacement of the mirror, such as a phase shift of 180° in the reference wave is produced in the acquisition plane, is made. The 180° phase shift is achieved by moving the mirror a distance of $\lambda/2$ towards the acquisition plane as shown in Figure 3.6(b); this small displacement barely modifies the amplitude of the reference field in the acquisition plane. The second hologram, stored in the even columns of the final hologram, is acquired in a new grid with the same sampling but with an offset of Δx in the x-axis, see Figure 3.6(a).

The distance between samples in the x-axis of the final hologram, formed by multiplexing the two subsampled holograms, is Δx.

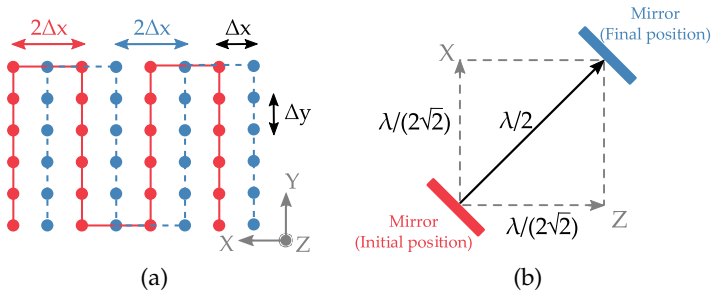

Figure 3.6: Hologram formation. (a) Acquisition grid for both subsampled holograms, and (b) displacement of the mirror between both acquisitions to introduce the 180° shift.

3.2.1.2 **Phase shifts modification and appearance of replicas in the spectrum of the reference antenna**

Formation of the phase shifts of the final hologram by multiplexing the two subsampled holograms will be explained through a numerical example. Consider an antenna measurement setup as the one described in Figure 3.5 such as the phase of the reference fields in the acquisition plane has the behavior shown in Figure 3.7(a), in where the 180° (or $\pi\, rad$) difference in the phase of both subsampled reference fields is clearly seen. The phase-shifts that these fields produce, can be obtained from the phase slope in the acquisition plane, depicted in Figure 3.7(b). The phase slopes of the reference fields for both positions of the mirror are identical and, for the sake of simplicity, its mean value, $\Delta\phi_{conventional} = -0.57$ rad will be considered from now on.

Sampling rate in the x-axis is $\lambda/3$ at 94 GHz for the subsampled holograms and thus, the final hologram sampling rate is $\lambda/6$. Therefore, the extension of the spectrum, as defined in (2.48) is $3k_0$ for this example.

If the conventional setup is considered, e.g. no displacement of the mirror is applied, the central position of the spectrum of the reference field will be $k_{r,x\,conventional} \simeq -0.54k_0$, applying (2.50) (see Figure 3.7(c)). However, when both positions of the mirror are considered, the phase-shift between samples of the reference field become $\Delta\phi_{proposed} = -0.57 + \pi = 2.57$ rad yielding a new term centered in $k_{r,x\,proposed} \simeq 2.45k_0$, $3k_0$ apart from the original image term, whose amplitude has been reduced as it is shown in Figure 3.7(c).

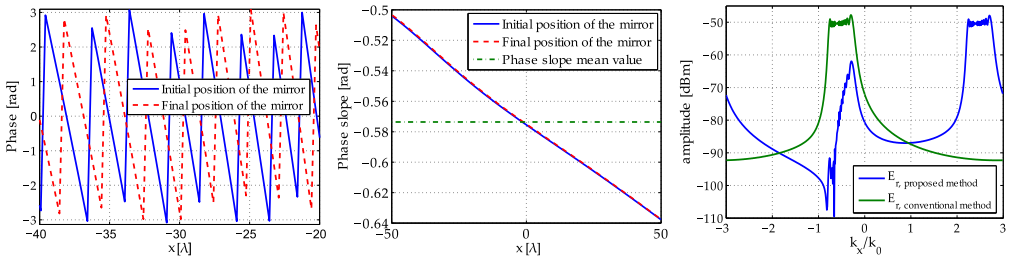

(a) (b) (c)

Figure 3.7: (a) Detail of the phase of both reference fields in a small region ($x[\lambda] = [-40, -20]$) of the acquisition plane, (b) phase slope of the two subsampled reference fields in the acquisition plane and (c), spectrum of the multiplexed reference antenna.

In the Appendix of **[II]** it is demonstrated that the original image terms of the spectrum of the reference field are canceled when plane reference waves are used.

Nevertheless when working with spherical reference fields, although the amplitude of the original image terms is reduced, they are not completely canceled. Position and tilt of the mirror have a big influence in the phase of the reference signal and therefore in the position of the hologram spectral terms and its shape and amplitude.

Figure 3.8 shows the effect of changing the length of the path of the reference signal for a given tilt of the mirror, $\theta_m = 63°$. For larger distances between the mirror and the reference antenna, the phase slope is almost plane (Figure 3.8(a)); the spectral terms of the reference field are narrower and the amplitude of the original term is highly attenuated (Figure 3.8(b)). This produces wider replica terms, with the shape of the spectrum of the AUT, that can be easily filtered, as shown in Figure 3.8(c). Additionally, holograms obtained for medium distances between the mirror and the reference antenna, present slightly narrower and distorted replicas of the image terms than can also be filtered without any problem.

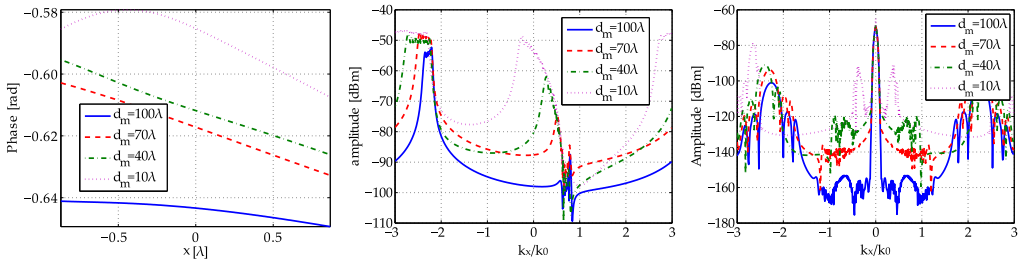

(a) (b) (c)

Figure 3.8: Influence of the distance between the reference antenna and the mirror for a mirror tilt of $\theta_m = 63°$. (a) Phase slope of the reference fields (b) spectrum of the reference signal and (c) spectrum of the final hologram.

On the other hand, Figure 3.9 shows the influence of the mirror tilt for a fixed distance, $d_m = 40\lambda$. From Figure 3.9(a) it can be clearly seen that larger tilts produce steeper slopes of the phase in the acquisition plane. The steeper the slope is, the narrower the image terms are (both, the original and the replica) and the highly attenuated the original term is (Figure 3.9(b)), thus, increasing the tilt of the mirror has similar effects than placing the mirror further from the reference antenna. The effect of the shape of the spectrum of the reference antenna in the final hologram is the same as in the previous case. Wider reference field spectra, produce narrower and distorted hologram image terms.

Thanks to the fact that the width of the spectral terms of the hologram, and thus, overlapping with original terms, can be also controlled with the mirror tilt,

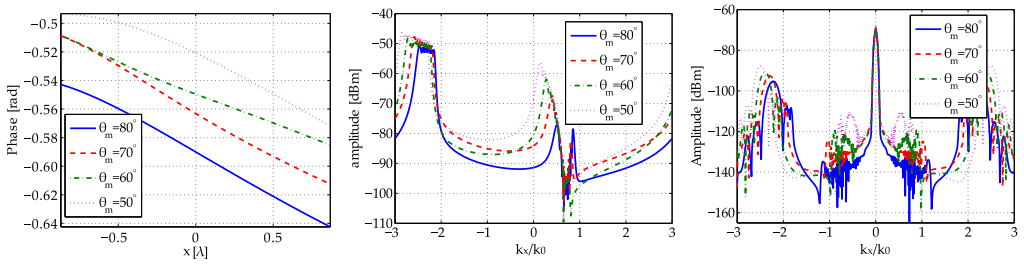

(a) (b) (c)

Figure 3.9: Influence of the tilt of the mirror for a distance of $d_m = 40\lambda$ between the mirror and the reference antenna. (a) Phase slope of the reference fields (b) spectrum of the reference signal and (c) spectrum of the final hologram.

there is no need of employing plane reference waves or placing the mirror at larger distances from the reference antenna. Therefore the desired replica of the image term can be correctly filtered even tough the original image term is not completely canceled.

3.2.1.3 Corrections: low pass filtering and amplitude correction

Since only a fraction of the spectral density of the image term (the replica) is filtered during the phase retrieval process, a small correction in the retrieved amplitude has to be made. The correction factor can be obtained from the analysis of the reference field. The power spectral density of the reference signal is distributed between the replica and the not completely canceled image term, as shown in Figure 3.10(a), and thus, when filtering only the replica, not all the power is taken into account, yielding to lower amplitude signals when the filtered spectrum is transformed back to the spatial domain, Figure 3.10(b).

The correction factor for the retrieved amplitude can be obtained by calculating the difference between the measured amplitude of the reference antenna and the amplitude obtained after filtering its spectrum with the same filter that will be used for the AUT phase retrieval, as shown in Figure 3.10(b).

On the other hand, and depending on the amount of overlapping between the original image term and the filtered replica, the retrieved phase of the AUT is contaminated with high frequency noise that can be eliminated by filtering the obtained phase with a low-pass filter.

Figure 3.11(a) shows the correction process for the amplitude of a lens antenna measured at 94 GHz while Figure 3.11(b) shows the low-pass filtering process applied to correct the error of the retrieved phase.

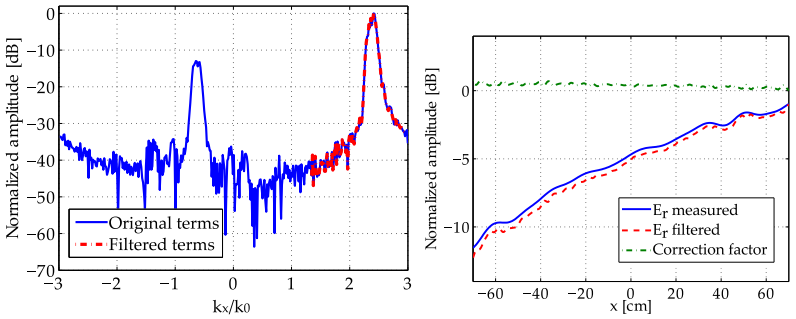

(a) (b)

Figure 3.10: Amplitude correction factor calculation. (a) Spectrum of the reference antenna, and (b) detail of the normalized amplitude of the measured reference antenna compared to the amplitude obtained after filtering the spectrum.

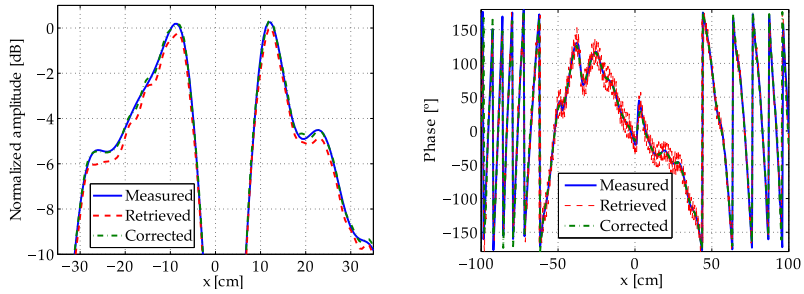

(a) (b)

Figure 3.11: Corrections applied to the retrieved amplitude and phase of a lens antenna at 94 GHz. (a) Detail of the amplitude in the central part of the acquisition plane, and (b) phase of the AUT in the acquisition plane.

A full measurement process for three different types of AUTs is detailed in **[II]** as well as a comparison between the quality of the results obtained with the proposed method and with the conventional one from NF amplitude and phase acquisition described in Section 2.1. The error of the phase retrieval process is significantly reduced with the proposed method due to the larger separations of the image terms, that allows an easier filtering. Furthermore, the use of radiated waves reduce the cost and complexity of the system compared to systems employing synthesized reference waves.

3.3 Broadband antenna measurement technique

Although the previously proposed setups improve the performance of the phase retrieval method based on off-axis indirect holography, these are monochromatic methods and neither the conventional technique nor the proposed methods are efficient to characterize broadband antennas in their whole working frequency range, specially if different spatial acquisitions have to be made for each frequency.

The third proposed method is based on an extrapolation of the off-axis indirect holography and can be employed for efficient phaseless characterization of broadband antennas. The physical layout of the components is exactly the same as the one used in conventional setups, see Figure 2.6(a) for further detail, whereas main differences lie in the data acquisition process and the filtering domain.

A frequency sweep along a set of equally spaced frequencies must be made at each spatial acquisition point, hence a hologram is recorded at each point of the acquisition grid in the FD as

$$\begin{aligned} H(\vec{r},\omega) = |E_{aut}(\vec{r},\omega) + E_r(\vec{r},\omega)|^2 = |E_{aut}(\vec{r},\omega)|^2 + \\ |E_r(\vec{r},\omega)|^2 + E_{aut}(\vec{r},\omega)E_r^*(\vec{r},\omega) + E_{aut}^*(\vec{r},\omega)E_r(\vec{r},\omega), \end{aligned} \tag{3.6}$$

being ω the angular frequency and $\vec{r}$, E_{aut} and E_r the position in the acquisition plane, the components of the fields of the AUT and the reference antenna respectively, as previously defined.

The modified hologram can be obtained as shown in (3.7), if an extra measurement is done to characterize the square amplitude of the AUT, although this is not strictly necessary.

$$\begin{aligned} H_m(\vec{r},\omega) &= H(\vec{r},\omega) - |E_{aut}(\vec{r},\omega)|^2 - |E_r(\vec{r},\omega)|^2 \\ &= E_{aut}(\vec{r},\omega)E_r^*(\vec{r},\omega) + E_{aut}^*(\vec{r},\omega)E_r(\vec{r},\omega). \end{aligned} \tag{3.7}$$

The inverse FT of the modified hologram produces the following signal in the TD:

$$h_m(\vec{r},t) = e_{aut}(\vec{r},t) \otimes e_r^*(\vec{r},-t) + e_{aut}^*(\vec{r},-t) \otimes e_r(\vec{r},t) \tag{3.8}$$

where e_{aut} and e_r are the inverse FTs of E_{aut} and E_r respectively.

The hologram is composed of the two cross-correlation or image terms (plus the autocorrelation terms if the complete hologram is employed). Hence, to retrieve the amplitude and phase of the AUT, it is necessary to filter the term cor-

responding to the convolution of $e_{aut}(\vec{r},t)$ and $e_r^*(\vec{r},-t)$ as

$$h_{mfiltered}(\vec{r},t) = \Pi(t_1,t_2)\{e_{aut}(\vec{r},t) \otimes e_r^*(\vec{r},-t)\}, \tag{3.9}$$

where $\Pi(t_1,t_2)$ is a rectangular window defined between t_1 and t_2. A numerical example of a modified hologram in the TD and the window used to filter the desired image term is shown in Figure 3.12.

Once the signal has been filtered in the TD, last step is the removal of the effect of the reference antenna back in the FD:

$$E_{aut}(\vec{r},\omega) \simeq \frac{H_{mfiltered}(\vec{r},\omega)}{E_r^*(\vec{r},\omega)} \tag{3.10}$$

where $H_{mfiltered}(\vec{r},\omega)$ is the FT of $h_{mfiltered}(\vec{r},t)$.

Thus, the field of the AUT is retrieved simultaneously for all the studied frequencies at every spatial acquisition point. The described process has to be repeated for all the points of the measurement grid.

Accuracy of the phase retrieval algorithm will depend mostly on the separation of the cross-correlation terms in the TD. This separation is determined by the starting times of the signals coming from the AUT and the reference antenna, t_{aut} and t_r and the spread of the image terms, $\Delta\tau$, as shown in Figure 3.12, and can be controlled with the position of the reference antenna and the length of the transmission line, L_{eff}, connecting it to the source [164].

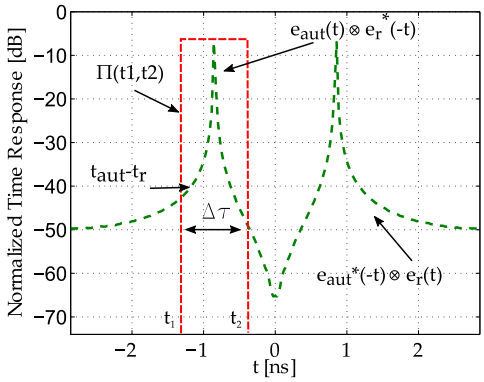

Figure 3.12: Spectrum of the modified hologram for a spatial acquisition point in the case L_{eff} is long enough so that the position of the image terms is swapped.

An extensive explanation of the main constraints of the setup regarding position of the antennas, L_{eff} and frequency sampling is given in [**III**]. Essentially,

L_{eff} must be chosen so that the position of the image terms of the hologram is swapped and $t_{aut} - t_r + \Delta\tau < 0$, and frequency sampling must satisfy the *Nyquist rule*:

$$\Delta f < \frac{1}{2T_{TD}} = \frac{1}{2(t_{aut} - t_r + \Delta\tau)} \tag{3.11}$$

being T_{TD} the duration of the signal.

Since the phase is retrieved point by point in the spatial domain, one of the main advantages of this method, opposite to conventional phaseless tecniques [33], is that spatial sampling requirements are the same as the ones required in complex acquisitions with amplitude and phase, that is $\lambda/2$ [34]. As a consequence, positioners accuracy is not as relevant as in conventional techniques for the phase retrieval process (accuracy is still necessary to perform NF-FF transformations based on PWE if no probe positioning correction algorithms are applied), and the method can be applied to mm- and submm-wave bands antenna characterization.

On the other hand, the main drawback of this developed method is that all the involved components, mainly the AUT, must be broadband. Characterization of narrowband antennas with this method could result in increased overlapping due to the spread of the computed time responses. Another disadvantage is that since the method is based on off-axis indirect holography, it is necessary to a-priori know the amplitude and phase of the reference antenna. For the validation of the proposed method, the reference field has been fully characterized; nevertheless, antennas with known amplitude and phase patterns [31] or phases obtained from simulation [108] can be employed in the field retrieval process to enable the use of amplitude-only acquisitions.

The method has been validated through numerical examples as well as through extensive measurement campaigns in the *Ka*- and *W*-bands. Results are presented in [**III**]. A graphic description of the implemented setups can be seen in Figure 3.13. Main difference between them is the path of the reference signal. In the *Ka*-band setup, overlapping is controlled with the length of a cable connecting the directional coupler and the reference antenna (Figure 3.13(a)), whereas in the *W*-band only two small waveguide sections were available and mirror reflection of the radiated reference signal is used to increase the path of the reference signal (Figure 3.13(b)) and control the position of the image terms.

3.3.1 **Efficient sampling**

Volume of data and, hence, scan-time is clearly still an issue in NF measurements at high frequency bands, in particular with holograms, or other phaseless

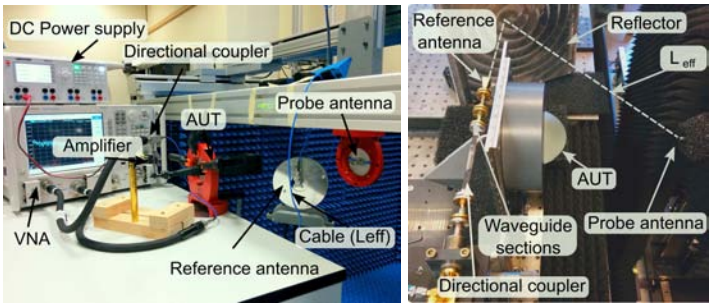

(a) (b)

Figure 3.13: Setups for the broadband phaseless method experimental validation. (a) Ka-band setup, and (b) *W*-band setup.

approaches, that need at least two different acquisitions: the hologram and the field of the reference antenna. Since in the proposed method the phase is retrieved point by point, the phase retrieval technique is not dependent on the geometry and standard non-redundant or efficient sampling schemes [76] can be directly applied to considerably reduce the number of acquisition points.

In order to validate the method the same measurement setup presented in [**III**] in the *Ka*-band is implemented, the acquisition being conducted in a reduced set of points. Results are presented in [**IV**] where for the studied example, characterization of a 25 dB SGH antenna, the reduced grid has 2055 points, while the equivalent grid has 13225 points. A comparison between the reduced and the regular grids is shown in Figure 3.14. For this case, a reduction by a factor of six is achieved.

3.3.2 Error analysis

A Monte Carlo analysis has been carried out with the purpose of obtaining the error bounds in the FF pattern of the AUT caused by positioning errors and noise presence when the proposed method for broadband antenna characterization using a reduced set of points is applied to measurements taken in the developed PNF measurement range, thus positioning errors and typical noise values achieved in the real measurement system are employed for the trials. The analysis has also been made for the case of considering a conventional acquisition of complex data over the equivalent regular grid which, from now on, will be considered the reference measurement. Behaviour of both methods is very similar in the presence of planarity errors [31], nevertheless uncertainties are slightly higher when XY positioning errors are considered. Presence of noise in the NF phaseless

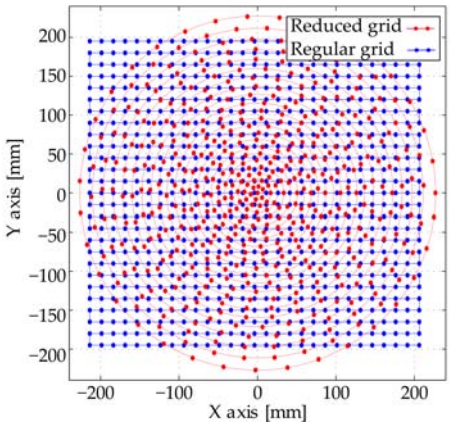

Figure 3.14: Comparison between the regular and the reduced grids. Only one of every four points is shown.

acquisition has a bigger impact in the FF pattern than the positioning errors, giving rise to the highest uncertainty values as it can be seen in Figure 3.15, showing the FF pattern of the AUT for random realizations of the Monte Carlo analysis considering each of the error terms independently.

Despite the impact of errors is higher for the proposed method, the obtained results are in very good agreement with the reference results allowing for considerably high reduction in acquisition time and data volume while performing wideband phaseless antenna measurements.

Main results have been published in [**IV**] and part of the statistical characterization by means of the Monte Carlo analysis is shown in Appendix B.

Performance of the proposed method is studied by means of measurements as well and the FF uncertainty of the proposed method is calculated with the pattern comparison technique described in [80] in relation to the reference measurement. Obtained uncertainty values are within the bounds obtained from the Monte Carlo analysis.

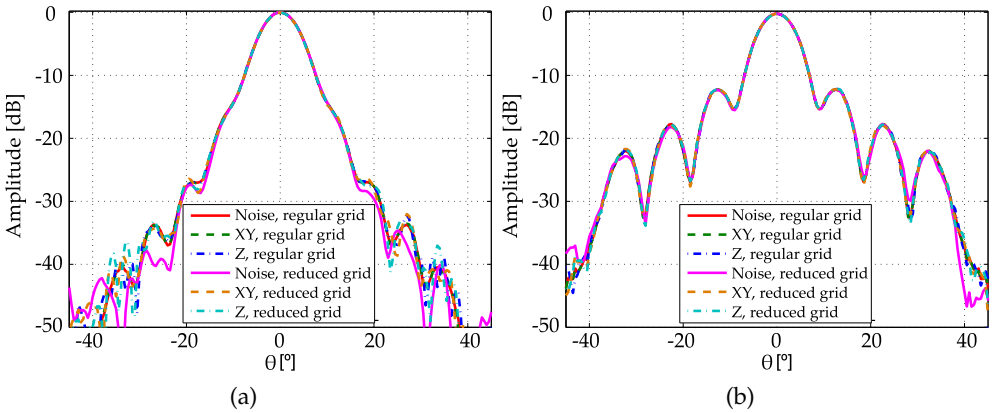

Figure 3.15: Random trials of the Monte Carlo method comparing the effect of the different type of errors in the FF at 38 GHz (valid margin of the NF-FF transformation is $\pm 36^{\circ}$). (a) Copolar component, $\phi = 0^{\circ}$, and (b) copolar component $\phi = 90^{\circ}$.

3.4 Summary

Novel off-axis indirect holography method and its application to antenna measurement and diagnostics are discussed in this chapter.

The experimental work of the author is devoted to develop new techniques based on the conventional approach that overcome the known limitations of indirect holography stated in Chapter 2. Three methods have been developed and validated numerically and experimentally at mm-wave bands.

The first developed method, presented in **[I]**, is a modification of the conventional setup with synthesized reference waves. The reference field is synthesized by means of mechanical shifts of the probe in the acquisition plane. This way the use of phase-shifters is avoided and hence, the cost and complexity of the setup are significantly reduced, while all the advantages regarding synthesized reference waves, such as overlapping or setup size reduction are still present.

Some of the approximations made for the development of the previous method are only valid when the probe is in the FF of the AUT. Nevertheless, as it has been experimentally proven, the method can provide accurate results even when that condition is not strictly fulfilled.

The main goal of the method described in **[II]** is to find a method to artificially increase the separation between the image terms in the spectral domain, as it happens in setups with synthesized reference waves, extending it to setups using radiated reference waves. Increasing the separation between the image terms

has several associated advantages: it is possible to work with the complete hologram and therefore, the extra measurement to characterize $|E_{aut}|^2$ in the *modified hologram* approach, is no longer needed; furthermore, larger separations allow to employ the method to characterize antennas with low directivity, which have wider spectra. As the separation of the image terms no longer depends on the physical position of the reference antenna, the aforesaid antenna can be placed closer to the AUT. This size reduction yields a less sensitive system to scan axis errors.

To achieve that larger separation, the hologram is formed by multiplexing two subsampled holograms obtained with a relative shift of 180° in the phase of the reference antenna. The phase-shift can be obtained by different means such as phase-shifters or mechanical displacements of the reference antenna. In **[II]** the phase-shift is obtained after introducing a mechanical displacement of $\lambda/2$ in a mirror employed to lead the reference field to the acquisition plane.

The previous methods retrieve the phase of the AUT after filtering in the spatial frequency domain for a given frequency and thus, their use is not appropriate for broadband antenna characterization as complete spatial acquisitions of the hologram and the reference antenna have to be made for all the desired frequencies, which is a very time consuming task.

The last developed method, presented in **[III]**, consists on a new efficient technique for the phaseless characterization of broadband antennas. The method is an extrapolation of the conventional Leith-Upatnieks technique in which a frequency sweep must be made at each spatial point of the acquisition grid. The phase retrieval is performed point by point in the acquisition grid, simultaneously for all the frequency band, by filtering the desired image term of the hologram in the TD.

One of the main advantages of the method is that it does not require phase shifts implementation, neither electrical nor mechanical and therefore, it can be easily adapted for a large number of frequency bands.

The technique does not depend on the acquisition geometry and as the phase is retrieved point by point, standard efficient sampling techniques can be directly applied. A reduction factor of 6 in the number of acquisition points is achieved in the results presented in **[IV]** compared to a conventional acquisition over a regular plane-rectangular grid.

Robustness of the broadband characterization method with efficient sampling, is assessed by means of Monte Carlo analyses when noise and positioning errors are present. Results of the statistical tests, presented also in **[IV]**, are compared to a reference acquisition of complex data over a regular grid, and still very accurate results are obtained even in the presence of noise or positioning errors.

CHAPTER

4

Novel off-axis holography techniques for electromagnetic imaging

This chapter is a brief overview of the novel developed methods based on indirect off-axis holography for imaging applications. The herein presented methods are focused on the accurate estimation of the reference field for better quality phase retrieval (see Section 4.1) and reduction of the complexity and cost of the imaging system by means of direct injection of the reference field to bypass part of the components of a conventional setup (see Section 4.2); a new efficient method for broadband SAR imaging is also presented (see Section 4.3).

The developed methods have been validated by means of numerical simulations and measurements and the results are presented in works **[V]**-**[VIII]**. Hence only the main concepts are summarized here.

4.1 Synthesized reference field estimation

As stated in Chapter 2, although advantageous, the synthesized reference waves setup cannot be always implemented, specially in those setups implemented at high frequency bands for antenna characterization or bistatic imaging applications in which the reference wave should be conveyed from the source to a power combiner on the receptor side by means of waveguide sections.

Nevertheless quasi-monostatic and multi-monostatic setups can benefit from the use of synthesized reference fields since transmitter and receiver antennas are placed close to each other and, in case of implementing raster scans, the whole RF block is moved together allowing for connection between both antennas.

As previously mentioned, some authors bypass the need of characterizing the reference field to remove its effect by introducing a slightly modification in the filtering process, assuming the synthesized reference is a perfectly plane wave [140, 141, 147, 148] of the form:

$$E_r(\vec{r}) = Ae^{-jk_0 r}. \tag{4.1}$$

In that case (see Section 2.4.2.2), the filtered image term of the spectrum of the hologram, (2.44), is displaced to the center of the spectrum, compensating the shift introduced by the plane reference wave during the hologram acquisition. The scattered field, E_s, is retrieved directly once it is Fourier-transformed back to the spatial domain and after compensating for the amplitude of the reference field [32]:

$$E_s(\vec{r}) = \frac{FT^{-1}\{h_{filtered}(\vec{k}) \otimes e^{jk_0 r}\}}{A}. \tag{4.2}$$

Other authors use analytic expressions of the phase of the plane reference field to avoid its characterization.

However, phase-shifters can introduce small phase errors [153] and amplitude variations increasing the overall error in the phase retrieval process. If the reference field is independently characterized, conventional phase retrieval following steps defined in equations (2.44) and (2.45) can be done at the expenses of adding extra time to the acquisition process [124, 149] and giving that it is possible to perform a full acquisition (amplitude and phase) of the reference field.

Further analysis of the reference wave synthesis reveals that insertion losses in the phase shifter are dependent on the phase shift value as well as on the input power. Hence, the amplitude of the reference field is not constant but modulated depending on the phase shifter state. In off-axis holography, the reference wave can be synthesized, depending on the sampling and the required separation between the image terms, generally through 2 [159], 3 [163] or 4 [124],[viii] different values of the phase shifter and therefore, the reference wave will have a periodic behavior in the direction in which the phase-shift is introduced with a period equal to the number of values of the phase shifter.

The amplitude of the reference field can be estimated directly from the hologram acquisition averaging several of the first measurement points. The acquisition plane has to be large enough so that the scattered field from the object can be neglected in that points and the main contribution to the hologram is due to the reference field (see Figure 4.1). Another option is to make the estimate from an independent acquisition of several points along the swept axis when the OUT is not present. Both options yield the same results when the acquisition plane is larger than the OUT, nevertheless, the latter option provides a more accurate estimate of the reference field if the dimensions of the OUT are similar to those of the acquisition plane or if it is part of a larger object.

Validation of this technique is presented in **[V]** for a quasi-monostatic setup at 15 GHz for the reconstruction of the same OUT used for one of the examples in [124], a square metal plate of 10 cm side with a hole of 2 cm of diameter. Phase retrieval in [124] is done after complete characterization of the reference field. The measurement setup is shown in Figure 4.1.

For the proposed technique, $\Delta\phi = 90^\circ$ and hence, 4 different phase values are cyclically repeated along the x-axis. The 4 values of the amplitude of the reference field corresponding to the 4 phase values, are estimated from the first 20 values of the first row of the acquisition plane, hence each value is calculated after averaging 5 different measurements. After that, the reference wave is computed for the complete acquisition plane by repeating the four estimated values.

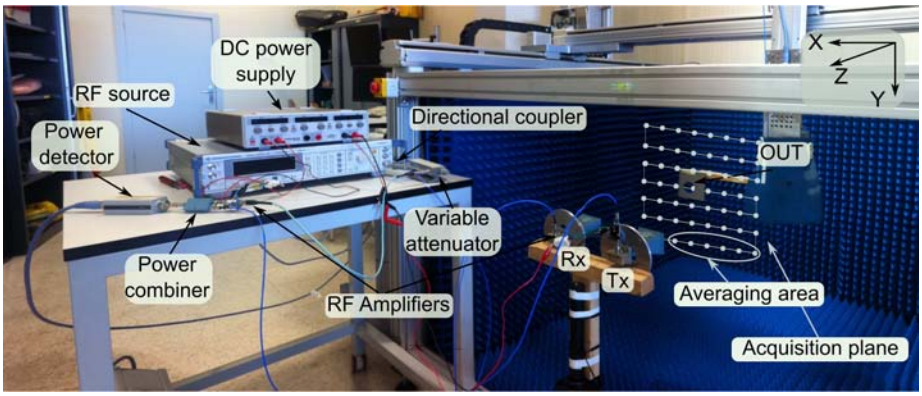

Figure 4.1: Quasi-monostatic setup with synthesized plane wave and estimation of the reference field.

A comparison of the results obtained with the proposed technique and the results from [124] is shown in Figure 4.2. Results are obtained from the computed reflectivity at $z = 0.5\,\mathrm{m}$ from the copolar component, E_y, of the retrieved field with the method described in [10]. The reconstructed profile from the estimated reference field from partial measurements is in very good agreement with the reconstructed profile after a complete characterization of the reference field.

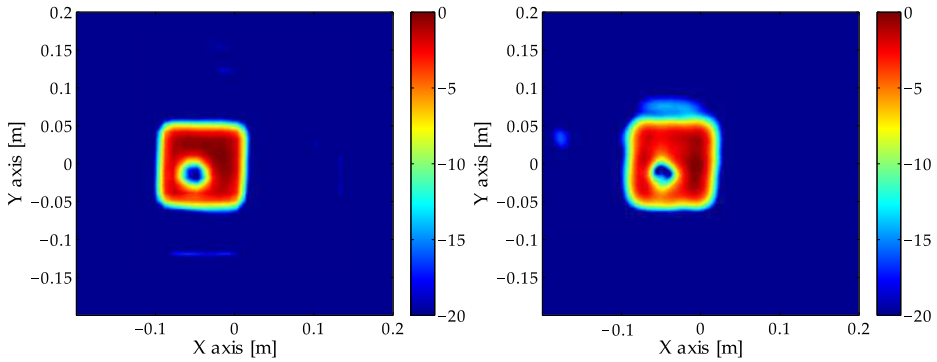

Figure 4.2: Comparison of the obtained results. (a) Retrieved reflectivity with partial characterization of the reference field and (b), retrieved reflectivity with complete characterization of the reference field.

4.2 Reference field injection by means of direct coupling

When setups are implemented by means of radiated reference fields, amplitude and phase characterization of the reference source, specially at mm- and submm-wave bands, can be a complex and very expensive task. As previously mentioned, some authors have resorted to *hybrid* approaches in which the amplitude of the reference source is measured and the phase is numerically modeled in the phase retrieval algorithm. In those cases, accurately knowing the phase center position of the reference antenna is mandatory and it can be necessary to employ iterative algorithms to precisely find the position of the reference source [108].

The use of synthesized reference waves solve the need for accurate characterization of the reference field (which has been already defined in [**V**]). Nevertheless, implementation of this type of setups require several different components, e.g. phase shifters, variable attenuators, directional coupler and power combiners that might not be available.

The use of mechanical shifts to bypass the employment of phase shifters has been presented in [**I**] for antenna characterization. The rest of components can also be avoided if the constant reference field is injected through direct coupling between the RX and TX antennas [iv]. In that case, a simplified phaseless scanner for phaseless imaging setups can be implemented only by means of the source, a power detector and the TX and RX antennas.

For the validation of this particular approach it has been chosen to implement a raster scan moving the OUT instead of the RF block. Similar results are expected in case the OUT has to remain static and the antennas have to be displaced.

4.2.1 Mechanical phase shifts

Mechanical displacements, as in [**I**], are introduced in the acquisition plane to achieve the same effect as when a regular grid and synthesized plane reference waves are employed. The displacements depend on the position of the original regular grid and therefore, they have to be calculated for each acquisition point. The process is similar to the one explained in section 3.1 for the antenna measurement problem but particularized to quasi-monostatic or monostatic setups where the roundtrip phase from the antennas to the OUT has to be taken into account.

For this configuration, assuming the TX and RX antennas are placed close to each other and the OUT is in their FF, the scattered field from the object can be expressed as:

$$E_s(x,y,z) \simeq \frac{A(x,y,z)}{R^2} e^{-j2kR}, \tag{4.3}$$

where $A(x, y, z)$ is a complex function dependent on the reflectivity of the OUT, and $R = \|\vec{R}\|_2$, being $\vec{R}$ a vector from the central point between the antennas to the center of the OUT as defined in Figure 4.3.

To introduce the mechanical phase shift, the OUT is displaced a small distance $\vec{d}$ in the direction of $\hat{R}$, the unitary vector of $\vec{R}$, such as the scattered field in the modified points of the acquisition plane, denoted with primed coordinates, can be approximated by

$$E_s(x', y', z') \simeq E_s(x, y, z)e^{-j2kd}. \tag{4.4}$$

The phase shifts are defined by the exponent in (4.4) for each point of the acquisition grid. The obtained three dimensional grid is a *layered grid* with as many layers as number of phase shifts per cycle ($\Delta\phi = 2\pi/N_\phi$), usually N_ϕ is 3 or 4 [124, 163]. The grid used in **[VI]**, for the validation of the proposed method is similar to the one shown in Figure 3.2 with $N_\phi = 4$ that was generated for the validation of a similar setup for antenna measurements presented in **[I]**.

The displacements have to be small enough so that the amplitude change can be neglected an the approximation in (4.4) remains valid.

4.2.2 Reference field injection

Since the phase shifts are mechanically introduced, the reference wave has to be a signal of constant amplitude to form the hologram, (3.2). Thus, the setup can be easily modified to inject that constant field through direct coupling between the TX and RX antennas, bypassing the need of using the rest of the components as depicted in Figure 4.3.

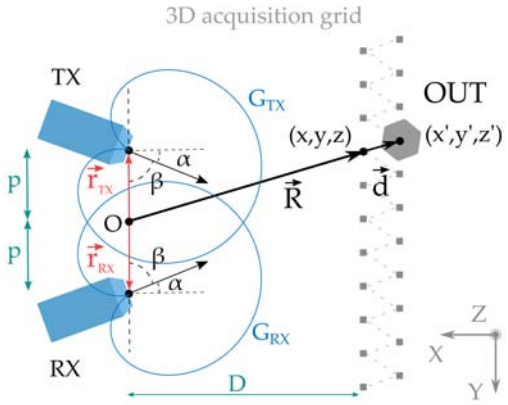

Figure 4.3: Bistatic setup for direct injection of the reference field.

The amount of power coupled between both antennas can be controlled with the separation between them, $2p$, and the angle (α) formed by the normal to the acquisition plane and the maximum of the antenna radiation pattern (see Figure 4.3 for further details). The coupled power is given by the *Friss* transmission equation:

$$P_r = P_{TX} G_{TX}(\beta) G_{RX}(\beta) \left(\frac{\lambda}{8\pi p} \right)^2 \tag{4.5}$$

being P_{TX} the power transmitted by the TX antenna, and $G_{TX}(\beta)$ and $G_{RX}(\beta)$ the gains of both TX and RX antennas in the direction in which the coupling is achieved.

A specific level of coupled power can be accomplished by carefully choosing the antenna type and by selecting the tilt and separation. Nevertheless, the introduced tilt and separation transforms the setup in a multistatic setup [165] and therefore, it is necessary to find a compromise so that the approximations in (4.3) and (4.4), for monostatic setups, remain valid. Or alternatively a generic formulation for multistatic systems can be considered for recovering the radar image for the retrieved complex field [112].

Characterization of the reference field can be made without resorting to full acquisition of its amplitude and phase by applying the previous method and estimating the field from the initial samples of the acquired hologram (See Section 4.1)and analytically computing the phase shifts associated to the displacements at each acquisition point.

4.2.3 Main sources of error

In addition to the already addressed main error contributors in indirect off-axis holography [31, 55, 143], especially related to the filtering process of the image terms, the approximations made in order to introduce the mechanical phase shifts and the direct injection of the reference field introduce new errors in the acquisition and phase retrieval process that have to be taken into account.

4.2.3.1 Error due to the monostatic approximation

Tilting the antennas in order to maximize and control the coupling, increases the path of the field from the TX to the RX antenna which is no longer $2d$ as indicated in (4.4).

The distance increment, due to the bistatic setup in order to achieve a $2d$ displacement is given by the following expression, assuming the point O in Figure 4.3

corresponds to the origin of coordinates:

$$e_b(x,y,z) = (\|\vec{R'} - \vec{r_{tx}}\|_2 + \|\vec{R'} - \vec{r_{rx}}\|_2) - (\|\vec{R} - \vec{r_{tx}}\|_2 + \|\vec{R} - \vec{r_{rx}}\|_2) - 2d, \quad (4.6)$$

where $\vec{R'} = \vec{R} + \vec{d}$ and $\vec{r_{tx}}$ and $\vec{r_{rx}}$ denote the position of the TX and RX antennas. As defined in Figure 4.3, $\|\vec{r_{tx}}\|_2 = \|\vec{r_{rx}}\|_2 = p$.

The maximum phase error is produced when the OUT is placed in the x-axis and therefore, can be expressed as

$$\begin{aligned} \varphi_b = k e_b(x = -D, y = 0, z = 0) &= k\left(2\|\vec{R'}\|_2 + 2\|\vec{R}\|_2 - 2d\right) \\ &= 2k\left(\sqrt{(D+d)^2 + p^2} - \sqrt{D^2 + p^2} - d\right). \end{aligned} \quad (4.7)$$

4.2.3.2 **Error due to multi-frequency acquisition**

Mechanical displacements to introduce the phase shifts are calculated for an specific frequency. For 3D object reconstruction, acquisition of the scattered field has to be made for multiple frequencies [109], hence different grids should be used for each of the frequencies with the consequent time increment.

Nevertheless, the phase retrieval method can tolerate certain phase error and still give good results and therefore, the same set of points can be used for a frequency acquisition if the bandwidth is relatively small. For that case, if the mechanical displacements are calculated to match the phase shifts at the central frequency, f_c, the error can be calculated as

$$\varphi_f(f) = 2d\,k - \Delta\phi = \frac{\Delta\phi}{k_c}k - \Delta\phi = \Delta\phi\left(\frac{f - f_c}{f_c}\right), \quad (4.8)$$

being k_c the wave number at the central frequency.

The maximum phase error will be introduced in the extremes of the frequency band for the maximum phase shift considered, $\Delta\phi$.

Performance of the method for a multi-frequency acquisition has been studied by means of a numerical example presented in **[VI]**. In that example the scattered field of a tilted isosceles trapezoid with dimensions of the parallel sizes of 4 and 2 cm (see Figure 4.4), is acquired in the frequency band from 285 GHz to 315 GHz. The grid is computed at the central frequency, that is 300 GHz, and 4 phase shifts of 90° are considered. The phase error in the extremes of the band, obtained from (4.8) is $\varphi_f(f = 315\,GHz) = 4.5°$.

A phase error from the bistatic approximation has to be considered as well. The geometry parameters for this setup are, as defined in Figure 4.3, $p = 2.75$ cm,

$\alpha = 45^\circ$ and $D = 10\,\text{cm}$. Since $\Delta\phi = 90^\circ$, and $\Delta\phi = 2kd$, the displacements are $d = \lambda_c/8$, being λ_c the wavelength of the central frequency. For this setup, the phase error due to the monostatic approximation given by (4.7), is $\varphi_b = 3.2^\circ$.

Those phase errors yield a mean and a maximum error of $-52\,\text{dB}$ and $-40\,\text{dB}$ respectively, computed as the Root Mean Square (RMS) of a direct acquisition with no errors and the retrieved reflectivity taking into account both type of errors. The impact of the errors has very low influence in the final result as it can be seen in the retrieved object profile shown in **[VI]** (depicted in Figure 4.4 as well).

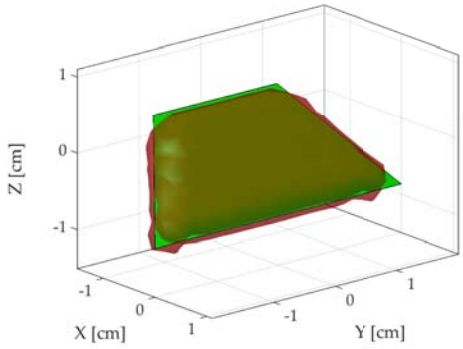

Figure 4.4: Retrieved 3D object profile for a simulation of a multifrequency acquisition. Isosurface $|J| = -10\,\text{dB}$. The original shape of the object is shown in transparent green while the retrieved shape is shown in solid red.

4.2.3.3 **Error due to the accuracy of linear stages**

Extensive error analyses of the positioning and periodic errors due to positioning accuracy have been made in [31, 55, 143]. In the developed work in **[VI]** only the upper bound, for the known linear stage accuracy d_{error} is calculated as

$$\varphi_p = 2kd_{error}. \tag{4.9}$$

4.2.4 **Phase retrieval and object profile reconstruction**

The reference field and the hologram have to be characterized independently. Characterization of the reference field is simple. The amplitude, C, of the constant field injected from the TX to the RX can be measured in the absence of any OUT. After that, the complete reference field, with amplitude and phase, can be computed for all the points of the acquisition grid by taking into account the phase shifts introduced by the mechanical displacements.

The image term of the hologram corresponding to $E_s e^{j2kd} \otimes C$, centered around $k_{r,x}$ (see Figure 2.8) can be filtered in the spatial frequency domain. Since the complete hologram is being considered, a certain degree of overlap could be expected depending on the selected spatial sampling.

Once the desired image term is filtered in the spatial frequency domain, the amplitude and phase of the scattered field are retrieved in the spatial domain after dividing by the computed reference field in the whole acquisition plane. Figure 4.5 shows as an example the retrieved amplitude and phase for the scattered field of the OUT characterized in the measurement example in **[VI]**.

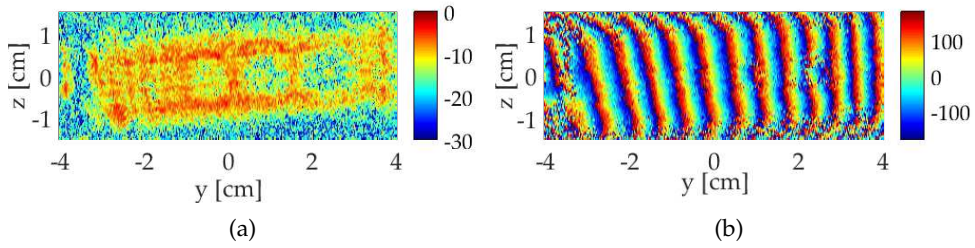

Figure 4.5: Retrieved field for a measurement example at 300 GHz. (a) Normalized retrieved amplitude (dB) and (b), retrieved phase (degrees).

After the amplitude and phase of the scattered field have been retrieved, the object profile reconstruction can be made with any of the conventional inverse scattering techniques already available in the literature. For the validation of the proposed technique the inverse Fast Multipole Method (iFMM) described in [125] is employed.

4.2.5 Experimental validation

The proposed technique has been experimentally validated. The results are gathered in **[VI]**, where the profile of a rectangular plate of 7 cm x 2 cm with holes of radii 9, 6, 3 and 1.5 mm is reconstructed from the phaseless measurement of the hologram at 300 GHz.

Main parameters of the measurement setup are $p = 2.25$ cm, $\alpha = 45^\circ$ and $D = 5$ cm (see Figure 4.3); 4 phase shifts of 90° each are employed, therefore $d = \lambda/8$. The reconstructed profile of the object is shown in Figure 4.6, where it can be observed that the shape of the metallic plate as well as the holes of different diameter are recovered despite the approximations made during the formulation of the method. Only the smallest hole of 1.5 mm radius is partially reconstructed while the rest of details are perfectly retrieved.

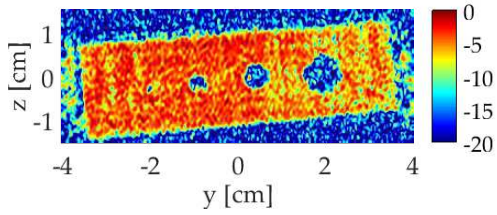

Figure 4.6: Profile reconstruction of the metalic plate with holes at 300 GHz. Reflectivity (normalized amplitude in dB).

4.3 Phaseless synthetic aperture radar for near-field broadband imaging

The method introduced in Section 3.3 for phaseless broadband characterization of antennas is suitable for SAR NF imaging applications when adapted to work in multi-monostatic setups. The setup can be implemented either by means of arrays of monostatic elements or a raster scan with a single element.

Multi-monostatic acquisitions are a good trade-off between complexity of the setup and quality of the results with respect to other possible arrangements such as bistatic or multistatic configurations. Complexity of multi-monostatic setups is proportional to the complexity of each of the employed elements which, in case of implementing the hereby proposed method, is reduced to a minimum. Figure 4.7 shows a scheme with the components of the setup for the case of considering a raster scan. The monostatic (or quasi-monostatic) element is formed by the TX and RX antennas and the reference field branch. The reference branch is formed by a directional coupler and a variable attenuator. The power of the reference branch is added to the acquired scattered field by means of a power combiner.

Aiming to reduce the complexity of the setup, the use of radiated reference waves, as in the phaseless broadband method for antenna characterization presented in [**III**]-[**IV**], has been discarded and the reference is conveyed directly from the source to the power combiner. Nevertheless, although the topology of the setup is similar to conventional off-axis holography setups with synthesized reference waves, for this case it is not necessary to employ neither electrical nor mechanical phase-shifts.

Despite the methodology is similar to the one presented in Section 3.3 for the phaseless broadband method for antenna characterization, some differences arise due to the quasi-monostatic arrangement of the elements.

The method can be divided in three different steps when non-redundant sampling techniques are applied: 1) The hologram is acquired over a frequency band

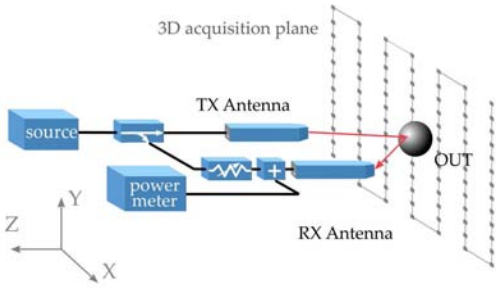

Figure 4.7: Proposed quasi-monostatic element for the setup validation by means of a raster scan.

at each point of the non-redundant acquisition grid and the phase retrieval is accomplished, 2) once the amplitude and phase of the scattered field are known in the non-redundant grid, an OSI has to be applied in order to obtain the complex field in a regular set of points. Step 3) consists in the OUT profile reconstruction. Since the scattered field of the OUT is known in amplitude and phase at this point, any of the available methods in the literature could be employed at this point.

Scalar calibration techniques for the proposed method have already been developed [150] in order to bypass the need of previously characterizing the reference field in amplitude and phase.

The hologram, H, is obtained at each point of the raster scan over a set of equally spaced frequencies. The *modified hologram*, after subtracting the squared amplitude of the scattered field $E_s(\vec{r},\omega)$ and the reference field $E_r(\vec{r},\omega)$ can be expressed as

$$\begin{aligned} H_m(\vec{r},\omega) = |E_s(\vec{r},\omega) + E_r(\vec{r},\omega)|^2 - |E_s(\vec{r},\omega)|^2 - \\ |E_r(\vec{r},\omega)|^2 = E_s(\vec{r},\omega)E_r^*(\vec{r},\omega) + E_s^*(\vec{r},\omega)E_r(\vec{r},\omega). \end{aligned} \tag{4.10}$$

In this case, considering that the elements in the reference branch exhibit a low-dispersion behavior, the reference field is a delayed field, proportional to $e^{-jt_d w}$, being t_d the delay associated to the propagation of the field through the elements of the reference branch.

In practice, the time response of the reference branch should be characterized to take into account the dispersion and mismatches between all the components since it will determine the minimum distance at which the OUT can be placed to avoid overlapping, as it will be shown next.

Post-processing of the hologram is analogous to the one followed in conventional off-axis holography but in the TD instead of the k-space. The modified hologram in the TD is defined by the following expression:

$$h_m(\vec{r},t) = e_s(\vec{r},t) \otimes e_r^*(\vec{r},t) + e_s^*(\vec{r},t) \otimes e_r(\vec{r},t). \tag{4.11}$$

4.3.1 Overlapping control and setup constraints

In [**III**], [164],[iv] a delay line in the reference branch played the role of the phase-shifter in conventional off-axis holography setups to control the position of the image terms of the hologram. Nevertheless, in this proposed method with the aim of simplifying the monostatic element, it has been proven that the delay line can be avoided if the set of constraints for overlapping control is slightly modified.

The initial point of the image term of the hologram that has to be filtered in order to retrieve the amplitude and phase of the scattered field is defined by $t_{min} - t_d$, where t_{min} denotes the starting time of the scattered field, and t_d, as previously defined, is the delay introduced in the reference branch (see Figure 4.9). In contrast to the approach followed in [**III**], in order to avoid overlapping of the image terms, the following condition has to be fulfilled for the proposed setup,

$$t_{min} - t_d > 0, \tag{4.12}$$

and therefore, the starting time of the signal has to be larger than the delay in the reference branch.

The previous condition imposes a restriction regarding the minimum distance between the OUT and the position of the antennas, d_{min}, which for a monostatic setup is defined as

$$d_{min} = \frac{ct_{min}}{2} \quad \Rightarrow \quad d_{min} < \frac{ct_d}{2}. \tag{4.13}$$

Hence, the minimum distance at which the OUT can be placed depends on the dispersion introduced by the elements of the setup and is a critical parameter when no delay lines are employed. Special care has to be taken in case of employing off-the-shelf components, since dispersion will be larger than in an integrated circuit made *ad-hoc* for the application.

A constant frequency response of all the components of the setup will produce an impulsive response in the TD making possible to retrieve the scattered field with very low error. Nevertheless some of the components can introduce variations and produce wider time responses. As shown in [**VI**] the variable attenuator, whose response changes depending on the selected attenuation value, is one of the most delicate components regarding this matter.

A detailed characterization of the time responses of the employed elements in the setup for the validation of the proposed method is included in **[VI]** for several numerical and experimental setups. Here, only a brief example to illustrate the influence of the duration of the signals in the position of the image terms of the hologram is shown. The example corresponds to the data obtained from a frequency sweep of 1600 points in the *Ka*-band in the central point of the grid employed for the reconstruction of the metallic letter *S* shown in **[VI]** when it is placed at 13.5 cm of the aperture of the antennas.

Figure 4.8 shows the frequency responses for the scattered field and the reference branch in the presented example as well as the measured holograms. The response of the scattered field is almost plane, which is traduced in a very narrow time response, while the amplitude of the reference branch presents slight variations along the frequency band which are traduced in a wider time response (see Figure 4.9).

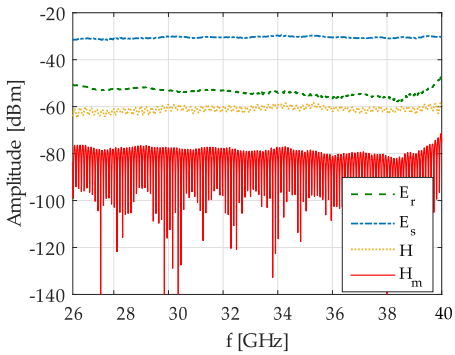

Figure 4.8: Frequency responses of the different terms of the hologram.

Figure 4.9(a) shows the time responses of the scattered and the reference fields and the modified hologram. A threshold of -25 dB is employed to obtain t_d and t_{min} which for this example are 1.5 ns and 5.3 ns respectively. The starting time of the image term of the hologram is $t_{min} - t_d = 3.8$ ns. If an extra delay of 4 ns is added to the reference branch, the starting time of the image term will be reduced 4 ns, making $t_{min} - t_d < 0$, as shown in Figure 4.9(b), and causing the corresponding overlapping in the terms of the hologram, as it can be seen in Figure 4.10(b).

The overlapping effect can be more clearly seen when the hologram is observed in the complete TD. Figure 4.10(a) shows the holograms for the case in which no delay line is considered. The complete hologram is shown together with the modified one as a reference. For this concrete case, the image term can also be filtered from the complete hologram, and therefore, characterization of

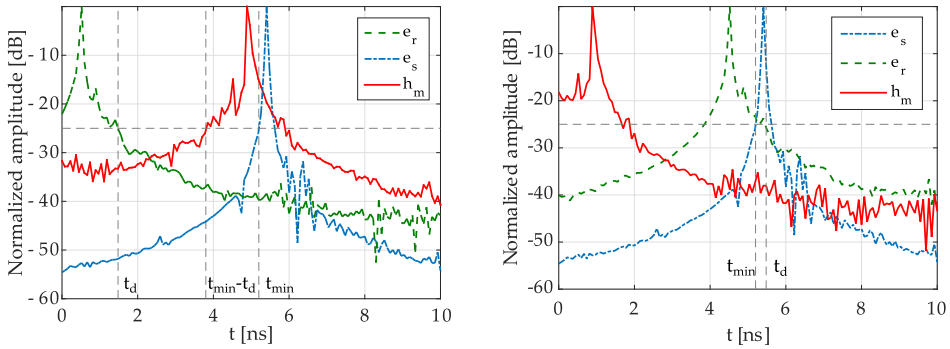

Figure 4.9: Time responses of the different terms of the hologram for different configurations of the reference branch. a) No delay line is considered and (b), a delay of 4 *ns* is considered.

$|E_s(\vec{r},\omega)|^2$ could be avoided. When a delay line of 4 ns is considered, Figure 4.10(b), a certain overlap is introduced in the modified hologram, although part of it can still be filtered. Nevertheless, in the case of considering the complete hologram, the overlapping with the autocorrelation terms makes very difficult any filtering process to retrieve the original scattered field.

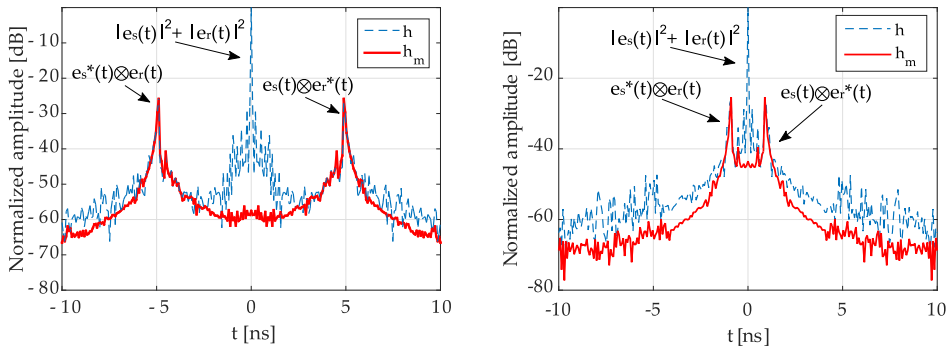

Figure 4.10: Hologram and modified hologram in the TD for different configurations of the reference branch. a) No delay line is considered and (b), a delay of 4 *ns* is considered.

The same rectangular filter, from 1.3 ns to 8 ns is applied to the modified hologram for both cases. Then the field is retrieved back in the FD just for the central

point of the acquisition grid. The error of the field retrieval process is obtained as

$$error[\%] = \frac{\|\vec{E}_{s,measured} - \vec{E}_{s,retrieved}\|_2}{\|\vec{E}_{s,measured}\|_2}. \tag{4.14}$$

being $\vec{E}_{s,measured}$ a vector containing the samples of the acquired scattered field with amplitude and phase used as a reference and, $\vec{E}_{s,retrieved}$ a vector containing the retrieved field with the proposed method. Error for both cases is represented in Figure 4.11 for all the frequency band. Mean error is 5.10 % for the case of not considering any delay line and 17.50 % for the case of including a 4 ns delay line.

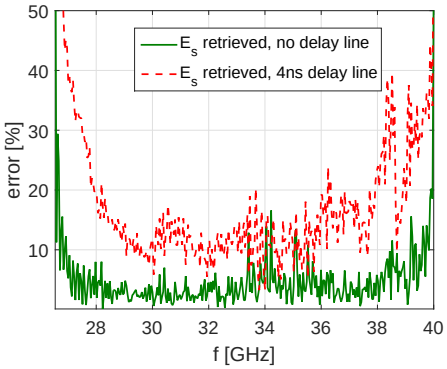

Figure 4.11: Error of the field retrieval for the central point of the acquisition plane for different configurations of the reference branch. a) No delay line is considered and (b), a delay of 4 ns is considered.

From the previous example, it can be concluded that the use of delay lines can be avoided if the dispersion is kept to a minimum. In case of employing elements with high-dispersive behavior, which will increase t_d, the method can still be employed. Nevertheless, it is necessary to resort to the use of delay lines long enough to completely swap the position of the image terms, as done in **[VI]** and [164].

Restrictions regarding the frequency sampling rate are the same than the ones applied in **[III]** and [149]. Samples must be taken according to the *Nyquist criterion* so that $\Delta f = 1/(2t_{max})$, being t_{max} the maximum extension of the TD, defined as $t_{min} - t_d + \Delta\tau$, with $\Delta\tau$ the duration of the image term of the hologram (see Figure 3.12 for further detail).

4.3.2 Non-redundant sampling

Sampling rate in monostatic setups is twice the required sampling rate for bistatic setups or complex antenna measurement [10], that is $\lambda/4$. Furthermore, in conventional off-axis holography, this rate has to be doubled, up to $\lambda/8$, due to the spatial bandwidth of the squared fields [75, 124].

One of the main advantages of the proposed method, in contrast to conventional off-axis holography, is that the phase is retrieved independently at each spatial point in the TD and therefore, sampling restrictions due to the spatial bandwidth of the squared signals do not apply.

Furthermore, the proposed method can be used with standard *array thinning* techniques that allow for further reduction of the acquisition points in raster scans, or the use of sparse arrays. For the validation of this method, the non-redundant sampling theory [76] introduced in section 2.3, and already adapted to work with monostatic acquisitions [124], is employed.

Reduction factor depends on parameters such as the object size (the radius of a virtual sphere enclosing the object, a), the maximum working frequency, f_{max}, the radius of the acquisition plane, ρ_{max}, and the distance between the OUT and the antennas, D. Other parameters such as the excess bandwidth and the oversampling [76] are also important to determine the number of points of the non-redundant grid. Table 4.1 gathers the main parameters of the setups developed for the validation of the method presented in **[VI]**.

Table 4.1: Main parameters for the non-redundant sampling employed in the validation examples in **[VI]**.

OUT	a [cm]	D [cm]	ρ_{max} [cm]	f_{max} [GHz]	reduced points	regular $\lambda/4$ sampling	reduction factor
Pyramid (simulation)	3.9	7.5	20	40	4200	35727	8.5
Metallic letters (measurement)	4	13.5	20	40	3192	35727	11.2
Box with object (measurement)	9	13	16	40	11206	22865	2

Excess bandwidth and oversampling factors are set to 1.2.

If the parameters from the pyramid and the metallic letters setups are compared, it can be seen than smaller distances between the OUT and the monostatic element for an object of similar dimensions, causes lower reduction factors. On the other hand, comparison of both measurement examples show that larger OUTs dimensions yields denser non-redundant grids.

4.3.3 Direct application examples

Versatility of the method allows for its use in different frequency bands as well as in applications in many fields such as security and personnel screening, non-destructive inspection, through the wall imaging, detection of buried objects in GPR applications, etc.

Among the presented examples for the validation of the proposed techniques gathered in **[VI]** and **[VII]**, two of them are worth mentioning due to its direct application. In the first of them, the phaseless SAR method for broadband NF imaging is employed in a setup for non-destructive inspection of small objects. In the second example, a setup for through the wall imaging is implemented with an *ad-hoc* designed monostatic element in order to keep the dispersion to a minimum and validate the proposed approach with no delay lines.

4.3.3.1 Non-destructive inspection

In this example the profile of a staple remover of 6 cm x 5 cm x 1.5 cm inside a cardboard box of 14 cm x 11 cm x 4 cm covered with foam is reconstructed.

The box is placed at 13 cm of the aperture of the antennas, two small horns of 15 dB gain in the *Ka*-band vertically polarized, and moved along a plane polar grid of 11206 points creating a synthetic aperture of 804 cm^2.

The scattered field is acquired in just one spatial sweep simultaneously for all the frequencies. For this example, 201 equally spaced points from 26.5 GHz to 40 GHz. The reference branch is independently characterized when no OUT is present. Further details of the described example can be found in **[VII]**.

Time response of the reference branch is shown in **[VI]**. The reference field vanishes at $t_d = 1.5$ ns and therefore, applying (4.13), the minimum distance at which the OUT can be placed to avoid overlapping is 22.5 cm. Nevertheless, this distance does not take into account the delays that can be introduced in the path of the direct signal and for this example can be considerably reduced due to the 90 cm cable employed to connect the RX antenna to the power combiner (see Figure 4.12).

Number of points of the reduced grid could be slightly reduced for larger distances between the OUT and the antennas. However, dynamic range would decrease and therefore, a trade-off between both parameters has to be set.

Figure 4.13 shows the retrieved profile of the staple remover for a reflectivity amplitude isosurface at -10 dB. Shape and dimensions of the object are accurately retrieved.

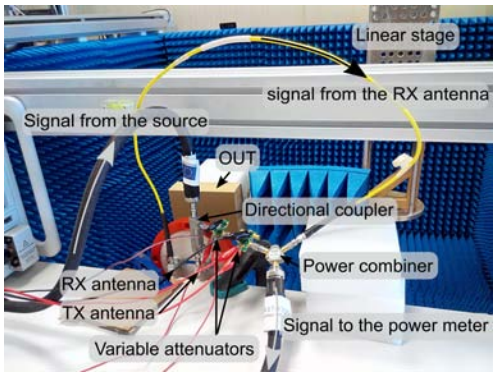

Figure 4.12: Setup for the non-destructive inspection example.

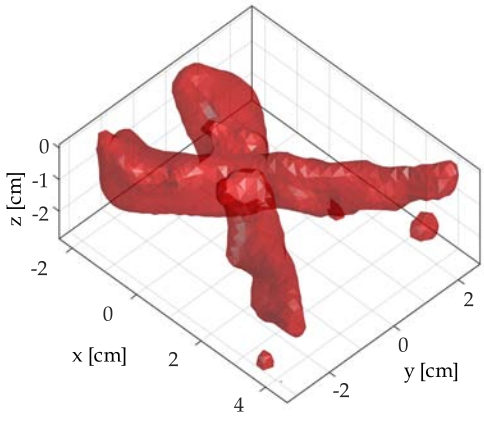

Figure 4.13: Retrieved profile for the staple remover inside the box. Normalized reflectivity isosurface at -10 dB.

4.3.3.2 Through the wall inspection

In this case, the method is employed in a setup for through the wall inspection [**VIII**]. An interferometric circuit containing the directional coupler and the power combiner has been implemented in microstrip technology. The circuit has been manufactured using Arlon 25N of 203 μm. Coupling factor is designed to be within -40 dB and -50 dB, after characterizing the direct signal attenuation through the considered walls. Different circuits should be designed for other kind of walls, so the levels of the reference signal and the scattered field are balanced.

The same horn antennas used in the previous example in Section 4.3.3.1 have been considered instead of integrating microstrip antennas in the interferometric circuit, because of their stable behavior within the frequency band and low

coupling characteristic. For additional details about this example, please refer to [**VIII**].

Figure 4.14 shows the setup for a 1.3 cm plasterboard wall. The OUT consists of a 10 cm square metallic plate with a 4 cm diameter hole and a 3.2 cm metallic pipe, and placed 10 cm behind the wall. The scanned aperture is 64 cm x 16.5 with a sampling step of $\lambda/4$ at 40 GHz.

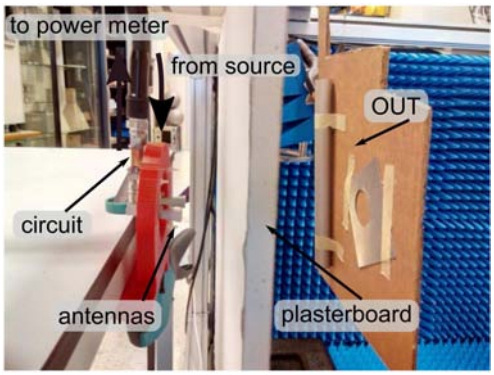

Figure 4.14: Setup for the through the wall inspection example.

The thickness of the wall and the shape, dimensions and position of the OUT are perfectly retrieved, as observed in Figure 4.15. Furthermore, due to the time-gating process during the field retrieval, the effect of the walls could be suppressed, if desired.

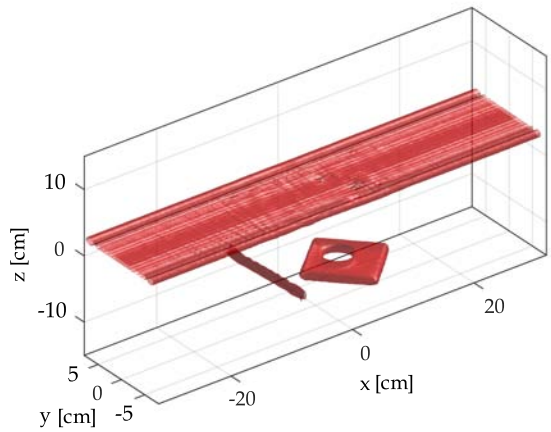

Figure 4.15: Retrieved profiles for the plasterboard wall and the objects behind. Normalized reflectivity isosurface at -10 dB.

Examples at lower frequency bands for imaging thicker types of walls such as bricks and mortar have also been included in [**VII**] with very good results.

It is worth mentioning that this application is not compatible with the non-redundant sampling techniques employed in the previous examples, as it is not possible to *a priori* known the size of the OUT, behind the wall needed to compute the reduced set of points.

4.4 Summary

The first of the proposed techniques for enhanced phaseless imaging introduces a method for the estimation of the reference signal from a partial acquisition of the hologram. It can be employed in setups with synthesized reference waves using either mechanical or electrical phase shifts. Since the independent characterization of the reference field, in amplitude and phase, is not required, acquisition time is reduced as well as the complexity of the system in case of including switching devices for the simultaneous acquisition of the hologram and the reference field [31].

The second method described in this chapter aims for a reduction of the number of components of the setup by means of the use of radiated reference fields directly coupled from the TX to the RX antenna and controlling the overlapping of the image terms via mechanical displacements. The setup can be fully implemented with the TX and RX and linear stages or micropositioners for the 3D movement which introduces the mechanical displacements. Hence, the only limitation is the accuracy of the positioners to obtain the phase shifts. Nevertheless, as the field retrieval is done in the spatial frequency domain, more restrictive sampling requirements are needed to avoid overlapping in a monostatic configuration.

The last proposed technique allows for broadband phase retrieval providing a frequency sweep is made at each of the acquisition points of the hologram. The setup can be implemented by means of a raster scan with a quasi-monostatic element or using an array or elements. In both cases, the layout of the element (formed by a directional coupler, a power combiner, a variable attenuator and the antennas) is equivalent to the layout used in conventional off-axis holography with synthesized waves. Dispersion of the components in the reference branch has to be kept to a minimum in order to control overlapping of the image terms.

As the amplitude and phase of the scattered field are retrieved point by point sampling requirements are imposed by the algorithm used for the OUT profile reconstructions, generally $\lambda/4$.

Furthermore, the proposed techniques are compatible with array thinning techniques as long as the approximate size of the OUT is known.

The technique for the estimation of the reference signal can be employed in the second method for an estimation of the amplitude of the reference field while the phase shifts can be calculated from the mechanical displacements. Scalar calibration techniques to characterize the reference field from the measurement of a known OUT are also available in the literature to be applied to the last proposed technique for broadband phaseless SAR. Therefore the phaseless profile reconstruction techniques can be implemented exclusively from scalar acquisitions with very low error.

All of the proposed techniques are part of a two step approach. First, the field is retrieved after processing the hologram and then, the profile of the OUT can be reconstructed applying inverse scattering methods already available in the literature. If non-redundant sampling techniques are applied, an extra step with the OSI has to be implemented to interpolate the retrieved field in the reduced set of points to a regular grid, required for most of the inverse scattering techniques.

Finally, it is worth mentioning that the proposed techniques have been validated through numerical examples and measurements with very good results. Applications such as through-the-wall imaging and profile reconstruction for non-destructive testing have been evaluated in the developed measurement system, giving promising results in very good agreement with reality.

CHAPTER

5

Conclusions and future research

5.1 Conclusions

This doctoral dissertation focuses on the development of new efficient measurement techniques for antenna measurement and diagnostics and also for imaging applications. The developed techniques aim to reduce the cost and complexity of the setup and the acquisition time. Concurrently a PNF measurement range has been developed and validated by means of the measurement setups for the proposed techniques.

The dissertation is based on the research work reported in publications [**I**]-[**VIII**] and [A**I**],[B**I**] and [B**II**], and consists in a review of the state of the art, theoretical background, a description of the contributions of the author (Chapters 1-5), and two appendices summarizing the main features of the measurement range and its characterization.

The developed techniques are based on indirect off-axis holography, an interferometric technique that allows for the characterization of the electromagnetic fields by means of amplitude-only acquisitions.

Main research efforts have been directed to the synthesis of the reference signal for the creation of the hologram and to explore new possibilities in the filtering process with the objective of bypassing the known shortcomings of the conventional indirect off-axis technique. Main features of the developed methods are summarized in Table 5.1.

Table 5.1: Main features of the developed methods.

Publication	Application	Reference field	Phase retrieval filtering domain
[I]	Antenna diagnostics	Synthesized (mechanical shifts)	Frequency (conventional)
[II]	Antenna measurement	Radiated (mechanical shifts, multiplexed)	Frequency (replicas)
[III] & **[IV]**[a]	Antenna measurement	Radiated (no shifts)	Time (broadband)
[V]	Imaging	Synthesized (electrical shifts)	Frequency (conventional)
[VI]	Imaging	Radiated (mechanical shifts)	Frequency (conventional)
[VII][a] & **[VIII]**	Imaging	Synthesized (no shifts)	Time (broadband)

[a] Non-redundant sampling techniques have also been applied.

In antenna measurement and diagnostics applications, the use of indirect off-axis holography techniques contribute to a reduction in the complexity of the setups and increase their robustness since this techniques are not affected by errors associated to full measurements, such as cable flexing or thermal drift. Furthermore, it has been demonstrated that planarity errors in the acquisition process have lesser impact in these techniques.

Nevertheless, off-axis indirect holography exhibits some limitations, that will be addressed next, together with the proposed solution. The phase retrieval process requires the knowledge of the reference field in amplitude and phase. Usually, the measured amplitude and the phase obtained from simulations are combined, being the accurate positioning of the reference antenna one of the main sources of error as well as overlapping in the spectral domain.

The need for amplitude and phase characterization is overcome by employing synthesized reference fields by means of a sample of the source and a phase shifter. The use of synthesized waves also allow to displace the image terms of the hologram to the non-visible part of the spectrum and drastically reduce the overlapping issue. Nevertheless, phase shifters might not be available and are expensive devices, mainly above the *W*-band. The developed techniques for antenna measurements bypass the use of this device, employing mechanical displacements

instead, and reducing the overall cost of the setup. The use of mechanical displacements of the probe has been validated in case of employing synthesized reference waves for antenna applications in the*Ka*-band [**I**].

On the other hand, employing synthesized reference waves require conveying the signal from the source- to the receiver-end. This is a simple task in monostatic configurations where both elements are placed at a short distance, but it cannot always be implemented in antenna measurement setups, specially at mm- and submm-wave bands, where the cables are substituted for waveguide sections, due to the need of moving the probe antenna in the receiver-end along the acquisition plane. An alternative technique with radiated reference waves is proposed in [**II**]. The technique combines two different holograms obtained after introducing a mechanical displacement of the reference antenna. The multiplexing of both holograms allows to displace the image term to the non-visible part of the spectrum as with synthesized reference waves. Validation through measurements for different types of antennas in the *W*-band with good results, even for low-directivity antennas with wider spectra, has been accomplished.

Conventional off-axis holography is a monochromatic technique, the filtering is done in the spatial frequency domain after the field is acquired over an specific surface, and it cannot be applied efficiently in broadband antenna measurement. This drawback can be bypassed by means of a new technique [**III**] capable of retrieving the phase point-by-point in the spatial acquisition domain, if a frequency sweep is performed at each of the acquisition points, by means of a phase retrieval in the TD. The proposed technique is also suitable for the implementation of standard non-redundant sampling techniques [**IV**] allowing for a great reduction of the acquisition points [**IV**].

For imaging systems, developments in fabrication technology have contributed to the appearance of multiple applications in the mm- and submm-wave bands focused on security and surveillance and non-destructive inspection of objects, structures, etc. Usually, real-time processing is demanded for these type of applications, making necessary to resort to direct detection systems, mainly in the submm-wave band. Thus, indirect off-axis holography has become a good alternative to the active imaging systems employing heterodine reception.

In this field, the use of synthesized reference waves is very convenient allowing simpler and more compact setups. Although characterization of the reference field is not strictly necessary, when done, the accuracy and quality of the system can be improved. Part of the work presented in [**V**] presents a new technique for the accurate characterization of the reference field from a few samples of the hologram.

Alternative techniques have also been successfully developed in order to bypass the devices needed for the synthesis of the reference antenna, i.e. directional coupler and phase shifter, by direct injection of the reference field through coupling between antennas, simplifying the complexity and size of the monostatic transceiver to a minimum [**VI**].

Finally, an effective technique for monostatic SAR, based on the same principles of broadband antenna measurements have been proposed and validated in [**VII**] and [**VIII**] for non-destructive testing and security applications with excellent results.

To summarize, the following contributions and achievements can be highlighted as main conclusions of this doctoral thesis:

- Substitution of phase shifters for mechanical displacements.
- Displacement of the image-terms to the non-visisble region of the spectrum by means of the use of radiated reference waves and hologram multiplexing.
- Accurate characterization of the synthesized reference field from partial analysis of the hologram.
- Application of non-redundant sampling techniques for the reduction of the acquisition points.
- Development of a new efficient point-by-point phase-retrieval technique for broadband characterization of antennas and 3D monostatic SAR.
- Development of a PNF measurement range for antenna measurement and for the validation of all the proposed techniques.

5.2 Future work and viability of the research

Correct performance and versatility of the developed measurement range is backed for a large amount of developed research works, besides the ones that conform this dissertation, that have made extensive use of the system such as those presented in [i]-[xiii], [b]-[e],[g],[i]. Furthermore the system has been also employed for the implementation of several demonstrators in the framework of different European and national founded projects [166].

Nevertheless, further work can be done in the measurement system to improve its performance, obtain better error characterization and extend the upper working frequency [43, 167]. Together with phase errors due to cable flexing and

thermal variations, positioning errors comprising scanner planarity and probe positioning accuracy are one of the main sources of error at higher frequency bands [168].

The effect of the errors due to phase acquisition is mitigated by means of the proposed algorithms based on indirect off-axis holography. Nevertheless, positioning errors could be reduced if a laser tracker and active positioning correction algorithms such as Z- or k-correction techniques are employed [22, 168, 169]. Multiple reflections reduction techniques [72, 170] should also be included in order to reduce their effect, also predominant in frame-scanners as the one implemented.

Regarding possible lines of work in antenna measurement techniques, main research efforts are directed now towards accurate characterization of the reference antenna from scalar measurements only.

Concerning imaging applications, next steps should be pointed to the implementation of demonstrators with multi-monostatic arrays, with potential applications in the fields of non-destructive testing and structural analysis.

The developed point-by-point phase retrieval technique [**VII**] can be hybridized with imaging algorithms capable of working with arbitrary acquisition domains [112], thus overcoming the limitation of requiring canonical scattered field acquisition domains (planar, cylindrical, spherical) for electromagnetic imaging. This technique is also suitable for antenna measurements with arbitrary domains [**III**], where the Sources Reconstruction Method has been successfully applied [28].

Bibliography

[1] M. Sierra-Castañer, A. Muñoz-Acevedo, F. Cano-Fácila, and S. Burgos, "Overview of novel post-processing techniques to reduce uncertainty in antenna measurements," in *Advanced Topics in Measurements*, M. Z. Haq, Ed. Intech, 2012, ch. 9.

[2] L. J. Foged, G. Barone, and F. Saccardi, "Antenna measurement systems using multi-probe technology," in *2015 IEEE Conf. on Antenna Meas. Applicat. (CAMA)*, Nov. 2015, pp. 1–3.

[3] J. A. Gordon, D. R. Novotny, M. H. Francis, R. C. Wittmann, M. L. Butler, A. E. Curtin, and J. R. Guerrieri, "Millimeter-wave near-field measurements using coordinated robotics," *IEEE Trans. on Antennas and Propag.*, vol. 63, no. 12, pp. 5351–5362, Dec. 2015.

[4] D. Titz, F. Ferrero, and C. Luxey, "Development of a millimeter-wave measurement setup and dedicated techniques to characterize the matching and radiation performance of probe-fed antennas," *IEEE Antennas and Propag. Mag.*, vol. 54, no. 4, pp. 188–203, Aug. 2012.

[5] F. Las-Heras and T. Sarkar, "A direct optimization approach for source reconstruction and NF-FF transformation using amplitude-only data," *IEEE Trans. on Antennas and Propag.*, vol. 50, no. 4, pp. 500–510, Apr. 2002.

[6] B. Fuchs, L. L. Coq, and M. D. Migliore, "Fast antenna array diagnosis from a small number of far-field measurements," *IEEE Trans. on Antennas and Propag.*, vol. 64, no. 6, pp. 2227–2235, Jun. 2016.

[7] C. Cappellin, A. Frandsen, S. Pivnenko, G. Lemanczyk, and O. Breinbjerg, "Diagnostics of the SMOS radiometer antenna system at the DTU-ESA spherical near-field antenna test facility," in *2007 2nd European Conf. on Antennas and Propag. (EuCAP)*, Nov. 2007, pp. 1–6.

[8] K. Liu, Q. Ye, and G. Meng, "Surface error diagnosis of large reflector antenna with microwave holography based on active deformation," *Electronics Lett.*, vol. 52, no. 1, pp. 12–13, 2016.

[9] R. Appleby and R. N. Anderton, "Millimeter-wave and submillimeter-wave imaging for security and surveillance," *Proc. of the IEEE*, vol. 95, no. 8, pp. 1683–1690, Aug. 2007.

[10] D. M. Sheen, D. L. McMakin, and T. E. Hall, "Three-dimensional millimeter-wave imaging for concealed weapon detection," *IEEE Trans. on Microw. Theory and Techn.*, vol. 49, no. 9, pp. 1581–1592, Sep. 2001.

[11] X. Zeng, A. Fhager, P. Linner, M. Persson, and H. Zirath, "Experimental investigation of the accuracy of an ultrawideband time-domain microwave-tomographic system," *IEEE Trans. on Instrum. and Meas.*, vol. 60, no. 12, pp. 3939–3949, Dec. 2011.

[12] M. M. Tajdini, B. González-Valdés, J. A. Martínez-Lorenzo, A. W. Morgenthaler, and C. M. Rappaport, "Efficient 3D forward modeling of GPR scattering from rough ground," in *2015 IEEE Int. Symp. on Antennas and Propag. USNC/URSI National Radio Science Meeting*, Jul. 2015, pp. 1686–1687.

[13] R. de Jongh, M. Hajian, and L. Ligthart, "Time domain antenna measurements: implementation and verification of a novel technique," in *1997 27th European Microw. Conf. (EuMC)*, vol. 1, Sep. 1997, pp. 470–475.

[14] Y. Huang, M. Bury, Y. Yashchyshyn, A. Yarovoy, R. De Jongh, S. Maqbool, and Y. Lu, "Time-domain measurements of broadband antennas," in *2nd European Conf. on Antennas and Propag. (EuCAP)*, Nov. 2007, pp. 1–4.

[15] E. C. Fear, J. Bourqui, C. Curtis, D. Mew, B. Docktor, and C. Romano, "Microwave breast imaging with a monostatic radar-based system: a study of application to patients," *IEEE Trans. on Microw. Theory and Techn.*, vol. 61, no. 5, pp. 2119–2128, May 2013.

[16] S. Licul and W. A. Davis, "Ultra-wideband (UWB) antenna measurements using vector network analyzer," in *2004 IEEE Antennas and Propag. Soc. Int. Symp. (AP-S)*, vol. 2, Jun. 2004, pp. 1319–1322.

[17] A. Kalinin, "Anechoic chamber wideband antenna measurements," *IEEE Aerosp. Electron. Syst. Mag.*, vol. 21, no. 1, pp. 21–24, Jan. 2006.

[18] J. Schoukens, R. M. Pintelon, and Y. J. Rolain, "Broadband versus stepped sine FRF measurements," *IEEE Trans. on Instrum. and Meas.*, vol. 49, no. 2, pp. 275–278, Apr. 2000.

[19] X. Zeng, "Time domain systems for microwave imaging: accuracy evaluations and prototype design," Ph.D. dissertation, Department of signals and sistems, Chalmers University of Technology, Göteborg, Sweden, 2013.

[20] T. Hansen and A. Yaghjian, "Formulation of probe-corrected planar near-field scanning in the time domain," *IEEE Trans. on Antennas and Propag.*, vol. 43, no. 6, pp. 569–584, Jun. 1995.

[21] S. R. Nichols, R. Dygert, and D. Wayne, "Advances in antenna measurement instrumentation and systems," in *2012 6th European Conf. on Antennas and Propag. (EuCAP)*, Mar. 2012, pp. 3190–3194.

[22] S. Gregson, J. McCormick, and C. Parini, *Principles of Planar Near-Field Antenna Measurements*, ser. Electromagnetic Waves. Institution of Engineering and Technology (IET), 2007.

[23] "IEEE recommended practice for near-field antenna measurements," *IEEE Std 1720-2012*, pp. 1–102, Dec. 2012.

[24] A. Arboleya, "Escáner xyz para medidas de radiación y dispersión," Master's thesis, Escuela Politécnica de Ingeniería. Universidad de Oviedo, Gijón, Spain, Jul. 2012.

[25] M. Migliore and G. Panariello, "A comparison of interferometric methods applied to array diagnosis from near-field data," *2001 IEE Proc. on Microw., Antennas and Propag.*, vol. 148, no. 4, pp. 261–267, Aug. 2001.

[26] S. Razavi and Y. Rahmat-Samii, "A new look at phaseless planar near-field measurements: limitations, simulations, measurements, and a hybrid solution," *IEEE Antennas and Propag. Mag.*, vol. 49, no. 2, pp. 170–178, Apr. 2007.

[27] T. Isernia, G. Leone, and R. Pierri, "Radiation pattern evaluation from near-field intensities on planes," *IEEE Trans. on Antennas and Propag.*, vol. 44, no. 5, pp. 701–, May. 1996.

[28] Y. Álvarez, F. Las-Heras, and M. R. Pino, "The sources reconstruction method for amplitude-only field measurements," *IEEE Trans. on Antennas and Propag.*, vol. 58, no. 8, pp. 2776–2781, Aug. 2010.

[29] R. Pierri, G. D'Élia, and F. Soldovieri, "A two probes scanning phaseless near-field far-field transformation technique," *IEEE Trans. on Antennas and Propag.*, vol. 47, no. 5, pp. 792–802, May. 1999.

[30] S. Costanzo and G. Di Massa, "Wideband phase retrieval technique from amplitude-only near-field data," *Radioengineering*, vol. 17, no. 4, pp. 8–12, Feb. 2008.

[31] G. Junkin, T. Huang, and J. Bennett, "Holographic testing of terahertz antennas," *IEEE Trans. on Antennas and Propag.*, vol. 48, no. 3, pp. 409–417, Mar. 2000.

[32] V. Schejbal, V. Kovarik, and D. Cermak, "Synthesized-reference-wave holography for determining antenna radiation characteristics," *IEEE Antennas and Propag. Mag.*, vol. 50, no. 5, pp. 71–83, Oct. 2008.

[33] J. Laviada and F. Las-Heras, "Phaseless antenna measurement on non-redundant sample points via Leith-Upatnieks holography," *IEEE Trans. on Antennas and Propag.*, vol. 61, no. 8, pp. 4036–4044, Aug. 2013.

[34] A. Yaghjian, "An overview of near-field antenna measurements," *IEEE Trans. on Antennas and Propag.*, vol. 34, no. 1, pp. 30–45, Jan. 1986.

[35] P. Petre and T. Sarkar, "Differences between modal expansion and integral equation methods for planar near-field to far-field transformation," *J. of Electromagn. waves and applications*, vol. 10, no. 2, pp. 269–271, 1996.

[36] NSI Antenna Measurement Solutions. near-field 101. Last visited: 2016-07-12. [Online]. Available: http://www.nearfield.com/aboutus/near-field101.aspx

[37] M. H. Francis, A. C. Newell, K. R. Grimm, J. Hoffman, and H. E. Schrank, "Comparison of ultralow-sidelobe-antenna far-field patterns using the planar-near-field method and the far-field method," *IEEE Antennas and Propag. Mag.*, vol. 37, no. 6, pp. 7–15, Dec. 1995.

[38] P. Petre and T. K. Sarkar, "Planar near-field to far-field transformation using an equivalent magnetic current approach," *IEEE Trans. on Antennas and Propag.*, vol. 40, no. 11, pp. 1348–1356, Nov. 1992.

[39] D. M. Kerns, "Plane-wave scattering-matrix theory of antennas and antenna-antenna interactions: Formulation and applications," *Journal of Research of the National Bureau of Standards–B Mathematical Sciences*, vol. 808, no. 1, Jan.–Mar. 1976.

[40] Y. Rahmat-Samii, L. Williams, and R. Yaccarino, "The UCLA bi-polar planar-near-field antenna-measurement and diagnostics range," *IEEE Antennas and Propag. Mag.*, vol. 37, no. 6, pp. 16–35, Dec. 1995.

[41] T. Brockett and Y. Rahmat-Samii, "A novel portable bipolar near-field measurement system for millimeter-wave antennas: construction, development, and verification," *IEEE Antennas and Propag. Mag.*, vol. 50, no. 5, pp. 121–130, Oct. 2008.

[42] J. Demas and T. Speicher, "Innovative mechanical designs for scanners," in *AMTA Proc. 1997*, 1997.

[43] L. L. Coq and B. Fuchs, "Design and manufacturing of a high accuracy planar scanner for millimeter wave applications," in *2014 IEEE Conf. on Antenna Meas. Applications (CAMA)*, Nov. 2014, pp. 1–4.

[44] E. Joy, C. Burns, and G. Rodrigue, "A study of the accuracy of far field patterns based on near field measurements," in *1973 IEEE Antennas and Propag. Soc. Int. Symp. (AP-S)*, vol. 11, Aug. 1973, pp. 57–60.

[45] A. D. Yaghjian, *Upper-bound errors in far-field antenna parameters determined from planar near-field measurements: Analysis*. US Dept. of Commerce, National Bureau of Standards, 1974.

[46] A. Newell, "Error analysis techniques for planar near-field measurements," *IEEE Trans. on Antennas and Propag.*, vol. 36, no. 6, pp. 754–768, Jun. 1988.

[47] E. B. Joy, "Near-field qualification methodology," *IEEE Trans. on Antennas and Propag.*, vol. 36, no. 6, pp. 836–844, Jun. 1988.

[48] J. Wang, "An examination of the theory and practices of planar near-field measurement," *IEEE Trans. on Antennas and Propag.*, vol. 36, no. 6, pp. 746–753, Jun. 1988.

[49] D. Paris, W. Leach, and E. Joy, "Basic theory of probe-compensated near-field measurements," *IEEE Trans. on Antennas and Propag.*, vol. 26, no. 3, pp. 373–379, May. 1978.

[50] A. G. Repjar, A. C. Newell, and M. H. Francis, "Accurate determination of planar near-field correction parameters for linearly polarized probes," *IEEE Trans. on Antennas and Propag.*, vol. 36, no. 6, pp. 855–868, Jun. 1988.

[51] S. Pivnenko, J. M. Nielsen, and O. Breinbjerg, "Very high-accuracy calibration of radiation pattern and gain of a near-field probe," in *2014 8th European Conf. on Antennas and Propag. (EuCAP)*, Apr. 2014, pp. 1690–1694.

[52] A. Newell, "Cross-polarization uncertainty in near-field probe correction [amta corner]," *IEEE Antennas and Propag. Mag.*, vol. 51, no. 5, pp. 214–219, Oct. 2009.

[53] A. P. Mynster, J. M. Nielsen, and S. Pivnenko, "Electrical alignment of antenna coordinate system in a planar near-field setup," in *2011 5th European Conf. on Antennas and Propag. (EuCAP)*, Apr. 2011, pp. 678–682.

[54] L. Foged, "Deliverable A1.2D2. Recomendations and comparative investigations for near-field antenna measurement techniques and procedures," Antenna Centre of Excellence, Tech. Rep., 2007.

[55] V. Schejbal, J. Pidanic, V. Kovarik, and D. Cermak, "Accuracy analyses of synthesized-reference-wave holography for determining antenna radiation characteristics," *IEEE Antennas and Propag. Mag.*, vol. 50, no. 6, pp. 89–98, Dec. 2008.

[56] T. Milligan, "Aperture sampling requirements in planar near-field and pattern calculations," *IEEE Antennas and Propag. Mag.*, vol. 38, no. 5, pp. 60–63, Oct 1996.

[57] E. Joy, "Windows '96 for planar near-field measurements," in *Proc. IEEE Int. Antennas and Propag. Symp.*, 1996, pp. 280–85.

[58] O. M. Bucci and M. D. Migliore, "A new method for avoiding the truncation error in near-field antennas measurements," *IEEE Trans. on Antennas and Propag.*, vol. 54, no. 10, pp. 2940–2952, Oct. 2006.

[59] E. Martini, O. Breinbjerg, and S. Maci, "Reduction of truncation errors in planar near-field aperture antenna measurements using the gerchberg-papoulis algorithm," *IEEE Trans. on Antennas and Propag.*, vol. 56, no. 11, pp. 3485–3493, Nov. 2008.

[60] D. J. van Rensburg, "Scan-plane reduction techniques for planar near-field antenna measurements," *IEEE Antennas and Propag. Mag.*, vol. 46, no. 6, pp. 179–184, Dec. 2004.

[61] L. L. Coq, O. Lafond, and M. Himdi, "Flip test procedure for positioning system errors and antenna phase centre determinations," in *2010 4th European Conf. on Antennas and Propag. (EuCAP)*, Apr. 2010, pp. 1–4.

[62] J. Romeu, P. Escobar, and S. Blanch, "Probe positioning errors in planar near field measurements. a plane wave synthesis approach," in *1995 IEEE Antennas and Propag. Soc. Int. Symp. (AP-S)*, vol. 1, Jun. 1995, pp. 264–267.

[63] S. F. Razavi and Y. Rahmat-Samii, "Resilience to probe-positioning errors in planar phaseless near-field measurements," *IEEE Trans. on Antennas and Propag.*, vol. 58, no. 8, pp. 2632–2640, Aug. 2010.

[64] L. Corey and E. Joy, "Far-field antenna pattern calculation from near-field measurements including compensation for probe positioning errors," in *1979 IEEE Antennas and Propag. Soc. Int. Symp. (AP-S)*, vol. 17, Jun. 1979, pp. 736–739.

[65] P. Agrawal, "A method to compensate for probe positioning errors in an antenna near field test facility," in *1982 IEEE Antennas and Propag. Soc. Int. Symp. (AP-S)*, vol. 20, May 1982, pp. 218–221.

[66] L. A. Muth and R. L. Lewis, "A general technique to correct probe position errors in planar near-field measurements to arbitrary accuracy," *IEEE Trans. on Antennas and Propag.*, vol. 38, no. 12, pp. 1925–1932, Dec. 1990.

[67] M. Farouq, M. Serhir, and D. Picard, "Reconstruction over a regular grid of antenna near field measurement based on irregular near field data," in *2014 8th European Conf. on Antennas and Propag. (EuCAP)*, Apr. 2014, pp. 1078–1081.

[68] F. D'Agostino, F. Ferrara, C. Gennarelli, R. Guerriero, and M. Migliozzi, "An efficient iterative procedure to correct the positioning errors in the plane-polar scanning," in *2015 Loughborough Antennas Propag. Conf. (LAPC)*, Nov. 2015, pp. 1–5.

[69] C. Bin, Z. h. Xue, and X. w. Xu, "The research of using unequally spaced fast fourier transforms algorithm to eliminate the position error of the antenna near field measurement," in *2010 9th Int. Symp. on Antennas Propag. and EM Theory (ISAPE)*, Nov. 2010, pp. 299–301.

[70] C. H. Schmidt, M. A. Qureshi, and T. F. Eibert, "Plane wave based near-field far-field transformation with adaptive field translations," in *2011 30th URSI General Assembly and Scientific Symp.*, Aug. 2011, pp. 1–4.

[71] M. Winebrand and J. Aubin, "Improving the accuracy of near-field antenna measurements using time gating techniques," in *2010 14th Int.Symp. Antenna Tech. and Applied Electromagn. American Electromagn. Conf. (ANTEM-AMEREM)*, Jul. 2010, pp. 1–3.

[72] F. J. Cano-Fácila, S. Burgos, F. Martín, and M. Sierra-Castañer, "New reflection suppression method in antenna measurement systems based on diagnostic techniques," *IEEE Trans. on Antennas and Propag.*, vol. 59, no. 3, pp. 941–949, Mar. 2011.

[73] F. J. Cano-Fácila, S. Burgos, and M. Sierra-Castañer, "New methods to reduce leakage errors in planar near-field measurements," in *2011 5th European Conf. on Antennas and Propag. (EUCAP)*, Apr. 2011, pp. 3581–3585.

[74] ——, "Novel method to improve the signal-to-noise ratio in far-field results obtained from planar near-field measurements," *IEEE Antennas and Propag. Mag.*, vol. 53, no. 2, pp. 215–220, Apr. 2011.

[75] O. Bucci and G. D'Élia, *Advanced Sampling Techniques in Electromagnetics*, ser. Rev. Radio Sci. 1993–1995. Oxford University Press, 1996, pp. 177–204.

[76] O. Bucci, C. Gennarelli, and C. Savarese, "Fast and accurate near-field far-field transformation by sampling interpolation of plane polar measurements," *IEEE Trans. on Antennas and Propagat.*, vol. 39, pp. 48–55, Jan. 1991.

[77] F. D'Agostino, F. Ferrara, C. Gennarelli, R. Guerriero, and M. Migliozzi, "An effective nf-ff transformation technique with planar spiral scanning tailored for quasi-planar antennas," *IEEE Trans. on Antennas and Propag.*, vol. 56, no. 9, pp. 2981–2987, Sept. 2008.

[78] F. D'Agostino, F. Ferrara, C. Gennarelli, R. Guerriero, M. Migliozzi, and I. D. Colibus, "Experimental tests on a near-field to far-field transformation technique using a nonconventional plane-rectangular scanning," in *2013 Loughborough Antennas and Propag. Conf. (LAPC)*, Nov. 2013, pp. 208–212.

[79] S. Burgos, "Contribution to the uncertainty evaluation in the measurement of the main antenna parameters," Ph.D. dissertation, Escuela Técnica Superior de Ingenieros de Telecomunicación, Universidad Politécnica de Madrid, Madrid, Spain, Sep. 2009.

[80] A. Newell and G. Hindman, "Antenna pattern comparison using pattern subtraction and statistical analysis," in *5th European Conf. on Antennas and Propag. (EuCAP)*, Apr. 2011, pp. 2684–2687.

[81] L. Foged, B. Bencivenga, L. Durand, O. Breinbjerg, S. Pivnenko, C. Sabatier, H. Ericsson, B. Svensson, A. Alexandridis, S. Burgos, M. Sierra-Castañer, J. Zackrisson, and M. Boettcher, "Error calculation techniques and their application to the antenna measurement facility comparison within the european antenna centre of excellence," in *2007 2nd European Conf. on Antennas and Propag. (EuCAP)*, Nov. 2007, pp. 1–6.

[82] S. Burgos, S. Urosa, M. Sierra-Castañer, C. Martínez-Portas, and J. L. Besada, "Uncertainty analysis in antenna measurements," in *2009 3rd European Conf. on Antennas and Propag. (EuCAP)*, Mar. 2009, pp. 2182–2185.

[83] M. H. Francis, "Estimating uncertainties in antenna measurements," in *2013 7th European Conf. on Antennas and Propag. (EuCAP)*, Apr. 2013, pp. 2493–2495.

[84] M. Castañer, S. Martínez, F. Jiménez, and J. Besada, "Error analysis and simulator in cylindrical near field antenna measurement systems," in *2007 IEEE Antennas and Propag. Soc. Int. Symp. (AP-S)*, Jun. 2007, pp. 1649–1652.

[85] B. Taylor and C. Kuyatt, "NIST technical note 1297. guidelines for evaluating and expressing the uncertainty of NIST measurement results," National

Institute of Standards and Technology, United States Department of Commerce Technology Administration, Tech. Rep., 1994 Edition.

[86] S. Pivnenko, J. E. Pallesen, O. Breinbjerg, M. S. Castañer, P. C. Almena, C. M. Portas, J. L. B. Sanmartín, J. Romeu, S. Blanch, J. M. González-Arbesu, C. Sabatier, A. Calderone, G. Portier, H. Eriksson, and J. Zackrisson, "Comparison of antenna measurement facilities with the DTU-ESA 12 ghz validation standard antenna within the eu antenna centre of excellence," *IEEE Trans. on Antennas and Propag.*, vol. 57, no. 7, pp. 1863–1878, Jul. 2009.

[87] A. Newell, G. Hindman, and S. Gregson, "Antenna pattern comparisons used in nist 18-term error assessments on numerous near-field ranges," in *2013 7th European Conf. on Antennas and Propag. (EuCAP)*, Apr. 2013, pp. 4076–4077.

[88] D. M. Sheen, D. L. McMakin, and T. E. Hall, "Near-field three-dimensional radar imaging techniques and applications," *Applied Optics*, vol. 49, no. 19, pp. E83–E93, Jul. 2010.

[89] J. C. Wiltse, "History of millimeter and submillimeter waves," *IEEE Transactions on Microwave Theory and Techniques*, vol. 32, no. 9, pp. 1118–1127, Sep. 1984.

[90] R. Appleby and H. B. Wallace, "Standoff detection of weapons and contraband in the 100 GHz to 1 THz region," *IEEE Trans. on Antennas and Propag.*, vol. 55, no. 11, pp. 2944–2956, Nov. 2007.

[91] S. Oka, H. Togo, N. Kukutsu, and T. Nagatsuma, "Latest trends in millimeter-wave imaging technology," *Progress In Electromagn. Research Let.*, vol. 1, pp. 197–204, 2008.

[92] S. Mochizuki, S. Oka, N. Matsumiya, H. Togo, and N. Kukutsu, "Near-field millimeter-wave imaging with 77-ghz-band monostatic-radar module," in *2013 IEEE Antennas and Propag. Soc. Int. Symp. (AP-S)*, Jul. 2013, pp. 808–809.

[93] A. Tamminen, "Developments in imaging at millimeter and submillimeter wavelengths," Ph.D. dissertation, School of Electrical Engineering, Aalto University, Espoo, Finland, Sep. 2013.

[94] "Recommendation ITU-R P.676-10 (09/2013). Attenuation by atmospheric gases. Last visited: 2016-07-12." [Online]. Available: http://bit.ly/1Ota1lN

[95] K. van Caekenberghe, K. F. Brakora, and K. Sarabandi, "A 94 GHz OFDM frequency scanning radar for autonomous landing guidance," in *2007 IEEE Radar Conf.*, Apr. 2007, pp. 248–253.

[96] J. Hasch, E. Topak, R. Schnabel, T. Zwick, R. Weigel, and C. Waldschmidt, "Millimeter-wave technology for automotive radar sensors in the 77 GHz frequency band," *IEEE Trans. on Microw. Theory and Techn.*, vol. 60, no. 3, pp. 845–860, Mar. 2012.

[97] L. Yujiri, "Passive millimeter wave imaging," in *2006 IEEE MTT-S Int. Microw. Symp. Digest (MTT)*, Jun. 2006, pp. 98–101.

[98] R. Appleby, R. Anderton, S. Price, and N. e. a. Salmon, "Mechanically scanned real-time passive millimeter-wave imaging at 94 ghz," in *2003 Proc. SPIE*, vol. 5077, 2003, pp. 1–6.

[99] B. B. Hu and M. C. Nuss, "Imaging with terahertz waves," *Opt. Lett.*, vol. 20, no. 16, pp. 1716–1718, Aug 1995.

[100] M. Kemp, P. Taday, B. Cole, and et al, "Security applications of terahertz technology," in *2003 Proc. SPIE*, vol. 5070, 2003, pp. 44–52.

[101] P. F. Goldsmith, C. T. Hsieh, G. R. Huguenin, J. Kapitzky, and E. L. Moore, "Focal plane imaging systems for millimeter wavelengths," *IEEE Trans. on Microw. Theory and Techn.*, vol. 41, no. 10, pp. 1664–1675, Oct. 1993.

[102] E. Heinz, T. May, D. Born, G. Zieger, S. Anders, G. Thorwirth, V. Zakosarenko, M. Schubert, T. Krause, M. Starkloff, A. Krüger, M. Schulz, F. Bauer, and H.-G. Meyer, "Passive submillimeter-wave stand-off video camera for security applications," *Journal of Infrared, Millimeter, and Terahertz Waves*, vol. 31, no. 11, pp. 1355–1369, 2010.

[103] J. T. Johnson, I. J. Gupta, and R. J. Burkholder, "Comparison of monostatic and bistatic radar images," in *2001 IEEE Antennas and Propag. Soc. Int. Symp. (AP-S)*, vol. 4, Jul. 2001, pp. 281–284 vol.4.

[104] Y. Álvarez, Y. Rodríguez-Vaqueiro, B. González-Valdés, S. Mantzavinos, C. M. Rappaport, F. Las-Heras, and J. . Martínez-Lorenzo, "Fourier-based imaging for multistatic radar systems," *IEEE Trans. on Microw. Theory and Techn.*, vol. 62, no. 8, pp. 1798–1810, Aug. 2014.

[105] G. Yates, A. Horne, A. Blake, and R. Middleton, "Bistatic SAR image formation," *IEE Proceedings - Radar, Sonar and Navigation*, vol. 153, no. 3, pp. 208–213, 2006.

[106] P. Bezoušek and V. Schejbal, "Bistatic and multistatic radar systems," *Radioengineering*, vol. 17, no. 3, pp. 53–59, 2008.

[107] G. Krieger, H. Fiedler, D. Houman, and A. Moreira, "Analysis of system concepts for bi- and multi-static sar missions," in *2003 IEEE Int. Geosci. Remote Sensing Symp. (IGARSS)*, vol. 2, Jul. 2003, pp. 770–772 vol.2.

[108] A. Tamminen, J. Ala-Laurinaho, and A. Räisänen, "Indirect holographic imaging at 310 GHz," in *European Radar Conf. (EuRAD)*, Oct. 2008, pp. 168–171.

[109] A. Broquetas, J. Palau, L. Jofre, and A. Cardama, "Spherical wave near-field imaging and radar cross-section measurement," *IEEE Trans. on Antennas and Propag.*, vol. 46, no. 5, pp. 730–735, May 1998.

[110] J. M. García, "Off-axis holography in microwave imaging systems," Ph.D. dissertation, Departament de Telecomunicació i Enginyeria de Sistemes. Universitat Autònoma de Barcelona, 2015.

[111] D. Smith, O. Yurduseven, B. Livingstone, and V. Schejbal, "Microwave imaging using indirect holographic techniques," *IEEE Antennas and Propag. Mag.*, vol. 56, no. 1, pp. 104–117, Feb. 2014.

[112] Y. Álvarez, J. Martínez-Lorenzo, F. Las-Heras, and C. Rappaport, "An inverse fast multipole method for geometry reconstruction using scattered field information," *IEEE Trans. on Antennas and Propag.*, vol. 60, no. 7, pp. 3351–3360, Jul. 2012.

[113] S. Oka and S. Leclair, "Image mining of evanescent microwave data for nondestructive material inspection," in *Proc. of the 4th Int. Conf on Intelligen Processing and Manufacturing of Materials, IPMM*, Sendai, Japan, May 2003.

[114] W. Zhang, L. Li, and F. Li, "Multifrequency imaging from intensity-only data using the phaseless data distorted Rytov iterative method," *IEEE Trans. on Antennas and Propag.*, vol. 57, no. 1, pp. 290–295, Jan. 2009.

[115] "IEEE std 521-2002 (revision of IEEE std 521-1984). IEEE standard letter designations for radar-frequency bands," Institute of Electrical and Electronics Engineers, Tech. Rep., 2003.

[116] "The Mathworks, Inc. MATLAB and Simulink for Technical Computing. Last visited: 2016-07-12." [Online]. Available: https://www.mathworks.com

[117] "FEKO Suite 6.2 features. Last visited: 2016-07-12." [Online]. Available: https://www.feko.info

[118] C. A. Balanis, *Antenna Theory: Analysis and Design*, 2nd ed. John Wiley Sons, 1997.

[119] M. H. Francis, "Aperture-sampling requirements," *IEEE Antennas and Propagation Magazine*, vol. 39, no. 5, pp. 76–81, Oct. 1997.

[120] N. Wang, Z.-h. Xue, S.-M. Yang, R. Liu, and X. Xu, "Aperture field rebuilding in antenna time domain planar near field measurement," in *2008 Int. Conf. on Microw. and Millimeter Wave Tech. (ICMMT)*, vol. 1, Apr. 2008, pp. 403–406.

[121] S. Pivnenko, "Planar near-field antenna measurements: theory and practice. short course on antenna measurements. european school of antennas," Jun. 2012.

[122] R. Scholte and N. B. Roozen, "Improved data representation in NAH applications by means of zero-padding," in *2003 10th Intern. Congress on Sound and Vibration*, 2003.

[123] M. Soumekh, "Bistatic synthetic aperture radar inversion with application in dynamic object imaging," in *1991 Int. Conf. on Acoustics, Speech, and Signal Processing (ICASSP)*, Apr. 1991, pp. 2577–2580 vol.4.

[124] J. Laviada, Y. Álvarez López, A. Arboleya-Arboleya, C. García-González, and F. Las-Heras, "Inverse scattering with phase retrieval based on indirect holography via synthesised plane-waves," *IET Microw., Antennas, Propag.*, vol. 6, no. 12, pp. 1389–1398, Sep. 2012.

[125] Y. Álvarez, J. Laviada, L. Tirado, C. García, J. . Martínez, F. Las-Heras, and C. M. Rappaport, "Inverse Fast Multipole Method for Monostatic Imaging Applications," *IEEE Geoscience and Remote Sensing Lett.*, vol. 10, no. 5, pp. 1239–1243, Sep. 2013.

[126] S. Caorsi, G. L. Gragnani, and M. Pastorino, "Two-dimensional microwave imaging by a numerical inverse scattering solution," *IEEE Trans. on Microw. Theory and Techn.*, vol. 38, no. 8, pp. 981–980, Aug. 1990.

[127] O. Bucci, C. Gennarelli, and C. Savarese, "Representation of electromagnetic fields over arbitrary surfaces by a finite and nonredundant number of samples," *IEEE Trans. on Antennas and Propag.*, vol. 46, no. 3, pp. 351–359, Mar. 1998.

[128] A. Capozzoli, C. Curcio, G. D'Élia, and A. Liseno, "Phaseless antenna characterization by effective aperture field and data representations," *IEEE Trans. on Antennas and Propag.*, vol. 57, no. 1, pp. 215–230, Jan. 2009.

[129] D. Gabor, "Microscopy by reconstructed wave-fronts," *Proc. of the Royal Soc. of London A: Math., Physical and Eng. Sci.*, vol. 197, no. 1051, pp. 454–487, Jul. 1949.

[130] E. N. Leith and J. Upatnieks, "Reconstructed wavefronts and communication theory," *J. of the Optical Soc. of America*, vol. 52, no. 10, pp. 1123–1128, Oct. 1962.

[131] Y. Aoki, "Microwave holography by a two-beam interferance method," *Proc. of the IEEE*, vol. 56, no. 8, pp. 1402–1403, Aug. 1968.

[132] E. Rope and G. Tricoles, "Visible images by wavefront reconstruction with microwaves," in *1969 IEEE Antennas and Propag. Soc. Int. Symp. (AP-S)*, vol. 7, Dec. 1969, pp. 137–138.

[133] G. Papi, V. Russo, and S. Sottini, "Microwave holographic interferometry," *IEEE Trans. on Antennas and Propag.*, vol. 19, no. 6, pp. 740–746, Nov. 1971.

[134] P. Napier, "Reconstruction of radiating sources," Ph.D. dissertation, Electrical and Electronic Engineering School, University of Canterbury, Christchurch, New Zealand, Apr. 1971.

[135] P. Napier and R. Bates, "Antenna - aperture distributions from holographic type of radiation-pattern measurement," *Proc. of the Institution of Electrical Engineers*, vol. 120, no. 1, pp. 30–34, Jan. 1973.

[136] J. Bennett, A. Anderson, P. McInnes, and A. Whitaker, "Microwave holographic metrology of large reflector antennas," *IEEE Trans. on Antennas and Propag.*, vol. 24, no. 3, May 1976.

[137] A. Anderson, "Microwave holography," *Proc. of the Institution of Electrical Engineers*, vol. 124, no. 11, pp. 946–962, Nov. 1977.

[138] G. Tricoles and N. Farhat, "Microwave holography: Applications and techniques," *Proc. of the IEEE*, vol. 65, no. 1, pp. 108–121, Jan. 1977.

[139] T. Huang, J. Bennett, and G. Junkin, "A holographic technique for millimetre-wave antenna near-field/far-field transformation," in *1995 IEEE Antennas and Propag. Soc. Int. Symp. (AP-S)*, Apr. 1995, pp. 41–44 vol.1.

[140] D. Smith, M. Leach, S. Dlay, and W. Woo, "A novel technique for the determination of the radiation patterns of medium gain antennas from scalar intensity measurements," in *2003 6th Int. Symp. on Antennas, Propag. and EM Theory (ISAPE)*, Oct. 2003, pp. 373–376.

[141] M. Leach, D. Smith, S. Skobelev, and M. Elsdont, "An improved holographic technique for medium-gain antenna near field measurements," in *2nd European Conf. on Antennas and Propag. (EuCAP)*, Nov. 2007, pp. 1–6.

[142] P. H. Gardenier, "Antenna aperture phase retrieval," Ph.D. dissertation, Electrical and Electronic Engineering School, University of Canterbury, Christchurch, New Zealand, Apr. 1980.

[143] J. Pidanic, V. Schejbal, and D. Cermak, "Analysis of periodic errors for synthesized-reference-wave-holography," *Radioengineering*, vol. 18, no. 4, pp. 561–566, Dec. 2009.

[144] G. A. Deschamps, "Some remarks on radio-frequency holography," *Proc. of the IEEE*, vol. 55, no. 4, pp. 570–571, Apr. 1967.

[145] D. Smith, M. Leach, M. Elsdon, and S. Foti, "Indirect holographic techniques for determining antenna radiation characteristics and imaging aperture fields," *IEEE Antennas and Propag. Mag.*, vol. 49, no. 1, pp. 54–67, Feb. 2007.

[146] L. Zhiping, W. Zhengpeng, and W. Jianhua, "A high precision holographic phaseless near-field method," in *7th European Conf. on Antennas and Propag. (EuCAP)*, Apr. 2013, pp. 3594–3598.

[147] D. Smith, S. Skobelev, and M. Leach, "A modified holographic technique for antenna measurements," in *2008 8th Int. Symp. on Antennas, Propag. and EM Theory (ISAPE)*, Nov. 2008, pp. 46–49.

[148] D. Smith, V. Schejbal, and L. Prouza, "A modified holographic technique for cylindrical near-field antenna measurements," in *6th European Conf. on Antennas and Propag. (EuCAP)*, Mar. 2012, pp. 2528–2532.

[149] J. Laviada, Y. Álvarez López, A. Arboleya-Arboleya, C. García-González, and F. Las-Heras, "Interferometric technique with nonredundant sampling for phaseless inverse scattering," *IEEE Trans. on Antennas and Propag.*, vol. 62, no. 2, pp. 739–746, Feb. 2014.

[150] J. Laviada and F. Las Heras, "Scalar Calibration for Broadband Synthetic Aperture Radar Operating with Amplitude-Only Data," *IEEE Antennas and Wireless Propag. Lett.*, vol. PP, no. 99, pp. 1–1, 2015.

[151] A. Enayati, A. Tamminen, J. Ala-Laurinaho, A. V. Räisänen, G. A. E. Vandenbosch, and W. D. Raedt, "THz holographic imaging: A spatial-domain technique for phase retrieval and image reconstruction," in *2012 IEEE MTT-S Int. Microw. Symp. Digest (MTT)*, Jun. 2012, pp. 1–3.

[152] I. Yamaguchi and T. Zhang, "Phase-shifting digital holography," *Opt. Lett.*, vol. 22, no. 16, pp. 1268–1270, Aug 1997.

[153] G. Junkin, "Phase Shifting Holography for Thz Near-Field/Far-Field Prediction," *Progress In Electromagnetics Research Lett.*, vol. 44, pp. 15–21, 2014.

[154] ——, "Planar Near-Field Phase Retrieval Using GPUs for Accurate THz Far-Field Prediction," *IEEE Trans. on Antennas and Propag.*, vol. 61, no. 4, pp. 1763–1776, Apr. 2013.

[155] S. de Nicola, A. Geltrude, M. Locatelli, K. Al-Naimee, R. Meucci, and F. T. Arecchi, "Infrared Holography for wavefront reconstruction and interferometric metrology," in *Advanced holography- Metrology and imaging*. InTech, 2011.

[156] C. F. Stubenrauch, J. D. Norgard, J. E. Will, and K. MacReynolds, "Far-field antenna patterns determined from infrared holograms," in *1999 IEEE Int. Symp. Antennas Propag. Soc. (AP-S)*, vol. 3, 1999, pp. 1996–1999.

[157] D. Smith, M. Leach, and A. Sambell, "An indirect holographic method for determining antenna radiation patterns and imaging antenna fields," in *2002 IEEE Antennas and Propag. Soc. Int. Symp. (AP-S)*, vol. 3, 2002, pp. 706–709 vol.3.

[158] D. Smith and M. Leach, "3D imaging of antenna fields from electronically synthesised scalar intensity patterns," in *2003 Asia-Pacific Conf. on Appl. Electromagnetics APACE*, Aug. 2003, pp. 50–53.

[159] D. Smith, M. Leach, and A. Sambell, "Microwave indirect holographic imaging using an adaptation of optical techniques," *IEEE Microw. and Wireless Compon. Lett.*, vol. 13, no. 9, pp. 379–381, Sep. 2003.

[160] O. M. Bucci and T. Isernia, "Electromagnetic inverse scattering: Retrievable information and measurement strategies," *Radio Sci.*, vol. 32, no. 6, pp. 2123–2137, Nov. 1997.

[161] J. Adametz, F. Gumbmann, and L. P. Schmidt, "Inherent resolution limit analysis for millimeter-wave indirect holographic imaging," in *2011 German Microw. Conf.*, Mar. 2011, pp. 1–4.

[162] V. Schejbal, V. Kovarik, and D. Cermak, "Synthesized-reference-wave holography for determining antenna radiation characteristics," *IEEE Antennas and Propag. Mag.*, vol. 50, no. 5, pp. 71–83, Oct. 2008.

[163] D. Smith, M. Leach, M. Elsdon, and S. Foti, "Indirect holographic techniques for determining antenna radiation characteristics and imaging aperture fields," *IEEE Antennas and Propag. Mag.*, vol. 49, no. 1, pp. 54–67, Feb. 2007.

[164] J. Laviada, Y. Álvarez López, C. García-González, C. Vázquez-Antuña, S. Ver-Hoeye, M. Fernández-García, G. Hotopan, R. Camblor, and F. Las-Heras, "A novel phaseless frequency scanning based on indirect holography," *J. of Electromag. Waves and Applications*, vol. 27, no. 4, pp. 430–438, 2013.

[165] T. Vaupel and T. F. Eibert, "Comparison and application of near-field ISAR imaging techniques for far-field Radar cross section determination," *IEEE Trans. on Antennas and Propag.*, vol. 54, no. 1, pp. 144–151, Jan. 2006.

[166] "List of research projects of the TSC-UNIOVI research group. Last visited: 2016-07-12," http://tscuniovi.grupos.uniovi.es/investigacion/proyectos.

[167] D. J. van Rensburg, "Factors limiting the upper frequency of mm-wave spherical near-field test systems," in *2015 9th European Conf. Antennas and Propag. (EuCAP)*, May 2015, pp. 1–4.

[168] D. J. van Rensburg and G. Hindman, "An overview of near-field submillimeter wave antenna test applications," in *2008 14th Conf. on Microw. Tech., COMITE*, April 2008, pp. 1–4.

[169] D. S. Fooshe, "Application of error correction technologies to near-field antenna measurement systems," in *IEEE Conf. on Aerospace Applications*, vol. 1, Feb 1996, pp. 141–149 vol.1.

[170] Y.-T. Hsiao, Y.-Y. Lin, Y.-C. Lu, and H.-T. Chou, "Applications of time-gating method to improve the measurement accuracy of antenna radiation inside an anechoic chamber," in *2003 IEEE Int. Symp. Antennas Propag. Soc. (AP-S)*, vol. 3, June 2003, pp. 794–797 vol.3.

[171] "Siepel electromagnetic absorber. Last visited: 2016-07-12," http://www.siepel.com.

[172] "IAI high precision series linear actuators. Last visited: 2016-07-12," http://www.intelligentactuator.com.

[173] A. Newell, "Error analysis techniques for planar near-field measurements," *IEEE Trans. on Antennas and Propag.*, vol. 36, no. 6, pp. 754–768, Jun. 1988.

[174] P. I. Popa, S. Pivnenko, J. M. Nielsen, and O. Breinbjerg, "60 GHz antenna measurement setup using a VNA without external frequency conversion," *2014 36th Annu. Symp. of Antenna Meas. Techniques Assoc. (AMTA)*, 2014.

[175] A. Newell, "Reducing measurement time and estimated uncertainties for the NIST 18 term error technique," in *2008 30th Annu. Symp. of Antenna Meas. Techniques Assoc. (AMTA)*, Aug. 2008, pp. 1–9.

Appendices

APPENDIX

A

XYZ scanner design and main features

A.1 Measurement system design

A versatile horizontal frame scanner of 1.5 x 1.5 x 1.1 m has been developed. A multi-axis positioner, together with several holding accessories for the probe allows for different type of planar acquisitions as well as cylindrical or arbitrary 3D scanning. The working range of the system is approximately 5 GHz to 320 GHz. Main features of the system have been presented in [A**I**] with a diagnostics application and in [**V**] for imaging applications.

Figure A.1(a) shows a side view of the system with the workstation, whereas Figure A.1(b) shows a measurement example of an X-band antenna with the RF components of the system.

The measurement system can be subdivided in three different subsystems as schematically shown in Figure A.2: mechanical, RF and control subsystems.

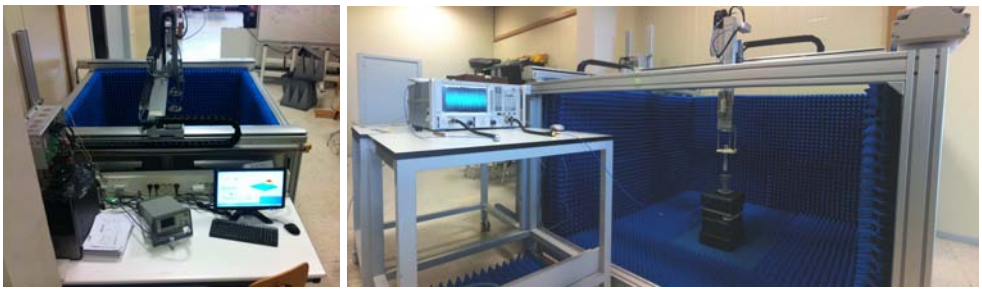

(a) (b)

Figure A.1: Measurement range. (a) Workstation and side view, (b) measurement setup example.

Main components and interactions of these subsystems will be described in the following sections of the appendix.

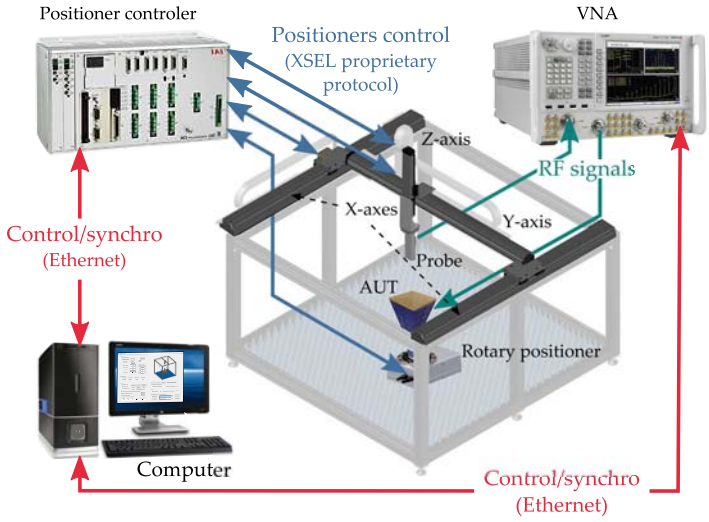

Figure A.2: Scheme of the measurement systems components and interactions. Blue for the mechanical, green for the RF and red for the control subsystems.

The multi-axis positioner is mounted on top of an aluminum chassis of 1.5 x 1.5 x 1.1 m which prevent the positioners from bending and vibration during their movement and also acts a lean structure for the electromagnetic absorber or Radar Absorbing Material (RAM) panels.

Thin aluminum plates are employed to back the RAM. The plates are equipped with handles for easy mounting and unmounting them allowing access to the

measurement area. Wideband HYFRAL APM-9 pyramidal absorber from Siepel [171] is employed. The absorber is 89 mm height and works from 1 GHz to 200 GHz with reflectivity ranging from -6 to -52 dB. Reflectivity characterization with respect to that of a metallic plate for normal incidence at 1 m distance is shown in Figure A.3 together with manufacturer data.

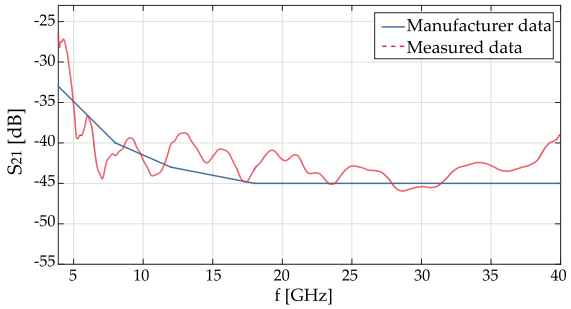

Figure A.3: RAM reflectivity for normal incidence at 1 m.

Flexible rails on the side of the linear positioners are used to insert the wires for feeding an communication with the positioners. Also a 10 m RF cable for measurements up to 40 GHz is inserted. The effect of the change in the curvature of the rails in the cable during the measurements have been studied for several frequencies. Figure A.4 shows the effect of the cable variations for an YZ plane of 24 cm x 24 cm at 20 GHz.

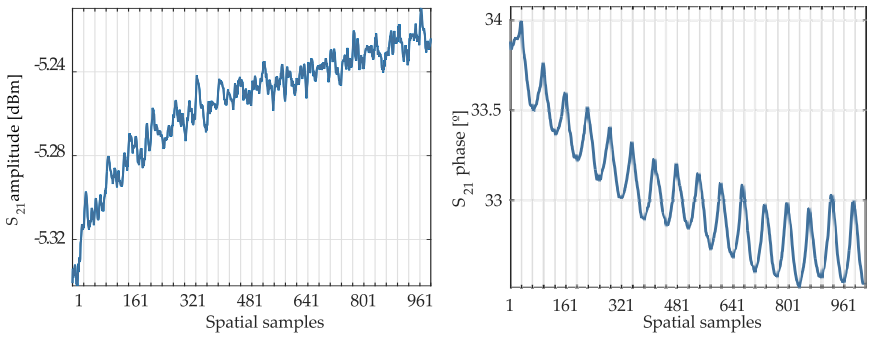

(a) (b)

Figure A.4: Effects of the cable flexing in the S_{21} parameter. (a) Amplitude and (b), phase. Vertical grid marks are coincident with direction changes of the positioner.

Several holding accessories for the probe (or OUTs in the case of scattering measurements), allow to point the probe in different directions in order to perform different type of acquisitions.

A.1.1 **Mechanical subsystem**

The mechanical subsystem is formed by the positioner controller and the positioners, both from IAI [172]. The multi-axis controller can control 6 independent axis simultaneously by means of a proprietary language denominated X-SEL. The PNF measurement system is implemented by means of 4 linear stages, 2 of them in master/slave configuration for the x-axis, one for the y-axis and other for the Z-axis. Thus, as it will be shown in Section A.1.3, multiple planar surfaces as well as arbitrary 3D surfaces can be created. A rotary actuator was been added latter to the system in order increase functionality and to perform other types of measurements such as cylindrical.

Main features of each axis positioner are shown in Table A.1. Maximum speed of the whole system has been fixed to 150 mm/s to cope with the limitations imposed by the most restrictive axis. Positioning resolution is 0.010 mm for the linear positioners and 0.005° for the rotary positioner. Antennas or structures up to 12 kg can be employed with the linear positioners and up to 8 kg if they are mounted on the rotary positioner.

Table A.1: Main features of the positioners.

Axis	Maximum speed	Acceleration	Repeatability	Travel distance	Maximum payload
x	950 mm/s	0.3 G	±0.01mm	1500 mm	80 Kg
y	800 mm/s	0.3 G	±0.01mm	1500 mm	40 Kg
Z	200 mm/s	0.3 G	±0.01mm	400 mm	12 Kg
Rotary	800 °/s	0.3 G	±0.005°	-	8 Kg

A.1.2 **Radiofrequency subsystem**

Configuration and devices of the RF subsystem can vary depending on the type of measurement. For amplitude and phase measurements the basic RF subsystem consist in a frequency synthesized and a coherent receptor which are usually implemented by means of a VNA. A sample of the source is usually taken right before the AUT and conveyed back to the VNA to use as reference. For this purpose, a directional coupler has to be included between the VNA and the AUT. RF amplifiers can also be employed in the probe and/or AUT branches.

On the other hand, for phaseless acquisitions, the coherent receiver can be replaced with direct detectors and depending on the type of phase retrieval method, the reference field may not been needed, yielding much simpler setups. Never-

theless, for the developed indirect off-axis holographic techniques in this doctoral thesis, the RF setup needs to be slightly modified.

In the case of employing radiated reference fields, an extra antenna needs to be added. This reference antenna radiates a sample of the RF source, obtained by means of a directional coupler in its output (see Figure 2.6(a) for further details). A variable attenuator or amplifier is also required to balance the level between the AUT and reference antenna branches.

If synthesized reference waves are employed, the reference branch is implemented by means of a phase-shifter and a power combiner is employed to add the reference signal to the signal received by the probe (see Figure 2.6(b)).

The available antennas are shown in Table A.2. OEWG are the preferred option for antenna measurement in NF, nevertheless SGH are also employed, mainly for scattered field measurements. RF measurement devices and their working ranges are gathered in Table A.3. Other commonly employed devices such as amplifiers, variable attenuators or power combiners are available up to 40 GHz while directional couplers are available up to 110 GHz.

Table A.2: Available probe antennas.

Probe	Covered frequency bands							
antennas	C	X	Ku	k	Ka	V [a]	W	220-320 GHz
SGH [b]	15 (x2)	15 (x2)	15 (x2)	15 (x2)	25 (x2) 12 (x2)	-	15 (x2)	-
OEWG [b]	5 (x2)	5 (x2)	5 (x2)	5 (x2)	5 (x2)	5 (x2)	5 (x2)	5 (x3)

[a] Antennas for this band only cover from 50 to 75 GHz.
[b] Typical gain [dB]. (xN): number of available antennas.

Table A.3: Available measurement devices.

	Covered frequency bands							
Devices	C	X	Ku	k	Ka	V	W	220-320 GHz
VNA	Agilent PNA-X [a]						-	-
Extension modules	-	-	-	-	-	-	VDI / Rohde	VDI
Power detector	Agilent E4416A N8487A Sensor					Agilent E4416A V8486A Sensor	Agilent E4416A V8486A Sensor	-
RF Source	Rohde & Swartz					-	-	-

[a] calibration up to 67 GHz.

A.1.3 **Control subsystem**

The core of the control subsystem is a dedicated computer with the control interface and the communication and synchronization between the mechanical and RF subsystems. Serial communication over ethernet is employed for the synchronization with the controller while Standard Commands for Programmable Instruments (SCPI) is employed for the remote control of the measurement devices. Connections are made employing ethernet or GPIB depending on the measurement device using for each setup.

The control interface has been implemented in MATLAB. A graphical user interface has been included for an easy an intuitive use. The main window is shown in Figure A.5.

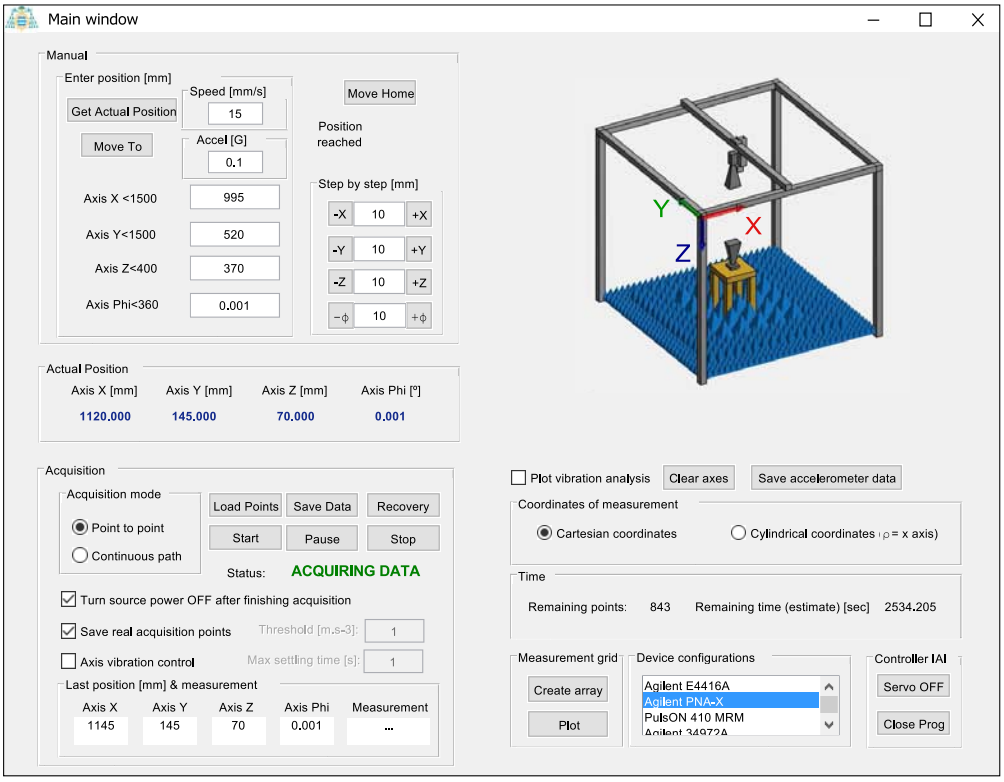

Figure A.5: Main window of the control interface.

From the main window it is possible perform several actions. The *Manual* panel can be employed for manual displacements of the positioners and speed and acceleration selection whereas automated measurements can be created in different steps: 1) selection of the coordinates between Cartesian or cylindrical; 2) selection of the measurement device from the list of available devices in the

Devices configuration list; 3) creation of the acquisition grid from the *Measurement grid* panel (previously created grids can also be loaded at this point from the *Load points* button in the *Acquisition* panel); and finally, 5) configuration of the measurement mode: on the fly measurements can be performed for monochromatic acquisitions whereas the point-by-point option is required for multi-frequency acquisitions.

Once all the parameters are configured the measurement can be controlled with the buttons of the *acquisition* panel. The measurements can be canceled, paused, saved when finished or recovered if any error occurred. Actual position is shown in the *Actual position* panel while the remaining points and a estimate of the remaining measurement time is shown in the *Time* panel.

Other options such as turning off the RF source after the measurements, include the real acquisition points together with the ideal acquisition grid when saving the measurement or switching on the vibration control can be activated in the *acquisition panel*. Vibration control is made by means of an accelerometer fixed to the probe holding accessory. Vibration effects in the point-by-point acquisitions, can introduce errors in the measurement specially at high frequencies. It is possible to establish a threshold to allow for probe stabilization before performing each point acquisition.

Figure A.6 shows an example of the type of window created when a measurement device is selected from the *device configuration* list. In this example, the *Agilent PNA-X* has been selected. From this configuration window is possible to set the main parameters of the measurement such as source power, frequency range and number of points and several parameters for the dynamic range and noise control. It is also possible to directly configure the measurement device using its own interface and then get the configuration from the *Obtain PNA-X settings?* panel.

Finally the grid creation window opened from the *Create array* button is shown in Figure A.7. In this window it is possible to select the acquisition surface from all the possible combinations that can be obtained with the linear and rotary setups. The central point of the acquisition plane and the number of points and step size in each dimension are the rest of the inputs.

The most typical predefined grids that can be created automatically in the control interface are plane rectangular, plane polar and cylindrical grids. Plane rectangular and plane polar surfaces can be created in the XY, XZ and YZ planes, whereas cylindrical acquisition surfaces are created only in the vertical (Z-axis) direction due to the need of employing the rotary positioner, which has to be fixed in horizontal (xy-plane) position. Apart from the predefined acquisition surfaces, arbitrary rectangular trajectories can be created automatically from the

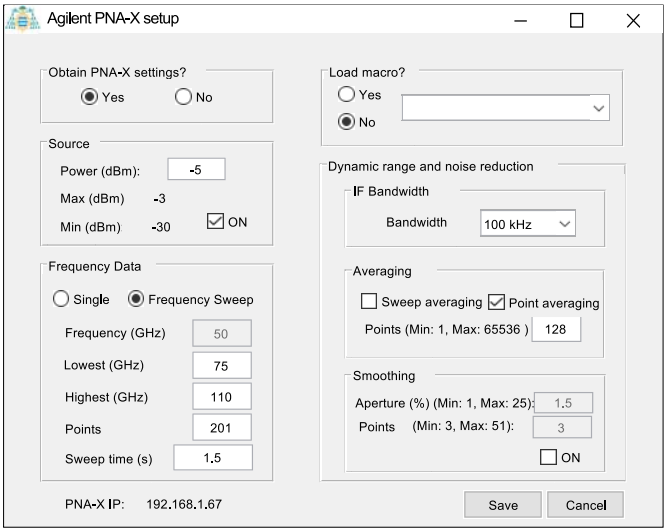

Figure A.6: Example for a RF measurement device configuration window.

Figure A.7: Window for the grid creation of predefined acquisition surfaces.

grid creation window. User defined acquisition grids can be loaded directly in the main window if needed.

APPENDIX

B

Error analysis

B.1 Error sources characterization

The error characterization has been performed following the procedures described in the Antenna Centre of Excellence recommendations [54] and IEEE recomended practices for NF measurements [23]. These procedures, for PNF measurement systems are based in the NIST 18-term uncertainty model [173].

B.1.1 Error analysis by means of measurement comparison

Self-comparison test are employed to assess the changes in the FF pattern of the AUT after specific changes are made in the measurement system in order to independently modify the effect of an individual uncertainty term.

Then pattern subtraction and statistical analysis [80] are employed to estimate the uncertainty that the studied error term introduces in the measurement of an specific parameter of the FF pattern such as the gain, the SLL or the position of the FF pattern maximum.

The error can be characterized by means of the ratio of an ESS to the signal (S) of the FF parameter as

$$(ESS/S)_{dB} = 20 * \log_{10}\{10^{\Delta_{dB}/20} - 1\}, \tag{B.1}$$

being Δ the difference between patterns.

The ESS as a function of the angle can be viewed as a distribution of the estimated uncertainty and thus, its RMS is the standard deviation of the error distribution. It can be used as an estimate of the uncertainty introduced by each individual error source in the analysis of each antenna parameter.

As an example [80] the uncertainty in the measurement of a sidelobe can be obtained as

$$\Delta_{dB} = 20 * \log_{10}\{1 + 10^{(ESS-SL)/20} - 1\}, \tag{B.2}$$

where SL is the sidelobe level of the measurement expressed in dB.

A multiple of the RMS level of the ESS can be employed for an increased confidence level in the estimated uncertainty. The RMS of the ESS represents a confidence level associated to 1σ, that is a 39.4%, thus 6 or 9 dB should be added in order to expand the confidence levels to 2σ or 3σ respectively or equivalently to an 86.5% or a 98.2%.

B.1.2 Error analysis by means of simulations

Quantification of error can also be made by means of simulations. In this case, a reference measurement representing an error-free measurement is employed to obtain a reference FF pattern. The initial set of data is then modified to simulate the effect of the studied errors an the uncertainty can be estimated employing the ESS.

Monte Carlo analysis can be implemented with simulation data for a statistically characterization of the effect of the individual error term. In the Monte Carlo method, the behavior of the individual error terms is statistically modeled and then, a high number of random realizations is performed [B**I**]. The empirical output of the method, the FF radiation pattern in this case, is fit to a normal prob-

ability distribution defined by its mean and standard deviation which defines the uncertainty of the error term.

B.1.2.1 **Error simulation tool**

A simulation tool for the analysis of the effect of mechanical errors has been implemented and presented in [B**I**]. The tool allows for simulation planar measurements in each of the three Cartesian planes and can model random or systematic errors for probe positioning and AUT and probe pointing and alignment. It is possible to use predefined types of antennas such as SGH or OEWG although user defined antennas can also be measured by defining their magnetic equivalent currents in the aperture.

A graphic user interface has been developed in order to ease the use of the tool. The main window of the developed interface is shown in Figure B.1. The tool has been validated though comparison with measurements as shown in [B**I**].

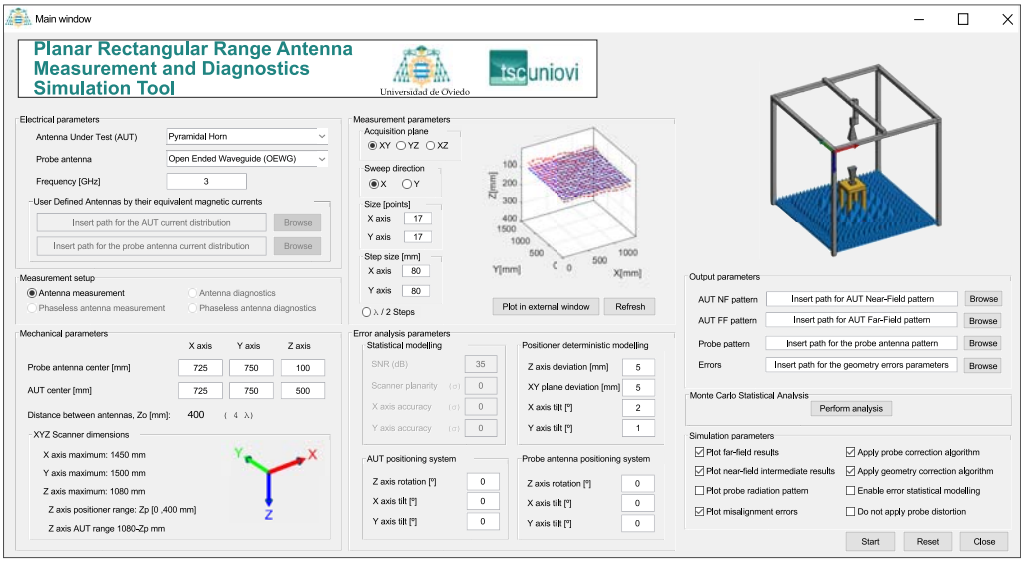

Figure B.1: Main interface of the error simulation tool.

Probe and AUT selection is made in the *electrical parameters* panel in the left upper corner. Position of the AUT and the central point is defined in the *mechanical parameters* panel in the lower left corner. Acquisition plane can be defined in the controls of the central panels. The acquisition plane containing the positioning errors is represented together with the error-free acquisition plane. Errors in the probe pointing and alignment introduce modifications in the radiation pattern of the probe, that can also be depicted in an auxiliary window.

It is possible to apply probe correction algorithms and to visualize the intermediate steps of the process such as the NF computed fields in the acquisition plane.

Finally, the core of the simulator can be used to implement the Monte Carlo analyses for the statistical characterization of the effect of mechanical errors in the FF pattern presented in [**IV**] and [B**II**] whose results will be shown in the following section.

B.1.3 **Individual terms characterization procedures**

Error characterization has been partially assessed as part of the developed measurement system. The studied error terms, those related to the measurement system, as well as the employed method are shown in Table B.1

Table B.1: Quantified error sources.

Source of error	Evaluation method	
	Test on measurement system	Simulations
1) Noise and dynamic range	X	X
2) Crosstalk and leakage	X	-
3) Cable flexing	X	-
4) Thermal drift	X	-
5) Random errors	X	-
6) Multiple reflections (probe/AUT)	X	-
7) Scanner planarity (z-error)	-	X
8) Probe positioning (xy-error)	-	X

The error terms listed in Table B.1 and their characterization procedure are explained next:

1) Measurement of the noise floor is done by disconnecting the AUT, afterwards the dynamic range of the system is obtained as the difference between the maximum power level and the floor noise [54]. The uncertainty level can be obtained with respect to the desired parameter (peak level, SLL, etc.) by means of (B.1) and (B.2).

2) Crosstalk corresponds to the unwanted coupling between two ports of a a measurement system whereas leakage is the unwanted coupling due to imperfections in the signal sources, cables, connectors, etc. Characterization of both errors is done simultaneously by performing two acquisitions: first with the AUT terminated with a load and covered with absorber; and second, with a terminated probe also covered with absorber. The measured

data are transformed to FF and normalized to the FF peak of the reference pattern.

3) Error due to cable flexing is characterized from several acquisition of the reflection coefficient when the AUT is replaced with a short circuit. Since the reflection coefficient is measured, half of the maximum difference in those measurements is added to the amplitude and phase of the reference acquisition and transformed to the FF. Then the ESS is obtained by subtracting this pattern with the modified data to the reference FF pattern and the uncertainty can be obtained with (B.2) [174].

4) For the thermal drift effect characterization a long term acquisition of the field and temperature variation is made with static AUT and probe. Then the reference data are modified with the observed variation and the uncertainty is obtained in the FF by means of (B.1) and (B.2). The peak-to-peak variation of the amplitude is randomly added to the reference amplitude, and the phase variation is added to the reference phase as an offset [174].

5) Random errors arise from noise in the electrical and mechanical subsystems. In PNF ranges, random errors can be estimated from the level of the PWS in the invisible region from an acquisition of the main cuts performed with $\lambda/4$ sampling [175]. The FF uncertainty can be estimated after obtaining the ESS relative to the peak level.

6) Multiple reflections between the probe antenna and the AUT can be characterized by range variation measurements with sampling steps of $\lambda/8$. The peak-to-peak variation can be use to modify the reference set and the uncertainty can be obtained in the FF with respect to the reference FF applying (B.1) and (B.2) [23].

   Another option for estimating the uncertainty due to multiple reflections is to perform 2 to 5 acquisition at relative distances of $\lambda/2$, then averaging the results to reduce the effect of the multiple reflections. Next, the FF obtained from the averaged results is employed as reference pattern and compared to the pattern obtained from one of the initial acquisitions [54].

7)-8) Finally, the effects of scanner planarity and probe positioning errors, as well as pointing effects, are studied by means of simulations employing the developed simulation tool that allows to consider different types of errors, random and systematically defined.

B.2 Performed error analyses

Main results of the performed analysis will be shown in this section for the mm- and submm-wave bands in which measurement instrumentation is available at the moment.

B.2.1 **Ka-band: effect of noise and mechanical errors in broadband phaseless antenna measurement**

The effect of noise and mechanical errors have been studied by means of Monte Carlo analysis for the developed method for broadband phaseless antenna characterization from a reduced set of points. Monte Carlo analysis have been performed also to study the effects of the same errors in a complex acquisition over a regular rectangular grid to compare the differences. As a reference field, the FF pattern of the antenna obtained from direct integration of its equivalent magnetic currents in the aperture, is computed.

At this point, it is worth noting that the intention of this analysis was not to obtain the upper bounds of the error for which the method can provide good enough results but to check the feasibility of the method in the developed measurement system prior to performing the measurements, thus, the errors have been modeled to match the accuracy specifications of the measurement system. The considered errors are shown in Table B.2

Table B.2: Error modeling for the Monte Carlo analysis.

Error source	Probability model
Positioning error (XY)	Uniform distribution ($\pm$1 mm)
Planarity error (Z)	Uniform distribution ($\pm$1 mm)
Noise	White Gaussian Noise according to a 45 dB SNR

150 Monte Carlo trials have been considered for both cases (phaseless over a reduced set of points and complex over a regular rectangular grid) and the probability distributions of several parameters such as directivity, position of the maximum and sidelobes and nulls level have been obtained for the main cuts of the FF pattern.

The results for the $\phi = 0^\circ$ cut of the FF pattern at 38 GHz are shown in Figure B.2 for the 150 trials of the Monte Carlo test in case of considering planarity errors and compared to the reference pattern. From a visual analysis it can be seen the effect of the considered planarity error does not have a big impact on the pattern within the valid angular region, delimited by black vertical dashed lines.

Those results are fit to a Gaussian distribution so that the uncertainty caused by the planarity errors can be easily obtained. Figure B.3 shows the error histograms for the studied parameters, while numerical values for the mean and standard deviations are gathered in Table B.3. The obtained results for the rest of considered errors are included in [**IV**].

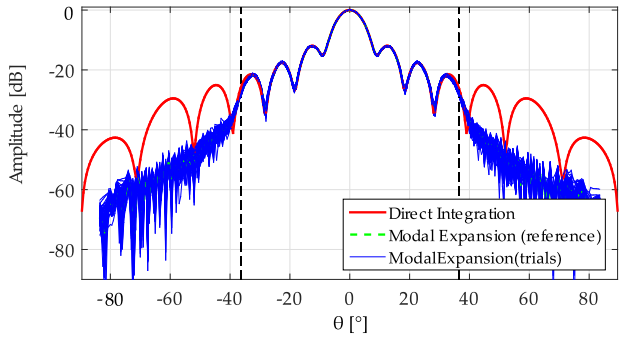

Figure B.2: FF pattern ($\phi = 0°$ cut) for the 150 trials of the Monte Carlo method. Valid angular region is delimited by the black vertical dashed lines.

Table B.3: Outputs of the Monte Carlo analysis for the study of planarity errors.

Parameter	Reference Level	Mean	Standard deviation
Directivity [dBi]	30.483	30.525	0.0233
Maximum position [°]	0.000	-0.003	0.0317
1st SLL [dB]	-12.500	-12.163	0.1380
2nd SLL [dB]	-18.080	-14.645	0.2210
1st null level [dB]	-16.28	-17.734	0.3025
2nd null level [dB]	-26.85	-25.484	0.8850

B.2.2 **W-band: effect of mechanical and electrical errors in diagnostics applications**

An statistical characterization of the influence of the mechanical inaccuracies by means of Monte Carlo analyses has been presented in [B**II**]. The procedure is identical to the one presented in the previous example but the studied parameter is the size of the aperture instead of the main parameters of the FF pattern.

A complimentary analysis was performed in order to characterize the main error sources in the actual measurement system in this band. The procedures defined in Section B.1.3 have been followed.

A 25 dB gain SGH has been employed as AUT whereas an OEWG as been used as a probe. A square YZ acquisition plane of 102 size has been defined at $X_0 = 210$ mm of the aperture of the AUT with $\lambda/2$ sampling at 110 GHz. Several frequencies between 75 and 110 GHz have been measured, nevertheless the error analysis is presented for 92.5 GHz, the central frequency of the band. Two frequency extension modules are employed to work in the *W*-band. Connections to the VNA are made at the intermediate frequency in the *Ku*-band, thus the errors

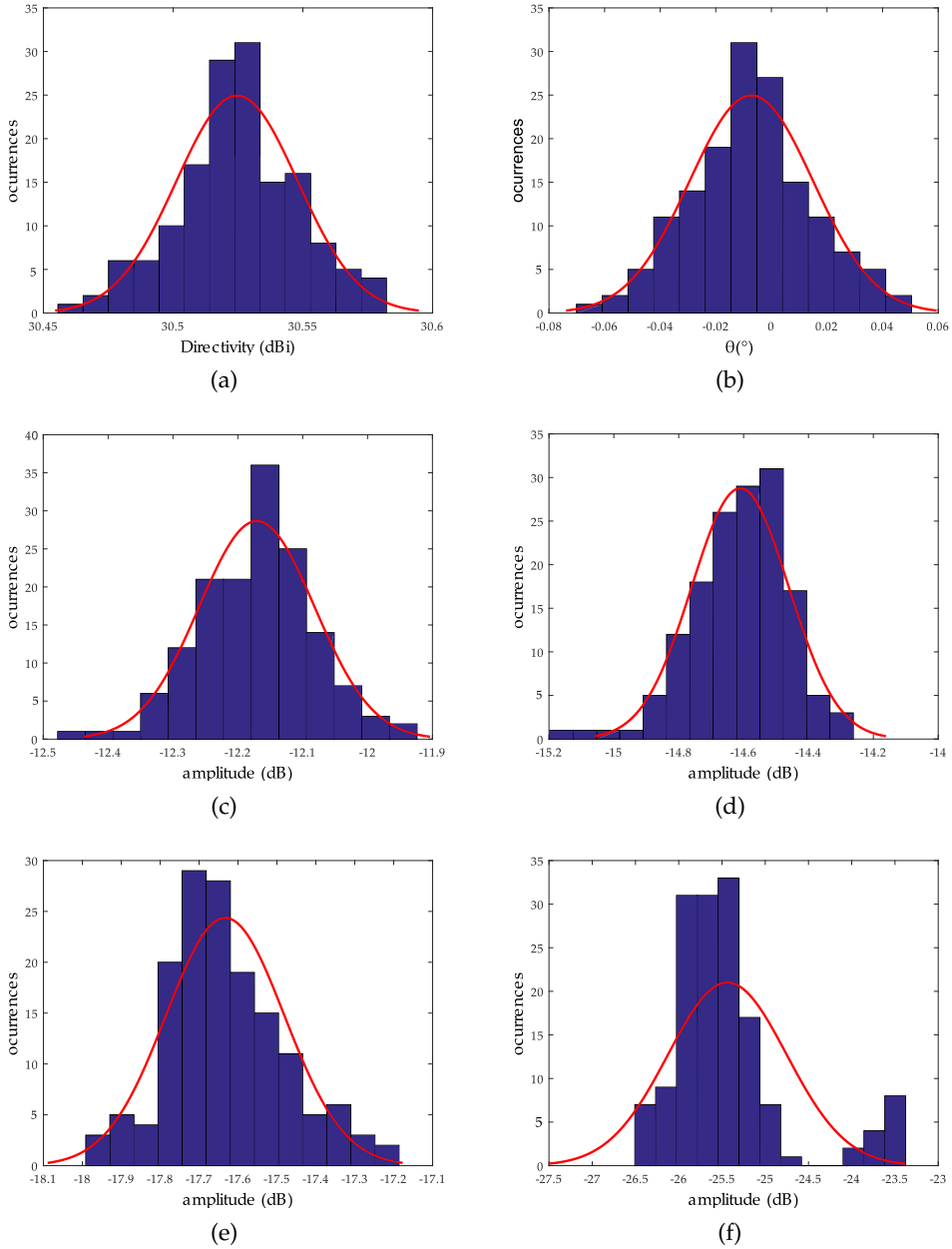

Figure B.3: Histogram characterization of the outputs of the Monte Carlo method for the FF pattern ($\phi = 90°$ cut) for different parameters (a) directivity, (b) position of the maximum, (c) value of the first SLL, (d) value of the second SLL, (e) value of the first null and (f) value of the second null.

due to cable flexing are expected to be small. The measurement setup can be seen in [B**II**].

It is worth noting that the measurements were initially planned for a diagnostics applications in which only the aperture field was desired, thus, the size of the acquisition plane is small for the FF characterization of the antenna being the valid margin of the transformation is $\pm 9.5^{\circ}$. This margin is not enough for an accurate characterization of the sidelobes and the truncation error is expected to be high. However, the truncation error has not been studied because further reduction of the acquisition plane would yield invalid results in the FF pattern.

The dynamic range is obtained by subtracting the noise floor level, -82 dBm from the maximum power, which is approximately -23 dBm as shown in Figure B.7(a). A 59 dB dynamic range is obtained for this setup with a source power of 11 dBm, an intermediate frequency filter bandwidth of 100 KHz, averaging of 16 traces and 23.5 ms sweep time.

Figures B.4 to B.8 show the results of the characterization of each of the studied error sources, and their effect in the FF from which the ESS is obtained with respect to a reference pattern for an error-free measurement at the center of the band (92.5 GHz). The reference pattern has been obtained by averaging 5 NF acquistions. Horizontal cuts are shown for $z = 0$ in the NF acquisitions, whereas the cut shown for the FF pattern for the ESS calculation corresponds to the $\phi = 0^{\circ}$ of the E_{θ} component. The numerical values of the ESS and the obtained uncertainty of each individual error term are gathered in Table B.4.

Table B.4: Uncertainty characterization relative to the peak level.

Error source	RMS(ESS) [dB]	Standard deviation (1σ) [dB]
Dynamic range	59	0.0097
Thermal drift	-39.3143	0.0935
Leakage	-68.0055	0.0035
Cable flexing	-67.9237	0.0035
Multiple reflections	-35.8515	0.1389
Random error	-82.5334	0.0006

For this case, it is clearly seen that the most noticeable errors are due to the multiple reflections and the thermal drift. Cable flexing error is rather small for this setup, although it is worth noting that the cables employed to connect the frequency extension modules to the VNA work in the *Ku*-band. Nevertheless, this is due to the small size of the acquisition plane. This error is expected to rise for larger acquisition planes mostly in the extremes and for changes of the sweep direction. The effect of multiple reflections can be partially removed if time gating technques are applied.

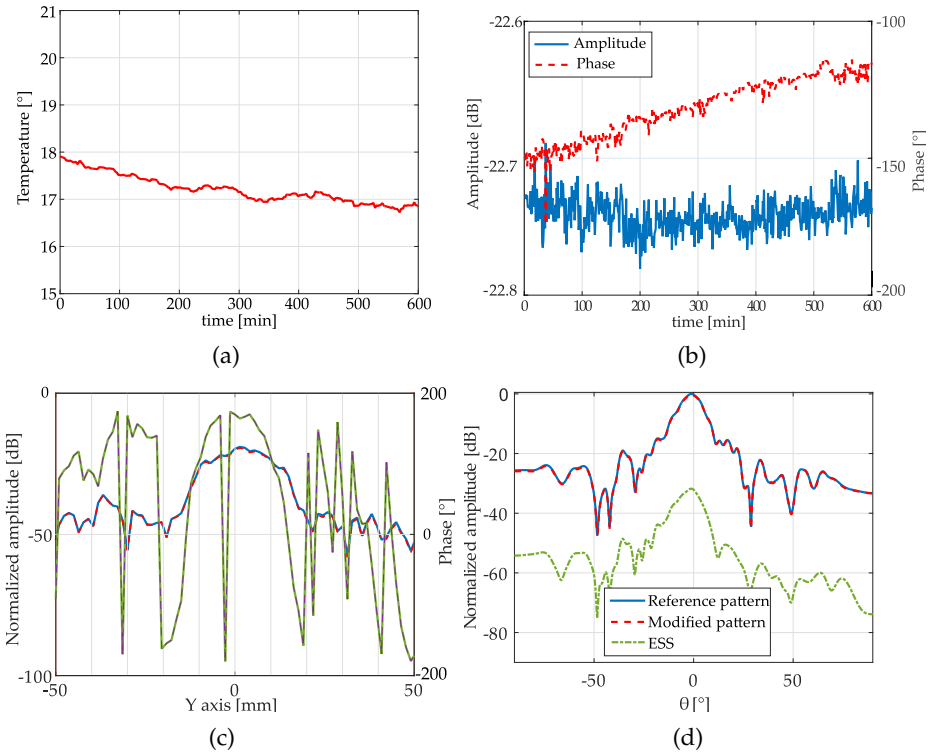

Figure B.4: Thermal drift characterization at 92.5 GHz. (a) Temperature variation during 600 minutes (maximum amplitude variation of 0.06 dB and phase of 4° per hour), (b) thermal drift effect for static AUT, (c) effect of the thermal drif in the NF measurements and (d), effect in in the FF pattern.

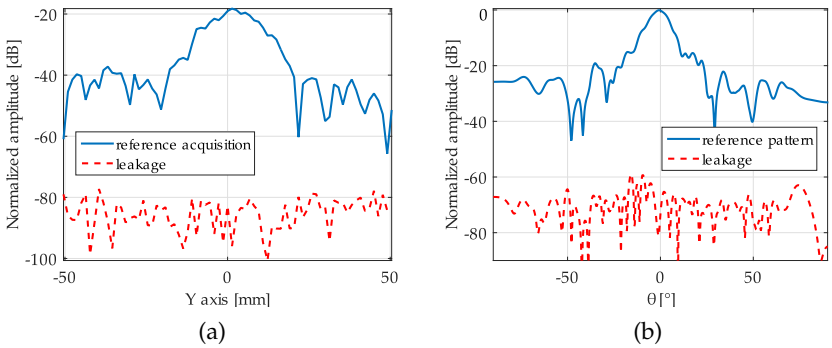

Figure B.5: Leakage characterization at 92.5 GHz. (a) Leakage level in the AUT branch for a NF acquisition, (b) effect in the FF pattern.

The combined uncertainty is obtained as the RSS of the individual uncertainties and for this setup has a value of $U_c = 0.1679$ dB. The expanded uncertainty

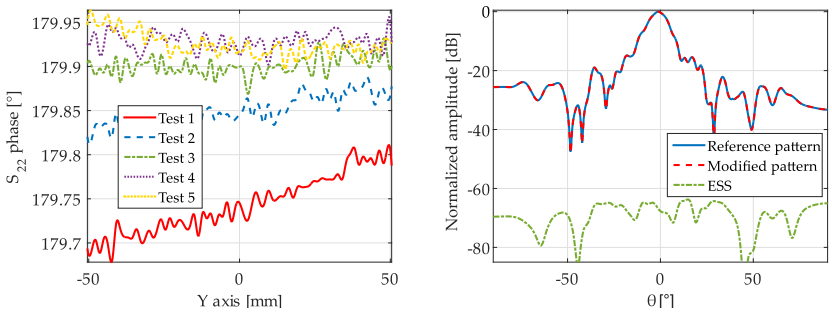

(a) (b)

Figure B.6: Cable flexing error characterization (downconversion frequency in the *Ku*-band). (a) Variation of the reflection coefficient of the short circuited AUT branch (maximum amplitude variation of $0.04\,dB$ and phase of $0.25°$), (b) effect the FF pattern.

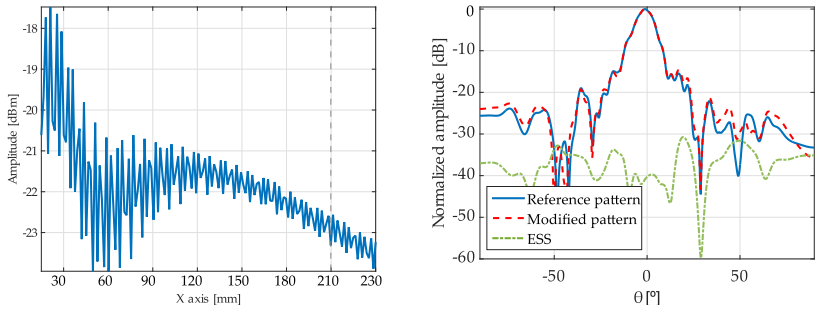

(a) (b)

Figure B.7: Multiple reflections characterization at 92.5 GHz. (a) Range characterization (the vertical dashed line represents the acquisition plane), (b) effect in the FF pattern.

at a confidence level of 98.29 is computed by multiplying U_c by a factor of 3 as explained in Section 1.3.1.3. Thus, the expanded uncertainty relative to the the peak level in the presented setup is $U_k = 0.5037$ dB.

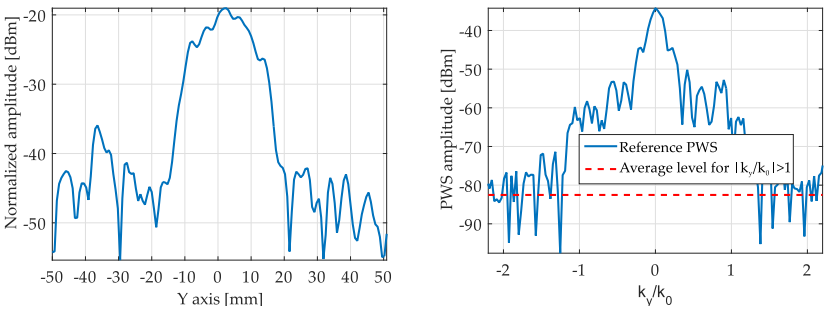

(a) (b)

Figure B.8: Random error characterization at 92.5 GHz. (a) Reference NF acquisition with 0.9λ, (b) PWS of the reference pattern.

B.2.3 **220-330 GHz band: effect of mechanical and electrical errors in antenna pattern determination**

A conventional antenna measurement setup has been implemented for the uncertainty analysis of the measurement system errors from 220 to 330 GHz. The error has been characterized in the complete band and will be shown for 4 different frequencies: 220, 270, 300 and 330 GHz.

An OEWG of 6 dB gain has been employed as an AUT, and an identical antenna has been used as probe. Acquisitions have been performed in an YZ plane of 100 mm x 200 mm at 20 mm of the antenna. Sampling has been fixed to $\lambda/2$ at 330 GHz, that is 0.4454 mm. The maximum dimension of the aperture of the AUT is approximately 1 mm, thus, valid margin of the transformation, defined in (2.20), is 68° for the horizontal cut and 78° for the vertical cut.

The VNA has been set for 201 frequency points, with 128 point averages and the intermediate frequency filter is 100 KHz yielding a sweep time of 0.1867 ms. The speed of the positioners has been limited to 5 mm/s thus vibrations due to the movement of the frequency extension module are minimized. Hence, each complete spatial acquisition requires 36 hours. Figure B.9 shows the calibration and alignment process before placing the RAM.

A more exhaustive error characterization has been made in this band with the characterization of the error sources 1) to 6) listed in Table B.1. Although numerical results are given for the four aforementioned frequencies, graphic results are only given for 300 GHz (see Figures B.9 -B.14). Horizontal cuts are shown for $z = 0$ in the NF acquisitions, whereas the cut shown in the FF for the ESS calculation corresponds to the $\phi = 0°$ of the E_θ component.

The noise floor is approximately -90 dBm while the maximum measured power in the acquisition plane is -22.68 dBm (see Figure B.13(a)), hence, a dynamic range of 62.9 dB is achieved in the presented setup.

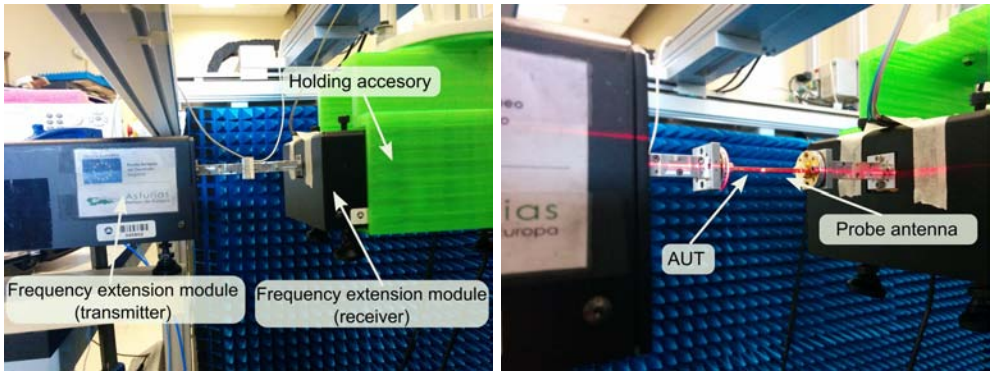

(a) (b)

Figure B.9: Antenna measurement setup for the 220 to 330 GHz band. (a) System calibration, (b) alignment process with laser level.

Table B.5 shows the value of the RSS of the ESS for the considered errors and the uncertainty they produce in the measurement of the peak level of the FF. The most larger errors are observed, as expected, for the cable flexing and the thermal drift, due to the lack of room temperature control. The rest of the studied error sources introduce an acceptable amount of error. It is worth noting that the cables employed to connect the frequency extension modules to the VNA work in the *Ku*-band.

Table B.5: Uncertainty characterization relative to the peak level for the measurements in the 220 to 330 GHz band.

	f=220 GHz		f=270 GHz		f=300 GHz		f=330 GHz	
Error source	ESS[a] [dB]	std [b] [dB]	ESS [dB]	std [dB]	ESS [dB]	std [dB]	ESS [dB]	std [dB]
Dynamic range	56.890	0.0124	56.960	0.0123	57.320	0.0118	56.190	0.0135
Thermal drift	-44.810	0.0498	-46.553	0.0408	-41.631	0.0219	-43.940	0.0550
Leakage	-107.812	0.0000	-117.499	0.0000	-108.874	0.0000	-101.008	0.0001
Cable flexing	-40.581	0.0809	-42.768	0.0629	-43.969	0.0548	-43.319	0.0591
Multiple reflections	-56.701	0.0127	-53.137	0.0191	-53.161	0.0191	-52.9552	0.0195
Random error	-93.861	0.0002	-95.904	0.0001	-94.865	0.0002	-97.880	0.0001

[a] The RSS of the ESS.
[b] Standard deviation (1σ).

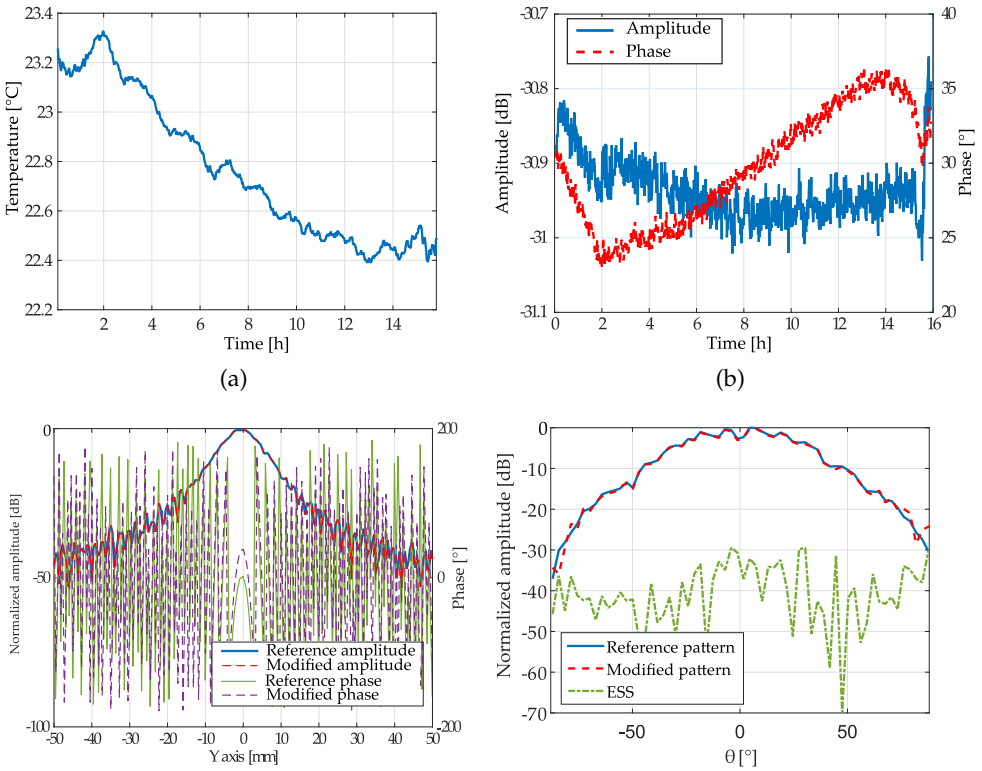

Figure B.10: Thermal drift characterization at 300 GHz. (a) Temperature variation during 16 hours (b) Thermal drift effect for static AUT during 16 hours (maximum amplitude variation of 0.120 dB and phase of 1.167° per hour), (c) effect of the thermal drift in the NF measurements and (d), effect in the FF pattern.

Finally Table B.6 shows the computed combined and expanded uncertainties. Values are between 0.15 and 0.30 dB. Nevertheless the effect of the thermal drift and the multiple reflections should be corrected. The use of phaseless techniques is recommended in this band as they can prevent the effect of the thermal drift and cable flexing errors. The rest of uncertainties associated to the probe and the acquisition (truncation of the acquisition plane, aliasing, etc.) should be added also to the computed values.

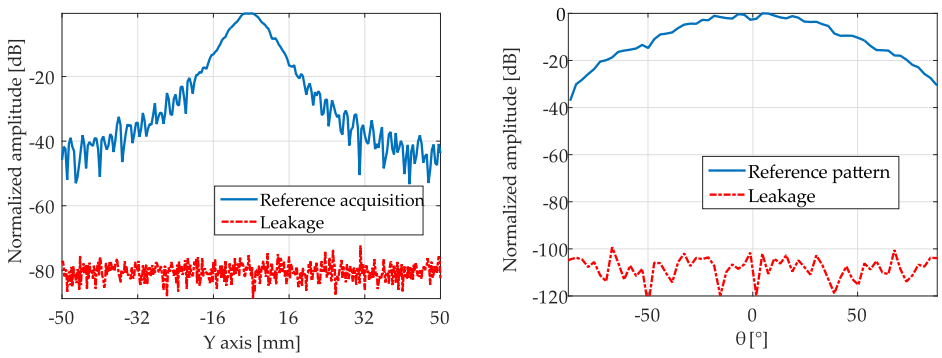

Figure B.11: Leakage characterization at 300 GHz. (a) Leakage level in the AUT branch for a NF acquisition, (b) effect in the FF pattern.

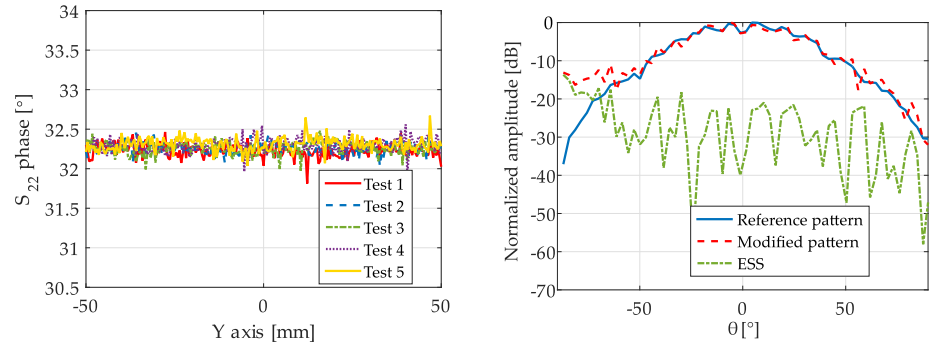

Figure B.12: Cable flexing error characterization, downconversion frequency in the *Ku*-band. (a) Variation of the reflection coefficient of the short-circuited AUT branch (maximum amplitude variation of 0.05 dB and phase of 0.6°), (b) effect in the FF pattern.

Table B.6: Combined and expanded uncertainty characterization relative to the peak level.

	f=220 GHz	f=270 GHz	f=300 GHz	f=330 GHz
Combined uncertainty, U_c [dB]	0.0967	0.0783	0.0631	0.0841
Expanded uncertainty, $U_k = 3U_c$ [dB]	0.2900	0.2350	0.1894	0.2524

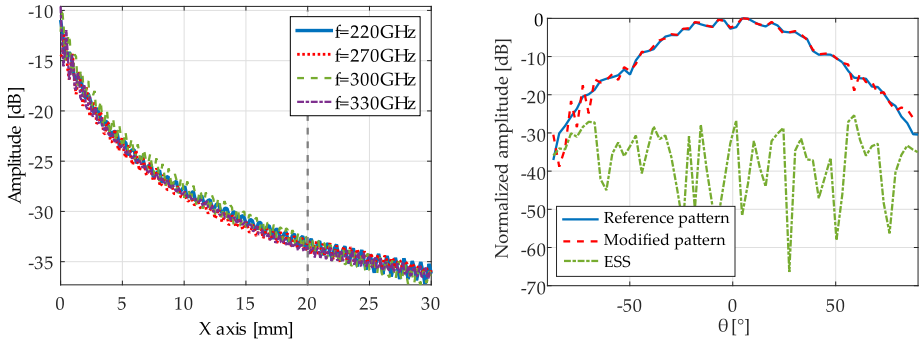

(a) (b)

Figure B.13: Multiple reflections characterization at 300 GHz. (a) Range characterization (the vertical dashed line represents the acquisition plane). Maximum amplitude variations of 1.6 dB, (b) effect in the FF pattern.

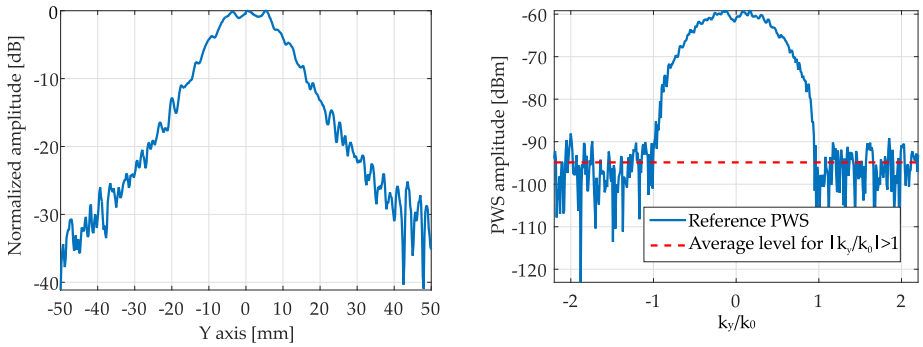

(a) (b)

Figure B.14: Random error characterization at 300 GHz. (a) Reference NF acquisition with 0.9λ sampling , (b) PWS of the reference pattern.

Publications

Impact factor report

This section gathers the main information regarding the journals and conferences in which the articles and the rest of the contributions composing this dissertation have been published.

Among the 11 works that form the dissertation, 6 of them have been published in journals indexed in the Science Citation Index (SCI) and in the Journal Citation Reports (JCR). Complete references of the journals wherein the works have been published can be found in Table P.1.

Table P.1: Complete references of the journals with published works.

Journal title	Publisher	ISNN	Periodicity	Abbreviation
Antenna and Wireless Propagation Letters	IEEE	1536-1225	Annual	AWPL
Journal of Infrared Millimeter and Terahertz Waves	Springer	1866-6892	Monthly	JIMTW
Transactions on Antennas and Propagation	IEEE	0018-926X	Monthly	TAP
Geoscience and Remote Sensing Letters	IEEE	1545-598X	Monthly	GRSL

Of those 6 articles, 3 of them have been published in the IEEE Transactions on Antennas and Propagation (TAP) and the rest in the IEEE Antenna and Wireless Propagation Letters (AWPL), the Springer Journal of Infrared Millimeter and Terahertz Waves (JIMTW) and the IEEE Geoscience and Remote Sensing Letters (GRSL) respectively. Main metrics defined by the JCR and also Eigenfactor metrics are gathered in Table P.2. All the works have been published in journals from the first and second quartile.

The rest of works corresponds to oral presentations in conferences. As it can be seen in Table P.3, showing main information about the conferences, the 4 con-

ferences have an International Standard Book Number (ISBN) and the proceedings are available in the digital library of the IEEE and therefore, all of them might be considered as relevant publications following the National Commission for the Evaluation of Research Activity (CNEAI) guidelines for a positive evaluation [1].

Table P.2: Metrics and rank in the *Engineering, Electrical and Electronic* category.

Journal	JCR metrics (2015)		Eigenfactor metrics		JCR Rank in category		
	Impact Factor	Total cites	Score	Article influence	Total journals	Rank	Quartile
AWPL [b]	1.751	5502	0.02613	0.843	255 (82)[a]	90 (22)	Q2 (Q2)
JIMTW[c]	1.851	911	0.00403	0.503	255	80	Q2 (Q2)
TAP[c, d]	2.053	20883	0.04319	0.829	255 (82)	67 (19)	Q2 (Q1)
GRSL[c]	2.228	5572	0.01608	0.756	255	56	Q1

[a] Numbers inside brackets indicate the rank of the journal in the *Telecommunications* category when the journal is included in that category.
[b] Publication year of the work presented in **[I]** is 2014 (IF=1.579, Q2 (Q2)).
[c] 2016 metrics are not available yet for publications **[II]**,**[III]** and **[VIII]**.
[d] Publication year of the work presented in **[V]** is 2013 (IF=2.459, Q1 (Q1)).

Table P.3: Conferences information.

Conference	Proceedings publisher	ISBN	Periodicity	Venue & date
2015 9th European Conference on Antennas and Propagation (EUCAP 2015)	IEEE	978-88-907018-5-6	Annual	Lisbon, Portugal 13–17 Apr. 2015
2016 10th European Conference on Antennas and Propagation (EUCAP 2016)	IEEE	-	Annual	Davos, Switzerland 10–15 Apr. 2016
2013 IEEE Antennas and Propagation Society International Symposium (APSURSI 2013)	IEEE	978-1-4673-5317-5	Annual	Orlando, Florida (US) 7–13 Jul. 2013
2014 IEEE Conference on Antenna Measurements & Applications (CAMA 2014)	IEEE	978-1-4799-3678-6	Annual	Antibes, France 16–12 Nov. 2014

[1] CNEAI resolution from November 26th, 2015 regarding positive evaluation of conference contributions: papers published in conference proceedings , when these proceedings are comparable vehicle for the dissemination of knowledge to the journals included in the JCR Science Edition. In this case each contribution may be considered of medium or low relevancy.

Errata

Publication [IV]

Page 4, Table III: rows for the *1st null* and *2nd SLL* for 38 GHz are interchanged.

Publication [V]

Page 3, first column, third paragraph: it should read " ... on the first 20 *columns of the first row*... Thus, each possible value is estimated from five *columns*".

Publication [VI]

Page 2, first column, fourtg paragraph: it should read "...close enough *one to* each other... with the *distance*...".

Page 3, second column, equation (11): it should read "... $e_b(x = -D, y = 0, z = 0)$...".

Page 4, second column, fifth paragraph: it should read "... one numerical and other experimental...".

Page 5, first column, fourth paragraph: it should read "... $\varphi_b = 3.2^\circ$ and $\varphi_f = 4.5^\circ$...".

Page 5, second column, first paragraph: it should read "...$\varphi_b = 11^\circ$... value only takes *place*... significant impact *on*...".

Page 5, second column, second paragraph: it should read "... and *the* distance...".

Page 6, first column, first paragraph: it should read "... whose diameter (1.5 mm) is still...".

Publication [VII]

Page 10, second column, first paragraph: it should read: "... characteristics *have* been observed...".

Publication I

J. Laviada, **A. Arboleya-Arboleya**, Y. Álvarez-López, C. García-González and F. Las-Heras **"Phaseless antenna diagnostics based on off-axis holography with synthetic reference wave,"** *IEEE Antennas and Wireless Propagation Letters*, vol. 13, pp. 43–46, 2014.

I

I

Phaseless antenna diagnostics based on off-axis holography with synthetic reference wave

Jaime Laviada, Ana Arboleya-Arboleya, *Student Member, IEEE*, Yuri Álvarez-López, *Member, IEEE*, Cebrián García-González, *Student Member, IEEE*, and Fernando Las-Heras, *Senior Member, IEEE*

***Abstract*—An antenna diagnostics method based on off-axis holography is presented in this paper. In this novel phaseless antenna measurement setup, the reference wave is synthesized by means of a mechanical phase shifting and, therefore, the use of a phase shifter is avoided, yielding an accurate low-cost antenna diagnostics system. The technique is validated by means of simulation as well as measurement. Accurate results prove the system capability for antenna diagnostics tasks.**

I. Introduction

Antenna diagnostics involves the detection of failures which prevent the antenna from achieving its ideal performance. The identification and correction of antenna design and manufacturing errors usually requires invasive techniques based on trial-error procedure whose technical and economical costs are directly related to the antenna complexity. Thus, the development of fast and accurate non-invasive methods for antenna faults detection has been of great interest in the last decade.

Non-invasive methods are usually based on acquiring the antenna radiated field and, after that, computing a set of key parameters such as the extremely near-field on the antenna aperture [1] or the equivalent currents on the antenna surface [2], [3]. Antenna manufacturing errors can be easily detected from the analysis of these parameters. For example, any distortion on the reflector antenna surface appears as a phaseshift in the retrieved near-field on the antenna aperture [1].

The computation of these parameters involves, in general, the acquisition of the amplitude and phase of the field. Although the amplitude acquisition is relatively simple at any frequency, the phase acquisition can be complex at high frequencies or in environments with poor thermal stability [4], [5].

In order to accomplish a succesful diagnostics from amplitude-only measurements, several phase retrieval techniques for radiated fields are available in the literature. Many of them rely on iterative schemes (e.g., [6], [7]) relating the fields (or equivalent currents) in two (or more) different surfaces.

The authors are with the department of Electrical Engineering\\ Universidad de Oviedo\\ Campus Universitario, 33203 Gijón, Asturias, Spain\\ Authors' email: {jlaviada, aarboleya, yalopez, cgarciag, flasheras }@tsc.uniovi.es

This work has been supported supported in part by the European Union under COST Action IC1102 (VISTA); by the Ministerio de Ciencia e Innovación of Spain /FEDER under projects TEC2011- 24492 (iScatt), CSD2008-00068 (Terasense) and MICINN-11-IPT-2011-0951-390000 (Tecnigraf); by the Gobierno del Principado de Asturias (PCTI)/FEDER-FSE under projects PC10-06, EQUIP08-06, FC09-C0F09-12, EQUIP10-31; by grants BP-11-169 of the Gobierno del Principado de Asturias and BES-2009-024060.

On the other hand, iteration-free phase retrieval can be accomplished by means of the Leith-Upatnieks holography [8] if a conveniently characterized source is included in the setup. This source can be replaced by a synthesized reference wave which enables a total control of the system (see [9] and the references therein). Despite of the flexibility of this setup, it involves the use of digital phase shifters which can considerably increase the cost of the overall setup at high frequencies.

In this letter, the Leith-Upatnieks approach is applied to the antenna diagnostics by synthesizing the reference wave through the mechanical displacement of the probe antenna. Thus, the inverse scattering scheme in [10] is reformulated in order to apply it to fault antenna measurements. It results in a simplified, low-cost scheme that can be used to carry out accurate antenna diagnostics.

II. Antenna diagnostics via enhanced Leith-Upatnieks holography

A. Setup for the phase retrieval

In the Leith-Upatnieks holography, the field from the antenna under test (AUT) is combined with a reference field, whose amplitude and phase are known on the acquisition surface, yielding the following received hologram:

$$I(\vec{r}) = \left| E_{AUT}\left(\vec{r}\right) + E_r\left(\vec{r}\right) \right|^2, \tag{1}$$

wherein E_{AUT} is the field radiated by the antenna under test and E_r is the field of the reference antenna. Multiple setups have been proposed in the literature to implement this interferometry scheme (e.g., [5]). A conventional assumption is to approximate the reference field by a plane wave so $E_r\left(\vec{r}\right) = A\exp(-jk_0\hat{k}\cdot\vec{r})$ being k_0 the free space wavenumber and $\hat{k}$ the unitary propagation vector of the plane wave.

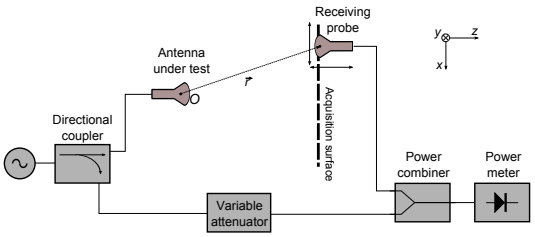

Figure 1. Setup for the phaseless diagnostics based on Leith-Upatnieks holography.

Next, it will be shown that the setup in Fig. 1, which does not employ a phase shifter as conventional schemes [11], [12], can enable an acquisition equivalent to the one in (1). In this scheme, the field received at the probe antenna located at the acquisition point defined by $\vec{r}$ is given by:

$$I(\vec{r}) = \left|E_{AUT}\left(\vec{r}\right) + C\right|^2, \tag{2}$$

wherein C is the constant signal injected though the variable attenuator branch. This variable attenuator is used to balance the power between the two branches arriving to the power combiner. Its value is only tuned at the beginning of the measurement so that the amplitude of the constant signal matches approximately the value of the field due to the AUT.

If the probe antenna is displaced a distance $\vec{d} = d\frac{\vec{r}}{\|\vec{r}\|_2}$, then the field at the modified acquisition point $\vec{r}\,' = \vec{r} + \vec{d}$ is given by:

$$E_{AUT}(\vec{r}\,') \approx E_{AUT}(\vec{r})e^{-jk_0 d}. \tag{3}$$

Thus, the received hologram at the modified point is given by:

$$I(\vec{r}\,') \approx \left|E_{AUT}\left(\vec{r}\right)e^{-jk_0 d} + C\right|^2 = \left|E_{AUT}\left(\vec{r}\right) + Ce^{jk_0 d}\right|^2. \tag{4}$$

Eq. (4) shows that if the appropriate displacement is chosen for each original point, then sampling in the modified points results in the same acquired hologram as in the case of using the conventional acquisition points together with an interfering plane-wave. As a consequence, the use of a phase shifter, which can be complex and expensive at high frequencies, is replaced by a three dimensional movement that can be carried out with micropositioners.

It is important to note that the approximation in (3) is only valid if the probe is in the far-field of the antenna. However, in the results section, it will be shown that this approximation can provide accurate results for diagnostics purposes although this condition is not strictly fulfilled. The reason is that the maximum displacement is $d = \pm\lambda/2$, which results in a phase shift of $\pm 180°$. These electrically small movements make possible to assume that the amplitude remains unchanged whereas the phase is linearly modified.

B. Postprocessing algorithm

In the indirect holography, two different postprocessing techniques are possible depending on the sampling rate. In order to understand the one that is used in this letter, let us consider the spectrum of the acquired hologram which is given by the Fourier transform of (1). In this section, it is assumed that phase shifting is applied along the x-axis without loss of generality. The wavenumber of the synthesized plane-wave is denoted by k_x^{pw}; then, the received hologram is given by:

$$\begin{aligned} I\left(x,y\right) &= \left|E_{AUT}\left(x,y\right) + Ce^{-jk_x^{pw}x}\right|^2 \\ &= |C|^2 + \left|E_{AUT}\left(x,y\right)\right|^2 \\ &+ C^* E_{AUT}\left(x,y\right)e^{jk_x^{pw}x} + CE^*_{AUT}\left(x,y\right)e^{-jk_x^{pw}x}. \end{aligned} \tag{5}$$

The spectrum of the received hologram is calculated by means of the Fourier transform of the previous expression and it is shown in Fig. 2. In this figure, the tilde is used to denote Fourier transform and W is the bandwidth of the radiated field.

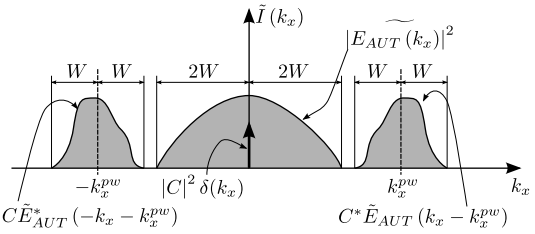

Figure 2. Spectrum of the acquired hologram.

Four terms can be identified in the spectrum. The first term corresponds to a Dirac delta function which is at the origin of the spectral axis. In addition, a second term, which corresponds to the Fourier transform of the squared amplitude of the field, is also centered at the origin of the spectral axis. The bandwidth of this term is twice the bandwidth of the radiated field E_{AUT}. The two remaining terms are centered at $\pm k_x^{pw}$and correspond to the spectrum of the radiated field as well as the spectrum of its complex conjugate. Thus, if one of these two terms is isolated, then the spectrum (and so the amplitude and phase) of the radiated field can be retrieved.

According to [13], the spatial bandwidth of the radiated field for planar acquisition can be consider as $W = k_0$ in the region of interest. Hence, the wavenumber of the equivalent plane wave must be at least $k_x^{pw} = 3k_0$ to avoid spectral overlapping.

The conventional way to implement the phase shifting along a given direction is to use a constant increment of the phase of the reference wave $\Delta\phi$ between consecutive samples. Under this assumption, the wave number of the equivalent plane wave is given by $k_x^{pw} = \frac{\Delta\phi}{\Delta x}$ [12], wherein Δx is the sampling step. Since the total bandwidth of the signal is $4W = 4k_0$, then the sampling step must be at least $\Delta x = \lambda/8$. According to this step size, the optimal phase increment is given by $\Delta\phi = 135°$.

Another possible way to retrieve the amplitude and phase is to use the so-called *modified hologram*. This hologram is computed by subtracting the squared amplitude of the reference and radiated field from the acquired hologram. By doing this, the two central terms in the Fig. 2 are removed. As a consequence, the two remaining spectra, which corresponds to the radiated field and its complex conjugate, can get closer. In particular, the optimal value of the wavenumber of the equivalent plane-wave is now given by $k_x^{pw} = k_0$. Thus, the total bandwidth of the modified hologram is $2W = 2k_0$ yielding a minimum sampling step size of $\Delta x = \lambda/4$. Thus, the optimal phase increment is given by $\Delta\phi = 90°$ in case of considering the modified hologram.

Although the use of the modified hologram requires a lower sampling rate, it involves a double acquisition in order to compute the hologram and the amplitude of the radiated field. Thus, the acquisition environment must be stable along both acquisitions. On the other hand, the direct processing of the received hologram involves a single acquisition (with the double of points).

In this work, a trade-off between both possibilities has been applied. Thus, the acquired hologram is directly processed without computing the modified hologram so that the need of two consecutive acquisitions is avoided. However, the phase shift and sampling rate are fixed to $\Delta\phi = 90^\circ$ and $\Delta x = \lambda/8$. The reason for this choice is that the equivalent wavenumber $k_x^{pw} = 2k_0$ and the maximum acquired spectral frequency $\frac{\pi}{\Delta x} = 4k_0$ enables centering the spectra. Although this set of parameter values results in certain overlapping with the central terms, it will be shown in the results section that it has not a significant impact in the final solution. The reason is that, although the spectrum of the central term corresponding to the square amplitude has a bandwidth of $2k_0$, this spectrum decays very quickly in practice as it comes from the convolution between two spectra which are expected to vanish at k_0. Thus, a certain degree of overlapping can be tolerated without significantly degrading the performance of the technique.

III. Antenna diagnostics examples

In this section, simulations and measurements are carried out to validate the performance of the proposed technique for antenna diagnostics purposes. In the case of simulation-based example (subsection III-A), the antenna is simulated and the radiated field is acquired in the modified points. After that, a constant signal is added and the squared amplitude of the resulting signal is processed to retrieve the amplitude and phase of E_{AUT}.

Concerning the measurement example (subsection III-B), the combined signal is acquired with a vector network analyzer (VNA) and, after that, the squared amplitude is postprocessed. Thus, no phase information is used at any point.

A. Simulated patch array

In this example, a two dimensional array of rectangular patches, as shown in Fig. 3, is considered. The elements are placed on a substrate with electrical permittivity $\epsilon_r = 2.2$ and thickness $h = 2.87\,\text{mm}$ with uniform amplitude and phase feeding. The working frequency is $3\,\text{GHz}$. The method of moments is used to simulate this array. Green's function for multilayered planar substrates is used and, consequently, the substrate and ground plane are considered as infinite.

The acquisition surface, which is two meters over the patch array plane, is a square plane of edge equals to $5\,\text{m}$. The phase shifting is applied along the x-axis with a phase increment $\Delta\phi = 90^\circ$. The sampling steps for each direction are $\Delta x = \lambda/8$ and $\Delta y = \lambda/2$.

In order to check the accuracy of the method, the following error is computed:

$$e[\%] = \frac{\|\mathbf{E}_{ret} - \mathbf{E}_{ref}\|_2}{\|\mathbf{E}_{ref}\|_2} \cdot 100, \tag{6}$$

wherein $\mathbf{E}_{ret}$ is a vector containing the samples of the field radiated by the antenna retrieved at the acquisition points whereas $\mathbf{E}_{ref}$ is a vector containing the samples of the field directly computed by means of the method of moment. In this analysis, only the main component of the field is considered (y-component).

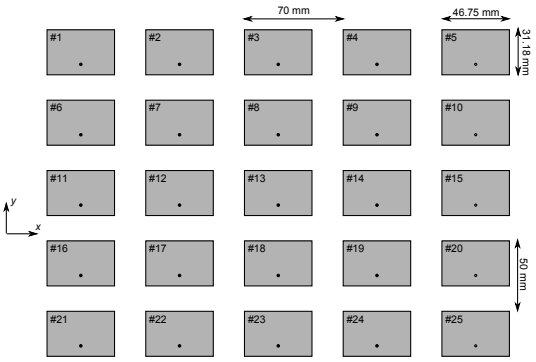

Figure 3. Array of rectangular patches. Dots near the lower edge of each patch represent the feeding point.

A failure in the element #12 is considered next. This failure is modeled by zero feeding of this element. The total error in this case is 2.15% and, therefore, accurate results can be expected for diagnostics purposes. After backpropagating the retrieved field to the antenna aperture [14], the fault element can be clearly identified as shown in Fig. 4a. The robustness of the algorithm in case of noisy environments is also considered. Thus, Fig. 4b corresponds to the field backpropagated to the aperture in the case of a signal to noise ratio equal $10\,\text{dB}$. Despite of the strong noise, the backpropagated field is still accurate enough to identify the fault element. Thus, the effect of the noise is not expected to spoil the performance of the phase retrieval algorithm for diagnostics purposes.

B. Obstacle in front of a horn antenna

A horn antenna with an obstacle between the antenna and the acquisition surface is considered in this example. The working frequency is fixed at $30\,\text{GHz}$.

The dimensions of the acquisition surface, which is placed at $20\,\text{cm}$ from the aperture plane, are $40\,\text{cm} \times 34\,\text{cm}$. An 'U'-shaped obstacle is placed at $5\,\text{cm}$ from the horn in order to check if it can be detected. Foam is used to hold the obstacle over the antenna so minor perturbations are expected due to the supporting structure.

After retrieving the amplitude and phase, the field was back-propagated to multiple planes [14] in order to find the position and shape of the obstacle. Fig. 6 shows the backpropagated field in the plane at $15\,\text{cm}$ wherein the U-shaped object can be clearly detected.

IV. Conclusions

An indirect holography scheme for antenna diagnostics applications has been presented. In the implemented setup, the reference wave has been synthesized by means of a mechanical displacement of the probe. Thus, plane waves beyond the visible spectrum can be synthesized without requiring a phase shifter.

The optimal phase shifting and sampling rates have also been discussed on theoretical basis. A trade-off solution has

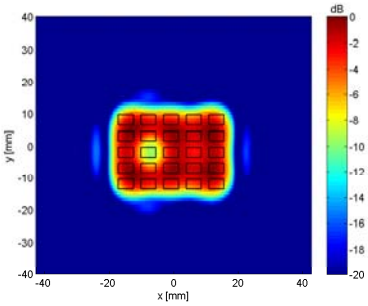

(a) SNR=∞

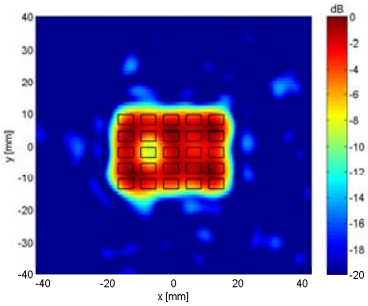

(b) SNR=10 dB

Figure 4. Normalized retrieved field distribution in the aperture of the patch array antenna.

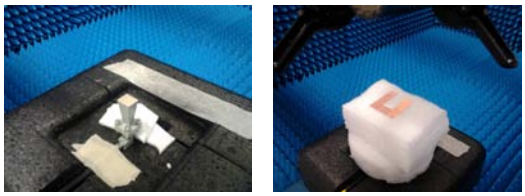

(a) (b)

Figure 5. Measurement setup for the horn antenna with obstacle: a) antenna without any obstacle; b) antenna with a 'U' obstacle.

been proposed by considering a non-significant overlapping between some spectral terms.

Although the mechanical phase shifting is based on a far-field approximation, numerical simulations have shown that the final error is low enough to enable successful application in antenna diagnostics methods. The presented results from amplitude-only measurements confirm the validity of the proposed scheme for antenna diagnostics.

REFERENCES

[1] Y. Álvarez, C. Cappellin, F. Las-Heras, and O. Breinbjerg, "On the comparsion of the spherical wave expansion-to-plane wave expansion and the sources reconstruction method for antenna diagnostics," *Progress In Electromagnetics Research*, vol. 87, pp. 245–262, 2008.

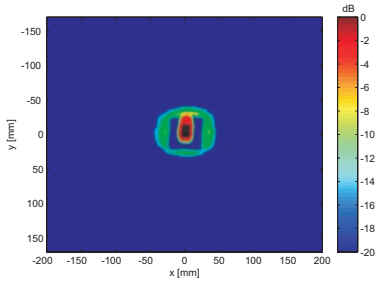

Figure 6. Field backpropagated for horn antenna with a 'U'-shaped obstacle.

[2] Y. Alvarez, F. Las-Heras, and M. Pino, "Reconstruction of equivalent currents distribution over arbitrary three-dimensional surfaces based on integral equation algorithms," *IEEE Trans. Antennas Propagat.*, vol. 55, no. 12, pp. 3460 –3468, Dec. 2007.

[3] J. Araque and G. Vecchi, "Field and source equivalence in source reconstruction on 3D surfaces," *Progress In Electromagnetics Research*, vol. 103, pp. 67–100, 2010.

[4] G. Hislop, L. Li, and A. Hellicar, "Phase retrieval for millimeter- and submillimeter-wave imaging," *IEEE Trans. Antennas Propagat.*, vol. 57, no. 1, pp. 286–289, Jan. 2009.

[5] G. Junkin, T. Huang, and J. Bennett, "Holographic testing of terahertz antennas," *IEEE Trans. Antennas Propagat.*, vol. 48, no. 3, pp. 409 –417, Mar. 2000.

[6] Y. Alvarez, F. Las-Heras, and M. R. Pino, "The sources reconstruction method for amplitude-only measurements," *IEEE Trans. Antennas Propagat.*, vol. 58, no. 8, pp. 2776–2781, Aug. 2010.

[7] P. Li and L. Jiang, "An iterative source reconstruction method exploiting phaseless electric field data," *Progress In Electromagnetics Research*, vol. 134, pp. 419–435, 2013.

[8] E. N. Leith and J. Upatnieks, "Reconstructed wavefronts and communication theory," *J. Opt. Soc. Amer.*, vol. 52, pp. 1123–1128, 1962.

[9] J. Laviada and F. Las-Heras, "Phaseless antenna measurement on non-redundant sample points via Leith-Upatnieks holography," *IEEE Trans. Antennas Propagat.*, vol. 61, no. 8, pp. 4036–4044, Aug. 2013.

[10] J. Laviada, Y. Álvarez López, C. García-González, A. Arboleya, and F. Las-Heras, "A modified phaseless inverse scattering setup based on indirect holography implemented at submillimeter-wave band," *IEEE Trans. Antennas Propagat.*, vol. 61, no. 9, pp. 4876–4881, Sep. 2013.

[11] V. Schejbal, V. Kovarik, and D. Cermak, "Synthesized-reference-wave holography for determining antenna radiation characteristics," *IEEE Antennas Propagat. Mag.*, vol. 50, no. 5, pp. 71 – 83, Oct. 2008.

[12] D. Smith, M. Leach, M. Elsdon, and S. J. Foti, "Indirect holographic techniques for determining antenna radiation characteristics and imaging aperture fields," *IEEE Antennas Propagat. Mag.*, vol. 49, no. 1, pp. 54 –67, Feb. 2007.

[13] A. Yaghjian, "An overview of near-field antenna measurements," *IEEE Trans. Antennas Propagat.*, vol. 56, no. 1, pp. 30–45, Jan. 1986.

[14] J. Hanfling, G. Borgiotti, and L. Kaplan, "The backward transform of the near field for reconstruction of aperture fields," in *Antennas and Propagation Society International Symposium, 1979*, vol. 17, 1979, pp. 764–767.

Publication II

A. Arboleya, J. Ala-Laurinaho, J. Laviada, Y. Álvarez, F. Las-Heras and A.V. Räisänen **"Millimeter-wave phaseless antenna measurement based on a modified off-axis holography setup,"** *Journal of Infrared, Millimeter, and Terahertz Waves*, vol. 37, no. 2, pp. 160–174, February 2016.

II

J Infrared Milli Terahz Waves
DOI 10.1007/s10762-015-0215-z

Millimeter-Wave Phaseless Antenna Measurement Based on a Modified Off-Axis Holography Setup

Ana Arboleya[1] · Juha Ala-Laurinaho[2] · Jaime Laviada[1] · Yuri Álvarez[1] · Fernando Las-Heras[1] · Antti V. Räisänen[2]

Received: 28 August 2015 / Accepted: 29 September 2015

Abstract A novel scheme for planar near-field phaseless antenna measurement based on off-axis holography is presented. Separation of the image terms of the hologram is artificially increased by multiplexing the measurements of two sub-sampled holograms generated with two 180° phase-shifted reference waves. Combination of both sub-sampled holograms produces replicas of the image terms at half a period distance of the originals in the spectral domain, while the amplitude of the original image terms is highly reduced, easing the filtering process of the desired replica. The higher separation of the image terms reduces overlapping making the method suitable also for the characterization of medium and low gain antennas in the near-field. As the separation is artificially increased, the reference antenna can be placed close to the antenna under test allowing to reduce the scan distance and the sensitivity to scan axis errors. Nevertheless, spatial multiplexing requires the retrieved data to be spatially low-pass filtered to remove the effect of the aliasing. Mirror reflection is used for illuminating the acquisition plane with the reference wave, being the phase shift achieved by means of a mechanical displacement of the mirror. The effect of the location of the reference antenna on the position and shape of the image terms and their replicas has been studied through numerical simulations for a setup in the W-band. Experimental validation of the method is presented for the characterization of three different antennas at 94 GHz.

✉ Ana Arboleya
aarboleya@tsc.uniovi.es

[1] Departamento de Ingeniería Eléctrica, Universidad de Oviedo, 33203 Gijón, Spain

[2] Department of Radio Science and Engineering and MilliLab, Aalto University, 00076 Espoo, Finland

Published online: 21 October 2015

Keywords Phaseless · Antenna measurement · Diagnostics · Near-field · Off-axis · Holography · Millimeter-wave

II

1 Introduction

Characterization of antennas in near-field (NF) involves the acquisition of amplitude and phase information so the far-field (FF) radiation pattern or the aperture fields for antenna diagnostics can be obtained after post-processing the complex acquired data. Nevertheless, phase acquisition, fundamentally at mm- and submm-wave bands, is a very challenging and expensive process due to the need of keeping a stable phase reference which demands not only a very stable source but also steady temperature conditions and high mechanical accuracy [1–4].

The aforementioned difficulties of the phase measurement process have motivated the development of the so-called phaseless techniques, the interferometric technique being one of the most employed methods to retrieve the phase of the antennas. This technique, based on recording the intensity pattern formed by the field of the antenna under test (AUT) and the field of a reference antenna, which is previously known in amplitude and phase, as introduced by Gabor in the optics field [5], and then modified to use an off-axis reference by Leith and Upatnieks [6], is often refered to as off-axis indirect holography. Holography was first used for antenna metrology by Bennett [7] and Anderson [8].

The off-axis technique relies on the filtering of one of the terms of the hologram in the *k*-space, whose position depends on the angle formed by the reference antenna and the acquisition plane [4]. In conventional setups (see Fig. 1a), this reference antenna has to be placed far from the AUT in order to illuminate the acquisition plane with a plane wave. This leads to bigger dimensions of the setup (scan plane distance and size) and higher sensitivity to scan axis errors [4, 9]. Another option to create the plane wave reference is to use a shaped, e.g., parabolic mirror. This requires accurate and expensive machining. Also, the reflector could then be used directly as a collimator in a compact antenna test range setup [10]. Some numerical experiments have demonstrated the advantages of using spherical wave-fronts as reference signals for the characterization of highly directive antennas [4].

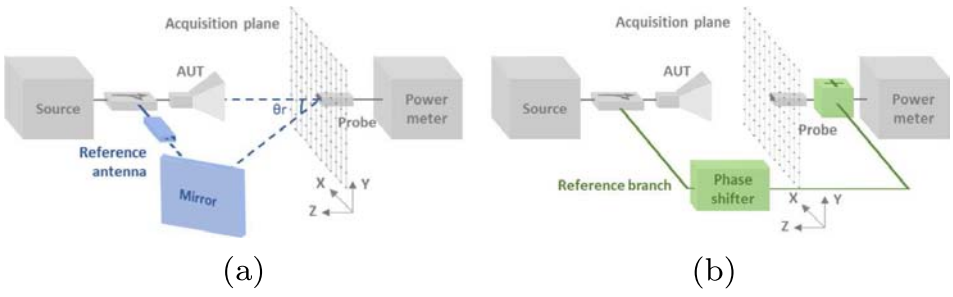

Fig. 1 Schemes for the holography setups. **a** Conventional setup with mirror reflection of the reference antenna and **b** synthesized reference antenna setup

Further development of the conventional off-axis setup has been done to achieve better results in the filtering process. The use of the so called *modified holograms* without the auto-correlation terms allows for a reduction of the separation between the AUT and the reference antenna, and consequently, for a reduction of the sampling rate. This enables to lower the scan distance and the sensitivity to error positioning of the probe antenna [4]. However, an extra measurement for the independent characterization of the intensity of the AUT is needed in order to subtract its effect from the complete hologram.

Substitution of the radiated reference wave by a synthesized one allows to control the phase shifts and, therefore, the separation of the cross-correlation terms, although a denser sampling is needed in order to extend the frequency spectrum domain [11, 12]. However, the cited works have been validated in the X-band and they are not likely to be used at higher frequency bands wherein the connection between the directional coupler and the moving probe (see Fig. 1b) should be made with waveguide components.

It is possible to avoid the use of phase shifters by implementing three-dimensional scans to mechanically introduce the phase shifts [13], although the majority of planar measurement ranges cannot perform this type of acquisition, as they are limited to plane acquisitions.

In this contribution, a novel setup in which the separation between the cross-correlation terms of the hologram is artificially increased by combining two sub-sampled holograms with a phase difference of 180°, is proposed. The desired phase difference is produced by a small movement of the flat reference wave mirror shown in Fig. 1a. Hence, although the sampling rate has to be slightly increased due to the wider spatial bandwidth of the acquired interferometric signal in the k-space, it is possible to work with the complete hologram. This avoids the need of an additional measurement for AUT characterization to subtract its auto-correlation term, and makes possible to place the reference antenna close to the AUT as in the *modified holograms* setups. Diminishing the size of the setups overcomes the problems associated to the use of large acquisition planes [4].

This bigger separation of the image terms of the hologram eases the filtering process allowing to reduce the error of the phase retrieval with respect to the conventional off-axis holography method. Thanks to this, it is possible to use the proposed method for the characterization of medium and low gain antennas, with wider spectra, although, as it will be shown in Section 4.2, the results are also improved for the case of measuring high gain antennas.

As a counterpart, due to the sub-sampling, a low-pass spatial filtering is needed in order to correctly retrieve the signal of the AUT, affected by aliasing, as well as a correction of the level of the retrieved amplitude.

2 Proposed Method

In off-axis holography, a hologram, $H(\vec{r})$, is obtained after squaring the sum of an intensity pattern created by the field components of the AUT, $E_{aut}(\vec{r})$, and the reference antenna, $E_r(\vec{r})$, acquired by the probe. As the amplitude of the reference antenna

is previously known, its effect is removed directly from the hologram, given by the following expression

$$\begin{aligned} H(\vec{r}) &= |E_{aut}(\vec{r}) + E_r(\vec{r})|^2 - |E_r(\vec{r})|^2 \\ &= |E_{aut}(\vec{r})|^2 + E_{aut}(\vec{r})E_r^*(\vec{r}) + E_{aut}^*(\vec{r})E_r(\vec{r}) \end{aligned} \tag{1}$$

where $\vec{r}$ defines the position of the probe and $()^*$ indicates complex conjugate.

After *Fourier* transforming to the k-space, the hologram, $h(\vec{k})$, is given by

$$h(\vec{k}) = \widetilde{H(\vec{r})} = \widetilde{|E_{aut}(\vec{r})|^2} + \widetilde{E_{aut}(\vec{r})} \otimes \widetilde{E_r^*(\vec{r})} + \widetilde{E_{aut}^*(\vec{r})} \otimes \widetilde{E_r(\vec{r})} \tag{2}$$

being $\widetilde{()}$ the *Fourier Transform* (FT) and $\otimes$ the convolution operator. The first term is called the auto-correlation term and the following two, containing information about the amplitude and phase of the AUT, are known as cross-correlation or image terms.

The separation of the cross-correlation terms in the k-space can be controlled with the off-axis angle of the reference antenna, θ_r (see Fig. 1a). In particular, the center of the cross-correlation terms is located at

$$k_{r,x} = \pm\Delta\phi/\Delta x = \pm k_0 \sin\theta_r \tag{3}$$

considering the reference antenna is placed with the offset in the x-axis [14]. In the previous formulation, $\Delta\phi$ is the phase difference between consecutive samples of the reference signal in the acquisition plane, Δx is the sampling rate, and k_0 is the wavenumber.

If the separation of the terms is enough to avoid overlapping, the image term $(\widetilde{E_{aut}(\vec{r})} \otimes \widetilde{E_r^*(\vec{r})})$ can be filtered and the complex magnitude of the AUT can be retrieved back in the spatial domain, after dividing by the expression of the conjugate of the reference antenna.

According to [2], the spatial bandwidth for the radiated field for a planar acquisition can be considered as $W = k_0$. Hence, as it is shown in Fig. 2a, to avoid overlapping with a conventional setup, $k_r \geq 3k_0/2$.

Nevertheless, for a radiated reference wave, the maximum offset angle is restricted to 90° and, therefore, $k_{r,max} = k_0 = 2\pi/\lambda$ [15]. This separation may not be enough to avoid the overlap between the aforementioned spectral components in (2) (see Fig. 2a for a graphical description), specially when working in the NF with medium and low gain antennas which have wider spectra. Besides, to illuminate the acquisition plane with a plane wave, as it is usually done in conventional setups, the reference

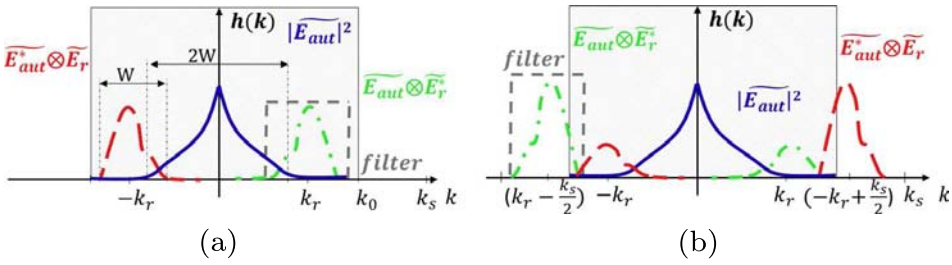

Fig. 2 Spectrum of the hologram. **a** Conventional setup and **b** proposed setup with the replicas and the original terms. The *central shaded box* indicates the visible part of the spectrum

antenna has to be placed far away from the AUT, being also necessary to increase the separation and the size of the acquisition plane, which makes the setup more sensitive to scan axis errors [4].

The use of synthesized reference waves removes the offset angle limitation and makes possible to displace the cross-correlation terms to the non-visible part of the k-space ($k > \pm k_0$), providing a denser sampling rate is used to extend its limits, defined by $k_s = \pm\pi/\Delta x$ [12, 16].

The proposed setup is an intermediate solution to artificially increase the separation of the cross-correlation terms while using a radiated reference wave. The method relies on the spatial multiplexing of two sub-sampled holograms. The first hologram is recorded from the initial position of the the mirror and its samples are stored in the even columns of the final hologram. The second hologram, stored in the odd columns, is recorded after introducing a mechanical displacement of $\lambda/2$ in the mirror position (see Fig. 3b) which produces a phase shift of 180° in the phase of the reference wave in the acquisition plane, while leaving the amplitude practically unchanged. After that, a hologram is composed by interleaving the columns, i.e., the samples acquired along the y-axis, of the two measured holograms (see Fig. 3a).

When working with the two sub-sampled reference signals, two *replicas* at $k_s/2$ of the original cross-correlation terms appear, so that the hologram has five terms, the auto correlation term, the two image terms, and the two *replicas* of the image terms as schematically shown in Fig. 2b.

If the reference signal is a plane wave, due to the phase-shift between the signals, the original cross-correlation terms are canceled while the amplitude of the *replicas* is reinforced (see Appendix) allowing to easily filtering one of that *replicas*. Nevertheless, for spherical wave fronts, as the phase difference between consecutive samples of the signal is not constant in the acquisition plane, the original cross-correlation terms are not completely canceled, being this the main drawback of using spherical wave fronts as reference signal. This will be analyzed in the *Numerical simulations* section.

Nonetheless, the use of spherical reference wave fronts as reference signals has many advantages such as the reduction of the scan plane size and distance to the AUT, and the reduction of the distance between the AUT and the reference antenna. This reduction in size of the setup, as stated in [4], helps to reduce the scan errors and the sensibility of the system.

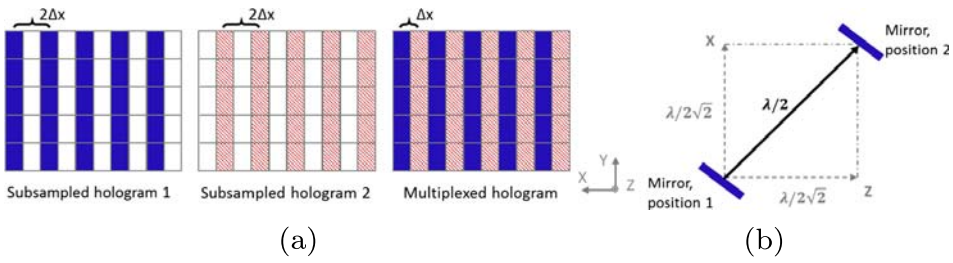

Fig. 3 Hologram recording method. **a** Hologram composition by multiplexing data from the two subsampled holograms and **b** mirror displacement for the 180° phase shift in the second hologram samples

Other advantages of using a spherical reference wave front are the possibility of controlling the scan plane edge illumination, being able to lower the reference on-axis sidelobes, and the reduction of the dynamic range needed in the k-space as the cross-correlation terms no longer have the shape of the AUT spectrum but a narrower one [4].

However, as the filtered term corresponds to the *replica* of the image term, the retrieved signal back in the spatial domain is contaminated with high-frequency noise. In order to correctly retrieve the AUT signal, a low-pass filtering process is necessary after the phase retrieval process.

Thanks to the aforementioned advantages, it is possible to reduce the error of the phase-retrieval with respect to the conventional setup as it will be shown in the numerical and experimental validation sections.

3 Numerical Simulations

In order to study the influence of the type of the reference wave front in the cancellation of the original image terms of the hologram and the shape and position of its *replicas*, the setup is first simulated, using MATLAB, for three different reference fields.

The conventional setup is simulated first by keeping the mirror fixed for the whole acquisition of the hologram with a sampling rate of $\lambda/6$, while the proposed method is implemented by multiplexing two sub-sampled holograms corresponding to the two different positions of the mirror, each of them with a sampling rate of $\lambda/3$ to compose a final hologram also with a sampling rate of $\lambda/6$. For both cases, the extension of the k-space is $k_s = \pm\pi/\Delta x = \pm 3k_0$. The method is also studied for the case of multiplexing two plane waves instead of the spherical waves with a phase shift of 180° and the same amplitude than the spherical ones, to verify the correct cancellation of the aforementioned terms of the spectra.

The AUT is a vertically polarized rectangular aperture of 2.5 λ by 2 λ at 94 GHz. A WR10 pyramidal horn, placed at 100 λ from the AUT in the x-axis and 20 λ in the z-axis, is used as a reference antenna. The acquisition plane is 160 λ by 160 λ placed at a distance of $z_0 = 50\lambda$ of the AUT aperture. And the mirror is placed at 20 λ from the reference antenna with a 45° tilt in the x-axis.

The phase difference between consecutive samples along the x-axis is shown in Fig. 4a for the first position of the mirror. This phase difference is not shown for the second position of the mirror since it is identical. In order to simulate the plane-waves, they are given an angle so that the phase difference between consecutive samples is 45°, which is the mean phase difference of the previously described spherical waves.

With the obtained phase and according to Eq. 3, the cross-correlation terms are centered in $k_r = \pm 0.75k_0$, and the desired *replicas* placed at a distance of $3k_0$ of the originals, that is at $k_{r_{replicas}} = \pm 0.75k_0 \mp 3k_0 = \mp 2.25k_0$.

Figure 4b shows the spectrum of the reference antenna for the three studied cases. The spectrum of the reference wave for the conventional setup (dashed line) is formed of just one term centered in $0.75k_0$. The image terms of the hologram are in the same

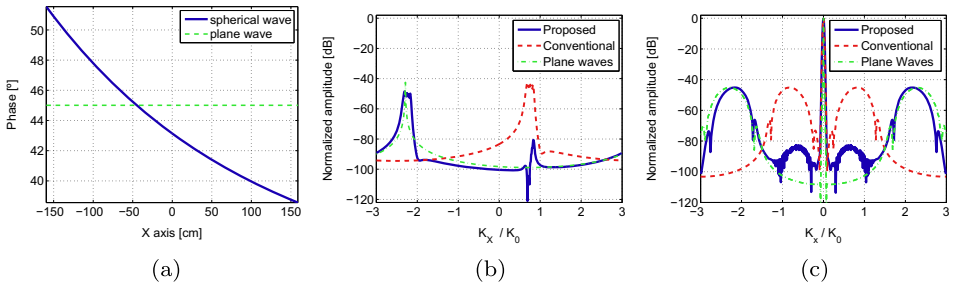

Fig. 4 Simulation results. **a** Phase slope of the reference waves, **b** x cut (y=0) of spectrum of the reference signal for the case of using spherical waves for the proposed and conventional setups and for the case of using plane waves, and **c** spectrum of the holograms for the different reference waves and setups

position (Fig. 4c) and depending on the spectral width of the AUT, might overlap with the auto correlation term introducing error in the filtering process.

The dotted-dashed line in Fig. 4b shows the spectrum of the reference wave in case of having two ideal plane waves with a 180° phase shift multiplexed. For this case, as it is demonstrated on the Appendix, the original image terms are canceled due to the phase shift, while the amplitude of the *replicas*, at $\mp 2.25k_0$, is reinforced. This would be the ideal situation, as the separation of the image terms of the hologram with the auto correlation term is maximized (see Fig. 4c).

Finally for the proposed setup (solid line in Fig. 4b), the original term at $0.75k_0$ is not completely canceled, whereas the *replica* appears in $-2.25k_0$ as expected. It is important to note that the spectral power density of the signal is distributed between the *replica* and the original term, i.e., the *replica* has lower amplitude than the image term for the conventional setup and this will affect the amplitude retrieval of the AUT and will have to be corrected, as it will be shown in the next section. The effect of the partial cancellation of the original terms can be seen in the hologram, Fig. 4c.

Although the original image terms are not completely canceled in the proposed setup, Fig. 4c shows that the overlapping between the *replicas* and the original image terms is less than the overlapping of the image terms and the auto correlation term in the conventional setup. This will be more clearly seen in the *measurement results* section wherein the noise and the non-ideal acquisition environment will deteriorate the quality of the holograms.

Besides, the use of spherical waves has many other advantages that have been previously mentioned such as the reduction of the size of the setup, lowering the scan errors and the sensitivity of the system, and the possibility of narrowing the spectrum of the image terms of the hologram according to the shape of the spectrum of the reference antenna [4], as it can be seen in Fig. 4c if the width of the *replicas* of the proposed setup is compared to the one obtained when considering plane waves.

4 Experimental Validation

In order to validate the proposed method, a measurement setup for phaseless antenna characterization in the W band has been implemented.

The measurements have been made in a planar measurement range. Three different antennas with different directivity have been studied at 94 GHz: A 64 mm circular lens antenna of 25 dB gain, feeded with a 10 mm length open ended waveguide (OEWG) antenna, a pyramidal horn antenna of 20 dB gain, and an OEWG antenna of 6 dB gain.

The reference antenna, another pyramidal horn antenna, is placed at 120 mm of the feeding point of the AUT and its radiation is directed towards the acquisition plane, at 125 mm of the aperture of the AUT by means of mirror reflection.

The element used as a mirror is a smoothened metallic plate of 290 mm by 221 mm with a 15° tilt in the x-axis, whose edges are surrounded by electromagnetic absorber. The details of the setup for the three different antennas are shown in Fig. 5.

4.1 Amplitude Correction

Due to the fact that only a fraction of the spectral density of the hologram is filtered during the phase retrieval, a small correction in the retrieved amplitude of the AUT also needs to be made. The power spectral density of the reference signal is distributed between the *replica* and the not completely canceled image term (Fig. 3b). This way, when filtering only the *replica*, not all the power is taken into account and the signal transformed back to the spatial domain has lower amplitude than the original. Therefore, prior to the hologram calculation, it is necessary to study the spectrum of the reference antenna independently, in order to obtain the correction factor to apply to the retrieved amplitude of the AUT.

To do that, the spectrum of the main component of the reference antenna, $E_r(\vec{r})$, which is characterized in amplitude and phase, is obtained as

$$e_r(\vec{k}) = \widetilde{E_r}(\vec{r}) \tag{4}$$

The part corresponding to the *replica* is filtered with the same window that will be used in the phase retrieval process, a rectangular window $\Pi(k_1, k_2)$ defined from

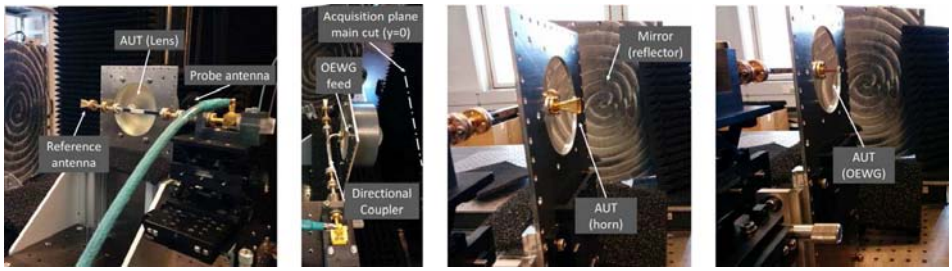

Fig. 5 Measurement setup for the setup validation at 94 GHz before placing the electromagnetic absorber. **a** *Rear* view of the setup for the lens antenna, **b** *top* view of the setup for the lens antenna, **c** *front* view of the setup for the horn antenna, and **d** *front* view of the setup for the OEWG antenna

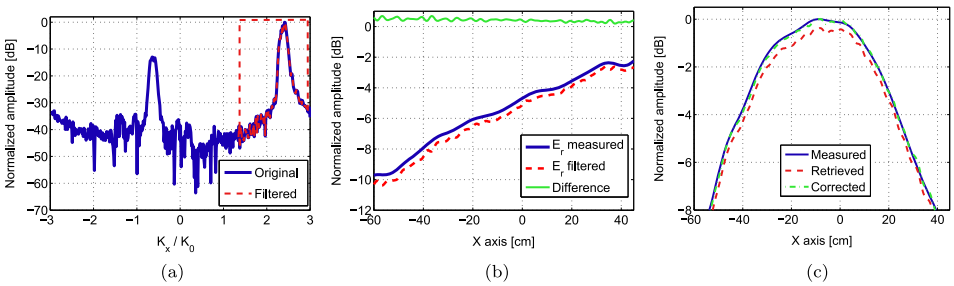

Fig. 6 Analysis of the horn reference antenna for the amplitude correction of the retrieved signal. **a** Spectrum of the reference signal, **b** detail of the normalized amplitude of the measured reference antenna compared to its amplitude after filtering in the spectral domain, and **c** detail of the amplitude correction of the retrieved signal of the AUT for a horn antenna

k_1 to k_2, as shown in Fig. 6a for the horn antenna used as reference antenna in this measurement example.

$$e_{r_{filtered}}(\vec{k}) = e_r(\vec{k})\Pi(k_1, k_2) \tag{5}$$

Then the filtered signal is transformed back to the spatial domain by means of an inverse FT denoted by $\widetilde{(\cdot)}^{-1}$ as indicated in Eq. 6, and its amplitude is compared to the measured amplitude, obtaining the correction factor, CF, defined in Eq. 7.

$$E_{r_{filtered}} = \widetilde{(e_{r_{filtered}})}^{-1} \tag{6}$$

$$CF[dB] = E_r(\vec{r})[dB] - E_{r_{filtered}}(\vec{r})[dB] \tag{7}$$

It is important to note that the correction factor is only dependent on the reference antenna, for this case the mean of CF is 0.38 dB as it is shown in Fig. 6b. The correction is shown for the case of applying the correction factor to the horn antenna as an AUT in Fig. 6c.

4.2 Measurement Results

Both phaseless setups, the conventional and the proposed one, have been implemented in order to compare their performance for the three different types of antennas. A direct acquisition of amplitude and phase has also been made with the

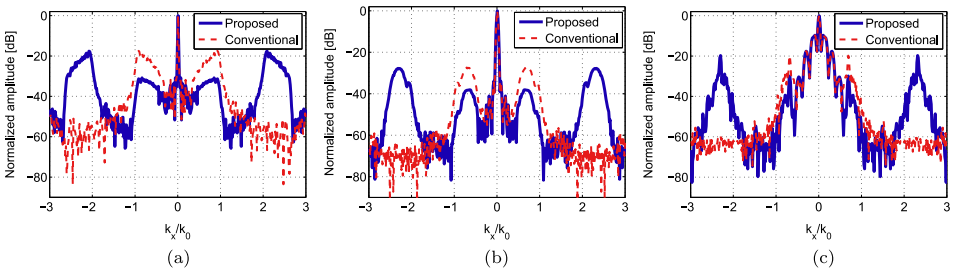

Fig. 7 Spectrum of the holograms for the proposed and conventional setups. **a** OEWG antenna, **b** horn antenna, and **c** lens antenna

purpose of using it as reference and quantify the error of the phase retrieval methods (see Eq. 8). All the results are shown for an x-cut of the AUT ($y = 0$), which is horizontally polarized.

First step of the phase retrieval algorithm is the calculation of the spectrum of the hologram as defined in Eq. 2, to filter the desired image term (or *replica*). The hologram spectra are shown for both setups in Fig. 7. The filter extension for the conventional setups goes from $-2k_0$ to $-0.3k_0$ approximately, while the one used in the proposed setups goes from $-3k_0$ to $-k_0$.

It is clearly seen that the image terms are wider for less directive antennas, Fig. 7a, b, and in the case of the conventional setup, they overlap with the auto correlation term, introducing error in the filtering process, while for the proposed setup, the position of the *replica* and the amplitude reduction of the original image terms, ease the filtering process allowing to correctly retrieve the signal.

Directive antennas, despite having narrower image terms, have wider auto correlation terms, Fig. 7c, therefore, unless special care is given to leveling the AUT and

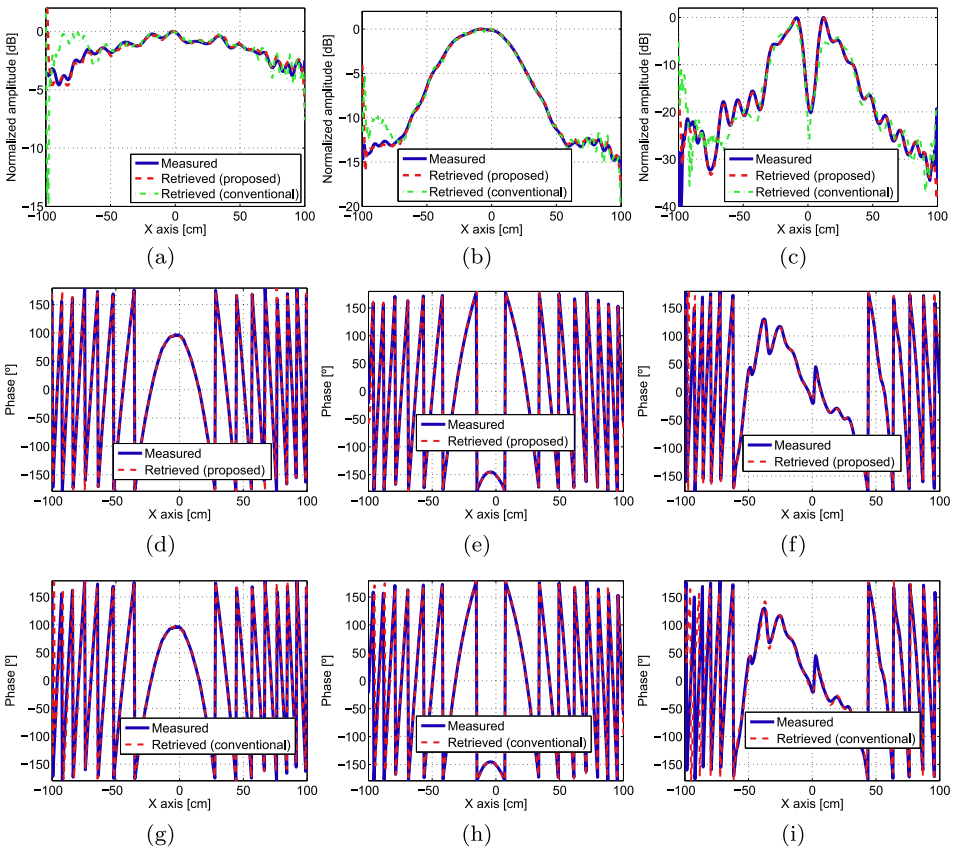

Fig. 8 Retrieved fields compared to the direct acquisition for the proposed and conventional setups. **a** Amplitude of the OEWG, **b** amplitude of the horn, **c** amplitude of the lens, **d** phase of the OEWG, proposed setup, **e** phase of the horn, proposed setup, **f** phase of the lens, proposed setup, **g** phase of the OEWG, conventional setup, **h** phase of the horn, conventional setup, and **i** phase of the lens, conventional setup

the reference antenna branches by adding attenuators or amplifiers, the overlapping of the terms of the hologram will be very high for the conventional setup. With the proposed setup, it is still possible to correctly filter the desired term without the need to resort to auxiliary components to level the branches.

Once the hologram has been filtered, the amplitude and phase of the AUT can be retrieved after transforming the filtered data back to the spatial domain and compensating for the effect of the reference signal. In case of the proposed setup, the amplitude correction method and a low pass filter to eliminate the ripple introduced by the aliasing have to be applied.

The retrieved amplitude for the conventional and proposed setups is compared to the direct measured amplitude for the three antennas in Fig. 8a–c. With the proposed setup, the error is lower on the edges of the acquisition plane due to the overlapping reduction of the spectral terms. The retrieved phase is also shown, compared to the directly measured one, in Fig. 8d–f for the proposed setup and in Fig. 8g–i for the conventional setup.

As the error of the retrieval process is reduced on the edges of the acquisition plane, another advantage of the proposed setup is that the valid angular margin of the NF-FF transformation, depending on the size of the acquisition plane, is also increased in case the data have to be transformed to FF.

To quantify the quality of the phase retrieval method, the following error metric is defined:

$$e[\%] = 100\frac{|E_{meas} - E_{ret}|}{|E_{meas}|} \tag{8}$$

where E_{meas} is the measured field (in amplitude and phase), and E_{ret} is the retrieved field with the off-axis holography method. The error is calculated for the three antennas in case of using both setups and depicted in Fig. 9 where the better performance of the proposed method is clearly observed for the whole acquisition plane, but mainly on the edges.

As the error of the phase retrieval seems to be higher in those areas corresponding to low amplitude levels of the AUT, a weighted mean error is defined as follows:

$$e_w[\%] = \frac{1}{N}\sum_{i=1}^{N} |e[\%](i)||E_{ret}(i)| \tag{9}$$

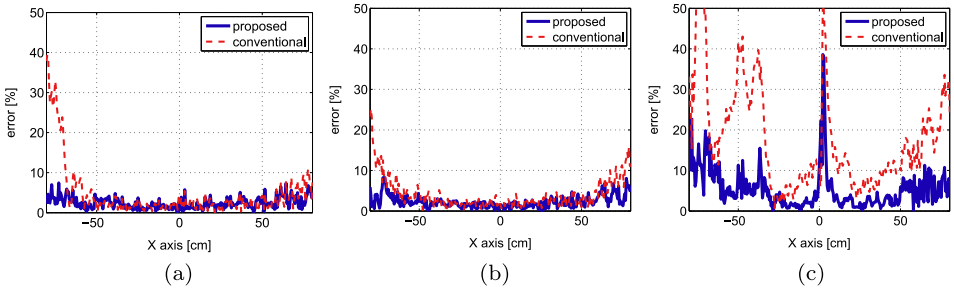

Fig. 9 Error of the phase retrieval process for the proposed and conventional setups. **a** OEWG antenna, **b** horn antenna, and **c** lens antenna

Table 1 Mean error of the phase retrieval technique for the conventional and the proposed methods for the three studied antennas

	Conventional setup		Proposed setup	
	Mean (%)	Weighted mean (%)	Mean (%)	Weighted mean (%)
OEWG	4.64	3.62	2.41	2.04
Horn	4.13	1.64	2.31	1.03
Lens	17.91	3.10	5.38	0.87

Both types of error are gathered in Table 1. The high error in the central part of the acquisition plane for the lens is due to the null in the amplitude and it is compensated with the use of the weighted mean error. As it is observed, the performance of the proposed setup is better for all the studied cases, regardless of the type and directivity of the antennas.

5 Conclusions

A novel setup based on off-axis holography is proposed. By means of multiplexing two subsampled holograms with a 180° phase shift, it is possible to achieve larger separation of the image terms while keeping the reference antenna close to the AUT.

For the validation of the setup, mirror reflection has been used to illuminate the acquisition plane with the reference wave, and the phase shift of the reference signal has been obtained by introducing a mechanical displacement of the mirror for the acquisition of the second subsampled hologram.

As the separation of the image terms, *replicas* in this case, is larger than for the conventional setup, the proposed method is suitable for low and medium directive antenna measurement. Furthermore, it has also been demonstrated that the proposed method also improves the results for directive antennas without the need of introducing extra components in the setup or leveling the amplitude of the reference and antenna branches, as it happens in conventional setups.

The increment in the separation of the image terms is achieved artificially without the need of physically increase the distance between the AUT and the reference antenna. This allows to reduce the size of the setup, regarding the size and distance of the acquisition plane, consequently decreasing the scan errors and the system sensitivity.

In case of maintaining the size of the acquisition plane, it has been demonstrated that the error of the retrieved signal is lowered on the edges of the acquisition plane with the proposed setup, allowing to increase the valid angular margin of the NF-FF transformation.

The use of spherical wave fronts as reference is also advantageous as the edge of the image terms can be controlled and the dynamic range of the hologram can be reduced as the image terms no longer have the shape of the AUT antenna [4].

Table 1 Mean error of the phase retrieval technique for the conventional and the proposed methods for the three studied antennas

	Conventional setup		Proposed setup	
	Mean (%)	Weighted mean (%)	Mean (%)	Weighted mean (%)
OEWG	4.64	3.62	2.41	2.04
Horn	4.13	1.64	2.31	1.03
Lens	17.91	3.10	5.38	0.87

Both types of error are gathered in Table 1. The high error in the central part of the acquisition plane for the lens is due to the null in the amplitude and it is compensated with the use of the weighted mean error. As it is observed, the performance of the proposed setup is better for all the studied cases, regardless of the type and directivity of the antennas.

5 Conclusions

A novel setup based on off-axis holography is proposed. By means of multiplexing two subsampled holograms with a 180° phase shift, it is possible to achieve larger separation of the image terms while keeping the reference antenna close to the AUT.

For the validation of the setup, mirror reflection has been used to illuminate the acquisition plane with the reference wave, and the phase shift of the reference signal has been obtained by introducing a mechanical displacement of the mirror for the acquisition of the second subsampled hologram.

As the separation of the image terms, *replicas* in this case, is larger than for the conventional setup, the proposed method is suitable for low and medium directive antenna measurement. Furthermore, it has also been demonstrated that the proposed method also improves the results for directive antennas without the need of introducing extra components in the setup or leveling the amplitude of the reference and antenna branches, as it happens in conventional setups.

The increment in the separation of the image terms is achieved artificially without the need of physically increase the distance between the AUT and the reference antenna. This allows to reduce the size of the setup, regarding the size and distance of the acquisition plane, consequently decreasing the scan errors and the system sensitivity.

In case of maintaining the size of the acquisition plane, it has been demonstrated that the error of the retrieved signal is lowered on the edges of the acquisition plane with the proposed setup, allowing to increase the valid angular margin of the NF-FF transformation.

The use of spherical wave fronts as reference is also advantageous as the edge of the image terms can be controlled and the dynamic range of the hologram can be reduced as the image terms no longer have the shape of the AUT antenna [4].

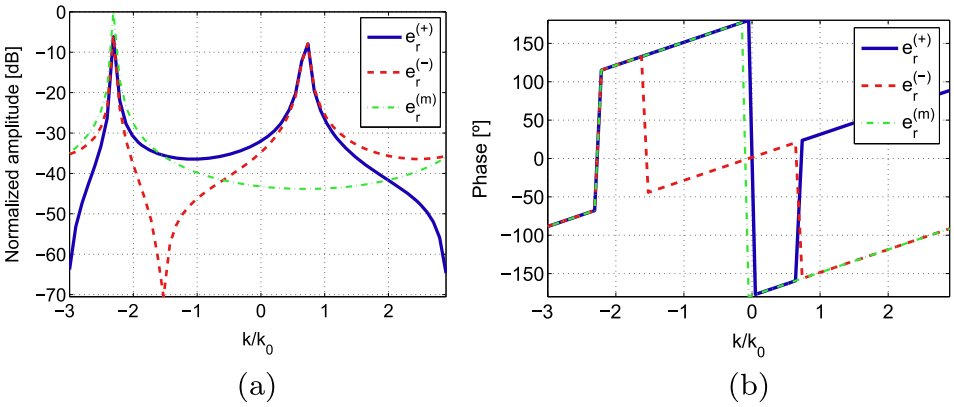

Fig. 10 Spectrum of the subsampled signals interspersed with zeros and the resulting multiplexed. **a** Normalized amplitude and **b** phase

alternating signs for each element and therefore, the expression in Eq. 13 can be rewritten as

$$E_r^{(m)}(n\Delta x) = \sum_n E_r(n\Delta x) e^{-j\frac{\pi}{\Delta x}x} \delta(x - n\Delta x) \tag{14}$$

and substituting Eq. 10 in Eq. 14 the reference signal becomes

$$E_r^{(m)}(n\Delta x) = A_r e^{-j\frac{\Delta\phi-\pi}{\Delta x}x} \sum_n \delta(x - n\Delta x) \tag{15}$$

and its FT corresponds to the following expression:

$$e_r^{(m)}(k) = \widetilde{E_r}(n\Delta x) = \frac{A_r}{k_s} \sum_n \delta(k - nk_s + \frac{\Delta\phi - \pi}{\Delta x}) \tag{16}$$

being k_s the period of the spatial frequency domain defined as $1/2\Delta x$.

The spectrum of the signals defined in Eqs. 11 and 12 should have *replicas* every $k_s/2$ due to the sub-sampling in the spatial domain, while in Eq. 16 there is only one term of the reference signal per period placed on $k = -(\Delta\phi - \pi)/\Delta x + nk_s$. It can be concluded that for a perfect plane wave, the original terms of the spectrum are canceled due to the phase shift while the *replicas* are reinforced.

An example for the case of considering the spectrum of two plane waves as defined in Eqs. 11 and 12 with phase difference between consecutive samples of 45° in the acquisition plane, and the signal obtained after multiplexing them, as defined in Eq. 16, is shown in Fig. 10. The sampling rate is $\lambda/6$ for the multiplexed signal, while the original plane waves are sampled at $\lambda/3$ and interspersed with zeros. The original terms are centered in $0.75k_0$ (see Eq. 3), while the *replica* appears at a distance of $k_s/2 = 3k_0$, that is, at $-2.25k_0$. It is clearly seen that, due to the phase shift of 180° between both plane waves around $0.75k_0$, the original terms are completely canceled as shown in Fig. 10b, and only the *replica* in $-2.25k_0$ remains.

References

1. A. Räisänen, J. Ala-Laurinaho, A. Karttunen, J. Mallat, A. Tamminen, M. Vaaja, 4th European Conference on Antennas and Propag. (EuCAP), pp. 1–3 (2010).
2. A. Yaghjian, IEEE Trans. Antennas Propag. **34**(1), 30 (1986).
3. T. Huang, J. Bennett, G. Junkin, 9th International Conf. on Antennas and Propag., (Conf. Publ. No. 407) pp. 41–44 vol.1 (1995).
4. G. Junkin, T. Huang, J. Bennett, IEEE Trans. on Antennas Propag. **48**(3), 409 (2000).
5. D. Gabor, Proc. of the Royal Soc. of London A: Math., Physical and Eng. Sci. **197**(1051), 454 (1949).
6. E.N. Leith, J. Upatnieks, Journal of the Optical Soc. of America **52**(10) 1123 (1962).
7. J. Bennett, A. Anderson, P. McInnes, A. Whitaker, IEEE Trans. on Antennas and Propag. **24**(3) (1976).
8. A. Anderson, Proc. of the Institution of Electrical Engineers, **124**(11), 946 (1977).
9. V. Schejbal, J. Pidanic, V. Kovarik, D. Cermak, IEEE Antennas Propag. Mag. **50**(6), 89 (2008).
10. A. Olver, Antennas and Propagation, 1991. ICAP 91. Seventh International Conference on (IEE) **1**, 99 (1991).
11. D. Smith, S. Skobelev, M. Leach, 8th International Symposium on Antennas, Propag. and EM Theory, 2008. ISAPE 2008 pp. 46–49 (2008).
12. V. Schejbal, V. Kovarik, D. Cermak, IEEE Antennas Propag. Mag. **50**(5), 71 (2008).
13. J. Laviada Martinez, A. Arboleya-Arboleya, Y. Álvarez Lopez, C. García-González, F. Las-Heras, IEEE Antennas Wireless Propag. Lett. **13**, 4 (2014).
14. D. Smith, M. Leach, M. Elsdon, S. Foti, IEEE Antennas and Propagation Magazine **49**, 54 (2007).
15. D. Smith, M. Leach, S. Dlay, W. Woo, 6th International Symposium on Antennas, Propag. and EM Theory pp. 373–376 (2003).
16. D. Smith, M. Leach, A. Sambell, IEEE Microw. and Wireless Compon. Lett. **13**(9), 379 (2003).

II

Publication III

III

A. Arboleya, J. Laviada, J. Ala-Laurinaho, Y. Álvarez, F. Las-Heras and A.V. Räisänen **"Phaseless characterization of broadband antennas,"** *IEEE Transactions on Antennas and Propagation,* vol. 64, no. 2, pp. 484-495, Feb. 2016.

III

This is the author's version of an article that has been published in this journal. Changes were made to this version by the publisher prior to publication.
The final version of record is available at http://dx.doi.org/10.1109/TAP.2015.2511789

Phaseless Characterization of Broadband Antennas

Ana Arboleya, Jaime Laviada, Juha Ala-Laurinaho, Yuri Álvarez, *Senior Member, IEEE,*
Fernando Las-Heras, *Senior Member, IEEE,* and Antti V. Räisänen, *Fellow, IEEE*

III

***Abstract*—A new efficient method for broadband antenna characterization from phaseless acquisitions in the frequency-domain is presented. The phase-retrieval technique is based on an extrapolation of the off-axis indirect holography. In common with the conventional approach, the power of the interferometric field of the antenna under test and a reference antenna, whose field is known in advance, as well as the power of the antenna under test alone, is measured at the desired frequencies. Nevertheless, the phase retrieval is accomplished independently at each spatial point by filtering in the time-domain rather than in the *k*-space. Thus, the dependency of the phase retrieval on the position accuracy is reduced and it can be accomplished simultaneously at all frequencies without resorting to iterative schemes. Moreover, it yields a less dense sampling and a phase retrieval algorithm not dependent on the geometry of the acquisition. The method is illustrated with a numerical example in the W-band as well as with two near-field measurement examples in the K_a- and W-bands.**

***Index Terms*—Antenna Measurement, Diagnostics, Phaseless, Broadband, Off-axis Holography, Leith-Upatnieks.**

I. Introduction

BROADBAND antennas have attracted great attention in the last years due to their applications in fields such as radar, multichannel frequency communications, Ultra Wide Band systems, etc.

Different measurement techniques have been developed in order to accurately characterize broadband antennas; these methods can be classified fundamentally into time-domain (TD) or frequency-domain (FD) methods [1].

There are different approaches to perform measurements in the TD, being pulse generator based systems the main one [2]–[4]. The dynamic range of these systems may not be sufficient, especially if network analyzers with TD modules are used to generate the signals. Thus, the distance between the Antenna Under Test (AUT) and the probe antenna has to be reduced [3]. Specific formulation for planar near-field (PNF) measurements in the TD has been developed [5], [6] alleviating this problem.

This work has been partially supported by the European Science Foundation under the RNP NEWFOCUS programme; by the Ministerio de Ciencia e Innovación of Spain /FEDER under project MIRIIEM-TEC2014-54005-P and TEC2014-55290-JIN; by the Gobierno del Principado de Asturias through the PCTI 2013-2017 GRUPIN14-114 and by predoctoral grant BP11-169; by grant LINE 525-002; and by the Academy of Finland through the DYNAMITE project.

A. Arboleya, J. Laviada, Y. Álvarez and F. Las Heras are with Departamento de Ingeniería Eléctrica of Universidad de Oviedo, Gijón E-33203 Spain (e-mail: aarboleya@tsc.uniovi.es, jlaviada@tsc.uniovi.es, yalopez@tsc.uniovi.es, flasheras@tsc.uniovi.es).

J. Ala-Laurinaho and A.V. Räisänen are with the Department of Radio Science and Engineering and MilliLab, Aalto University School of Electrical Engineering, Espoo FI-00076, Finland (e-mail: juha.ala-laurinaho@aalto.fi, antti.raisanen@aalto.fi).

Manuscript received Month day, year; revised Month day, year.

Main advantages of TD measurements are: a) the reduction of the reflections caused by mismatch and multipath by means of time gating techniques, b) simple equipment setup, and c) efficiency, as the antenna can be characterized for all the frequencies from one spatial acquisition [2].

On the other hand, these methods present some disadvantages such as: a) excessive acquisition time for complete three dimensional characterization of antennas, b) presence of ringing patterns in the TD for narrow-band antennas and c) reduction of the signal-to-noise (S/N) ratio and, consequently, the measurement accuracy, caused by the decay of the pulse spectrum at higher frequencies.

The previous methods in the TD require acquisitions of amplitude and phase data, at least for near-field (NF) measurements, to compute the far-field (FF) pattern. The instrumentation needed for those complex acquisitions is more expensive than the one required for phaseless acquisitions.

Additionally, phase acquisition can be complicated at mm- and submm-wave frequencies or in environments with poor thermal stability [7], [8]. Furthermore, errors due to cable flexing [9] or the accuracy of the positioners [10] become more relevant at higher frequencies.

FD techniques are the most employed for conventional antenna measurement [7]–[13]. Moreover, several methods based on wave expansions or equivalent currents for different acquisition geometries have been developed [14]–[16] for NF and FF acquisitions.

The main advantage of FD antenna characterization is the high accuracy and the number of the available techniques. On the other hand, broadband antenna analysis with conventional FD techniques could be very time-consuming for a high number of frequencies as data have to be independently acquired and processed for each of the analyzed frequencies.

Opposite to the TD techniques, several phaseless antenna characterization methods have been developed in the FD. These methods are divided into two main families: iterative and interferometric phase-retrieval methods.

Iterative methods are based on the acquisition of amplitude data in at least two independent surfaces [16], [17]. The phase of the field in each surface is retrieved after an iterative process. Those systems are very popular because they involve minor changes in the measurement system, nevertheless, main disadvantages are the stagnation problems and the high acquisition time, as two or more acquisition surfaces are needed.

Interferometric phase-retrieval techniques are based on the knowledge of a reference field (amplitude and phase) that is combined with the AUT field, creating an interference pattern that makes possible the retrieval of the phase of the AUT in the spatial frequency domain [18]–[23]. These interferometric techniques were originally introduced by Gabor in the optics

field [24] and adapted to work with an off-axis reference signal by Leith and Upatnieks [25], thus are usually referred to as Leith-Upatnieks or indirect off-axis holography.

Accuracy of these indirect holography methods can be limited by errors in the characterization of the reference source and the overlapping between the spectra of the reference antenna and the AUT. A complete analysis of error sources can be found in [7], nevertheless the use of synthesized reference sources and modified holograms allows for an error reduction and a better performance of the phase-retrieval algorithms [22].

Other authors have developed hybrid methods based on the use of a modified probe [26]. This probe is composed by two identical antennas placed at a fixed distance and interfering each other through a microstrip circuit. The phase retrieval is performed by means of a minimization procedure of the phase difference between both probes for all the frequencies. Although the hybrid method can be applied to wideband antenna characterization, it requires a fixed sampling rate determined by the separation of the probes. Besides, the use of non linear minimization may suffer from local minima stagnation [27]. Separation of the antennas must be larger than half a wavelength to avoid coupling, hence several acquisition subsets have to be combined. Thus, the quality of the positioning, which is a handicap at mm-wave band and above, is expected to have an impact in the final result.

The proposed technique is a FD method capable of phaseless broadband antenna characterization. As it is based on off-axis holography, it is necessary to perform two amplitude-only spatial acquisitions to obtain the hologram and the squared amplitude of the AUT, providing the reference antenna is previously characterized.

In conventional off-axis holography, the phase is retrieved simultaneously for all the points of the measurement grid, after finishing a complete spatial acquisition, by filtering one of the terms of the hologram in the *k*-space. After that, the operation is repeated for each frequency. In contrast, for the proposed method, the phase is retrieved in the following way: for each spatial point in the measurement grid, a frequency sweep is performed and the hologram is obtained in the FD. Then, the phase retrieval is done, simultaneously for all the frequencies at that specific grid point, after filtering the desired term of the hologram in the TD and removing the effect of the reference antenna (a detailed explanation is given in Section II).

Main advantages with respect to the conventional method are listed next: 1) The phase of the AUT is retrieved point-by-point hence the accuracy of the positioners is not as relevant as in conventional techniques, and the method can be applied to mm- and submm-wave bands antenna characterization with reduced uncertainties regarding the mechanical errors of the system [10], although accuracy is still necessary to perform the NF-FF transformation if no probe positioning correction algorithms are to be applied. 2) The technique is not dependent on the geometry of the acquisition either and therefore, non-redundant sampling techniques can be directly applied [20] to considerably reduce the number of acquisition points. 3) Overlapping of the terms of the spectrum of the hologram can be easily controlled by increasing the physical length of the reference antenna branch (see Fig. 1) and sampling

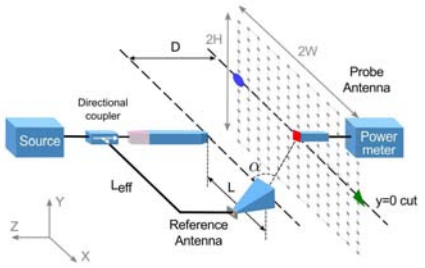

Fig. 1. Off-axis holography scheme for broadband antenna measurement. The holograms will be studied in the indicated points of the acquisition plane.

requirements are the same as the ones required in complex acquisitions with amplitude and phase, that is $\lambda/2$ [14]. In the conventional off-axis holography the sampling has to be at least $\lambda/4$ [21]–[23] or even denser and it might also be needed to resort to the use of phase shifters, which are challenging at high frequencies, for less directive antennas to reduce overlapping.

The herein presented technique is developed for a PNF acquisition although it can be directly applied to FF acquisitions and used in other geometries.

This paper is structured as follows. The proposed phase retrieval technique is explained in Section II. A simulation example of a broadband antenna in the W-band is shown in Section III. Two measurement setups in the W- and K_a-band are presented in Section IV. Finally, main conclusions are drawn.

II. Method

The basis of the method for the point-by-point phase retrieval in the TD is developed in Section II-A. After the method is explained, the setup limitations regarding the selection of the main parameters such as the frequency sampling or the position of the antennas and the measurement steps will be addressed in Section II-B and Section II-C respectively.

A. Off-axis holography extrapolation for broadband phaseless antenna characterization

For the proposed technique, the physical arrangement of the elements is identical to the one in conventional off-axis schemes (see Fig. 1). The setup would benefit from the use of a variable attenuator or a variable gain amplifier to level the power of both antenna branches and increase the dynamic range of the system [21]. Keeping a constant dynamic range of the hologram as well as completely illuminating the acquisition plane with the reference signal is mandatory for a low error in the phase retrieval algorithm.

At each point of the acquisition plane the field is acquired along a set of equally spaced frequencies giving an interferometric signal:

$$H(\vec{r},w) = |E_{aut}(\vec{r},w) + E_{ref}(\vec{r},w)|^2 = |E_{aut}(\vec{r},w)|^2 + |E_{ref}(\vec{r},w)|^2 + E_{aut}(\vec{r},w)E^*_{ref}(\vec{r},w) + E^*_{aut}(\vec{r},w)E_{ref}(\vec{r},w), \quad (1)$$

being $\vec{r}$ the position vector defining the position of the probe antenna in the acquisition plane and w the angular frequency. The asterisk indicates the complex conjugate. E_{aut} is the field radiated by the AUT and E_{ref} is the field radiated by the reference antenna, noting that both, E_{aut} and E_{ref}, refer to the field component received by the probe antenna. The acquisition process can be repeated for the other component of the field just by changing the polarization of the AUT.

Then, by considering only one of the outputs of the directional coupler at a time, the square amplitude of the AUT and the reference antenna can be separately characterized and the modified hologram can be computed as:

$$\begin{aligned} H_m(\vec{r},w) &= H(\vec{r},w) - |E_{aut}(\vec{r},w)|^2 - |E_{ref}(\vec{r},w)|^2 \\ &= E_{aut}(\vec{r},w)E^*_{ref}(\vec{r},w) + E^*_{aut}(\vec{r},w)E_{ref}(\vec{r},w). \end{aligned} \quad (2)$$

The inverse *Fourier Transform* (FT) of the modified hologram produces the following signal in the TD, which has to be obtained at every point of the $2W \times 2H$ measurement grid:

$$\begin{aligned} h_m(\vec{r},t) = e_{aut}(\vec{r},t) \otimes e^*_{ref}(\vec{r},-t) + \\ e^*_{aut}(\vec{r},-t) \otimes e_{ref}(\vec{r},t). \end{aligned} \quad (3)$$

where $\otimes$ denotes a convolution, and e_{aut} and e_{ref} represent the inverse FT of the radiated fields.

A schematic representation of the modified hologram in the TD is shown in Fig. 2. The hologram is composed of the two cross-correlation terms thus, to retrieve the amplitude and phase of the AUT, it is necessary to filter the term corresponding to the convolution of $e_{aut}(\vec{r},t)$ and $e^*_{ref}(\vec{r},t)$ as indicated in (4) providing no time overlap is present.

$$h_{mfiltered}(\vec{r},t) = \{e_{aut}(\vec{r},t) \otimes e^*_{ref}(\vec{r},-t)\}R(t_1,t_2), \quad (4)$$

wherein $R(t_1,t_2)$ represents the rectangular time window from t_1 to t_2. The parameter constraints that allow to perform a correct filtering will be discussed in the next section.

Once the signal has been filtered in the TD, last step, as in the conventional off-axis approach, is the removal of the effect of the reference antenna back in the FD:

$$E_{aut}(\vec{r},w) \simeq \frac{H_{mfiltered}(\vec{r},w)}{E^*_{ref}(\vec{r},w)}. \quad (5)$$

The error of the phase retrieval algorithm will depend mostly on the separation of the cross-correlation terms in the TD. This separation is determined by the starting times of the signals coming from the AUT and the reference antenna, t_{aut} and t_{ref}, and from their spread or duration, defined as $\Delta\tau_{aut}$ and $\Delta\tau_{ref}$, as it can be seen in Fig. 2, and it will be addressed in the following section.

B. Setup limitations

According to the modified hologram scheme depicted in Fig. 2 two conditions can be established: a) time overlap can be avoided if the first condition of (6) is satisfied for all the sampling points, and b) frequency sampling must fulfill the expression in (7) [14].

$$\begin{cases} t_{aut} - t_{ref} > 0 & \text{original hologram} \\ t_{aut} - t_{ref} + \Delta\tau < 0 & \text{swapped terms hologram} \end{cases}, \quad (6)$$

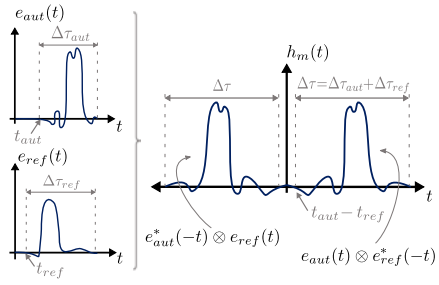

Fig. 2. Scheme of the AUT and reference signals in the TD and composition of the hologram for a specific point of the acquisition plane.

$$\Delta f < \frac{1}{2T} = \frac{1}{2(\Delta\tau + t_{aut} - t_{ref})}, \quad (7)$$

being T the duration of the signal.

The first condition, given in (6), can be used to determine whether the position of the antennas and the size of the acquisition plane allow for a correct separation of the spectral terms. Then, from the second condition, given in (7), the minimum frequency sampling that guarantees that all the requirements are met can be obtained.

Since t_{aut} and t_{ref} represent the time that takes the radiation to travel from the reference antenna and AUT to the probe antenna, the previous constraints can be expressed as a function of distance.

Considering a symmetric acquisition plane in relation to the position of the AUT, and regarding the first requirement, as detailed in the first part of (6), worst case scenario corresponds to one of the corners of the acquisition plane on the side closer to the reference antenna (▲ point in Fig. 1 for an horizontal cut).

The distance from the source to one of these corners (upper or lower corners of the acquisition plane corresponding to the worst case scenario) can be expressed as follows, neglecting the dispersion that can be introduced by the directional coupler and the antennas:

$$\sqrt{D^2+W^2+H^2} > \sqrt{D^2+(W-L)^2+H^2} + L_{eff}, \quad (8)$$

where W and H are the half width and the half height of the acquisition plane respectively, D is the distance from the aperture plane of the antennas to the acquisition plane, L is the distance between the center of the apertures of the AUT and reference antenna and L_{eff} is the effective length of the transmission line connecting the directional coupler and the reference antenna.

The upper limit for the previous condition when W and H go to infinite is given by:

$$L_{eff} < L. \quad (9)$$

The previous condition is expected to be never fulfilled as the geometrical arrangement of the antennas forces L_{eff} to be larger than the separation between antennas.

The effective length of the transmission line can be increased (and so t_{ref}) until both cross-correlation terms are

III

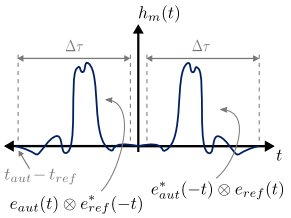

Fig. 3. Time-domain modified hologram with swapped cross-correlation terms.

swapped (see Fig. 3). In this case, the second condition in (6) has to be fulfilled, yielding the following expressions as a function of distance:

$$\sqrt{D^2+W^2+H^2}-(\sqrt{D^2+(W-L)^2+H^2}+ L_{eff})+c\Delta\tau<0, \tag{10}$$

$$L_{eff}-L>c\Delta\tau. \tag{11}$$

where c is the speed of light.

According to (11), to avoid time overlapping, it is necessary that the difference between the effective length of the transmission line and the separation of the antennas will be larger than the spread of the signal due to both antennas.

As the effective length of the transmission line has to be increased, denser frequency sampling will be demanded to correctly retrieve the AUT pattern. The frequency sampling defined in (7) can be expressed as a function of distance as follows:

$$\Delta f<\frac{c}{2(L_{eff}+L+c\Delta\tau)}. \tag{12}$$

Finally, as the method relies in the separation of one of the cross-correlation terms in the TD, to be able to filter this term with a minimum error it is necessary to guarantee that there is no time overlap. The field is acquired over a range of frequencies with a bandwidth B so that it can be expressed as:

$$E(\vec{r},w)=H_m(\vec{r},w)\Pi\left(\frac{w-w_c}{2\pi B}\right), \tag{13}$$

being w_c the angular frequency of the center of the band and $\Pi(x)$ the pulse function defined as:

$$\Pi(x)=\begin{cases}1 & \text{if } |x|\leq\frac{1}{2}\\ 0 & \text{otherwise}\end{cases}. \tag{14}$$

In the TD, after performing an inverse FT, the field will be spread by means of a convolution with a sinc function modulated with an exponential term, due to the frequency shifted pulse employed in (13):

$$e(\vec{r},t)=h_m(\vec{r},t)\otimes Bsinc(Bt)e^{jw_ct}. \tag{15}$$

The spread of the sinc function, approximately $1/B$, could result in the overlap of the TD responses for antennas with narrow bandwidth. For all the aforementioned facts, the method is suitable only for broadband antennas so that the spread of the cross-correlation terms is small enough to allow for a correct filtering of the desired term.

C. Measurement process

Prior to the AUT characterization, a calibration process, as in conventional off-axis holography, is needed. This calibration process only has to be done once, and consists on a complete characterization of the reference antenna in amplitude and phase in the same frequency range that will be used during the normal operation of the system.

Once the calibration has been accomplished, the following steps have to be performed:

1) A complete spatial acquisition with a frequency sweep at each point is performed considering only the branch of the AUT. The measured power corresponds to $|E_{aut}(\vec{r},w)|^2$.
2) With both antennas connected to the outputs of the directional coupler, the acquisition process is repeated and the measured power corresponds this time to the hologram $H(\vec{r},w)$.
3) The modified hologram, $H_m(\vec{r},w)$, is computed as in (2) and the phase retrieval algorithm is applied.
4) Steps 1), 2) and 3) are done to retrieve the main polarization of the AUT (the three antennas with the same polarization). In order to acquire the other component of the AUT its polarization needs to be changed, while maintaining the initial position of the probe and the reference antenna. Then steps 1), 2) and 3) have to be repeated.

Finally, once the amplitude and phase of the AUT have been retrieved for both field components, the far-field pattern and the aperture fields of the antenna could be calculated by any suitable method (NF-FF back propagation, source reconstruction technique, etc.).

It is worth noting that the first step, in which the amplitude of the AUT is characterized, is needed to compute the modified hologram, defined as in (2). This extra measurement allows for the removal of the auto-correlation terms of the hologram easing the filtering process. Furthermore, the final retrieved field of the AUT can be composed with this measured amplitude and the retrieved phase, improving error reduction.

Nevertheless, this first step could be omitted, reducing the number of acquisitions to one at the expense of using larger delay lines to increase the separation of the cross-correlation terms and a denser frequency sampling (see (12)). Error is expected also to be slightly higher for this case as $|E_{aut}(\vec{r},w)|^2$ is not measured and, therefore, the retrieved amplitude should be used.

Processing time for the phase retrieval for the proposed method is comparable to the time needed to retrieve the phase with the standard off-axis holography method. As both methods rely on the use of fast Fourier Transforms, the time needed to retrieve the phase is in the order of a few seconds for current computers and, therefore, it is negligible compared to the acquisition time of the data, which can vary from one method to another depending on the measurement system features (single frequency and continuous move acquisitions, frequency sweeps, etc.).

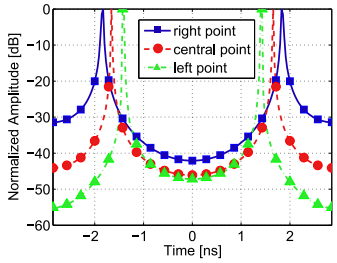

Fig. 4. Modified hologram in the time domain for the dielectric rod antenna. Trace colors are coincident with the study points shown in Fig. 1.

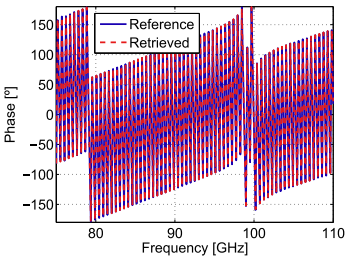

(a)

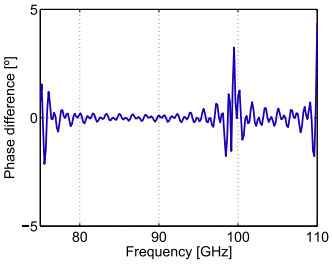

(b)

Fig. 5. Retrieved phase for the worst case in the acquisition plane, i.e. at the left point: (a) Retrieved and simulated phase; (b) Unwrapped difference between simulated and retrieved phase patterns.

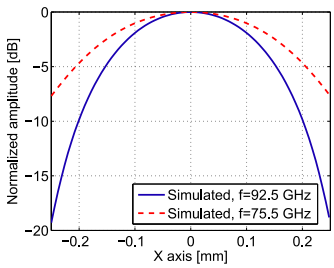

(a)

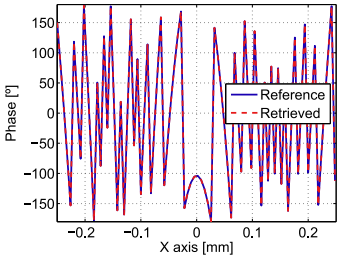

(b)

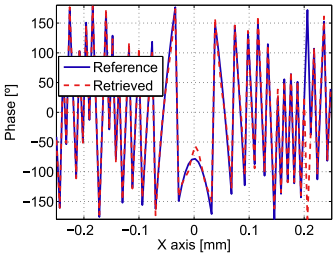

(c)

Fig. 6. Main cut of the H-plane for the dielectric rod antenna in the W-band. Comparison between retrieved and reference fields: (a) Normalized simulated amplitude for 92.5 GHz and 75.5 GHz; (b) Reference (simulated) and retrieved phase for 92.5 GHz; (c) Reference (simulated) and retrieved phase for 75.5 GHz.

III. Numerical Example

In order to study the capabilities of the phase retrieval algorithm for efficient broadband characterization of antennas, a numerical example for the characterization of a dielectric rod antenna will be shown next.

The rod antenna and the reference antenna (a horn antenna with a radiation pattern modeled as a $\cos^q(\theta)$ with $q = 1$) have been designed and simulated in the W-band, for 201 equally spaced frequency points ranging from 75 GHz to 110 GHz, with the computational electromagnetic software FEKO [28]. The frequency sampling rate has been set so that the requirement of (12) is thoroughly fulfilled.

Separation between the antennas is $L = 15$ cm and the acquisition plane, defined at $D = 50$ cm from the AUT antenna, is a 50 cm x 50 cm square with a sampling of 6 mm for both dimensions, being all the distances referred to the

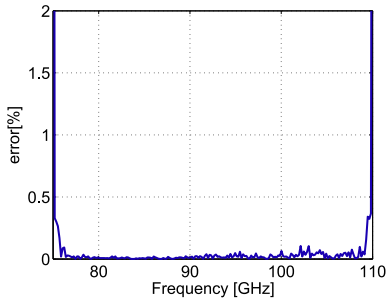

Fig. 7. Error of the phase retrieval algorithm for the dielectric rod antenna in the W-band.

III

center of the aperture planes of the antennas. The reference antenna has a tilt of $\alpha = 73°$ so it is pointing to the center of the acquisition plane and is connected to one of the outputs of the directional coupler by means of a transmission line that introduces a delay of 0.8 ns which corresponds to a L_{eff} of 144 mm if 0.6 is considered as the velocity factor (see Fig. 1). It is important to note that, for alleviating simulation time, sampling is larger than $\lambda/2$ for all the frequency band, and therefore, the retrieved data could not be used to perform a conventional aliasing free FF transformation.

Results for the E-plane (y=0 cut) copolar component are shown to illustrate the setup and the phase retrieval method capabilities.

Fig. 4 shows the modified hologram in the time domain as defined in (3) for three different points in the acquisition plane (shown in Fig. 1 with the same color and marker code). Although the position of those cross-correlation terms varies depending on the time the signals need to travel from the AUT and the reference antenna to the probe antenna, there is no overlap between the cross-correlation terms, and the desired term can be filtered for all the acquisition points with a rectangular window defined from -3 ns to 0 ns.

Fig. 5 a shows the retrieved phase for all the frequencies for the worst case of the spatial acquisition: as previously mentioned, this case corresponds to an acquisition point on the left side of the acquisition plane, on the reference antenna side (triangular marker in Fig. 1); the points on this side are closer to the reference antenna than to the AUT, so the second expression in (6) is minimized (dash-dotted hologram in Fig. 4). As it can be seen in Fig. 5 b for this case the phase is retrieved almost without error, being the maximum difference between the reference phase and the retrieved one of 3° in the central part of the band.

Once the phase is retrieved for all the acquisition points, the NF of the AUT in the acquisition plane can be obtained for each frequency. The measured amplitude and retrieved phase for the frequencies of 75.5 GHz and 92.5 GHz are shown in Fig. 6. The retrieved phase is compared to the phase obtained from simulations.

The retrieved phase of the AUT for the frequency of 92.5 GHz, central frequency of the band, is in very good agreement with the reference field obtained from the simulations with amplitude and phase data (error of 0.002 %). For 75.5 GHz, in the lower part of the band, the retrieved phase has some discrepancies (error of 0.3 %).

To quantify the quality of the phase retrieval method, the following error is calculated for all the frequencies:

$$error[\%] = 100 \frac{\| E_{sim} - E_{ret} \|_2}{\| E_{sim} \|_2}, \qquad (16)$$

where $\| \cdot \|_2$ is the Euclidean norm, E_{sim} is the field of the AUT obtained from simulations with phase information, and E_{ret} is the retrieved field of the AUT. The graphical representation of the error is shown in Fig. 7. Due to the filtering in the TD, the error is higher in the extremes of the frequency band [29], and therefore, it is advisable to discard the results in those extremes. The range of frequencies contaminated by this error is minimum in the case of using a rectangular window, as the one used in this work. However, it could be of interest to use other windows to reduce the mean error [29]. For this simulation example, mean error of the retrieval algorithm is 0.14 %.

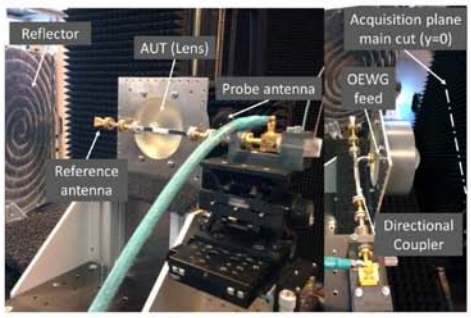

(a) (b)

Fig. 8. Setup for the W-band antenna measurement: (a) side view; (b) top view.

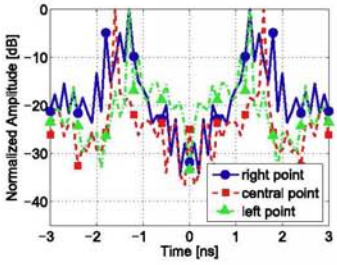

Fig. 9. Modified hologram in the time domain for the lens antenna. Trace colors are coincident with the study points shown in Fig. 1.

IV. Measurement Example

Two measurement examples with different types of antennas with different directivities and working frequency bands are presented to completely validate the method and the phase-retrieval algorithm. Slight modifications of the basic setup (see Fig. 1) such as the use of reflectors or amplifiers are introduced respectively in each of the presented setups.

A. W-band lens antenna measurement

A lens antenna was characterized in the W-band. The measurements were performed with the MilliLab PNF scanner described in [8]. The main components of the setup and the layout can be seen in Fig. 8.

The lens antenna is a 64 mm circular lens with a 1 cm length WR-10 OEWG feed, and a 20 dB gain horn is used as a reference antenna, both with horizontal polarization. Separation between the center of the aperture of the antennas is 105 mm yielding an effective length (L_{eff}) of 63 mm considering a velocity factor of $0.6c$. Mirror reflection of the reference signal is used in order to increase the path of the reference branch signal. The reflector, a planar metallic plate of

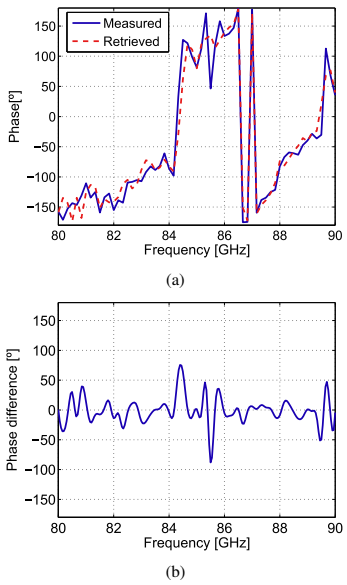

Fig. 10. Retrieved phase for the worst case in the acquisition plane, i.e. at the left point: (a) Retrieved and measured phase; (b) Difference between retreieved and measured phase patterns.

210 mm x 300 mm, is placed at 220 mm of the aperture plane of the reference antenna with a tilt of 60° so that the acquisition plane, at 150 mm of the aperture of the AUT, is illuminated with an almost constant amplitude.

The field acquisitions are performed for a cut in the x-axis of 200 mm with spatial sampling of $\lambda_m/2$, being λ_m the wavelength at maximum acquisition frequency (90 GHz). The measurement system does not allow for simultaneous multi-frequency acquisitions, therefore, 61 different spatial acquisitions for equally spaced frequencies between 80 GHz and 90 GHz have been done, guaranteeing the requirements in (12) are fulfilled.

With the purpose of quantifying the accuracy of the phase retrieval algorithm, AUT field amplitude and phase data acquisition is performed thus a comparison between the retrieved and the measured phase can be done.

As only a fraction of the bandwidth of the AUT is being characterized, the effect of the sinc convolution defined in (15) will introduce a spread in the cross-correlation terms of the spectrum complicating the filtering of the desired term. Nevertheless the frequency sampling is enough to retrieve the phase of the AUT with an acceptable error level.

As in the numerical example, the results are presented for the E-plane (y=0 cut).

Fig. 9 shows the modified hologram for three different points in the acquisition plane, using the color code indicated in Fig. 1. As it is expected, separation between cross-correlation terms decreases as the probe antenna is closer to the reference antenna, although for this case, the cross-correlation terms associated to the point in the right side of the acquisition plane (opposite to the reference antenna side) are spread, having its maximum in the same position than the terms corresponding to the left side of the acquisition plane. This might be due to some reflections of the reference signal with the holding structure for the AUT and also due to the poor resolution of the spectrum caused by the sparse frequency sampling.

A comparison between the retrieved and the measured phase for all the frequencies corresponding to the worst case scenario, probe antenna closer to the reference antenna, is shown in Fig. 10a. There are some discrepancies that can be clearly seen in Fig. 10b, showing the difference pattern. The differences are noticeable in the central part of the band, wherein the measured phase have some abrupt variations that are not present in the retrieved phase, probably due to the low density of the frequency sampling and because the signal level is lower in this section of the band.

Fig. 11 shows the measured amplitude and the retrieved phase of the AUT for two different frequencies, 87 GHz and 83.5 GHz. Both results of retrieved phase are in very good agreement with the measurements, being the error of the phase retrieval of 2.73 % and 3.24 % respectively for each frequency.

Finally, Fig. 12 shows the error of the phase retrieval for each of the frequencies of the band as defined in (16); mean error is 2.40%. Excluding the extremes of the frequency band, wherein the error rises due to the TD filtering, the highest level of error occurs at 80.8 GHz due to the different the level of the signals from the AUT and reference antenna in the acquisition plane.

This could be corrected by employing a variable attenuator to balance the signal level in both branches increasing the dynamic range of the system [21].

B. K_a-band pyramidal horn antenna measurement

A $20-$dB gain pyramidal horn antenna is characterized in the complete K_a-band from 26.5 GHz to 40 GHz in this measurement example. The measurements were done with the TSC-Uniovi PNF scanner [13]. The components and the layout can be seen in Fig. 13.

The reference antenna, a small horn, vertically polarized, is placed at 200 mm of the AUT (distances are measured from the center of the aperture planes of the antennas) and with a tilt of 52.5° so that its maximum field is outside the acquisition plane and the illumination of the acquisition plane is as uniform as possible. The reference antenna is connected to the directional coupler by means of an 80 cm coaxial cable whose effective length can be approximated by 48 cm considering a velocity factor of 0.6. The acquisition plane, at 260 mm of the AUT aperture is a 300 mm x 300 mm square. Spatial sampling is 3.7 mm, that is $\lambda/2$ at 40 GHz. For each spatial point, a frequency sweep of 401 points is performed, to thoroughly fulfill the requirements in (12). An amplifier is included in the AUT branch to balance the signal level of the AUT and the reference signal.

Results are shown for the H-plane (y=0) cut. The modified hologram in the TD can be seen in Fig. 14 for the three different points in the main cut of the acquisition plane

III

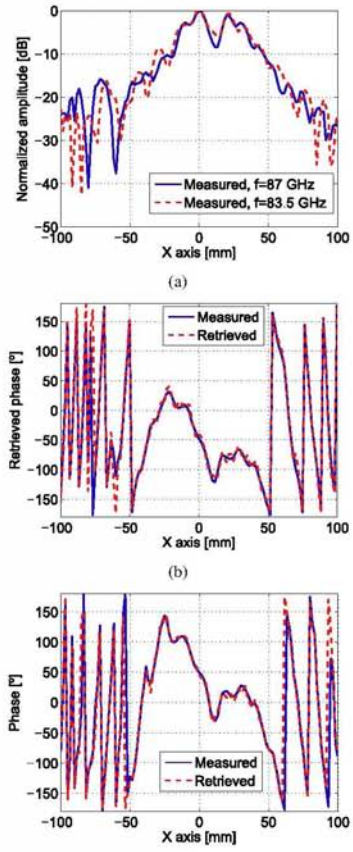

Fig. 11. Main cut of the H-plane for the lens antenna in the W-band. Comparison between retrieved and measured fields: (a) Normalized measured amplitude for 87 GHz and 83.5 GHz; (b) Measured and retrieved phase for 87 GHz; (c) Measured and retrieved phase for 83.5 GHz.

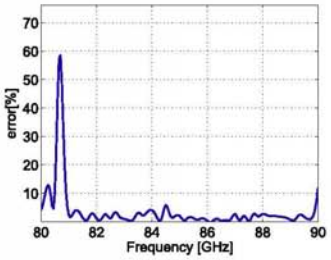

Fig. 12. Error of the phase retrieval algorithm for the lens antenna in the W-band.

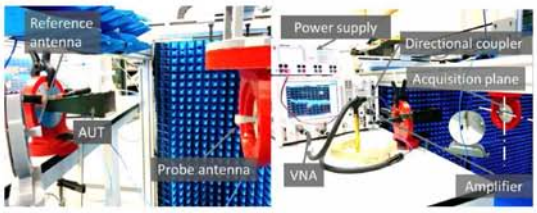

Fig. 13. Setup for the K_a-band antenna measurement: (a) position of the antennas; (b) complete setup.

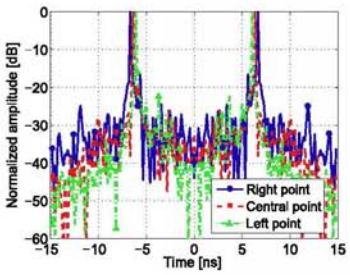

Fig. 14. Modified hologram in the time domain for the pyramidal horn antenna. Trace colors are coincident with the study points shown in Fig. 1.

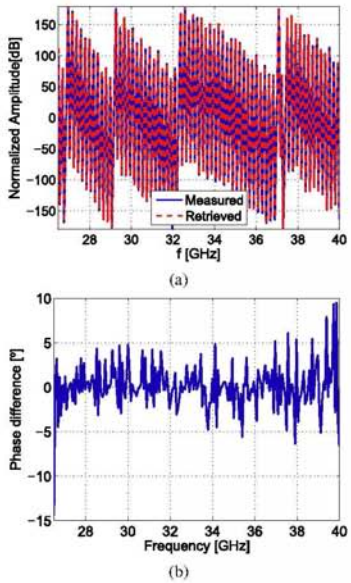

Fig. 15. Retrieved phase for the worst case in the acquisition plane, i.e. at the left point: (a) Retrieved and measured phase; (b) Unwrapped difference between retrieved and measured phase patterns.

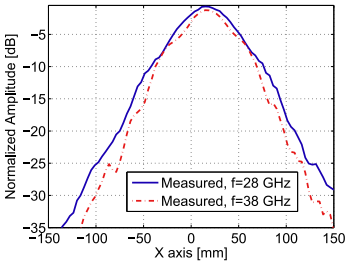

(a)

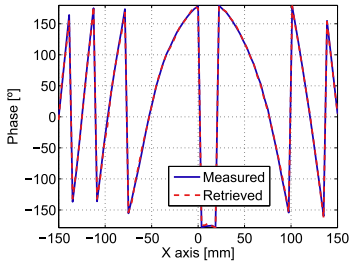

(b)

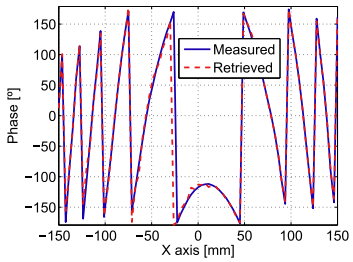

(c)

Fig. 16. Main cut of the E-plane for the pyramidal horn antenna in the K_a-band. Comparison between retrieved and measured fields: (a) Normalized measured amplitude for 28 GHz and 38 GHz; (b) Measured and retrieved phase for 28 GHz; (c) Measured and retrieved phase for 38 GHz.

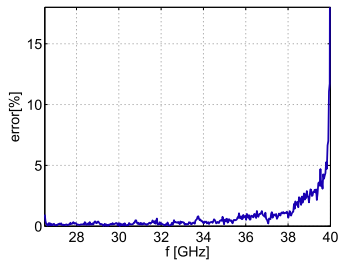

Fig. 17. Error of the phase retrieval algorithm for the horn antenna in the K_a-band.

highlighted in Fig. 1. As it can be clearly seen, all of the terms of the modified hologram can be easily filtered. A rectangular window 8.8 ns wide, centered in the maximum of the corresponding cross-correlation term in the negative side of the spectrum, will be used to filter the hologram in each spatial acquisition point.

The retrieved phase for the worst case (point with the triangular marker in Fig.1) is shown in Fig. 15 a and is in very good agreement with the measured phase. The difference pattern between the measured and the retrieved phase is depicted in Fig. 15 b. For most of the points, the error is less than 6°.

As in the previous examples, the final retrieved field is composed by the measured amplitude and the retrieved phase, and for this case it is depicted for 28 GHz and 38 GHz in Fig. 16. The retrieved fields are in perfect accordance with the measured ones, being the error 0.14 % and 1.07 % respectively for 28 and 38 GHz.

The representation of the error for the complete frequency band, as defined in (16) is shown in Fig. 17 being the mean error value 0.83 %. The mean error from 37 GHz to 40 GHz is much more higher (3.68 %) than for the rest of the band. Apart from the error introduced in the frequency band edges due to the TD filtering, the level of the reference branch decays in that upper part of the band causing a reduction of the dynamic range of the system, which explains the increase of the error.

If the hologram is processed without subtracting the amplitude of the AUT, which means that only one acquisition is needed for each field component characterization, but disabling the possibility of auto-correlation terms removal, the mean error of the phase retrieval increases from 0.83 % to 4.12 %.

The FF pattern of the data obtained with the proposed phase retrieval method is computed through the standard plane-rectangular NF-FF transformation [14] and compared to the FF pattern obtained from a set of NF data with direct phase acquisition. The uncertainty for the peak-level and the secondary lobe level (SLL) for both FF patterns is calculated following the procedure described in [30] in order to quantify the error introduced in the FF pattern when using phaseless acquisitions.

The procedure employs the root mean square (RMS) value of the equivalent stray signal (ESS) obtained as the difference of both FF patterns (the one obtained from amplitude and phase NF data and the one obtained from the phaseless acquisition) to calculate the uncertainty. The uncertainty values together with the RMS value of the ESS, are shown in Table I for the frequencies of 28 GHz and 38 GHz.

It is worth noting that for the frequency of 38 GHz, the phase retrieval error is quite high (see Fig. 17) and therefore, higher values of uncertainty are expected.

For this setup, the angular valid margin of the NF-FF transformation is 25° [14]. The secondary lobes are close to the previous defined limit so the uncertainty values have to be read carefully for this example. Despite of that, the uncertainty parameter for the frequency of 28 GHz is low and the one obtained for the frequency of 38 GHz is acceptable considering the error of the phase retrieval for this frequency

III

III

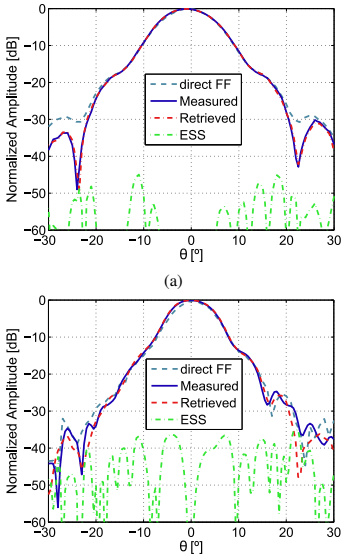

Fig. 18. Comparison of the FF patterns for the horn antenna in the k_a-band for the case of using direct FF acquisition, a set of NF amplitude-only data and the phase retrieval method and a complex NF acquisition with amplitude and phase. The ESS is calculated for both cases: (a) E_θ cut for $\phi = 0$ at 28 GHz; (b) E_θ cut for $\phi = 0$ at 38 GHz.

TABLE I
UNCERTAINTIES IN THE FF PATTERN CALCULATION FOR THE MAIN PARAMETERS OF THE RADIATION DIAGRAMS (THE SLL UNCERTAINTY IS CALCULATED CONSIDERING A SLL OF -33.5 dB).

$frequency$ $[GHz]$	ESS $RMS[dB]$	$Peak\,level$ $uncertainty[dB]$	SLL $uncertainty[dB]$
28	-61.1509	0.0076	0.3527
38	-47.5861	0.0362	1.5601

is quite high. The uncertainty parameters regarding the peak level are extremely low for both frequencies.

The E_θ cut for $\phi = 0$ of the FF patterns and the ESS are shown in Fig. 18. Finally, a direct FF acquisition over an spherical range is included for comparison purposes. Differences with respect to planar range with NF-FF transformation are mainly due to the planar range truncation error.

V. CONCLUSION

A new efficient method for broadband phaseless characterization of antennas from just two surface acquisitions is presented. The method is a modification of the conventional off-axis holography scheme and is presented for planar acquisitions, although extrapolation to other geometries is straightforward.

The phase retrieval is done independently point-by-point in the acquisition plane, after the field is acquired for a set of frequencies, by calculating and filtering the hologram in the time domain. Therefore, the proposed technique does not depend on the acquisition geometry nor on the accuracy of the positioners, making the method suitable to work at high frequency bands.

The method does not require increasing the spatial bandwidth to reduce spectral overlapping, as it happens in conventional off-axis holography methods, resulting in less acquisition points. In contrast, time responses overlap of the cross-correlation terms of the hologram can be easily controlled by introducing enough delay in the reference antenna branch or, alternatively, in the AUT branch.

The error of the phase retrieval and the dynamic range of the system are correlated to the power difference between the AUT and the reference branches; thus, the use of a variable attenuator to help leveling those branches is recommended.

Main drawback is that all the involved components, mainly the AUT, must be broadband. If the antenna is narrowband, the computed time responses will be spread (convoluted with a sinc of width $1/B$) and it could result in the overlap of the time domain responses. Also the complete characterization of the reference antenna in the acquisition plane is needed.

The method has been illustrated with several examples in the microwave and millimeter-wave bands. Very good results are obtained for all the studied cases.

REFERENCES

[1] Y. Huang, K. Chan, and B. Cheeseman, "Review of broadband antenna measurements," in *1st European Conf. on Antennas and Propag.. EuCAP 2006*, Nov. 2006, pp. 1–4.

[2] R. de Jongh, M. Hajian, and L. Ligthart, "Time domain antenna measurements: implementation and verification of a novel technique," in *27th European Microwave Conf.*, vol. 1, Sep. 1997, pp. 470–475.

[3] Y. Huang, M. Bury, Y. Yashchyshyn, A. Yarovoy, R. De Jongh, S. Maqbool, and Y. Lu, "Time-domain measurements of broadband antennas," in *2nd European Conf. on Antennas and Propag.. EuCAP 2007*, Nov. 2007, pp. 1–4.

[4] A. Kalinin, "Anechoic chamber wideband antenna measurements," *IEEE Aerosp. Electron. Syst. Mag.*, vol. 21, no. 1, pp. 21–24, Jan. 2006.

[5] T. Hansen and A. Yaghjian, "Planar near-field scanning in the time domain. Formulation," *IEEE Trans. Antennas Propag.*, vol. 42, no. 9, pp. 1280–1291, Sep. 1994.

[6] ——, "Formulation of probe-corrected planar near-field scanning in the time domain," *IEEE Trans. Antennas Propag.*, vol. 43, no. 6, pp. 569–584, Jun. 1995.

[7] G. Junkin, T. Huang, and J. Bennett, "Holographic testing of terahertz antennas," *IEEE Trans. Antennas Propag.*, vol. 48, no. 3, pp. 409–417, Mar. 2000.

[8] A. Räisänen, J. Ala-Laurinaho, A. Karttunen, J. Mallat, A. Tamminen, and M. Vaaja, "Measurements of high-gain antennas at THz frequencies," in *4th European Conf. on Antennas and Propag. (EuCAP)*, April 2010, pp. 1–3.

[9] A. V. Raisanen and J. Ala-Laurinaho, "Holographic principles in antenna metrology at millimeter and submillimeter wavelengths," in *Antennas and Propagation (EuCAP), 2015 9th European Conference on*, April 2015, pp. 1–2.

[10] A. Newell, "Error analysis techniques for planar near-field measurements," *IEEE Transactions on Antennas and Propagation*, vol. 36, no. 6, pp. 754–768, Jun. 1988.

[11] Y. Rahmat-Samii, L. Williams, and R. Yaccarino, "The UCLA bi-polar planar-near-field antenna-measurement and diagnostics range," *IEEE Antennas Propag. Mag.*, vol. 37, no. 6, pp. 16–35, Dec. 1995.

[12] T. Brockett and Y. Rahmat-Samii, "A novel portable bipolar near-field measurement system for millimeter-wave antennas: construction, development, and verification," *IEEE Antennas Propag. Mag.*, vol. 50, no. 5, pp. 121–130, Oct. 2008.

[13] A. Arboleya, Y. Álvarez, and F. Las-Heras, "Millimeter and submillimeter planar measurement setup," in *2013 IEEE Antennas and Propag. Soc. Int. Symp. (APSURSI)*, Jul. 2013, pp. 1–2.

[14] A. Yaghjian, "An overview of near-field antenna measurements," *IEEE Trans. Antennas Propag.*, vol. 34, no. 1, pp. 30–45, Jan. 1986.

[11] Y. Rahmat-Samii, L. Williams, and R. Yaccarino, "The UCLA bi-polar planar-near-field antenna-measurement and diagnostics range," *IEEE Antennas Propag. Mag.*, vol. 37, no. 6, pp. 16–35, Dec. 1995.
[12] T. Brockett and Y. Rahmat-Samii, "A novel portable bipolar near-field measurement system for millimeter-wave antennas: construction, development, and verification," *IEEE Antennas Propag. Mag.*, vol. 50, no. 5, pp. 121–130, Oct. 2008.
[13] A. Arboleya, Y. Álvarez, and F. Las-Heras, "Millimeter and submillimeter planar measurement setup," in *2013 IEEE Antennas and Propag. Soc. Int. Symp. (APSURSI)*, Jul. 2013, pp. 1–2.
[14] A. Yaghjian, "An overview of near-field antenna measurements," *IEEE Trans. Antennas Propag.*, vol. 34, no. 1, pp. 30–45, Jan. 1986.
[15] J. Wang, "An examination of the theory and practices of planar near-field measurement," *IEEE Trans. Antennas Propag.*, vol. 36, no. 6, pp. 746–753, Jun. 1988.
[16] S. Razavi and Y. Rahmat-Samii, "A new look at phaseless planar near-field measurements: limitations, simulations, measurements, and a hybrid solution," *IEEE Antennas Propag. Mag.*, vol. 49, no. 2, pp. 170–178, Apr. 2007.
[17] F. Las-Heras and T. Sarkar, "A direct optimization approach for source reconstruction and NF-FF transformation using amplitude-only data," *IEEE Trans. Antennas Propag.*, vol. 50, no. 4, pp. 500–510, Apr. 2002.
[18] D. Smith, M. Leach, M. Elsdon, and S. Foti, "Indirect holographic techniques for determining antenna radiation characteristics and imaging aperture fields," *IEEE Antennas Propag. Mag.*, vol. 49, no. 1, pp. 54–67, Feb. 2007.
[19] V. Schejbal, V. Kovarik, and D. Cermak, "Synthesized-reference-wave holography for determining antenna radiation characteristics," *IEEE Antennas Propag. Mag.*, vol. 50, no. 5, pp. 71–83, Oct. 2008.
[20] J. Laviada and F. Las-Heras, "Phaseless antenna measurement on non-redundant sample points via Leith-Upatnieks holography," *IEEE Trans. Antennas Propag.*, vol. 61, no. 8, pp. 4036–4044, Aug. 2013.
[21] J. Laviada Martínez, A. Arboleya-Arboleya, Y. Álvarez-López, C. García-González, and F. Las-Heras, "Phaseless antenna diagnostics based on off-axis holography with synthetic reference wave," *IEEE Antennas Wireless Propag. Lett.*, vol. 13, pp. 43–46, 2014.
[22] V. Schejbal, J. Pidanic, V. Kovarik, and D. Cermak, "Accuracy analyses of synthesized-reference-wave holography for determining antenna radiation characteristics," *IEEE Antennas Propag. Mag.*, vol. 50, no. 6, pp. 89–98, Dec. 2008.
[23] D. Smith, S. Skobelev, and M. Leach, "A modified holographic technique for antenna measurements," in *8th Int. Symp. on Antennas, Propag. and EM Theory. ISAPE 2008*, Nov. 2008, pp. 46–49.
[24] D. Gabor, "Microscopy by reconstructed wave-fronts," *Proc. of the Royal Soc. of London A: Math., Physical and Eng. Sci.*, vol. 197, no. 1051, pp. 454–487, Jul. 1949.
[25] E. N. Leith and J. Upatnieks, "Reconstructed wavefronts and communication theory," *Journal of the Optical Soc. of America*, vol. 52, no. 10, pp. 1123–1128, Oct. 1962.
[26] S. Costanzo and G. Di Massa, "Wideband phase retrieval technique from amplitude-only near-field data," *Radioengineering*, vol. 17, no. 4, pp. 8–12, Feb. 2008.
[27] S. Costanzo, G. Di Massa, and D. Migliore, "A novel hybrid approach for far-field characterization from near-field amplitude-only measurements on arbitrary scanning surfaces," *IEEE Trans. Antennas Propag.*, vol. 53, no. 6, pp. 1866–1874, Jun. 2005.
[28] "FEKO Suite 6.2 features." [Online]. Available: https://www.feko.info/about-us/News/feko-suite-6.2-feature-update-available .
[29] J. Laviada, A. Arboleya-Arboleya, Y. Álvarez-López, C. García-González, and F. Las-Heras, "Phaseless synthetic aperture radar with efficient sampling for broadband near-field imaging: theory and validation," *IEEE Trans. Antennas Propag.*, vol. 2, no. 2, pp. 573–584, Feb. 2015.
[30] A. Newell and G. Hindman, "Antenna pattern comparison using pattern subtraction and statistical analysis," in *5th European Conf. on Antennas and Propag. (EuCAP)*, Apr. 2011, pp. 2684–2687.

Ana Arboleya received de M.Sc. degree in telecommunication engineering from the University of Oviedo, Spain, in 2009, where she is currently working toward the Ph.D. degree. Since 2008, she has been working as a Research Assistant within the Signal Theory and Communications research group, TSC-UNIOVI, at the Department of Electrical Engineering in the University of Oviedo.
She was a Visiting Scholar in 2014 and 2015 in the Department of Radio Science and Engineering and MilliLab, in Aalto University, Finland.
Her major research interests comprise antenna diagnostics and measurement systems and techniques and high frequency imaging techniques and applications.

III

Jaime Laviada was born in Gijn, Spain. He received the M.S. degree in telecommunication engineering and the Ph.D. degree from the Universidad de Oviedo, Spain, in 2005 and 2010, respectively.
In 2006, he joined the research group Signal Theory and Communications of the Universidad de Oviedo, where he has been involved in multiple national and European projects as well as contracts with several companies. He was a Visiting Scholar in the Electromagnetics and Communications Lab, Pennsylvania State University, during 2007 and 2008. In 2015, he moved to the Antennas Group of the Universidad Pública de Navarra with a national postdoctoral fellowship collaborating in several applied research projects. Finally, he moved back to the Universidad de Oviedo where he currently holds a position as assistant professor.
His main research interests are in numerical techniques applied to imaging, antenna measurements, method of moments, and antenna pattern synthesis.

Juha Ala-Laurinaho was born in Parkano, Finland, in 1969. He received the Diploma Engineer (M.Sc.) degree in mathematics and D.Sc. (Tech.) degree in electrical engineering from TKK Helsinki University of Technology, Espoo, Finland, in 1995 and 2001, respectively. He has been with the TKK serving in the Radio Laboratory in 1995-2007 and from 2008 in the Department of Radio Science and Engineering, which is currently a part of the Aalto University School of Electrical Engineering. During 1995, he worked as a Research Assistant and, since 1996, he has been a Research Associate and currently he works as a Staff Scientist.
Dr. Ala-Laurinaho has been a Project Manager in many millimeter wave technology related projects. His current research interests are the antennas and antenna measurement techniques for millimeter and submillimeter waves, and the millimeter wave imaging.

Yuri lvarez (S06 M09 SM15) was born in Langreo, Spain, in 1983. He received the M.S. and Ph.D. degrees in telecommunication engineering from the University of Oviedo, Gijón, Spain, in 2006 and 2009, respectively. He was a Visiting Scholar at the Department of Electrical Engineering and Computer Science at Syracuse University, Syracuse, NY, USA, in 2006 and 2008, respectively; a Visiting Postdoc at the Gordon Center for Subsurface Sensing and Imaging Systems (CenSSIS)ALERT Center of Excellence, Northeastern University, Boston, MA, USA, from 2011 to 2014; and a Visiting Postdoc at ELEDIA Research Center (Trento, Italy), in 2015. He is currently an Assistant Professor at the Signal Theory and Communications of the University of Oviedo, Gijón, Spain. His interests and research studies have been focused on antenna diagnostics, antenna measurement techniques, RF techniques for indoor location, inverse scattering and imaging techniques, and phaseless methods for antenna diagnostics and imaging. Dr. Alvarez received the 2011 Regional and National Awards to the Best Ph.D. Thesis on Telecommunication Engineering (category: security and defense).

III

Fernando Las-Heras (M'86, SM'08) received the M.S. in 1987 and the Ph.D. in 1990, both in Telecommunication Engineering, from the Technical University of Madrid (UPM). From 1988 to 1990, he was a National Graduate Research Fellow. From 1991 to 2000 he held a position of Associate Professor at the Department of Signal, Systems and Radiocommunications of the UPM. From December 2003 he holds a Full-Professor position at the University of Oviedo where he was the Vice-dean for Telecommunication Engineering at the Technical School of Engineering at Gijón from 2004 to 2008. As of 2001 he heads the research group Signal Theory and Communications TSC-UNIOVI at the Dept. of Electrical Engineering of the University of Oviedo.

He was a Visiting Lecturer at the National University of Engineering in Peru in 1996, a Visiting Researcher at Syracuse University, New York, in 2000, and a short term Visiting Lecturer at ESIGELEC in France from 2005 to 2011. From 2005 he holds the Telefónica Chair ICTs and Smartcities at the University of Oviedo and from 2010 he is a member of the Science, Technology and Innovation Council of Asturias, and member of the board of directors of the IEEE Spain Section.

He has authored over 300 articles published in academic journals and proceedings of international conferences, mainly in the areas of antenna design and the inverse electromagnetic problem with applications in diagnostic, measurement and synthesis of antennas, phaseless techniques, propagation, and microwave to THz imaging and localization, as well as in engineering education.

Antti V. Räisänen (F'94) received the D.Sc.(Tech.) degree in EE from the Helsinki University of Technology (TKK) (now Aalto University), Espoo, Finland, in 1981. In 1989, he was appointed Professor Chair of Radio Engineering with TKK, after holding the same position pro tem in 1985 and 1987-1989. He has been a Visiting Scientist and Professor with the Five College Radio Astronomy Observatory (FCRAO) and the University of Massachusetts at Amherst (1978-1979, 1980, 1981); the Chalmers University of Technology (1983); the University of California at Berkeley (1984-1985); the Jet Propulsion Laboratory (JPL) and California Institute of Technology (1992-1993); Observatoire de Paris and Universite de Paris 6 (2001-2002), and Universidad Carlos III de Madrid (2013–2014).

He supervises research in millimeter-wave components, antennas, receivers, microwave measurements, etc., at the Aalto University, Department of Radio Science and Engineering and Millimetre Wave Laboratory of Finland - ESA External Laboratory (MilliLab). He has authored or coauthored over 500 scientific or technical papers and seven books, e.g., Semiconductor Terahertz Technology: Devices and Systems at Room Temperature Operation (Wiley, 2015).

Dr. Räisänen is Fellow of the Antenna Measurement Techniques Association (AMTA) since 2008. He was the recipient of the AMTA Distinguished Achievement Award in 2009. The Chair of Excellence by the University Carlos III of Madrid was awarded to him in 2013. He has been Conference Chairman of several international microwave and millimeter-wave conferences including the 1992 EuMC, and is serving as General Chair of the 2016 Global Symposium on Millimeter Waves. He was an Associate Editor of the IEEE Transactions on Microwave Theory and Techniques (2002-2005). He was a member of the Board of Directors of the European Microwave Association (EuMA) (2006-2011). He is currently Head of the Department of Radio Science and Engineering and Chair of the Board of Directors, MilliLab.

Publication IV

A. Arboleya, J. Laviada, J. Ala-Laurinaho, Y. Álvarez, F. Las-Heras and A. V. Räisänen **"Reduced set of points in phaseless broadband near-field antenna measurement: effects of noise and mechanical errors,"** in *10th European Conference on Antennas and Propagation (EUCAP'16),* pp. 1–5 (Convened sessions), Davos (Switzerland), 10–15 Apr. 2016.

IV

Reduced Set of Points in Phaseless Broadband Near-Field Antenna Measurement: Effects of Noise and Mechanical Errors

Ana Arboleya[1], Jaime Laviada[1], Juha Ala-Laurinaho[2], Yuri Álvarez [1],
Fernando Las-Heras [1], Antti V. Räisänen [2]
[1]Departamento de Ingeniería Eléctrica. Escuela Politécnica de Ingeniería, Gijón E-33202, Spain
[2]Department of Radio Science and Engineering and MilliLab.
Aalto University School of Electrical Engineering, Espoo FI-00076, Finland
Email: aarboleya@tsc.uniovi.es

IV

***Abstract*—A new method recently developed for planar near-field broadband phaseless antenna measurement is adapted to work with a reduced set of points. The method is an extrapolation of the conventional off-axis holography in which a frequency sweep is made at each point of the acquisition grid, and the phase is retrieved simultaneously for all the frequencies by filtering the hologram in the time-domain. As the phase is retrieved independently at each acquisition point, non redundant sampling techniques can be applied without the need of increasing the spatial bandwidth of the hologram. The bounds of the error in the far field pattern regarding the effect of mechanical errors and noise are studied by means of Monte Carlo simulations. A measurement example in the K_a band is presented to validate the method.**

***Index Terms*—antenna measurement, broadband, phaseless, off-axis holography, non-redundant, error analysis, Monte Carlo.**

I. Introduction

Different methods have been developed in order to characterize broadband antennas. These methods can be classified into time-domain (TD) or frequency-domain (FD), each one presenting advantages and disadvantages [1], [2].

TD techniques are the most employed techniques for broadband antenna characterization due to their high efficiency as the antenna is simultaneously characterized for the whole frequency band. Nevertheless they exhibit some drawbacks such as excessive acquisition time for complete spatial acquisitions or poor dynamic range [2]. Performance of conventional FD techniques for broadband antenna characterization is poor due to the need of carrying out a different spatial acquisition for each of the studied frequencies but, nevertheless, there are many different and very accurate techniques for near-field (NF) and far-field (FF) antenna characterization.

This work has been supported by the Ministerio de Ciencia e Innovación of Spain/FEDER under projects MIRIIEM-TEC2014-54005-P and TEC2014-55290-JIN; by the Gobierno del Principado de Asturias through the PCTI 2013-2017 GRUPIN14-114, by grant LINE 525-002-H2OCEAN, by the Academy of Finland through the DYNAMITE project and by the European Science Foundation under the RNP NEWFOCUS programme.

On the other hand, phase acquisition can be very challenging and expensive, specially at mm- and submm-wave bands, due to the need of keeping an accurate phase reference, which requires a very stable source and steady temperature conditions [3]. Phaseless techniques allow for the characterization of antennas by means of only-amplitude acquisitions, reducing the complexity of the measurement system. Furthermore, certain type of errors associated to phase measurements [4], such as flexing cable error, can be avoided with these techniques.

Other dominant sources of error in planar near-field (PNF) measurements are the probe positioning errors caused by the mechanical inaccuracies of the positioners. These errors can be easily identified and quantified by means of simulation [5]. By having knowledge of the effect that each of the error introduces in the acquisition results, the upper bounds and the tolerance of the setup to the studied errors can be established.

In this contribution, a recently developed method for phaseless broadband antenna characterization [6] is adapted to work with a reduced set of points [7]. The method is an extrapolation of the classical indirect off-axis holography method, first used for antenna metrology by Bennet [8].

The method is validated through simulation and a Monte Carlo analysis is performed to study the effect of the probe positioning errors. The results of the Monte Carlo analysis are used to determine the upper error bounds introduced in the FF pattern by these type of errors and to study the influence of each type of error separately.

After that, the method is validated through measurements and the uncertainty in the characterization of the directivity (Dir.), maximum (Max.), nulls and secondary lobe level (SLL) is obtained by means of antenna pattern comparison [9].

II. Overview of the Method

The proposed method is based on a four-step strategy consisting on the following sequential steps that are explained next: 1) A reduced set of points is obtained [7] and the interferometric field is acquired at them; 2) The phase retrieval

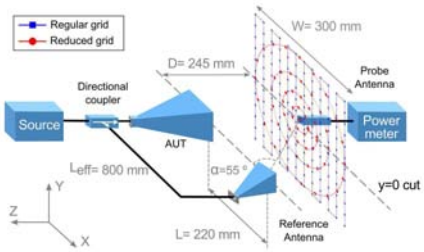

Fig. 1. Off-axis holography scheme for broadband antenna measurement.

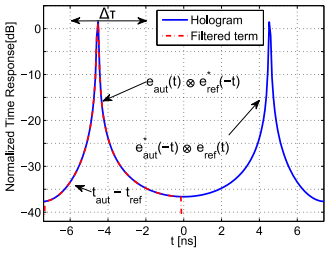

Fig. 2. Modified hologram in the time-domain for the numerical example employed in the Monte Carlo method including no error.

IV

is performed point by point in the acquisition plane simultaneously for all the frequencies [6]; 3) A Optimal Sampling Interpolation (OSI) is applied to the retrieved data to obtain the NF over a regular rectangular grid [7]; 4) Conventional NF-FF transformation is applied to the data [3]. A scheme of a typical layout for implementing the proposed method is shown in Fig. 1.

A. Phase Retrieval

At each point of the acquisition plane, the components of the fields are acquired along a set of equally spaced frequencies giving the following interferometric signal:

$$H(\vec{r},w) = |E_{aut}(\vec{r},w) + E_{ref}(\vec{r},w)|^2 = |E_{aut}(\vec{r},w)|^2 + |E_{ref}(\vec{r},w)|^2 + E_{aut}(\vec{r},w)E^*_{ref}(\vec{r},w) + E^*_{aut}(\vec{r},w)E_{ref}(\vec{r},w) \quad (1)$$

being $\vec{r}$ the position in the acquisition plane, w the angular frequency and E_{aut} and E_{ref} the fields of the AUT and the reference antenna respectively. The asterisk represents the complex conjugate of the field.

The amplitude and phase of the reference antenna have to be previously known in off-axis holography approaches and, as the square amplitude of the AUT can be separately acquired, the so-called modified hologram can be calculated as:

$$\begin{aligned} H_m(\vec{r},w) &= H(\vec{r},w) - |E_{aut}(\vec{r},w)|^2 - |E_{ref}(\vec{r},w)|^2 \\ &= E_{aut}(\vec{r},w)E^*_{ref}(\vec{r},w) + E^*_{aut}(\vec{r},w)E_{ref}(\vec{r},w) \end{aligned} \quad (2)$$

The inverse Fourier Transform (iFT) of the modified hologram produces the following signal in the TD:

$$h_m(\vec{r},t) = e_{aut}(\vec{r},t) \otimes e^*_{ref}(\vec{r},-t) + e^*_{aut}(\vec{r},-t) \otimes e_{ref}(\vec{r},t) \quad (3)$$

where e_{aut} and e_{ref} are the iFT of E_{aut} and E_{ref} respectively and $\otimes$ denotes the convolution operator.

The hologram is composed of the two cross-correlation terms as it can be seen in Fig. 2. To retrieve the phase of the AUT, the term corresponding to the convolution of $e_{aut}(\vec{r},t)$ and $e^*_{ref}(\vec{r},t)$ has to be filtered, providing no time overlap is present, as indicated in (4).

$$h_{mfiltered}(\vec{r},t) = \Pi(t_1,t_2)\{e_{aut}(\vec{r},t) \otimes e^*_{ref}(-\vec{r},t)\} \quad (4)$$

where $\Pi(t_1,t_2)$ is a rectangular window defined between t_1 and t_2.

To control the time overlap, the length of L_{eff} (see Fig. 1) can be modified so that $t_{aut} - t_{ref} + \Delta\tau < 0$, being t_{aut} and t_{ref} the time of travel of the signals from the AUT and the reference antenna to the acquisition plane, respectively, and $\Delta\tau$ the spread of the cross-correlation terms in the TD.

Once the signal has been filtered in the TD, last step is the removal of the effect of the reference antenna back in the FD:

$$E_{aut}(\vec{r},w) \simeq \frac{H_{mfiltered}(\vec{r},w)}{E^*_{ref}(\vec{r},w)} \quad (5)$$

The accuracy of the phase retrieval algorithm will depend mostly on the separation of the cross-correlation terms in the TD. It is also important to note that the use of the modified hologram in (2) requires an extra measurement for characterizing $|E_{aut}|^2$. Nonetheless the filtering process is easier and, as the real amplitude of the AUT is directly measured, the retrieved field can be composed using the measured amplitude and the retrieved phase, with the consequent error reduction.

B. Reduced Field Computation and Optimal Sampling Interpolation

In contrast to other hybrid approaches combining off-axis holography and non-redundant sampling [10], which require a modified set of non-redundant sampling points, the herein considered method can operate with standard non-redundant sampling since the phase retrieval is accomplished independently at each point of the acquisition grid.

Since a plane-polar grid is considered, the observation curves can be parametrized by a radial coordinate ξ and an azimuthal coordinate φ [7]. Although the previous points are equally spaced in a transformed coordinate system so that the bandwidth of the signal can be reduced to a minimum [7], they are not equally spaced in the standard Cartesian coordinate system as required by standard NF-FF algorithms. Thus, it is usual to resort to an OSI to compute the field at a regular grid.

The first step is to compute the reduced field, which exhibits minimum bandwidth in the transformed domain, by including a phase factor γ [7]:

$$F(\xi,\varphi) = e^{j\gamma(\xi)}E(\xi,\varphi) \quad (6)$$

In order to retrieve the field at a given coordinate (r,φ), two OSI are required. The first interpolation retrieves the field

at all the rings for the requested azimuth angle:

$$F(\xi_n, \varphi) = \sum_{m=m_0-p+1}^{p+1} F(\xi_n, \varphi_m) G_\varphi(\varphi - \varphi_m) \quad (7)$$

where G_φ is the interpolation function for a closed curve that can be expressed as a product of the Dirichlet function and a Tschebyscheff polynomial [7], $m_0 = \lfloor \varphi / \Delta\varphi \rfloor$ being $\Delta\varphi$ the sampling step along the φ coordinate and $2p$ is the number of samples used to calculate each point. After that, the field can be retrieved by interpolating the reduced field along the radial coordinate and removing the phase factor:

$$E(\xi(r), \varphi) = e^{-j\gamma(\xi)} \sum_{n=n_0-q+1}^{q+1} F(\xi_n, \varphi) G_\xi(\xi(r) - \xi_0) \quad (8)$$

In this case, the interpolation function is related to an open curve and, consequently, it is expressed as a function of a prolate spheroidal function and cardinal sine function and the remaining parameters are defined analogous to the azimuthal interpolation case.

III. Monte Carlo Analysis

A Monte Carlo method has been implemented in order to evaluate the uncertainty caused by the positioning errors and the noise in the main parameters of the FF pattern.

The dimensions and the physical layout of the elements, are shown in Fig. 1. The AUT is a 30 dB gain pyramidal horn, vertically polarized, and the reference antenna is a small 15 dB horn antenna placed at 200 mm of the AUT. The reference antenna has a 55° tilt so that is pointing to the center of the acquisition plane; the probe antenna is identical to the reference antenna.

The acquisition grid, at 245 mm of the aperture of the AUT has 2055 points, while the regular grid for the amplitude and phase acquisition has 13225 points. Therefore the acquisition time for the reduced set of points is reduced 6 times with respect to the regular grid. 201 equally spaced frequency points from 26.5 GHz to 40 GHz are considered.

The inputs to the Monte Carlo method are the equivalent magnetic currents (EMC) in the aperture of the AUT and reference antenna, and the ideal acquisition grid. For each trial, the acquisition grid is modified with positioning errors before calculating the radiated NF. A reference pattern is calculated from the EMC in the aperture of the AUT considering amplitude and phase data by means of direct integration.

Positioning errors are introduced separately to study the effect of planarity errors (Z-axis) and plane positioning errors (XY-plane). The error is modeled according to the positioners accuracy data given by the manufacturer following a uniform distribution with ± 0.1 mm limits for each axis. The effect of the noise has also been studied by adding White Gaussian Noise (WGN) to the radiated field according to a 45 dB Signal to Noise Ratio (SNR) level.

The effect of the errors in the main parameters of the FF pattern is obtained for 150 independent trials. Simulations are repeated for the case of considering amplitude and phase acquisitions on a regular grid that produces a FF pattern with the same valid angular margin than the reduced set of points, in order to compare the results. The outcomes of the method for two different frequencies are gathered in Tables I, II and III. The selected frequencies are 33 GHz, center of the band, and 38 GHz, in the upper side of the band but not affected for the windowing error introduced in the phase retrieval (see Fig. 3, Fig. 6 and [6] for further details).

First step for each trial is the phase retrieval, done simultaneously for all the frequencies at each point of the reduced set of points. To quantify its quality, the following mean error is calculated at each frequency considering all the spatial points:

$$error(f)[\%] = \frac{\| E_{sim}(f) - E_{ret}(f) \|_2}{\| E_{sim}(f) \|} \quad (9)$$

wherein $\| \cdot \|_2$ is the Euclidean norm, E_{sim} is the field of the AUT obtained from simulations with phase information, and E_{ret} is the retrieved field of the AUT.

Fig. 3 represents the mean error for each frequency as defined in (9) considering random trials of the Monte Carlo method for the different types of error. As the phase retrieval is performed point by point in the acquisition plane, relative positioning between each point is expected to have low influence in the phase retrieval error. Nevertheless the mean error increases from $0.18\,\%$ (considering no error) to approximately $0.5\,\%$ for the case of considering errors in XY or Z. This is due to the fact that the square amplitude of the AUT and the reference antenna have to be independently acquired to calculate the modified hologram in (2), and these acquisitions are affected by different errors whose impact in the final results is accumulated. Therefore the acquired fields will be different and the quality of the phase retrieval is slightly deteriorated.

The effect of the noise is more noticeable in the quality of the phase retrieval producing a mean error higher than the $2\,\%$ for some frequencies. The higher level of the phase retrieval error in presence of noise is closely related to the difference in the signal levels from the AUT and the reference branches, making impossible to retrieve the phase of the AUT if the level of the reference signal is more than 20 dB below the level of the AUT for a 45 dB SNR, as it is shown in the turquoise trace of Fig. 3. The previous values correspond to a random execution of the Monte Carlo Method. Mean error of the phase retrieval has been studied for all the trials and its statistical variation is shown in the first row of Tables I, II and III together with the rest of the studied parameters.

Next step after phase retrieval is to perform an OSI to obtain the NF in a regular grid to enable the use of conventional techniques for the NF-FF transformation. Fig. 4 shows the main cuts of the FF pattern for random trials of the Monte Carlo method for the two studied frequencies in order to compare the effect of the errors. As expected, the more noticeable differences are in the patterns corresponding to the reduced field affected by noise for levels below -28 dB. The rest of patterns exhibit an analogous behavior and are very similar inside the valid margin of the NF-FF transformation.

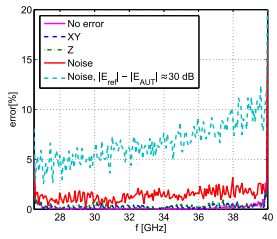

Fig. 3. Mean error of the phase retrieval at each frequency for random Monte Carlo trials, each one considering one type of error.

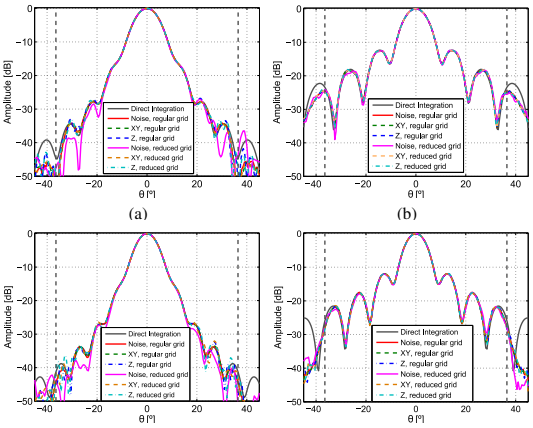

Fig. 4. Main cuts of the far-field patterns for random trials of the Monte Carlo method. (a) $\phi = 0°$ cut for 33 GHz, (b) $\phi = 90°$ cut for 33 GHz, (c) $\phi = 0°$ cut for 38 GHz, (d) $\phi = 90°$ cut for 38 GHz.Vertical grey lines at $\pm 36°$indicate the valid margin of the NF-FF transformation.

If the outcomes of the Monte Carlo method, shown in Tables I, II and III are analyzed, it can be clearly seen that the uncertainties obtained for the case of using the proposed method, phaseless, broadband and over a reduced set of points, are slightly higher than the uncertainties obtained with a complex acquisition over a regular grid of points for the case of considering XY positioning errors. As the OSI is done from error contaminated data from the phase retrieval, it also contributes to rise the error level. For the planarity errors the uncertainties are almost equal for the phaseless reduced set of points and the complex acquisition over the regular grid. This is due to the fact that planarity errors do not produce noticeable errors in indirect holography setups [11].

The uncertainty obtained for the case of adding noise with the proposed method is much higher, nevertheless, better SNR than the 45 dB used for this example can be easily achieved with a planar NF measurement system, reducing the effect of the error in the phase retrieval step. The combined uncertainty values for the three types of error, u_i, shown in Table IV, is calculated as:

$$u_c = \sqrt{\sum_{i=1}^{3} u_i^2} \tag{10}$$

TABLE I
STATISTICAL RESULTS OF THE MONTE CARLO ANALYSIS CONSIDERING RANDOM ERRORS IN THE XY POSITIONING OF THE SCANNER [1 2 3]

	Complex acquisition, regular grid				Phaseless acquisition, reduced grid			
	33 GHz		38 GHz		33 GHz		38 GHz	
Parameter	mean	std	mean	std	mean	std	mean	std
Phase ret. [%]	-	-	-	-	0.195	0.0855	0.158	0.0001
Dir [dBi]	29.572	0.0027	30.520	0.0029	29.571	0.0085	30.524	0.0267
Max [dB]	0.000	0.0026	-0.001	0.0029	-0.002	0.0071	-0.009	0.0261
1st SLL [dB]	-12.544	0.0699	-12.134	0.0110	-12.502	0.0513	-12.168	0.0986
1st null [dB]	-15.989	0.0160	-14.613	0.0145	-15.918	0.0686	-14.644	0.1848
2nd SLL [dB]	-18.435	0.0170	-17.767	0.0188	-18.512	0.0880	-17.598	0.1925
2nd null [dB]	-25.611	0.0435	-25.728	0.0475	-27.280	0.4671	-25.295	0.7511

[1] References (33 GHz): Dir=30.841 dBi, SLL1=-12.34 dB, Null1=-16.28 dB, SLL2=-18.08 dB, Null2=-28.23 dB.
[2] References (38 GHz): Dir=30.483 dBi, SLL1=-12.50 dB, Null1=-15.06 dB, SLL2=-17.68 dB, Null2=-26.85 dB.
[3] SLL and Null values for the $\phi = 90°$ cut.

TABLE II
STATISTICAL RESULTS OF THE MONTE CARLO ANALYSIS CONSIDERING RANDOM ERRORS IN THE PLANARITY OF THE SCANNER [1 2 3]

	Complex acquisition, regular grid				Phaseless acquisition, reduced grid			
	33 GHz		38 GHz		33 GHz		38 GHz	
Parameter	mean	std	mean	std	mean	std	mean	std
Phase ret. [%]	-	-	-	-	0.197	0.0001	0.195	0.0001
Dir [dBi]	29.569	0.0164	30.517	0.0185	29.570	0.0183	30.525	0.0233
Max [dB]	-0.007	0.0166	-0.010	0.0186	-0.006	0.0179	-0.007	0.0222
1st SLL [dB]	-12.626	0.1508	-12.138	0.0871	-12.520	0.1148	-12.171	0.0889
1st null [dB]	-15.989	0.1137	-14.648	0.1367	-15.936	0.1370	-14.610	0.1497
2nd SLL [dB]	-18.421	0.1177	-17.725	0.1305	-18.455	0.1508	-17.633	0.1520
2nd null [dB]	-26.251	0.7056	-25.727	0.4425	-26.909	0.5701	-25.438	0.6857

TABLE III
STATISTICAL RESULTS OF THE MONTE CARLO ANALYSIS ADDING NOISE TO THE ACQUISITION REPRESENTING 45 DB DYNAMIC RANGE[1 2 3]

	Complex acquisition, regular grid				Phaseless acquisition, reduced grid			
	33 GHz		38 GHz		33 GHz		38 GHz	
Parameter	mean	std	mean	std	mean	std	mean	std
Phase ret. [%]	-	-	-	-	0.401	0.0057	0.399	0.0057
Dir [dBi]	29.571	0.0058	30.520	0.0026	29.578	0.0384	30.537	0.0333
Max [dB]	-0.001	0.0056	-0.001	0.0026	-0.008	0.0368	-0.003	0.0317
1st SLL [dB]	-12.597	0.1415	-12.134	0.0113	-12.567	0.1748	-12.163	0.1380
1st null [dB]	-15.986	0.0371	-14.611	0.0175	-15.957	0.2317	-17.734	0.3025
2nd SLL [dB]	-18.433	0.0374	-17.760	0.0217	-18.597	0.3470	-14.645	0.2210
2nd null [dB]	-25.664	0.3062	-25.725	0.0549	-27.018	0.8627	-25.484	0.8850

IV. MEASUREMENT RESULTS

In order to validate the method, a 25 dB gain pyramidal horn antenna is characterized in the K_a band with a reduced set of points. The measurement setup, shown in Fig. 5, is the same used for the Monte Carlo method (see Fig. 1) in order to check if the uncertainty of the measurements is within the obtained bounds. 401 equally spaced frequency points are measured. Phase retrieval error is depicted in Fig. 6. Mean value of the error for the complete band is 1.39%, being its value of 1.78% and 0.88% at the frequencies of 33 and 38 GHz. However, the error tend to be higher in the upper part of the band because the power level of the reference antenna is lower for those frequencies.

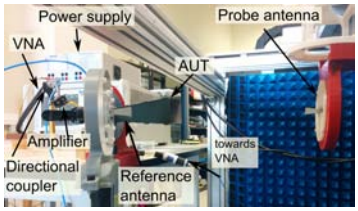

Fig. 5. Measurement setup.

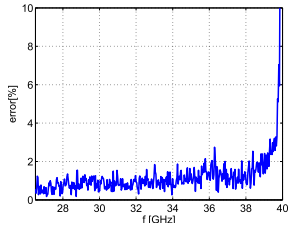

Fig. 6. Phase retrieval error for the measurements in the K_a band with the reduced set of points.

Finally the FF cuts are shown in Fig. 7 with the root mean square (rms) value of the equivalent stray signal (ESS) used to determine the uncertainties, gathered in Table IV as described in [9]. The uncertainty values of the measurements are in the same order than the values obtained from the combined uncertainty of the Monte Carlo analysis. Nevertheless, for some parameters the uncertainty of the measurements is slightly higher. This might be due to the fact that other type of errors such as multiple reflections and alignment error can be influencing the measurements.

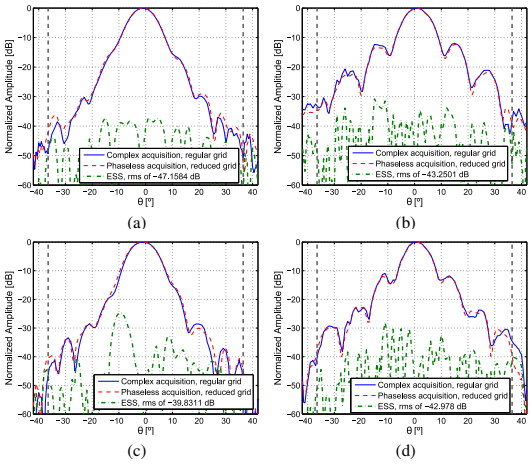

Fig. 7. Main cuts of the far-field patterns of the measured antenna. (a) $\phi = 0°$ cut for 33 GHz, (b) $\phi = 90°$ cut for 33 GHz, (c) $\phi = 0°$ cut for 38 GHz, (d) $\phi = 90°$ cut for 38 GHz. Vertical grey lines at $\pm 36°$ indicate the valid margin of the NF-FF transformation. The rms value of the ESS is shown in the legend of each figure.

TABLE IV
UNCERTAINTY RESULTS FOR THE MEASUREMENTS IN THE K_a BAND

	Measurements, reduced grid		Monte Carlo u_c, regular / reduced grid	
Parameter	std, 33 GHz	std, 38 GHz	std, 33 GHz	std, 38 GHz
Max [dB]	0.0595	0.0614	0.0331 / 0.0675	0.0416 / 0.0815
1st SLL [dB]	0.2317	0.2154	0.1193 / 0.3981	0.1425 / 0.3602
1st null [dB]	0.3960	0.2725	0.2481 / 0.5162	0.1757 / 0.3905
2nd SLL [dB]	0.6203	0.7101	0.3791 / 1.0166	0.2140 / 0.6361
2nd null [dB]	1.0988	1.2451	0.5734 / 1.2704	0.3608 / 1.1313

V. CONCLUSION

A new antenna measurement method based on indirect off-axis holography is presented. The method is capable of broadband phaseless antenna characterization from a reduced set of points; for this example a reduction factor of 6 can be achieved. The error bounds in the FF pattern caused by probe positioning errors and the presence of noise are statistically characterized by means of a Monte Carlo analysis and compared to the values obtained with a conventional acquisition of complex data over a rectangular grid.

The method is validated through measurements and the uncertainty for the main parameters of the FF pattern is obtained by means of antenna pattern comparison.

Uncertainty for the proposed method is slightly higher due to the cumulative effect of the error across the four steps of the algorithm but for the majority of parameters, the uncertainties are within the bounds obtained with the Monte Carlo method and are comparable to the values obtained with the complex acquisition over a regular grid.

REFERENCES

[1] J. Young, D. Svoboda, and W. Burnside, "A comparison of time- and frequency-domain measurement techniques in antenna theory," *IEEE Trans. Antennas Propag.*, vol. 21, no. 4, pp. 581–583, Jul. 1973.

[2] Y. Huang, K. Chan, and B. Cheeseman, "Review of broadband antenna measurements," in *1st European Conf. on Antennas and Propag.. EuCAP 2006*, Nov. 2006, pp. 1–4.

[3] A. Yaghjian, "An overview of near-field antenna measurements," *IEEE Trans. Antennas Propag.*, vol. 34, no. 1, pp. 30–45, Jan. 1986.

[4] J. Tuovinen, A. Lehto, and A. Raisanen, "A new method for correcting phase errors caused by flexing of cables in antenna measurements," *IEEE Trans. Antennas Propag.*, vol. 39, no. 6, pp. 859–861, Jun 1991.

[5] A. Newell, "Error analysis techniques for planar near-field measurements," *IEEE Trans. Antennas Propag.*, vol. 36, no. 6, pp. 754–768, Jun. 1988.

[6] A. Arboleya, J. Laviada, J. Ala-Laurinaho, Y. Álvarez, F. Las-Heras, and A. V. Räisänen, "Phaseless characterization of broadband antennas," *IEEE Trans. Antennas Propagat.*, vol. 64.[Accepted for publication].

[7] O. Bucci, C. Gennarelli, and C. Savarese, "Fast and accurate near-field far-field transformation by sampling interpolation of plane polar measurements," *IEEE Trans. Antennas Propagat.*, vol. 39, pp. 48–55, Jan. 1991.

[8] J. Bennett, A. Anderson, P. McInnes, and A. Whitaker, "Microwave holographic metrology of large reflector antennas," *IEEE Trans. Antennas Propag.*, vol. 24, no. 3, pp. 295–303, May 1976.

[9] A. Newell and G. Hindman, "Antenna pattern comparison using pattern subtraction and statistical analysis," in *5th European Conf. on Antennas and Propag. (EuCAP)*, Apr. 2011, pp. 2684–2687.

[10] J. Laviada and F. Las-Heras, "Phaseless antenna measurement on non-redundant sample points via Leith-Upatnieks holography," *IEEE Trans. Antennas Propag.*, vol. 61, no. 8, pp. 4036–4044, Aug. 2013.

[11] G. Junkin, T. Huang, and J. Bennett, "Holographic testing of terahertz antennas," *IEEE Trans. Antennas Propag.*, vol. 48, no. 3, pp. 409–417, Mar. 2000.

IV

Publication V

A. Arboleya, J. Laviada, Y. Álvarez-López and F. Las-Heras **"Versatile measurement system for imaging setups prototyping,"** *9th European Conference on Antennas and Propagation (EUCAP'15),* pp. 1–5 (Convened sessions), Lisbon (Portugal), 12–17 Apr. 2015.

Versatile Measurement System for Imaging Setups Prototyping

Ana Arboleya[1], Jaime Laviada[2], Yuri Álvarez[1], Fernando Las-Heras[1]
[1]Área de Teoría de la Señal y Comunicaciones, Universidad de Oviedo
Edif. Polivalente Mod. 8, Campus Universitario de Viesques. E-33202, Gijón (Asturias), Spain
Email: aarboleya@tsc.uniovi.es, yalopez@tsc.uniovi.es, flasheras@tsc.uniovi.es
[2]Grupo de Antenas, Universidad Pública de Navarra
Edif. de los Tejos, Sala de asociados, Planta 2, Campus Arrosadía, E-31006, Pamplona (Navarra), Spain
Email: jaime.laviada@unavarra.es

***Abstract*—An XYZ scanner and its potential capabilities for different types of electromagnetic imaging setups is described in this contribution. To illustrate the operation of the system, two different imaging techniques and setups are presented as examples. A phaseless measurement setup implemented at the Ku band, and a measurement setup based on amplitude and phase acquisitions for the W band.**

***Index Terms*—setup, imaging, measurement.**

I. Introduction

Inverse scattering techniques have received great interest due to the diversity of applications in fields such as medicine [1], security [2] or defense [3], and their non-destructive nature.

Depending on the application and the working frequency band, some techniques can be more suitable than others; e.g. complex acquisitions become extremely difficult in the millimeter and sub-millimeter bands owing to the need of keeping a constant phase reference, therefore, in order to lower the overall cost and complexity of the setups, phaseless approaches are becoming more popular [4]–[9].

The developed scanner, that has been previously validated through several measurement campaigns [6]–[10] and error characterization measurements [11], allow quick testing of different types of imaging setups in order to validate their correct working.

This contribution is structured as follows. First, a short description of the measurement system is made, indicating the main characteristics of the mechanical and Radiofrequency (RF) equipment. Next, two measurement examples to illustrate the system capabilities and the type of setups for imaging applications developed, are explained. Contribution is ended with the main conclusions of the work.

II. Measurement System Description

The XYZ scanner of the Universidad de Oviedo is a cost-efficient planar and cylindrical range measurement system that allows field measurements at microwave, mm- and sub-mm frequency bands (Fig. 1). The system has a modular design and it can be easily adapted to validate different setups including antenna measurements as well as inverse scattering problems. A complete description of the system can be found in [12].

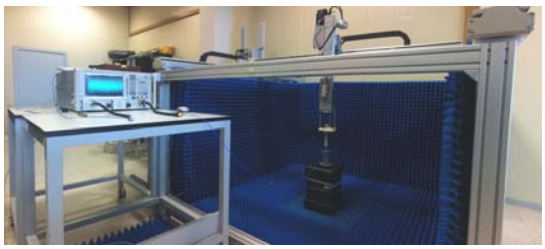

Fig. 1. XYZ Scanner of the Universidad de Oviedo.

A. Mechanical Subsystem

The mechanical subsystem is composed of a multi-axis linear stage that can perform sweeps in the XY, YZ and XZ planes and a rotary stage that also enables the system to perform cylindrical acquisitions. The positioners are remotely controlled from a PC interface and can reach 150 mm/s speed with relative precision of 0.01 mm.

The housing of the system is an aluminum chassis with a working area of 1500 mm x 1500 mm x 1100 mm, covered with electromagnetic pyramidal absorber.

B. Radiofrequency (RF) equipment

The RF subsystem equipment changes depending on the implemented application. Main component is a vector network analyzer with a working range from 10 MHz to 67 GHz that can be extended by two sets of frequency extension modules from 75 GHz to 110 GHz and from 220 GHz to 330 GHz. Depending on the setup, the system is complemented by several off-the-shelf components such as power combiners, phase shifters, directional couplers, etc.

III. Measurement examples

Two different setups are presented in this section to show the performance of the system and developed setups for imaging applications. First example is a phaseless setup based on off-axis holography in the K_u band at 15 GHz and second setup is presented to illustrate system performance at higher frequencies, in the W band.

Although the phaseless setup would be more suitable for the W band example, the lack of a phase shifter and a directional coupler in the W band, makes impossible to validate this specific setup in this band. Nevertheless, some experimental setups have been measured at sub-millimeter wave bands that demonstrate that phaseless indirect holographic setups are suitable for working in mm- and submm-wave bands. The lack of phase shifters in these bands have been overcame by introducing mechanical shifts in the acquisition plane [6].

Performance of the algorithms regarding the number of points depends on the size of the object whose profile is being reconstructed. Sampling requirements are less demanding for the second example with complex acquisitions, as it is possible to retrieve the object working with a sampling rate of $\lambda/4$. However, sampling requirements are stronger for the phaseless case, being necessary to work under $\lambda/8$ at least in one of the dimensions of the acquisition plane [7].

Concerning the CPU time of the algorithms, phaseless algorithms are generally a two-step algorithm in where, before performing the object reconstruction, it is necessary to execute the phase retrieval algorithm. Despite this additional stage, the phase retrieval is based on efficient Fourier Transforms. Consequently, the time increment is negligible with respect to the time required for solving a conventional inverse scattering problem. Error of the phase retrieval for this type of phaseless algorithms is less than 2% [8].

Otherwise, as the phaseless setup avoids the use of expensive devices such as a vector network analyzer, complexity and cost of this type of setup is lower than for the complex acquisition setup, making these systems a very attractive solution for the implementation of imaging applications.

V

A. Example I: Phaseless imaging setup at 15 GHz

In this case, an indirect holography setup based on synthesized plane waves [4], [5] has been extended for the case of considering the scattering from an unknown object.

Performance of this setup is illustrated by solving an inverse scattering problem where the object under analysis is a perforated square plate of size $10 \times 10\,\text{cm}$. The hole of $2\,\text{cm}$ radius, is moved $1\,\text{cm}$ from the center of the plate for each direction parallel to its edges.

The object has been measured at $15\,\text{GHz}$ with a quasi-monostatic setup shown in Fig. 2. The distance between the antennas is set to $d = 23.5\,\text{cm}$. The measurement surface is a $40 \times 32\,\text{cm}$ plane at $D = 1\,\text{m}$ from the antennas. A $1.5\,\text{mm}$ sampling is used in the x- and y- axes.

This type of setups based on off-axis holography, are founded on combining the scattered field from the Object Under Test (OUT), E_s, with a reference field, E_r, whose amplitude and phase are known [7]. The reference signal is synthesized from a sample of the source by means of a phase shifter and combined with the scattered field as shown in Fig.2, being the measured hologram:

$$H(x, y, z_0) = |E_s(x, y, z_0) + E_r(x, y, z_0)|^2 \tag{1}$$

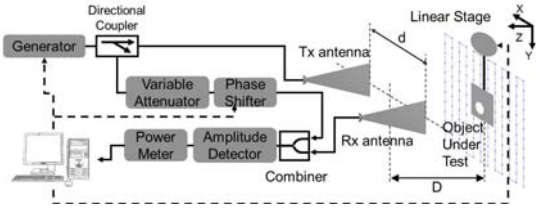

Fig. 2. Quasi-monostatic setup with synthesized plane-wave.

The synthesized reference signal is modeled as a plane wave as indicated in equation (2). E_0 represents the complex amplitude of the signal, while k_x^{pw} and k_y^{pw} define the wavenumber components of the plane wave for the x and y directions respectively.

$$E_r(x, y, z) = E_0 e^{-j(k_x^{pw} x + k_y^{pw} y)} \tag{2}$$

The acquired hologram can be further developed as indicated in equation (3), wherein the asterisk indicates the complex conjugate of the signals.

$$\begin{aligned} H(x, y, z_0) &= |E_s(x, y, z_0)|^2 \\ &+ |E_0 e^{-j(k_x^{pw} x + k_y^{pw} y)}|^2 \\ &+ E_0 E_s^*(x, y, z_0) e^{-j(k_x^{pw} x + k_y^{pw} y)} \\ &+ E_0^* E_s(x, y, z_0) e^{j(k_x^{pw} x + k_y^{pw} y)} \end{aligned} \tag{3}$$

From this point on, and without loss of generality, it will be assumed that the k_y^{pw} component is set to zero and the phase shift is applied along the x-axis so that the phase difference between two different acquisition lines is $\Delta\phi = \frac{\pi}{2}$. Thus, the phase shifter only needs to provide four different values.

If the Fourier Transform (FT) of the hologram is performed, it is possible to observe that the spectrum of the hologram ($\tilde{H}(k_x, k_y, z_0)$) is composed of the spectrum of E_s and E_s^* centered at the spectral points $\pm k_x^{pw}$ and scaled by E_0, and two other central terms regarding the square amplitude of the reference and the scattered signals.

The representation of the spectrum in equation (4) is shown in Fig. 3 wherein the tilde is used to denote Fourier Transform and W describes the bandwidth of the fields:

$$\begin{aligned} \tilde{H}(k_x, k_y, z_0) = FT\{H(x, y, z_0)\} = \\ |E_0|^2 \delta(k_x, k_y) + |\tilde{E}_s(x, y, z_0)|^2 + \\ E_0 \tilde{E}_s^*(-k_x - k_x^{pw}, -k_y, z_0) + \\ E_0^* \tilde{E}_s(k_x - k_x^{pw}, k_y, z_0) \end{aligned} \tag{4}$$

The term centered in k_x^{pw}, corresponding to the spectrum of the scattered field, can be filtered out, and the phase retrieval can be done after that, by performing the inverse Fourier Transform of the filtered term and dividing by the complex conjugate of the reference field.

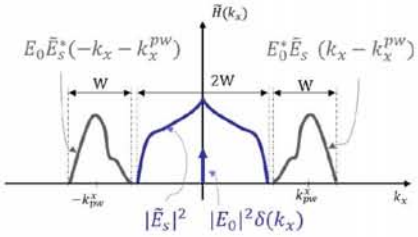

Fig. 3. Spectrum of the measured hologram.

To correctly filter out the desired term of the spectrum, the sampling rate and the phase shifts have to be carefully selected as indicated in equation (5) to get $k_x^{pw} \geq \frac{3W}{2}$

$$k_x^{pw} = \frac{\Delta\phi}{\Delta x} \tag{5}$$

In this example, with $\Delta\phi = \frac{\pi}{2}$ and $\Delta x \simeq \frac{\lambda}{13}$, the filtered term of the spectrum is centered around $k_x^{pw} = 3.25k_0$, beyond the visible margin of the spectrum ($2k_0$) and, therefore, overlapping is avoided.

As previously mentioned, postprocessing of the acquired data requires the knowledge of the synthesized reference source, so normally, an extra measurement is needed to characterize the reference signal.

The insertion losses of the phase shifter that has been employed in this setup depend on the desired phase shift as well as on the input power. Thus, the reference source will not have a uniform amplitude but a modulated one depending on the x-position. Since only four phase shifts have been employed, this amplitude is expected to be cyclically repeated. In order to estimate the amplitude of the reference source, we employ the average value measured on the first 20 rows of the acquisition plane where the scattered field can be neglected. Thus, each possible value is estimated from five rows. After that, the reference source for the entire acquisition plane is constructed by repeating the four estimated values with the corresponding phase, and there is no need of performing an independent acquisition to characterize the reference signal.

The retrieved amplitude and phase for the scattered field are shown in Fig. 4. The reflectivity computed from the previous values, using an inverse Fast Multipole Method (iFMM) as described in [13], is depicted in Fig. 5. An excellent agreement with the real object is found.

B. Example II: Amplitude and phase imaging setup for the W band

In this example, the quasi-monostatic setup is modified to work at 110 GHz, but image reconstruction is acomplished by processing the acquired amplitude and phase by means of the method described in [2]. An schematic ilustration of the setup is shown in Fig.6.

The object under analysis is composed by two door keys of an approximated size of 6×3 cm with small details. For

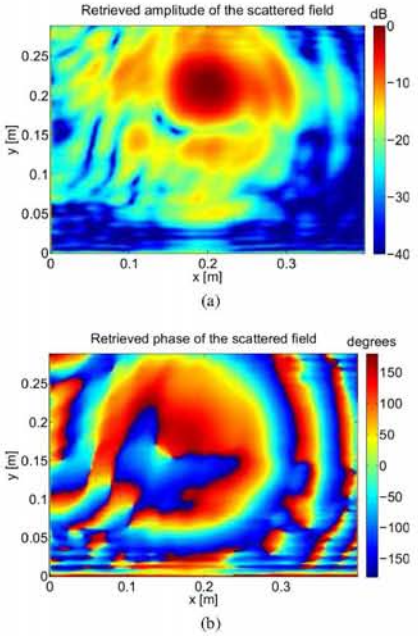

Fig. 4. Retrieved electric field: a) Normalized amplitude; b) Phase.

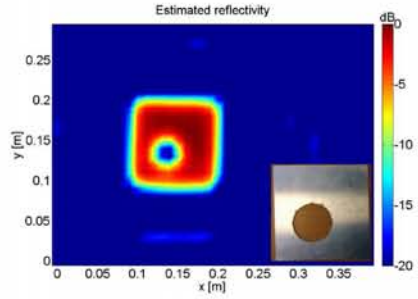

Fig. 5. Normalized estimated reflectivity from the phaseless acquisition.

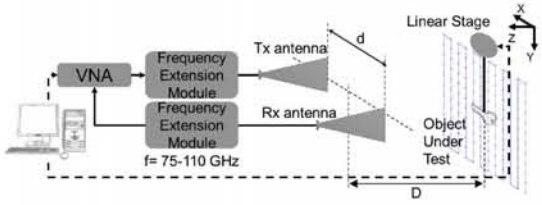

Fig. 6. Quasi-monostatic setup for amplitude and phase acquisition.

this setup the distance between antennas has been fixed to $d = 11$ cm. The measurement surface is a 15×20 cm plane at $D = 30$ m from the antennas and a 0.68 mm sampling is used in the x- and y- axes.

The reconstruction algorithm aims to obtain the reflectivity function, $f(x, y, z)$ that characterizes the OUT. The employed technique relies on the use of the Fourier Transforms so it can be efficiently implemented by the use of the Fast Fourier Transform (FFT) algorithm. Besides, this technique can be used with wide beamwidths and for OUT in the near field of the scanned aperture.

Instead of acquiring the data by means of a two dimensional sweep of the transmitter and receiver antennas, all the RF components are placed in a fixed position and the OUT is attached to the multiaxis linear stage and moved through the measurement surface previously defined. By doing this, the error introduced by the flexing of the cables is avoided.

As the OUT is moved through all the points of the acquisition plane, the recorded response in the receiver, would be, as defined in equation (6), the superposition of the reflectivity of each point of the target, multiplied by the roundtrip phase to that point:

$$s(x', y') = \int\int f(x, y, z) e^{-j2k\sqrt{(x-x')+(y-y')+(z-z')}} dxdy \tag{6}$$

wherein the primed coordinates indicate the position of the transceiver and the unprimed ones are used to define the position of the OUT. As in the previous example, k denotes the wavenumber for the working frequency.

Taking into account that the exponential term in equation (6) can be expressed as indicated in equation (7), the acquired scattered field can be further developed in terms of two dimensional Fourier Transforms (equation (8)).

$$e^{-j2k\sqrt{(x-x')+(y-y')+(z-z')}} = \int\int e^{jk_x'(x-x')+jk_y'(y-y')+jk_z z_0} dk_x' dk_y' \tag{7}$$

$$s(x', y') = \int\int FT_{2D}[f(x, y)] e^{jk_z z_0} e^{j(k_x' x' + k_y' y')} dk_x' dk_y' = FT_{2D}^{-1}[FT_{2D}[f(x, y)] e^{jk_z z_0}] \tag{8}$$

Being FT_{2D} and FT_{2D}^{-1} the two dimensional Fourier Transform and the inverse two dimensional Fourier Transform respectively.

Finally, using the Fourier Transform relations, the reflectivity of the OUT can be obtained as [2]:

$$f(x, y) = FT_{2D}^{-1}[FT_{2D}[s(x', y')] e^{-jk_z z_0}] \tag{9}$$

Wherein k_z can be calculated from equation (10)

$$k_x^2 + k_y^2 + k_z^2 = (2k)^2 \Longrightarrow k_z = \sqrt{4k^2 - k_x^2 - k_y^2} \tag{10}$$

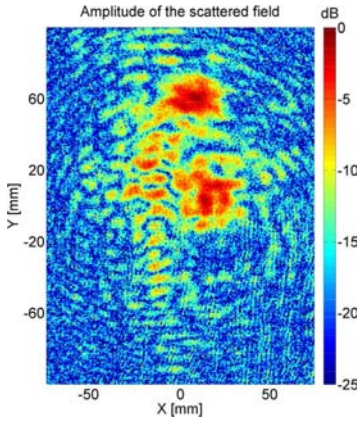

(a)

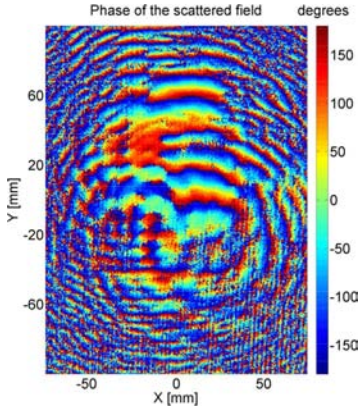

(b)

Fig. 7. Acquired electric field: a) Normalized amplitude; b) Phase.

The acquired amplitude and phase for the scattered field are shown in Fig. 7, and the computed reflectivity, depicted in Fig. 8, shows a very good agreement with the objects under study. Much smaller details can be retrieved at higher frequency bands at the expense of increasing the complexity and cost of the setup.

IV. Conclusion

A measurement system for quick prototyping of imaging setups is presented. Capabilities of the system are demonstrated with two different imaging setups in two different frequency bands.

The obtained results are in very good agreement with the studied targets for both cases, however, some differences can be outlined between both setups. Acquisition time is higher for the phaseless setup, whose sampling requirements are stronger in order to correctly retrieve the phase from the acquired data.

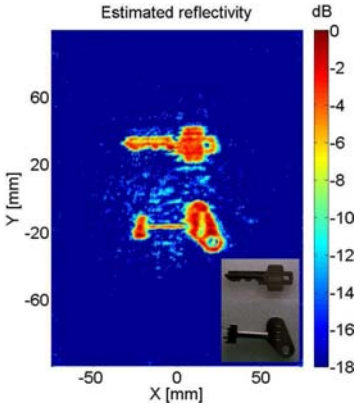

Fig. 8. Normalized estimated reflectivity from the complex acquisition.

Nevertheless, the cost and complexity of the scalar devices employed in the phaseless setups are much more lower than for the systems that work with amplitude and phase data, making phaseless systems very interesting despite the higher sampling rates.

Although in this examples targets were not concealed, this type of setups have proven to work very effectively with concealed or buried objects [2], [8] making them very suitable for this type of applications.

ACKNOWLEDGMENT

This work has been supported by Ministerio de Ciencia e Innovación of Spain/FEDER under projects TEC2011-24492, CSD2008-00068 and MICINN-11-IPT-2011-0951-390000, by Ministerio de Economía y Competitividad under postdoctoral fellowship FPDI-2013-16278, by the Gobierno del Principado de Asturias (PCTI)/FEDER-FSE under projects PC10-06, EQUIP08-06, FC09-C0F09-12, EQUIP10-31 and grant BP11-169 and by the European Union under COST IC1102 (VISTA) action.

REFERENCES

[1] E. J. Bond, X. Li, S. Hagness, and B. Van Veen, "Microwave imaging via space-time beamforming for early detection of breast cancer," *IEEE Trans. Antennas Propag.*, vol. 51, no. 8, pp. 1690–1705, Aug 2003.

[2] D. Sheen, D. McMakin, and T. Hall, "Three-dimensional millimeter-wave imaging for concealed weapon detection," *IEEE Trans. Microw. Theory Tech.*, vol. 49, no. 9, pp. 1581–1592, Sep 2001.

[3] Q. Dong and C. Rappaport, "Microwave subsurface imaging using direct finite-difference frequency-domain-based inversion," *IEEE Trans. Geosci. Remote Sens.*, vol. 47, no. 11, pp. 3664–3670, Nov 2009.

[4] D. Smith, M. Leach, M. Elsdon, and S. Foti, "Indirect holographic techniques for determining antenna radiation characteristics and imaging aperture fields," *IEEE Antennas Propag. Mag.*, vol. 49, no. 1, pp. 54–67, Feb 2007.

[5] V. Schejbal, V. Kovarik, and D. Cermak, "Synthesized-reference-wave holography for determining antenna radiation characteristics," *IEEE Antennas Propag. Mag.*, vol. 50, no. 5, pp. 71–83, Oct 2008.

[6] J. Laviada Martinez, Y. Alvarez-Lopez, A. Arboleya-Arboleya, C. Garcia-Gonzalez, and F. Las-Heras, "A modified phaseless inverse scattering setup based on indirect holography implemented at submillimeter-wave band," *IEEE Trans. Antennas Propag.*, vol. 61, no. 9, pp. 4876–4881, Sept 2013.

[7] J. Laviada, Y. A Ivarez Lopez, A. Arboleya-Arboleya, C. Garcia-Gonzalez, and F. Las-Heras, "Inverse scattering with phase retrieval based on indirect holography via synthesised plane-waves," *IET Microw., Antennas, Propag.*, vol. 6, no. 12, pp. 1389–1398, September 2012.

[8] J. Laviada, A. Arboleya-Arboleya, Y. Alvarez-Lopez, C. Garcia-Gonzalez, and F. Las-Heras, "Phaseless synthetic aperture radar with efficient sampling for broadband near-field imaging: Theory and validation," *IEEE Trans. Antennas Propag.*, vol. PP, no. 99, pp. 1–1, 2014.

[9] J. Laviada Martinez, A. Arboleya-Arboleya, Y. Alvarez-Lopez, C. Garcia-Gonzalez, and F. Las-Heras, "Phaseless antenna diagnostics based on off-axis holography with synthetic reference wave," *IEEE Antennas Wireless Propag. Lett.*, vol. 13, pp. 43–46, 2014.

[10] C. Garcia, A. Arboleya, Y. Alvarez, J. Laviada, and F. Las-Heras, "Measurement setup for profile reconstruction in the 90 ghz frequency band," in *2013 IEEE Antennas and Propag. Soc. Int. Symp. (APSURSI)*, July 2013, pp. 2261–2262.

[11] A. Arboleya-Arboleya, Y. Alvarez-Lopez, C. Garcia-Gonzalez, J. Laviada, and F. Las-Heras, "Error characterization tool for planar near-field antenna measurement and diagnostics applications," in *2014 IEEE Conf. on Antenna Meas. Applicat. (CAMA)*, Nov 2014, pp. 1–4.

[12] A. Arboleya, Y. Alvarez, and F. Las-Heras, "Millimeter and submillimeter planar measurement setup," in *2013 IEEE Antennas and Propag. Soc. Int. Symp. (APSURSI)*, July 2013, pp. 1–2.

[13] Y. Alvarez, J. Martinez-Lorenzo, F. Las-Heras, and C. Rappaport, "An inverse fast multipole method for geometry reconstruction using scattered field information," *IEEE Trans. Antennas Propag.*, vol. 60, no. 7, pp. 3351–3360, July 2012.

V

Publication VI

J. Laviada, Y. Álvarez-López, **A. Arboleya-Arboleya**, C. García-González and F. Las-Heras **"A modified phaseless inverse scattering setup based on indirect holography implemented at submillimeter-wave band,"** *IEEE Transactions on Antennas and Propagation*, vol. 61, no. 9, pp.4876–4881, Sept. 2013.

VI

This is the author's version of an article that has been published in this journal. Changes were made to this version by the publisher prior to publication.
The final version of record is available at http://dx.doi.org/10.1109/TAP.2013.2267714

A modified phaseless inverse scattering setup based on indirect holography implemented at submillimeter-wave band

Jaime Laviada, Yuri Álvarez-López, Ana Arboleya-Arboleya, Cebrián García-González, and Fernando Las-Heras[1]

***Abstract*—The aim of this paper is to present an enhanced phaseless inverse scattering setup and its implementation at the submillimeter-wave band. This setup is based on a modified indirect holography with synthesized reference signal so that a phase shifter is not required. Thus, a phaseless scanner can be built using a simple power detector resulting in a simplified measurement scheme very suitable to work in the millimeter-wave band and beyond. Mechanical phase shifting is used to bypass the use of electrical phase shifters. In addition, the reference signal is injected by coupling the transmitter and receiver antennas so that directional couplers and power combiners are avoided. New errors introduced by these techniques are analyzed and quantified. The method is validated with simulations as well as measurements at 300 GHz.**

***Index Terms*—phaseless acquisition, indirect holography, inverse scattering.**

I. Introduction

Millimeter and submillimeter technologies have attracted a large research effort in the last years. Some of the most important applications of the radiation at these frequencies are the defense and security scanners [1]. The main characteristics, which a *scanner* at these bands can provide if compared to one based on microwaves, are the higher resolution due to the reduced wavelength and the clothing transparency [2].

Most of the imaging algorithms that are used by electromagnetic scanners are based on inverse scattering methods which rely on amplitude and phase acquisition. Nonetheless, the phase acquisition is a complex matter at any frequency and, specially, at the millimeter-wave band and beyond. For these reason, several specific approaches for inverse scattering have been developed in the past. Some of them are derived from specific formulations such as the Born or Rytov approximations [3], [4] so that they have limitations to reconstruct strong scatterers.

Other authors have chosen to use a *two-step* strategies where, firstly, a general phase retrieval algorithm is applied and, after that, a conventional inverse scattering is used. Although this technique does not always exploit all the characteristics of the problem under analysis, it enables a modular analysis based on two independent stages. For each one, many general algorithms are available in the literature.

Regarding the first step, a large number of techniques are based on iterative schemes (e.g., [5], [6], [7], [8]) which usually require minor changes in the equipment with respect to the conventional amplitude and phase acquisition. The main weakness of these techniques is the associated risk of stagnation which can require some special care (e.g., [9]).

On the other hand, most of the *non-iterative* techniques are based on combining the desired signal with a *reference signal* that is known in amplitude and phase. The former techniques are usually known as *indirect holography* or Leith-Upatniekds holography [10] and they have shown very good properties to be used in the terahertz band [11]. The approach presented on this paper is based on this kind of phaseless methods.

The amplitude and phase characterization of a reference source at the millimeter- and submillimeter-wave bands can be a complex and expensive problem. In addition, the exact positioning of the reference source can be a complex matter at these frequencies and, therefore, some authors have considered a brute-force approach to find it accurately [12]. Thus, several techniques have been proposed to mitigate this drawback. One of the most promising techniques is based on using a synthesized wave which is combined with the radiated signal [13], [14]. In case of using a plane-wave as reference wave, this approach requires only a phase shifter with just three or four possible configurations (i.e., three or four possible phase shifts), a variable attenuator, a power combiner and a directional coupler [15].

In this paper, the setup presented by the authors in [15] for the inverse scattering problem based on indirect holography is extended to avoid the use of a phase shifter. Additional techniques are also presented to bypass the use of a variable attenuator, directional coupler and power combiner in case they are not available. Once the amplitude and phase have been retrieved, the inverse scattering techniques presented in [16] are applied to find the shape of the scanned object.

II. Phaseless inverse scattering

A. Basics of the Leith-Upatnieks holography

The Leith-Upatnieks holography [10], also known as off-axis or indirect holography, has been applied to electromagnetic field acquisition [11] to retrieve the amplitude and phase of a certain field, E_s. It is based on combining this field with a reference field, E_r, which is supposed to be known. Thus, the measured hologram is:

$$I\left(x,y,z\right)=\left|E_s\left(x,y,z\right)+E_r\left(x,y,z\right)\right|^2. \tag{1}$$

The reference field is usually chosen to be a plane-wave. Let us assume without loss of generality a plane-wave propagating towards $+z$:

$$E_r\left(x,y,z\right)=C\exp(-jk_z^{pw}z), \tag{2}$$

where C and k_z^{pw} are the amplitude and the wavenumber of the plane-wave, respectively. This plane-wave can be artificially generated (i.e., synthesized) with the help of a phase shifter [13].

Since it is possible to measure the square amplitude of the combined field I in (1), then it is also possible to acquire the amplitude of the field under analysis. Thus, the following modified hologram I_m can be constructed:

$$I_m=I-C^2-\left|E_s\right|^2=E_sE_r^*+E_s^*E_r \tag{3}$$

[1]This work has been supported by the Ministerio de Ciencia e Innovación of Spain /FEDER under projects TEC2011- 24492 (iScatt), CSD2008-00068 (Terasense) and MICINN-11-IPT-2011-0951-390000 (Tecnigraf); by the Gobierno del Principado de Asturias (PCTI)/FEDER-FSE under projects PC10-06, EQUIP08-06, FC09-C0F09-12, EQUIP10-31; by grants BP11-169, BES-2009-024060; contract FUO-EM-221-10, and by Cátedra Telefónica-Universidad de Oviedo.

The authors are with the Departamento de Ingeniería eléctrica, Universidad de Oviedo, Spain (e-mail: jlaviada@tsc.uniovi.es; yalopez@tsc.uniovi.es; aarboleya@tsc.uniovi.es; cgarciag@tsc.uniovi.es; flasheras@tsc.uniovi.es)

VI

wherein the asterisk is used to denote the complex conjugate. If the hologram is acquired in the YZ-plane, then the two terms of the modified hologram are centered at $\pm k_z^{pw}$ in the spectral domain and, therefore, they can be filtered out in order to retrieve the desired field.

It is important to remark that the modified hologram can only be acquired on a discrete set of points. If a phase increment $\Delta\phi$ is considered for each increment of the acquisition position in the z-axis, Δz, then it is possible to prove [13] that the wavenumber of the reference plane-wave is $k_z^{pw} = \frac{\Delta\phi}{\Delta z}$, and, therefore, the plane-wave can belong either to the visible or to the invisible region of the spectrum depending on the values $\Delta\phi$ and Δz.

This approach based on synthesized plane-waves has been adapted in [15] for the case of inverse scattering based on planar acquisitions. In the following sections, it will be detailed how it can be modified in order to avoid the use of the phase shifter employed in [13].

B. Mechanical phase shifting

In order to avoid the use of a phase shifter, we consider the setup shown in Fig. 1. In this setup, the acquired hologram is given by:

$$I(x,y,z) = |E_s(x,y,z) + C|^2, \tag{4}$$

where y and z are the coordinates of the object in the acquisition plane; C is a complex constant and $E_s(x,y,z)$ is the field received by the Rx antenna. If the Tx and Rx antennas are close enough each other whereas the object under test (OUT) is in the far field of both of them, then the received field with the distant is given by the following equation:

$$E_s(x,y,z) \approx \frac{A(x,y,z)}{R^2} e^{-j2kR}, \tag{5}$$

wherein k is the free-space wavenumber; $A(x,y,z)$ is a complex function that depends on the radar cross section of the OUT, the radiated power and the gains of the antennas; and $R = \left\|\vec{R}\right\|_2$ where $\vec{R}$ is a vector with origin at the middle point of the Tx and Rx antennas and with end at the center of the OUT. The main parameters involved in the previous description are depicted in Fig. 2.

Let us assume that the OUT is displaced $\vec{d} = d\hat{R}$, where $\hat{R}$ is a unitary vector defined as $\hat{R} = \vec{R} / \left\|\vec{R}\right\|_2$. If the magnitude of this displacement d is electrically small, then the scattered fields received by the Rx antenna for the conventional position (x,y,z) and the modified position (x',y',z') are related by the following expression:

$$E_s(x',y',z') \approx E_s(x,y,z)\, e^{-j2kd}. \tag{6}$$

Thus, the power received by placing the object in the modified positions can be approximated as:

$$\begin{aligned} I(x',y',z') &= |E_s(x',y',z') + C|^2 \\ &\approx \left|E_s(x,y,z)\, e^{-j2kd} + C\right|^2 \\ &= \left|E_s(x,y,z) + Ce^{j2kd}\right|^2. \end{aligned} \tag{7}$$

If the displacements are properly chosen depending on the position, then, the acquired power is the same at the one

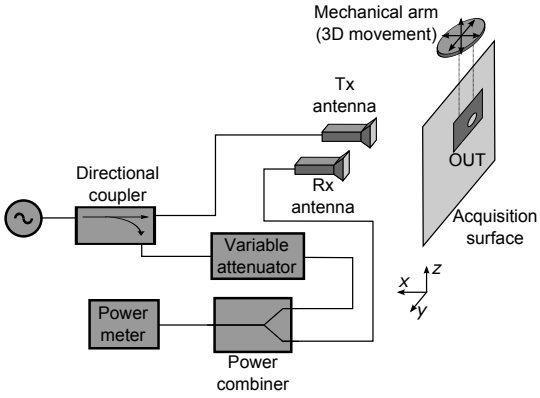

Figure 1. Scheme of the employed indirect holography setup.

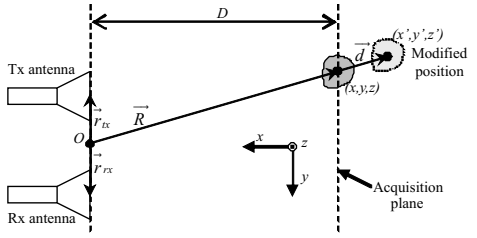

Figure 2. Displacement to produce the phase shift.

acquired in case of using a regular grid together with a plane-wave reference field as indicated by (1) and (2). The approximation introduced in (7) due to the bistatic setup results in a phase error because the length increment is not exactly $2d$. This error will be characterized and calculated in the section II-D.

In the proposed implementation, the phase shifts are chosen to correspond to a certain integer number N_ϕ per cycle. Thus, the phase increment is given by $\Delta\phi = 2\pi/N_\phi$ where N_ϕ is usually 3 or 4. As a consequence, the phase of the equivalent plane-wave at the sample points has a periodicity N_ϕ along the sampling in the z-direction. The relationship between the displacement and the phase shift is given by:

$$\Delta\phi = 2kd. \tag{8}$$

Thus, the maximum phase shift corresponding to $\pm 180^\circ$ is given by a $d = \pm\lambda/4$. These displacements are small enough to apply the approximation in (6) as it will be illustrated in the results sections.

Regarding the acquisition time,.the 3D positioning involves the mechanical arm moving over an overall path greater than the one in the more conventional 2D positioning. For the considered measurement example that will be shown later, the path length has been incremented around 28%. In practice, the overall time is only increased a 22% because of considering the time for the queries to the positioner and for the data transfer, which are common in both cases. In addition, our mechanical arm is more efficient for large displacements due

VI

to the acceleration and decelerations speeds and, therefore, the 3D acquisition benefits from it. In any case, overall measurement time is strongly dependent on the measurement facility.

In the case that a faster acquisition is required, it is important to note that Leith-Upathnieks holography with synthetic reference-wave can benefit from a noteworthy speed-up by hybridizing that holographic technique with the non-redundant sampling as it has been shown in [17] for the antenna measurement context.

It is also important to notice that, depending on the application, the mechanical displacements of the OUT could not be possible. However, the phase shift depends only on the relative displacement between the antennas and the OUT. Hence, it can be also achieved by moving the antennas instead of the OUT. In this case, the mechanical movement must be applied to the entire block containing the millimeter- or submillimeter-wave devices (e.g., antennas, multipliers, etc.) to avoid perturbations in the reference signal.

C. Injection of the reference signal through direct radiation

The scheme shown in Fig. 1 is relatively easy to implement at microwave frequencies. Nevertheless, some modifications have to be accomplished to use it in the millimeter- and submillimeter-wave bands. At these frequencies, the components are mainly based on waveguide technology to take advantage of the relatively low losses. In order to adapt the aforementioned scheme to the waveguide technology, the directional couplers and power combiners are usually replaced by waveguide directional couplers and magic tees. Commercial variable attenuators are also available at these frequencies. Nevertheless, this kind of components is still expensive and not always easy to implement. An alternative to bypass this inconvenient is to inject the reference signal through direct radiation.

This injection can be accomplished by conveniently rotating the Tx and Rx antennas a certain angle α with respect to its radiation maximums so that the coupled power, which is usually not desired in most of applications, is intentionally increased. The coupled power can also be controlled by the distance, $2p$, between the antennas. However, this distance is limited by the error discussed in section II-D1. These two parameters are the ones to be adjusted to balance the reference and scattered signals power.

This proposed setup is depicted in Fig. 3. The power of the reference wave, which is proportional to the square amplitude of the reference field $|C|^2$, is given by the well-known Friis transmission equation:

$$P_{ref} = P_{Tx} G_{Tx}(\beta)\, G_{Rx}(\beta) \left(\frac{\lambda}{8\pi p}\right)^2, \qquad (9)$$

where P_{Tx} is the power transmitted by the Tx antenna; and, $G_{Tx}(\beta)$ and $G_{Rx}(\beta)$ are the gains of the Tx and Rx antennas for the corresponding angle between the direction joining both antennas and the maximum radiation direction.

In the implementations that will be next shown, non-directive antennas have been chosen so that the coupled power

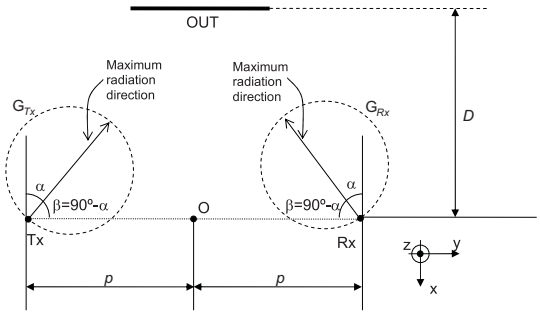

Figure 3. Bistatic setup for indirect holograpy with radiated reference signal.

is relative high even for low tilts. This kind of antennas waste power that it is radiated neither to the OUT nor to the Rx antenna. Thus, more enhanced approaches could be done by using ad hoc antennas as for example antennas with an appropriate secondary lobe in the direction joining both antennas.

D. Error analysis

The most significant errors in the indirect holography are related to the filtering in the spectral domain. The impact of these errors as well as the impact due to any other potential error because of working in the THz band (e.g, positioning accuracy) have been analyzed in [11] and, therefore, the analysis will not be repeated here. However, as a consequence of the reduction of the number of components, some new errors appear in the presented approach.

1) Error due to the monostatic approximation: As it has been previously mentioned, the bistatic setup involves an error because the path increment from the Tx antenna to the Rx antenna via the OUT is not exactly $2d$. In this section, this error is bounded. In order to simplify the notation, it will be assumed that the middle point between the Tx and Rx antennas, O, corresponds to the origin of coordinates.

If a total distance increment $2d$ is desired, then the distance difference is given by the following expression:

$$\begin{aligned} e_b &= \left(\left\|\vec{R}' - \vec{r}_{tx}\right\|_2 + \left\|\vec{R}' - \vec{r}_{rx}\right\|_2\right) \\ &- \left(\left\|\vec{R} - \vec{r}_{tx}\right\|_2 + \left\|\vec{R} - \vec{r}_{rx}\right\|_2\right) - 2d, \end{aligned} \qquad (10)$$

where $\vec{R}' = \vec{R} + \vec{d}$ is the modified position and, $\vec{r}_{tx}$ and $\vec{r}_{rx}$ are the positions of the Tx and Rx antennas, respectively. The maximum error is achieved when the object is placed in the x-axis according to the system of coordinates shown in Figs. 1, 2 and 3. Thus, the expression for the maximum phase error is given by:

$$\begin{aligned} \varphi_b &= k e_b(x = D, y = 0, z = 0) \\ &= 2k\left(\sqrt{(D+d)^2 + p^2} - \sqrt{D^2 + p^2} - d\right), \end{aligned} \qquad (11)$$

where $p = \|\vec{r}_{tx}\|_2 = \|\vec{r}_{rx}\|_2$ is half of the distance between the Tx and Rx antennas. Since any error on the phase of the plane

VI

wave introduces an equivalent error in the retrieved field, as it can be inferred from (7), then (11) gives us the maximum error of the phase of the retrieved field due to the bistatic setup.

2) Error due to the approximations in the multifrequency analysis: In order to reconstruct the depth of the object, it is necessary to measure the scattered field at multiple frequencies as indicated in [18], [19]. Since the displacement of the positioning points depends on the frequency, then a multi-frequency acquisition can require a significant increment of the number of points that can result on a considerably high measurement time.

If the bandwidth is relatively small, then it is possible to reuse the same set of points for all the frequencies. In order to minimize the error, this set of points is computed at the center frequency that will be denoted by f_c. The use of this approximation introduces the following error in the phase, which depends on the frequency:

$$\varphi_f(f) = 2d\,k - \Delta\phi = \Delta\phi\frac{k}{k_c} - \Delta\phi = \Delta\phi\left(\frac{f-f_c}{f_c}\right), \quad (12)$$

where k is the wavenumber at the working frequency, f; and k_c is the wave number at the center frequency, f_c. Thus, the maximum phase error due to this approximation is:

$$\varphi_f(f = f_{max}) = \Delta\phi\frac{\Delta B}{2f_c}, \quad (13)$$

where ΔB is the bandwidth of the measurement. As inferred from (13), the maximum of this error is achieved for the maximum phase shift $\Delta\phi$ under consideration.

It is also important to remark that, despite the reference signal will differ from the ideal one given in (2), the energy of this signal is still concentrated around $k_z = \frac{\Delta\phi}{\Delta z}$ so that the terms $E_s E_r^*$ and $E_s^* E_r$ can still be filtered out from the modified hologram.

3) Error due to the 3D positioner: The 3D positioners have a certain accuracy and, therefore, they cannot perfectly place the object. Grid errors have been studied in [11] at THz bands. Nonetheless, the positioning errors will also translate into phase shift errors according to the relationship given by (8). If the maximum positioning error is d_{error} , then the following maximum error is introduced:

$$\varphi_p = 2kd_{error}. \quad (14)$$

E. Phase and object retrieval from acquired data

In order to compute the modified hologram described in (3), the amplitude of the plane-wave, C, as well as the amplitude of the scattered field must be firstly measured. The former one is a constant value that is acquired by moving the object far enough.

The amplitude of the scattered field can be measured by reducing the coupling between the two antennas and repeating the measurement. Nonetheless, this step requires two entire measurements and it is not used in this paper. Instead of that, this amplitude is computed by filtering in the spectral domain as it is next detailed.

This filtering is possible because the terms $E_s E_r^*$ and $E_s^* E_r$ are centered at $k_z = \pm k_z^{pw} = \pm\frac{\Delta\phi}{\Delta z}$ whereas the term $|E_s|^2$ is centered at the origin of the spectrum of the hologram in (1) together with the spectrum of the reference signal. Thus, after computing the Fourier transform of the measured power without the square of the amplitude of the reference wave, the amplitude of the scattered field can be computed by just keeping the spectrum from $-k_z^{pw}/2$ to $k_z^{pw}/2$. Further details about the spatial bandwidth and center of each term in the hologram and modified holograph are given in [15].

After this filtering, the modified hologram is computed. A second filtering is applied to the spectrum of the modified hologram for $k_z > 0$ so that the term $E_s^* E_r$ is recovered. Finally, the scattered field is obtained by dividing this term by the plane-wave reference field in (2) and computing the complex conjugate of this division.

After retrieving the field, the inverse scattering technique in [16] is applied to find the profile of the object. In brief, this technique is based on an inverse-source formulation [20], which has been optimized by means of a multipolar expansion. The idea is to divide the scattered field (or observation) domain and the current (or reconstruction) domain in several groups, so that the interactions can be efficiently carried out by the well-known aggregation, translation, and disaggregation operations [16].

Finally, it is important to remark that the far-field condition to apply (6) is not strictly fulfilled in the following examples. It has been accomplished to ensure that the received power is over the sensitivity of the employed acquisition devices. No visible artifacts have been found due to this fact.

III. Results

Two examples, one numerical and the other experimental one, are considered in this section to validate the previous techniques. The number of possible phase shifts is set to $N_\phi = 4$ and, therefore, the displacements can be $-\lambda/8$, 0, $\lambda/8$ and $2\lambda/8$ to produce the corresponding phase shifts equal to -90°, 0°, 90° and 180°, respectively.

A. Multifrequency retrieval of a tilted trapezoid

The retrieval of a metallic plate with the shape of an isosceles trapezoid, which is rotated 45° around the y-axis, is considered in this example. The depth information is obtained by combining the retrieved data for each frequency [18], [19]. The length of the parallel edges of the isosceles trapezoid are 4 cm and 2 cm. The length of the remaining edges is 2 cm.

The system is simulated by considering $\cos^q(\theta)$ radiation patterns [21] with $q = 1$ for the Tx and Rx antennas which are separated a distance $2p = 5.5$ cm. The antennas are polarized in the z-direction. These radiation patterns are tilted $\alpha = 45^\circ$ to increase the power of the received reference signal.

A set of frequencies from 285 GHz to 315 GHz with a 1 GHz step is considered. Thus, the bandwidth is $\Delta B = 30$ GHz and the center frequency is $f_c = 300$ GHz. The displacements from the acquisition window are computed at the center frequency as detailed in section II-D2.

The field scattered by the plate is computed by physical optics by moving the object on a window spanning from $y = -3$ cm to $y = 3$ cm and from $z = -2$ cm to $z = -13$ cm.

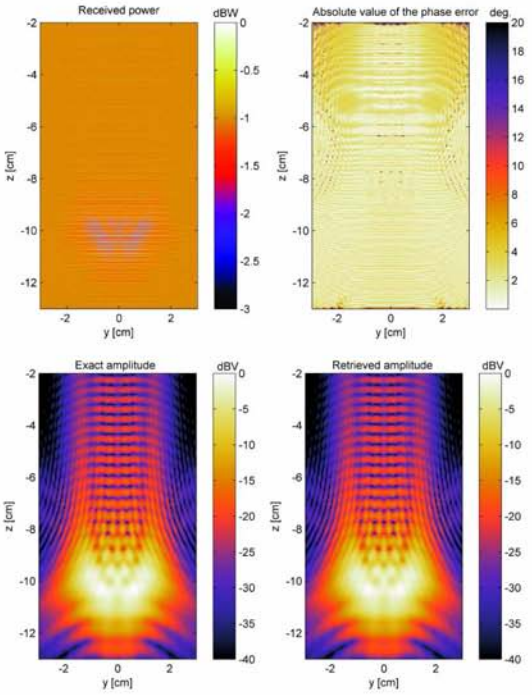

Figure 4. Received power, exact amplitude, retrieved amplitude and absolute value of the phase error for the trapezoid example at 315 GHz .

Please note that the acquisition window has an offset in the z-direction in order to capture the most significant contribution of the scattered field. The sampling steps are $\Delta y = \lambda_{min}/2$ and $\Delta z = \lambda_{min}/8$ where λ_{min} is the wavelength at the maximum frequency 315 GHz. The distance between the antennas and the acquisition window is $D = 10$ cm.

In order to validate the accuracy of the retrieved fields, the amplitude of the computed field as well as the absolute value of the phase error are shown in Fig. 4 together with the received power. The exact result is obtained by computing the field scattered by the plate without adding the direct coupling. This figure shows that the accuracy of the recovered amplitude and phase is very high without any visible artifacts.

After retrieving the amplitude and phase for each frequency, the inverse scattering technique presented in [16] is applied. The reflectivity is recovered in a 4 cm-side cube, discretized into 2 mm voxels. The obtained shape for the isosurface at -10 dB is shown in Fig. 5 which shows an excellent agreement with the original plate.

The evaluation of the errors introduced by the quasi-monostatic approach and the multifrequency acquisition yields a maximum error equals to $\varphi_b = 6.4°$ and $\varphi_f = 9°$, respectively. In order to evaluate the impact of all the errors in the final result, the root mean square error of the reflectivity is computed by using as a comparison the result obtained by direct acquisition. The maximum and average errors are -40 dB and -52 dB, respectively, so that the impact in the final result is not significant.

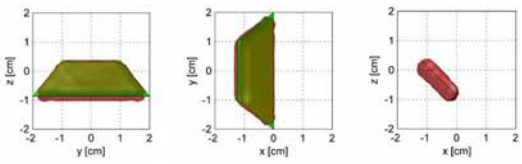

(a) YZ plane. (b) XY plane. (c) XZ plane.

Figure 5. Trapezoid plate (green color) and retrieved isosurface at -10dB (red color).

B. Plate with holes at 300 GHz

In the last example, a metallic plate with holes of radii 1.5 mm, 3 mm, 6 mm and 9 mm (see Fig. 8) is scanned at 300 GHz. The dimensions of the rectangular plate are 7 cm × 2 cm. The maximum positioning errors of the employed mechanical arm is 4 µm for each axis and, therefore, the worst case for the mechanical shifting can be considered to be $d_{error} = 7$ µm so that the maximum phase error due to the positioning is given by $\varphi_p = 5°$.

The Tx and Rx antennas are two open rectangular waveguides WR-03 and a distance between them is $2p = 5.5$ cm. The tilt to increase the coupling is $\alpha = 45°$ again. The distance between the antennas and the acquisition plane is $D = 5$ cm. The maximum phase error due to the bistatic approximation is given by $\varphi_b = 22°$. This error is higher than in the previous case due to the smaller distance to the acquisition plane. However, this maximum value only takes places on very specific positions (see Section II-D1) and, therefore, it is not expected to have a significant impact in the final reconstructed profile as it will be empirically shown next.

The plate is moved around a rectangular acquisition window of length 4 cm × 8 cm. The sampling step is $\Delta y = \Delta z = \lambda/4$.

A vector network analyzer (VNA) with a millimeter-wave extension is used to feed the Tx antenna. The Rx waveguide is also connected to the VNA by a second millimeter-wave extension but the phase information is discarded. The setup is shown in Fig. 6.

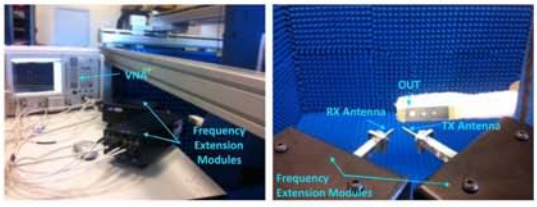

Figure 6. Setup for the plate with holes.

The acquired power is shown in Fig. 7. After data processing, the retrieved field is introduced into the inverse scattering algorithm [16] that yields the reflectivity shown in Fig. 8. In this case, the reconstruction domain is an 8×3 cm plane placed

VI

at $x = 0$ cm. This plane is discretized into 0.75 mm-side square patches. This result shows a very good agreement with the real shape. The holes of different radii are recovered with the only exception of the smallest one whose diameter (1.5 mm) which is still comparable to the wavelength and it is not clearly visible.

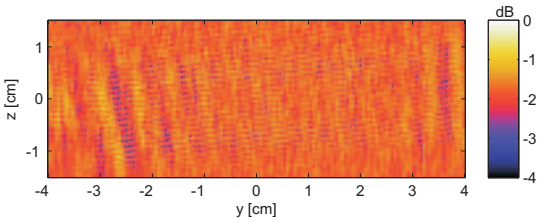

Figure 7. Normalized measured power for the plate with holes at 300 GHz.

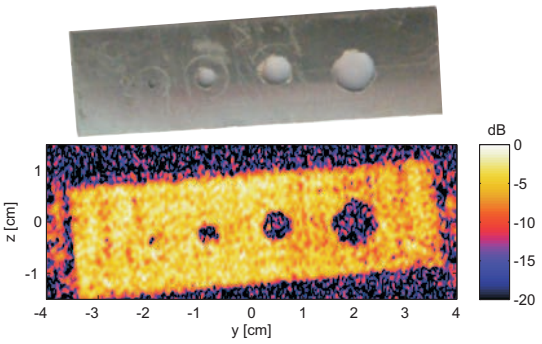

Figure 8. Retrieved shape of the plate with holes at 300 GHz. Original image above.

VI

IV. Conclusions

An inverse scattering technique setup based on a phaseless acquisition has been presented trying to avoid the expensive and complex acquisition of the phase information at the millimeter- and submillimeter-wave bands. The phase retrieval is based on the Leith-Upatnieks holography with a synthesized reference wave. The phase of this reference wave is achieved by a mechanical displacement so this setup avoids the use of phase shifter and, therefore, it reduces the number of required components if compared with the available approaches. The main drawback is that the mechanical phase shifting requires a three-dimensional positioner.

Reference signal injection by means of antenna coupling has also been presented to bypass the use of directional couplers, power combiners and variable attenuators in case these devices are not available. Implementation by means of non-directive probes have been shown to provide accurate results. Nevertheless, a more efficient setup can be approached by means of antennas designed to intentionally increase the coupling between them.

The technique have been validated at submillimeter-wave frequencies with simulations as well as measurements with excellent results. Three-dimensional reconstruction by using multifrequency data has also been successfully accomplished.

References

[1] K. B. Cooper, R. J. Dengler, N. Llombart, B. Thomas, G. Chattopadhyay, and P. H. Siegel., "THz imaging radar for standoff personnel screening," *IEEE Trans. Terahertz Science and Tech.*, vol. 1, pp. 169 – 182, Sep. 2011.

[2] R. Appleby and H. B. Wallace, "Standoff detection of weapons and contraband in the 100 ghz to 1 thz region," *IEEE Trans. Antennas and Propagation*, vol. 55, no. 11, pp. 2944–2956, Nov. 2007.

[3] L. L. Li, W. J. Zhang, and F. Li, "Tomographic reconstruction using the distorted Rytov iterative method with phaseless data," *IEEE Geoscience and Remote Sensing Letters*, vol. 5, no. 3, pp. 479–483, 2008.

[4] W. J. Zhang, L. L. Li, and F. Li, "Multifrequency imaging from intensity-only data using the phaseless data distorted Rytov iterative method," *IEEE Trans. Antennas Propagat.*, vol. 57, no. 1, pp. 290–295, Jan. 2009.

[5] L. Crocco, M. D'Urso, and T. Isernia, "Inverse scattering from phaseless measurements of the total field on a closed curve," *J. Opt. Soc. Am. A*, vol. 21, no. 4, pp. 622–631, Apr. 2004.

[6] S. Caorsi, A. Massa, M. Pastorino, and A. Randazzo, "Electromagnetic detection of dielectric scatterers using phaseless synthetic and real data and the memetic algorithm," *IEEE Trans. Geoscience and Remote Sensing*, vol. 41, no. 12, pp. 2745–2753, Dec. 2003.

[7] L. Liu, A. Trehan, and N. Nikolova, "Near-field detection at microwave frequencies based on self-adjoint response sensitivity analysis," *Inverse Problems*, vol. 26, no. 10, Oct. 2010.

[8] W. Zhang, L. Li, and F. Li, "Inverse scattering from phaseless data in the freespace," *Sci China F-Inf. Sci.*, vol. 52, pp. 1389–1398, 2009.

[9] S. F. Razavi and Y. Rahmat-Samii, "Phaseless planar near field measurements for scanned beams: Difficulties, a hybrid solution and measured results," in *Proc. IEEE Antennas Propaga. Society Int. Symp*, vol. 9-14, 2006, pp. 429–432.

[10] E. N. Leith and J. Upatnieks, "Reconstructed wavefronts and communication theory," *J. Opt. Soc. Amer.*, vol. 52, pp. 1123–1128, 1962.

[11] G. Junkin, T. Huang, and J. Bennett, "Holographic testing of terahertz antennas," *IEEE Trans. Antennas Propagat.*, vol. 48, no. 3, pp. 409 –417, Mar. 2000.

[12] A. Tamminen, J. Ala-Laurinaho, and A. V. Raisanen, "Indirect holographic imaging at 310 GHz," in *Radar Conference, 2008. EuRAD 2008. European*, Amsterdam, Netherlands, 30-31 Oct. 2008, pp. 168–171.

[13] V. Schejbal, V. Kovarik, and D. Cermak, "Synthesized-reference-wave holography for determining antenna radiation characteristics," *IEEE Trans. Antennas Propagat. Mag.*, vol. 50, no. 5, pp. 71 – 83, Oct. 2008.

[14] M. P. Leach, D. Smith, and S. P. Skobelev, "A modified holographic technique for planar near-field antenna measurements," *IEEE Trans. Antennas Propagat.*, vol. 56, no. 10, pp. 3342–3345, Oct. 2008.

[15] J. Laviada, Y. Álvarez Lopez, A. Arboleya-Arboleya, C. García-González, and F. Las-Heras, "Inverse scattering with phase retrieval based on indirect holography via synthesized plane-waves," *IET Microwave, Antennas and Propagation*, vol. 6, no. 12, pp. 1389–1398, 2012.

[16] Y. Álvarez, J. Laviada, L. Tirado, C. García, J. Martínez-Lorenzo, F. Las-Heras, and C. M. Rappaport, "Inverse fast multipole method for monostatic imaging applications," *to appear in IEEE Trans. Geoscience and Remote Sensing Letters*, pp. 1–6.

[17] J. Laviada and F. Las-Heras, "Phaseless antenna measurement on non-redundant sample points via leith-upatnieks holography," *to appear in IEEE Trans. Antennas and Propagation*.

[18] A. Broquetas, J. Palau, L. Jofre, and A. Cardama, "Spherical wave near-field imaging and radar cross-section measurement," *IEEE Transactions on Antennas and Propagation*, vol. 46, no. 5, pp. 730–735, May 1998.

[19] J. Martínez-Lorenzo, C. M. Rappaport, and F. Quivira, "Physical limitations on detecting tunnels using underground-focusing spotlight synthetic aperture radar," *IEEE Transactions on Geoscience and Remote Sensing*, vol. 49, no. 1, pp. 65–70, Jun. 2009.

[20] S. Caorsi, G. L. Gragnani, and M. Pastorino, "Two-dimensional microwave imaging by a numerical inverse scattering solution," *IEEE Trans. on Microwave Theory and Tech.*, vol. 38, no. 8, pp. 981–989, Aug. 1990.

[21] Y. T. Lo and S. W. Lee, Eds., *Antenna Handbook: Antenna Fundamentals and Mathematical Techniques*. New York: Van Nostrand Reinhold: Chapman & Hall, 1993.

Publication VII

J. Laviada, **A. Arboleya-Arboleya**, Y. Álvarez-López, C. García-González and F. Las-Heras **"Phaseless synthetic aperture radar with efficient sampling for broadband near-field imaging: theory and validation,"** *IEEE Transactions on Antennas and Propagation*, vol.62, no. 2, pp. 573–584, Feb. 2015.

Phaseless Synthetic Aperture Radar with Efficient Sampling for Broadband Near-Field Imaging: Theory and Validation

Jaime Laviada, Ana Arboleya-Arboleya, *Student Member, IEEE*, Yuri Álvarez-López, *Member, IEEE*, Cebrián García-González, *Student Member, IEEE*, and Fernando Las-Heras, *Senior Member, IEEE*

***Abstract*—This paper presents a broadband and phaseless synthetic aperture radar (SAR) with efficient sampling. The design relies on a novel phaseless monostatic element comprising a transmitter and a receiver. This element, together with a computationally inexpensive algorithm, can retrieve the phase of the monostatic scattered field at all the working band except for two small safety margins at the lower and upper frequencies. Furthermore, the phase retrieval works independently of the transmitter/receiver position. Consequently, conventional approaches to reduce the number of monostatic acquisition points can be employed. Thus, the proposed strategy is suitable to implement either arrays that benefit from a reduced number of low-complexity elements or raster scan systems that benefit not only from the cost reduction of the scanning components but also from a remarkable speed-up due to the reduced number of acquisition points. Moreover, in contrast to other off-axis schemes, the proposed system does not require neither mechanical nor electrical phase shifting and, therefore, it can be directly adapted to a large number of frequency bands. The performance of the system is validated by simulation and measurement examples in the millimeter-wave band.**

***Index Terms*—Leith-Upatnieks; indirect holography; phase retrieval; non-redundant sampling; multi-monostatic radar; synthetic aperture radar.**

I. Introduction

Electromagnetic imaging is a powerful technique that enables non-destructive inspection of objects that are covered by penetrable materials. Imaging can be accomplished by means of multiple arrangements of the transmitters and receivers. The most general setup, which allows arbitrary positions of the transmitters and receivers, is known as *multistatic*. On the other hand, if the number of transmitters is reduced to only one with the subsequent loss of available information, the setup is known as *bistatic*. In general, these setups can be reformulated as multistatic by moving the transmitter to different positions. Moreover, the bistatic setups can be employed to perform antenna measurements with minor modifications. The last group of techniques is based on arranging several pairs of transmitter/receiver to accomplish several monostatic acquisitions yielding a setup, which is usually known as *multi-monostatic*.

Multi-monostatic acquisitions enables a good trade-off between the quality of the results and the complexity of the system, which avoids complex routing of reference signals. This approach can be implemented by either an *array* of transmitters/receivers or by *raster scanning* by moving a single element, i.e., a transmitter/receiver pair, along the different acquisition positions. This latter strategy clearly reveals that this approach is equivalent to a *synthetic aperture radar* (SAR). The versatility of this scheme has been found to be of interest for a wide variety of applications including security and personnel screening [1], [2], [3], through-wall imaging [4], [5], and detection of buried objects in ground penetrating radar applications [6], including the terahertz band [7].

The complexity of a multi-monostatic system, and so the overall cost, is proportional to the *complexity of the monostatic element* comprising the transmitter/receiver pair. Another key factor in these scanning systems is the *number of acquisition points*, which has a direct impact on the cost of the system or the scanning time for the array or raster scan implementations. This paper proposes a new scheme compatible with the two aforementioned key points yielding *broadband and phaseless synthetic aperture radar (SAR) with efficient sampling*.

A conventional way to reduce the complexity of the scanning system is to resort to phase retrieval methods so that the system relies on *amplitude-only acquisition*. Research on phase retrieval methods has been developed along almost five decades with a large number of works, which have been unconnected in many cases. Each scheme provides a different number of features that are suitable for a given set of problems.

Table I summarizes the main features of the most popular schemes that are available in the literature. The features considered in this table include if the system: i) requires modifying the probe or only requires replacing the receiver front-end by a power sensor; ii) is based on an iterative strategy that can suffer from stagnation; iii) works at a single frequency, i.e., the phase retrieval is accomplished frequency by frequency; iv) is developed for a specific kind of acquisition (bistatic/multistatic or monostatic); and v) works independently of the acquisition surface. The last entry of the table is reserved to report if evidences of compatibility with efficient sampling techniques has been given.

The most widespread method in the literature relies on performing two (or more) *independent acquisitions*. This method

This work has been supported by the Ministerio de Ciencia e Innovación of Spain /FEDER under projects TEC2011- 24492 (iScatt), CSD2008-00068 (Terasense) and MICINN-11-IPT-2011-0951-390000 (Tecnigraf); by the Gobierno del Principado de Asturias (PCTI)/FEDER-FSE under projects PC10-06, EQUIP08-06, FC09-C0F09-12, EQUIP10-31; by Grants BP11-169, BES-2009-024060; Contract FUO-EM-221-10.

The authors are with the Departamento de Ingeniería Eléctrica, Universidad de Oviedo, Spain (e-mail: jlaviada@tsc.uniovi.es; aarboleya@tsc.uniovi.es; yalopez@tsc.uniovi.es; cgarciag@tsc.uniovi.es; flasheras@uniovi.es)

VII

is usually implemented by accomplishing two acquisitions at two parallel surfaces. An iterative technique is then applied by propagating the field from one surface to another to refine the phase value. A degree of independence between acquisitions is required as detailed in [8]. Additional acquisition surfaces have also been reported to improve the accuracy of the method [9]. In general, the acquisition surfaces are parallel planes, because the propagation can be efficiently accomplished by fast Fourier transforms (FFTs). However, satisfactory results have also been provided in the case of spheres [10] or cylinders [11]. The method has been successfully applied to antenna problems [12], [9] and bistatic imaging [13]. Moreover, the approach has been reported to be compatible with schemes to reduce the number of acquisition points [14]. One of the main drawbacks of this kind of approach concerns stagnation problems due to local minima that can only be avoided under certain conditions [15]. It is also worth mentioning that a variation of the method, consisting of acquiring the field by means of two probes with different characteristics, has also been successfully applied [8].

In the context of multistatic acquisitions for imaging problems, other authors have chosen to minimize the *cost function minimization* defined as the Euclidean distance between the power of the scattered field, which has been measured, and the power of the field scattered by a certain object, the shape of which is iteratively refined to minimize the aforementioned cost function [16]. A similar optimization, which also exploits a non-redundant sampling decreasing the number of transmitters and receivers, was later proposed [17]. The previous cost function has been reported to exhibit several local minima that can only be avoided if certain geometrical conditions are fulfilled [18]. In addition, previous techniques require the full knowledge, or a good estimation from a different phaseless technique, of the incident field [19].

To avoid convergence problems, other authors have developed *direct methods*, which in general are based on *interferometry approaches*. Among these approaches, some of the most successful are those based on a *modified probe*. This probe comprises two antennas and several power detectors so that the phase difference between the two antennas of the probe can be directly computed by vector algebra [20], [21]. Because this method can only compute the phase difference between two points, a strategy has to be implemented to retrieve the real phase. If a constant spatial sampling rate is used so that the sampling step is equal to the distance between the two antennas of the probe, then the phase can be directly computed by adding the differences [22]. Nevertheless, it clearly limits the sampling rates. This modified probe strategy, as well as some enhancements, has been successfully used to measure the millimeter wave antennas in a cylindrical setup that avoids the need for flexible cables and rotatory joints [23].

Other authors [21], [24] have increased the sampling step flexibility by looking for the phase solution in a space containing the fields, which are feasible according to the band-limited properties of the electromagnetic fields [25]. Furthermore, the wideband capabilities of this method have been also proven [26]. The performance of a system implenting this strategy has been analyzed for antenna measurement as well as multistatic inverse scattering problems involving different materials [27], [28], [29]. Despite the aforementioned flexibility, the approach still requires a half wavelength sampling.

In contrast to modified probe methods, other authors have preferred to develop systems based on *off-axis holography*, also known as Leith-Upatnieks holography [30]. This technique also relies on an interferometry so a reference signal, whose amplitude and phase are characterized, is combined with the radiated or scattered field along the acquisition domain [31]. If the reference signal fulfills a given set of properties [32], then the amplitude and phase field can be retrieved by moving from the spatial to the spatial spectral domain by means of a FFT.

To improve the flexibility of the off-axis holography, some authors have resorted to using a reference wave that is synthesized by means of a phase shifter [33], [34], [35]. Although conventional off-axis holography was developed for bistatic problems, this synthetic approach has also shown good properties for monostatic acquisitions [33], [36].

Nevertheless, off-axis approaches result in a considerable increment of the spatial sampling requirements, which can be as high as $\lambda/4$ and $\lambda/8$ for bistatic and multi-monostatic acquisition, respectively [37]. To the authors' best knowledge, the previous disadvantage can only be alleviated by resorting to non-redundant sampling [38]. In all the previous cases, phase retrieval in off-axis holography also operates processing the data frequency by frequency.

Because off-axis holography requires a transformation from the spatial domain to the spectral domain, it necessarily requires acquiring the field at different points. Consequently, the technique is not appropriate for a monostatic radar where there is only one transmitter and one receiver. Nonetheless, this limitation has been recently overcome for monostatic frequency scanning radars [39] by replacing the spatial domain by the frequency domain. Moreover, this modified off-axis holography is able to synthesize an (time-domain) appropriate reference wave without the need of resorting to phase shifting [33], [36], [35]. Consequently, this approach is an excellent candidate to reduce the complexity of multi-monostatic systems.

This paper exploits this element to achieve the aforementioned phaseless and broadband SAR. Moreover, because the technique retrieves the phase point by point, it does not suffer from the spatial bandwidth increment for off-axis holography reported in [37]. Consequently, conventional efficient sampling strategies are employed to further reduce the number of acquisition points.

It is also relevant to notice that, in addition to the broadband and lack of spatial bandwidth increment features, the system also overcomes other previous off-axis schemes [38], [36], as it avoids the use of electronic or mechanical phase shifting resulting in a very competitive scheme for high frequencies such as the *millimeter and submillimeter-wave bands*. Thus, the main features of the resulting system are summarized as follows: i) phaseless; ii) broadband; iii) compatible with near-field acquisition; iv) efficient sampling; and v) iteration-free.

VII

Table I
SURVEY OF PHASELESS METHODS.

	Setup modification	Iterative	Wideband	Context	Arbitrary surface	Efficient sampling
Several independent acquisitions [11], [8], [12], [13], [10], [9]	No	Yes	No	Bistatic	No	Yes
Simulated-Measured cost function [16], [17], [18], [19]	No	Yes	No	Multistatic	Yes	Yes
Modified probe [22], [23], [21], [24], [26], [27], [28]	Yes	No	Yes	Bistatic/ Multistatic	Yes	No
Spatial off-axis holography [30], [32], [31]	Yes	No	Yes	Bistatic	No	Yes
Synthetic off-axis holography [33], [40], [35], [38]	Yes	No	No	Bistatic/ monostatic	Yes	Yes
This approach	Yes	No	Yes	Monostatic	Yes	Yes

II. PHASE RETRIEVAL

A. Broadband off-axis holography for multi-frequency monostatic acquisition

Leith-Upatnieks holography [30] is based on acquiring the field resulting from the interference between the desired radiation and a *reference signal,* whose amplitude and phase are known. The approach involves acquiring the interferometric signal along a given set of spatial points:

$$I(\vec{r}) = |E_s(\vec{r}) + E_r(\vec{r})|^2 \tag{1}$$

being E_s the field scattered by the object under test (OUT) and E_r the reference field that is usually assumed to provide a linear phase shift along the acquisition surface:

$$E_r(\vec{r}) = e^{-jk_x x} \tag{2}$$

where the phase shift has been assumed along the x-axis without loss of generality and k_x is the phase constant. When applied to electromagnetic problems and, in particular, to multi-monostatic acquisitions, one of the main drawbacks of this approach is that *spatial sampling steps* must be as small as $\lambda/8$ to avoid spectral overlap [37]. In addition, although the phase shift can be easily achieved for bistatic acquisitions by employing an off-axis reference antenna [30], it is hard to achieve in monostatic acquisition where the only choice is to synthesize the reference wave by means of a phase shifter. Nevertheless, agile phase shifting at high frequencies such as the submm-wave band is technologically challenging.

In the context of *frequency scanning* antennas, an approach based on Leith-Upatnieks holography has been recently proposed [39], [41]. This technique was designed for monostatic radar systems based on a frequency scanning antenna. [42]. This approach relies on applying a set of equivalent operations in the frequency and time domains in contrast to the spatial and spectral domains of the conventional off-axis holography. As a consequence, a wideband approach which does not require a phase shifter is achieved.

The herein proposed phaseless and wideband SAR is based on this approach. For this purpose let us consider the multi-monostatic scanning array for phaseless acquisition depicted in Fig. 1. This system pursues to obtain the amplitude and phase of the scattered field for a set of monochromatic waves from power-only data. For this end, each element of the array includes a directional coupler, a variable attenuator, a power combiner, a power detector, and the transmitting and receiving antennas. Each element acquires the power of the signal resulting from the combination of the scattered field together with a fraction of the original source, which is referred to as *reference signal*. This last branch is attenuated to balance the power of both branches. Hence, the acquired signal is given by

$$I(\vec{r},\omega) = |E_s(\vec{r},\omega) + E_r(\vec{r},\omega)|^2, \tag{3}$$

where $\vec{r}$ is the position of the monostatic element, ω is the angular frequency, and E_s is the field scattered by the object under test (OUT) and received by the Rx antenna at point 3 (see Fig. 1).

The reference signal E_r corresponds to the fraction of the source signal that flows through the directional coupler, variable attenuator, and power combiner. If the mismatch between the components of the reference branch is negligible, it is useful to note that this signal can be decomposed as the product of the reference signal without the variable attenuator, which is denoted by $E_r'(\omega)$, times the frequency response of the variable attenuator, which is denoted by $C(\omega)$, i.e., $E_r(\vec{r},\omega) = C(\vec{r},\omega)\,E_r'(\omega)$. Because the value of the reference branch depends on the voltage applied to the variable attenuator, the reference signal must be conveniently

VII

characterized for all possible attenuation values as detailed in Section II-C.

Although an ideal attenuator would provide a constant attenuation in the band of interest, it has been assumed that this attenuation can suffer (moderate) changes over the considered frequency range. The effect of this non-constant attenuation and the subsequent dispersion will be discussed in the Results section. It is also important to notice that an ideal combiner has been assumed in (3). However, the considerations for the dispersion of this element are analogous to those for the non-constant attenuation.

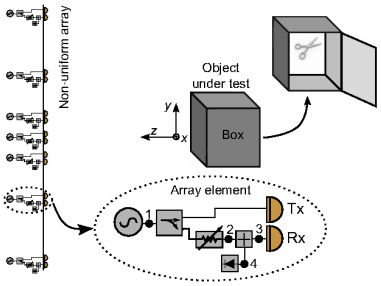

Figure 1. Proposed multi-monostatic scanning array. Inset shows a detail of a single element. An application example related to the non-destructive evaluation of a box is also depicted.

If the aforementioned elements exhibit a low-dispersion behavior, then the reference field corresponds to a perfectly delayed field:

$$E_r(\omega) \propto e^{-jt_d\omega}, \tag{4}$$

where t_d is the *time delay* associated to the propagation of the reference signal from point 1 to point 4 in Fig. 1. Thus, the duality between the conventional off-axis equations (1)-(2) and the proposed approach modeled by (3)-(4) becomes clear. It is important to notice that in contrast to [39] a delay line, which plays the role of the phase shifter in conventional off-axis holography, has not been explicitly included in the block diagram depicted in Fig. 1. It will be shown in Section II-B that the lack of a delay line can also be employed as long as a set of conditions, which are detailed in Section II-B, are met.

The postprocessing of the interferometric signal is analogous to the approach followed in conventional off-axis holography [37]. Thus, the following modified hologram can be computed by subtracting the amplitude of the scattered and reference fields:

$$\begin{aligned} I_m(\vec{r},\omega) &= I(\vec{r},\omega) - |E_s(\vec{r},\omega)|^2 - |E_r(\vec{r},\omega)|^2 \\ &= E_s(\vec{r},\omega)\bar{E}_r(\vec{r},\omega) + \bar{E}_s(\vec{r},\omega)E_r(\vec{r},\omega), \end{aligned} \tag{5}$$

where the upper bar denotes complex conjugate. Details about the acquisition of the square amplitude of the scattered field $|E_s(\vec{r},\omega)|^2$ are given in Section II-D.

If the inverse Fourier transform is applied to the previous signal, then the modified hologram can be expressed in the time-domain as:

$$i_m(\vec{r},t) = e_s(\vec{r},t) * e_r(\vec{r},-t) + e_s(\vec{r},-t) * e_r(\vec{r},t), \tag{6}$$

where e_s and e_r are the impulse responses corresponding to the scattered and reference signals, and the asterisk operator denotes convolution. As will be discussed in the next section, an appropriate design of the reference signal avoids the time-domain overlap of both terms in (6) and, consequently, the retrieval of the scattered field $E_s(\vec{r},\omega)$.

B. Parameter constraints

To achieve correct performance of the phase retrieval algorithm, the system has to satisfy a series of constraints. Figure 2, which shows the time-domain modified hologram, will be used to illustrate the restrictions.

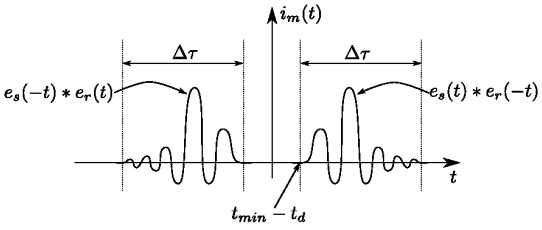

Figure 2. Time-domain modified hologram.

Several parameters have been defined in this figure. The starting time of the scattered signal $e_s(\vec{r},t)$ is denoted by t_{min}. As pointed out in [39], this parameter is directly proportional to the distance between the object under test and the transmitter/receiver pair. The width of the scattered signal in the time domain is given by $\Delta\tau$. In the case of high-frequency approximations (e.g., reflectivity calculations), this delay is directly proportional to the maximum dimension of the object under test [39].

If the dispersion associated with the variable attenuator can be neglected, then the reference signal $e_r(\vec{r},t)$ can be considered as an ideal impulse (i.e., a Dirac delta function) delayed t_d. According to Fig. 2, the overlap between the two components of the modified hologram (see Eq. (6)) can be avoided if the following condition for the *time delay* is fulfilled:

$$t_d \leq t_{min}. \tag{7}$$

This condition evidences that the lack of a delay line in the reference branch also avoids the responses overlap as long as the delay introduced by the components in that branch is shorter than the time required by the scattered signal to reach the combiner. A similar strategy was also proposed in [41] for a submm-wave radar. However, an additional time response was included in the modified hologram of [41] as some terms could not be canceled due to the different approach to obtain the interferometry signal.

Another possibility was also introduced in our initial work on phase retrieval for a microwave frequency scanning radar [39] where an electrically large delay line was used so that the time responses in Fig. 2 were swapped avoiding also the time domain overlap in the modified hologram. Nevertheless, the herein presented strategy based on an electrically short delay

line is found to be more advantageous since it provides more *compact* implementations.

Because the minimum travel time for the scattered field is given by $t_{min} = 2d_{min}/c$, where c is the speed of light and d_{min} is the minimum distance between the monostatic element and the OUT, it is convenient to keep the electrical distance along the reference wave path *as electrically short as possible* to enable a reduction of the minimum distance from the array elements to the OUT.

The second constraint is devoted to guarantee that the time-domain signal in Fig. 2 is correctly sampled in the frequency domain. It can be calculated by following the reasoning in [39]. Because a frequency sampling step Δf enables the correct characterization of signals spreading up to $t_{max} = 1/2\Delta f$, the correct sampling is achieved if the frequency step satisfies

$$\Delta f < \frac{1}{2\left(\Delta\tau + t_{min} - t_d\right)}. \tag{8}$$

In practice, the reference signal will not be an ideal impulse due to the dispersion in the variable attenuator and directional coupler. This *dispersion* entails a spread of both terms in (6). Because the reference signal has to be measured in the calibration stage, this spread can be conveniently characterized and, in case of need, safety margins in (7) and (8) can be included. Nevertheless, the implemented demonstrator, which is detailed in the Results section, shows a low dispersion even in the case of using generic off-the-shelf components. Consequently, reliable results can be achieved without needing to resort to safety margins.

C. Calibration

Analogous to conventional Leith-Upatnieks holography, this calibration step, which requires the measurement of the amplitude and phase of the reference wave, has to be carried out only once. Thus, the S parameter between the source port and the power detector, i.e., points 1 and 4 in Fig. 1, must be measured without the presence of an object under test. This acquisition must be carried out at the same frequencies that will be used during the normal operation of the system.

Once the reference wave has been characterized, the application of the phase retrieval technique detailed in Section II-A enables us to obtain E_s at all frequencies. It is important to notice that the propagation through the directional coupler and power combiner can introduce some delay in the signal. Depending on the inverse scattering algorithm, this delay must be compensated as discussed in Section IV.

D. Measurement steps

Once the calibration has been performed, the following steps have to be accomplished for each acquisition point:

1) The variable attenuator is configured for maximum attenuation. Thus, the reference wave is expected to be much lower than the scattered signal. Consequently, the measured power can be considered to correspond to the term $|E_s|^2$.
2) The attenuation is changed so that the power (averaged along the acquisition frequencies) measured in the previous step and the power (also averaged along the acquisition frequencies) of the reference wave measured in the calibration are as similar as possible. The measured power corresponds to the hologram $I(\omega) = |E_s(\omega) + E_r(\omega)|^2$.
3) The phase retrieval is accomplished to obtain $E_s(\omega)$.

Once the full multi-monostatic field has been retrieved at the entire set of acquisition points, inverse scattering algorithms can be applied. In this paper, the reflectivity calculation detailed in [43] is applied.

E. Non-redundant sampling for multi-monostatic acquisitions

The signal corresponding to the *square amplitude* of an electromagnetic field $|E|^2$ has a spatial bandwidth, which is twice the spatial bandwidth of a conventional acquisition [44], [14]. Moreover, *multi-monostatic* acquisitions also involve doubling the spatial bandwidth [1]. Thus, *phaseless multi-monostatic* acquisition involves very strong sampling requirements of $\lambda/8$ [37] that results in either very dense, and, consequently, expensive arrays, or long acquisition times for raster scan.

Nevertheless, the approach previously described enables retrieval of the amplitude and phase at each acquisition point. Hence, square amplitude sampling rules are not required, as the system can be considered equivalent to a conventional monostatic full acquisition, bypassing the restrictive sampling associated with conventional phaseless setups. Thus, sampling increments of $\Delta x = \Delta y = \lambda/4$ as required by multi-monostatic setups [1] can be employed without the need to resort to denser sampling.

Despite this advantage, the resulting sampling is still very dense. Nevertheless, because this novel phase retrieval system enables the full acquisition of the signal, it is compatible with standard *array thinning* techniques that enable reducing the number of elements. To illustrate this fact, the *non-redundant sampling theory* [25] will be used. This method has been successfully employed in antenna measurements [45] as well as in multistatic inverse scattering [17], [18]. Moreover, it has been recently considered for multi-monostatic acquisitions [38].

In short, this approach requires computing a parameterization of the observation domain as well as a phase factor $\psi(\vec{r})$ for the acquisition surface. Both terms depend on the dimensions of an imaginary convex surface enclosing the object under test. As shown in [25], the introduction of the phase factor into the scattered field enables minimizing the spatial bandwidth of the field and, therefore, the sampling, which is now carried out in the parametric domain, is considerably reduced. The field modified by the phase factor is referred to as the *reduced field*. After the acquisition and reduction, the field can be efficiently computed at any point inside the acquisition surface by means of an optimal sampling interpolation (OSI) [25].

In the case of multi-monostatic acquisitions, modified phase factors and sampling steps must be considered [38]. In particular, the approach can be summarized as follows:

1) The acquisition points are chosen according to the convex surface enclosing the object under test. In this step, it has to be considered that the reduced multi-monostatic field has twice the spatial bandwidth of a conventional bistatic acquisition [38] . Thus, the spatial sampling frequency must be twice of that for antenna measurements [25].
2) After the amplitude and phase of the field have been retrieved according to the three steps described earlier, the *reduced field* is computed as $F(\vec{r}) = E(\vec{r})e^{j2\psi(\vec{r})}$ where $\psi(\vec{r})$ is the phase factor detailed in [25]. It is important to notice that the factor $x2$ in the exponent is due to the multi-monostatic acquisition as detailed in [38].
3) The field is retrieved at any point inside the acquisition surface by means of an OSI [25].

According to [25], the acquisition points depend on the OUT as well as on the frequency. Thus, these points must be calculated in the *worst case scenario*, i.e., considering the largest virtual convex surface enclosing the object under test as well as the highest frequency.

As will be shown in the Results section, this strategy enables us to improve the efficiency of the sampling while it is still possible to retrieve the field in a uniform grid, satisfying the theoretical sampling of $\lambda/4$ for monostatic fields [1]. Other possible strategies to reduce the acquisition points, which are compatible with the element design presented in this work, are the increment of the sampling steps [1] at the expense of decreasing the maximum angular field of view [46] or the use of sparse arrays techniques that have shown very good results for multistatic acquisitions [47].

VII

III. Numerical Results

To evaluate the performance of the previous approach, the system is simulated by means of the commercial software Feko [48]. The OUT is simulated by means of physical optics to alleviate the simulation time. The transmitter and receiver antennas are modeled by means of a $\cos^q$ radiation pattern with $q = 1$.

Once the monostatic field has been calculated, the interferometry signal is computed by adding a reference wave given by a Gaussian function in the time-domain. The time delay, i.e., the mean of the Gaussian function, is chosen as the time the light needs to travel 2 cm, i.e., $t_d = 66.7$ ps whereas the dispersion is modeled by the typical deviation parameter that is set to 1.2 ps.

The OUT is a metallic cut-off pyramid analyzed in the band from 25 GHz to 40 GHz. The number of frequencies is set to 100. The bottom and top faces of the pyramid are rectangles of dimensions $6\lambda_{min} \times 8\lambda_{min}$ and $2\lambda_{min} \times 4\lambda_{min}$, where λ_{min} is the wavelength at the maximum frequency ($f = 40$ GHz). The height of the pyramid is $2\lambda_{min}$. To compute the optimal sampling, the radius of the virtual sphere enclosing the OUT is required [25]. According to the previous dimensions, this parameter is given by $a = 5.1\lambda_{min}$.

The acquisition surface corresponds to a plane-polar setup as detailed in [38]. The maximum radius is set to $\rho_{\max} =$ 20 cm and the acquisition plane is placed at $D = 7.5$ cm from the OUT. The excess bandwidth and oversampling factors are set to 1.2 [25], resulting in 4200 acquisition points, i.e., the points where the transmitter/receiver pair is placed.

Once the amplitude and phase have been retrieved in the non-uniform plane-polar setup, the field is computed in a uniform square grid, with dimensions $W_x = W_y = 40$ cm that contains the plane-polar acquisition surface. The sampling increments in the square grid are set to $\Delta x = \Delta y = \lambda/4$ fulfilling the theoretical spatial bandwidth for multi-monostatic acquisitions. The scattered field at the points outside the maximum acquisition radius ρ_{max} is set to zero. In contrast to the number of acquisition points, the number of the uniform grid points inside the radius of the acquisition surface ρ_{max} is $35,727$. Despite this strong reduction, it will be shown next that this approach entails a negligible error. Figure 3 depicts the simulation setup described including all the relevant parameters.

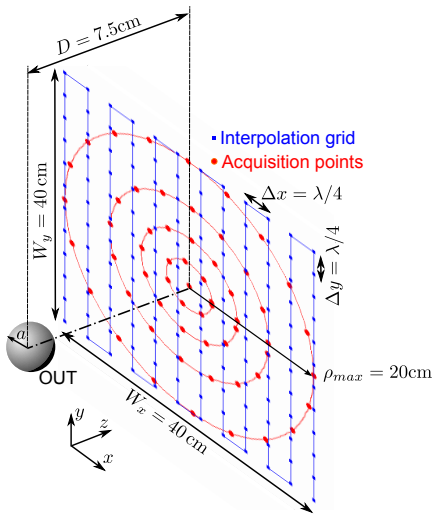

Figure 3. Simulation setup. Acquisition and interpolation points have been subsampled to improve the graphical representation.

To validate the approach, the following error is defined at each frequency:

$$e[\%] = \frac{\|\mathbf{E}_{true} - \mathbf{E}_{ret}\|_2}{\|\mathbf{E}_{true}\|_2} \cdot 100, \tag{9}$$

where $\mathbf{E}_{ret}$ is a vector containing the samples of the field in the uniform grid after the phase retrieval and interpolation, $\mathbf{E}_{true}$ is a sample vector corresponding to the field directly computed at the rectangular uniform grid and $\|\cdot\|_2$ is the Euclidean norm.

Figure 4, which compares two different filtering windows to separate the time-domain components in (6), shows the error at each frequency. In both cases, the error is high at the first and last frequencies due to the time-domain filtering. Thus, it is highly recommended that the results at such frequencies be discarded. Figure 4 also shows that it is recommended to

employ a Hamming window rather than a rectangular window to guarantee a larger number of useful frequencies. The main drawback associated with the Hamming window is that the error in the central frequencies is slightly higher than that for the rectangular window. Results at these frequencies, however, are expected to be accurate enough to be employed by the inverse algorithms in both cases.

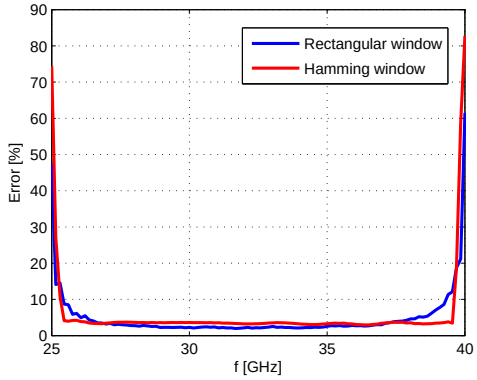

Figure 4. Difference between the retrieved and exact field for rectangular and Hamming window.

In the reconstruction of the geometry, the first and last five frequencies are discarded due to the aforementioned error. Moreover, only 19 uniformly spaced frequencies are considered, because additional frequencies do not contribute to increase the reconstruction accuracy [43]. The results for the object reconstruction are shown in Fig. 5 by means of a light gray mesh that corresponds to the reflectivity isosurface of amplitude -11 dB [43]. The figure depicts only the results corresponding to the profile reconstruction from the retrieved and interpolated field. The figure does not show the results corresponding to the reconstruction from direct computation, because no significant differences are visible.

IV. Measurements Results

A demonstrator of the previous concepts is implemented by means of a *raster scan* in the K_a band (26.5-40 GHz). The transmitter and receiver antennas, which are two identical horns in this implementation, are fixed and the object is moved through a plane. This strategy is used instead of moving the transmitter and receiver, because the (bulky) network analyzer was used to implement the source and receiver in this demonstrator. However, results are expected to be equivalent to those ones obtained when implementing either array or raster scanning by moving the Tx/Rx jointly.

Figure 6 shows the components of the setup. A wideband directional coupler (Agilent 87301D) is used to sample a fraction of the transmitter signal, i.e., the reference signal. The attenuator is implemented by cascading two voltage variable attenuators (Hittite HMC985LP4KE); each of them provides an attenuation range of 35 dB.

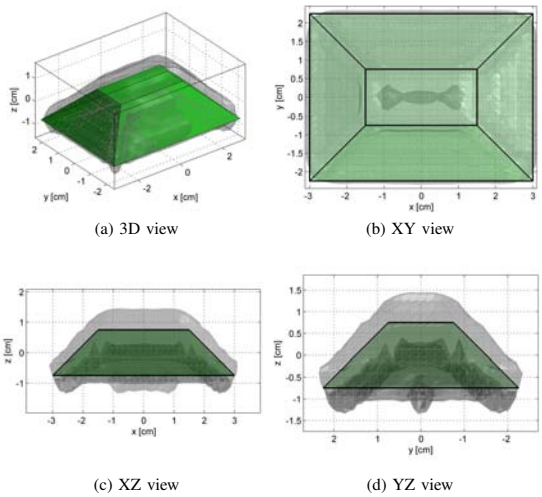

(a) 3D view (b) XY view

(c) XZ view (d) YZ view

Figure 5. True truncated pyramid profile (solid green surface) and reconstructed reflectivity (light gray mesh: -11 dB amplitude isosurface).

In the first example, a power combiner is not used to produce the interferometry. Instead, both signals are sent to a vector network analyzer (VNA) and combined by software in the postprocessing. Connections to the VNA are identified in the conceptual scheme of the experimental setup (Fig. 7) as well as in the implemented setup (Fig. 6). This VNA connection arrangement was chosen because it enables knowing the real amplitude and phase of the scattered field that is required to calculate the error introduced by the phase retrieval. In this case, the field is sampled at 201 equally spaced frequency points in the K_a band.

In the second example, the setup includes a power combiner (Keysight 11636C) to take into account also any possible degradation due to this component (see Fig. 8). Since the setup is still implemented by mean of off-the-shelf components, distances between components are not as minimized as possible. Thus, a flexible cable with length 0.9 m has been included to connect the output of the Rx antenna to the corresponding power combiner input. Since this connection results in an artificial increment of time to received the signal at the power combiner ($t_{\min}$), the frequency sampling must be increased to take into account this fact. Hence, the number of frequency points in this example is 1601.

The algorithm detailed in [43] is used again to retrieve the profile of the OUT. The profile reconstruction algorithm expects as input the field referred to the *phase center* of the antennas. Nevertheless, the phase retrieval algorithm retrieves the field referred to the points 1 and 4 in Fig. 1. As previously discussed, some delay is expected due to the directional coupler, connector transitions, power combiner and waveguide propagation before the antennas. In practice, it can be easily compensated by correcting the phase by a linear factor, i.e., multiplying the retrieved field by $\exp(jkL)$ where L is an equivalent distance accounting for the aforementioned

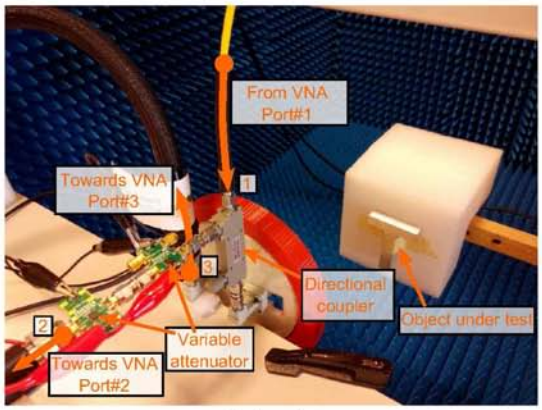

(a) Rear view.

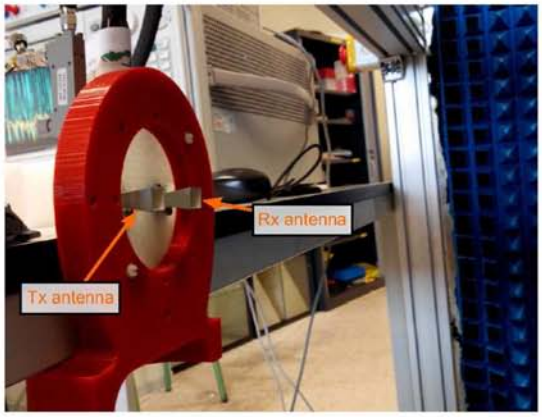

(b) Front view.

Figure 6. Implemented setup for raster scanning: a) Rear view; b) Front view.

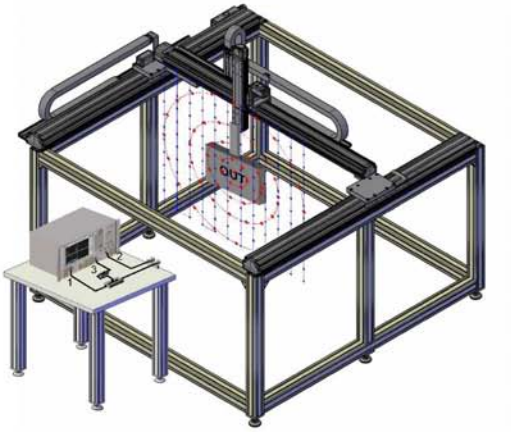

Figure 7. Scheme of the raster scanning setup with two channel acquisitions, i.e., without power combiner.

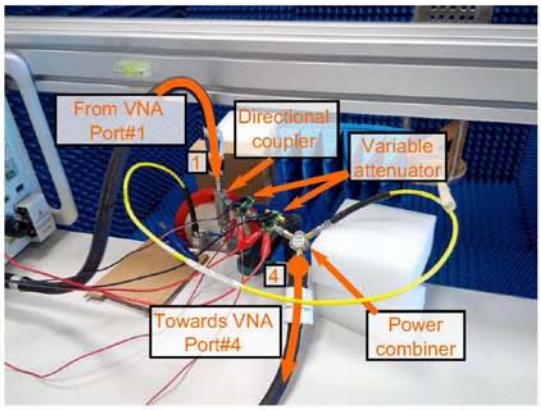

Figure 8. Setup including power combiner.

propagation. This parameter can be found by applying a linear sweep in L to find the best focused image.

A. *Characterization of the reference signal*

To evaluate the characteristics of the reference signal, the time-response between points 1 and 4 (see Fig. 1) is analyzed for the demonstrator setup including the power combiner (Fig. 8). This response is estimated by computing the inverse Fourier transform of the S_{41} parameter for different attenuation values. In particular, the maximum and minimum attenuation values are considered. In addition, the response for an arbitrary intermediate attenuation level is also considered. The respective average attenuation values in the working band for the three considered cases are 108 dB, 37 dB and 55 dB. To characterize the maximum attenuation levels, which would yield a signal below the sensitivity of the VNA, the S-parameters of the second variable attenuator as well as the S-parameters of the first variable attenuator plus the directional coupler and power combiner were first measured. After that, the global S-parameters were computed by cascading both.

Figure 9 shows the *normalized* values of the time-response, revealing that the reference signal has maximum peak at approximately $t = 0.96$ ns and the spread calculated for a given threshold of -25dB is approximately 1.5 ns. Thus, it can be considered that the reference signal vanishes beyond $t_{min} = 1.5$ ns, and, consequently, the objects under test must be placed at a minimum distance of $d_{min} \geq t_{min} \cdot c/2 = 22.5$ cm. However, this distance can be considerably reduced in practice, because the direct signal also suffers a significant delay due to the directional coupler and waveguide sections before the antennas, which contributes to avoid the spectra overlap previously discussed.

B. *Profile reconstruction*

Several metallic letters, which have a depth of 1 cm, are used as OUT (see inset in Fig. 10). All these objects can be enclosed

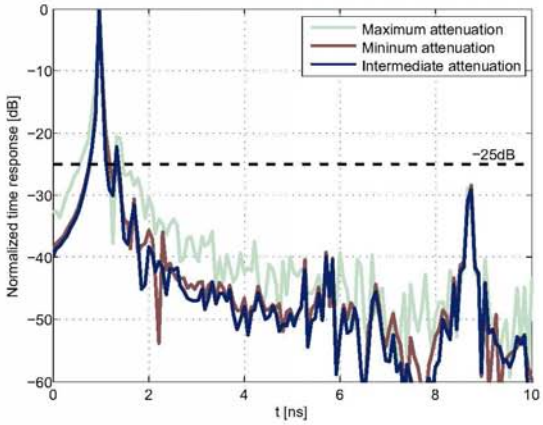

Figure 9. Normalized time response between points 1 and 4 of Fig. 1.

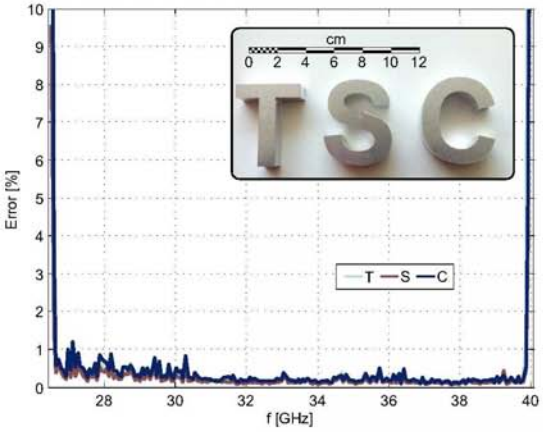

Figure 10. Error in frequency for the objects under test shown in the inset.

by a spherical surface of radius $a = 4\,\text{cm}$. The distance to the acquisition plane is $D = 13.5\,\text{cm}$, and the maximum radius of the plane-polar acquisition is $\rho_{max} = 20\,\text{cm}$, resulting in 3192 monostatic acquisition points. After retrieving the phase at the acquisition points, the field is calculated by means of OSI in a square grid of size $40\,\text{cm} \times 40\,\text{cm}$, which contains the acquisition surface again. As in the simulation example, the number of points in the square grid with $\Delta x = \Delta y = \lambda/4$ lying inside the surface of radius ρ_{max} is 35,727.

Because the acquisition of the field at all the points in the square grid would involve a prohibitive measuring time for a raster scanning, the error will be computed only at the plane-polar acquisition points. This approach does not allow to compute the error introduced by the OSI. However, it still enables to properly characterize the error introduced by the phase retrieval approach.

Figure 10 shows the error after applying a Hamming window. As in the simulation, the error in the first and last frequencies is contaminated by a strong error, but the results at the rest of frequencies are reliable, with an error below 1.5%.

Once the monostatic scattered field has been retrieved, the first and last five frequencies are discarded to avoid the aforementioned error. Moreover, the scattered field is subsampled in the frequency domain so that only 25 equally spaced frequencies survive to be used in the reconstruction process. As previously mentioned, additional frequencies would not result in a better profile reconstruction. Figures 11, 12 and 13 show the profile reconstruction corresponding to the -10 dB reflectivity amplitude isosurface.

Finally, an application example concerning non-destructive inspection is presented. As previously discussed, a power combiner is used to physically add the signals instead of using independent acquisitions channels for the reference and scattered signals. In this case, a stapler remover is packed into a cardboard box and covered with foam as shown in Fig. 14. The dimensions of the box are $14\,\text{cm} \times 11\,\text{cm} \times 4\,\text{cm}$. Consequently, it can be enclosed by an sphere of radius $a = 9\,\text{cm}$. The box is

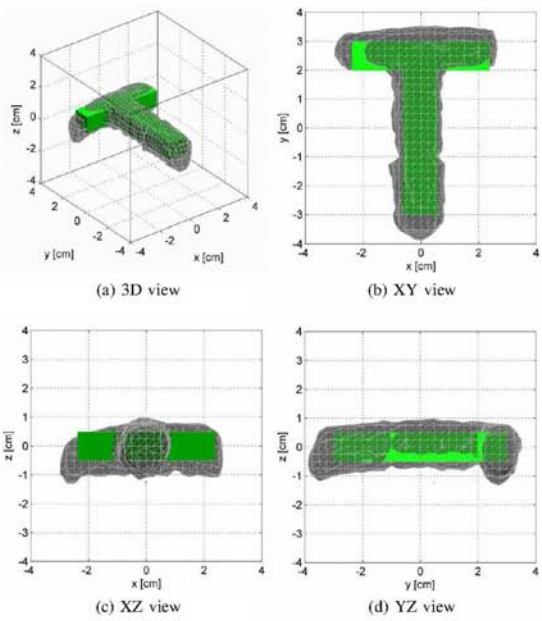

(a) 3D view (b) XY view

(c) XZ view (d) YZ view

Figure 11. True profile for 'T'-shaped geometry (solid green surface) and reconstructed reflectivity (light gray mesh: $-10\,\text{dB}$ amplitude isosurface).

scanned by means of the setup previously described (see Figs. 6 and 7). In this case, the acquisition distance is $D = 13\,\text{cm}$, and the acquisition radius $\rho_{max} = 16\,\text{cm}$. The number of acquisition points is $11,206$. A conventional sampling of $\lambda/4$ would result in $22,865$ acquisition points inside the circle of radius ρ_{max}.

Figure 15 shows the profile reconstruction for the normalized reflectivity isosurface corresponding to $-10\,\text{dB}$, proving that the phaseless system retains excellent capabilities to

VII

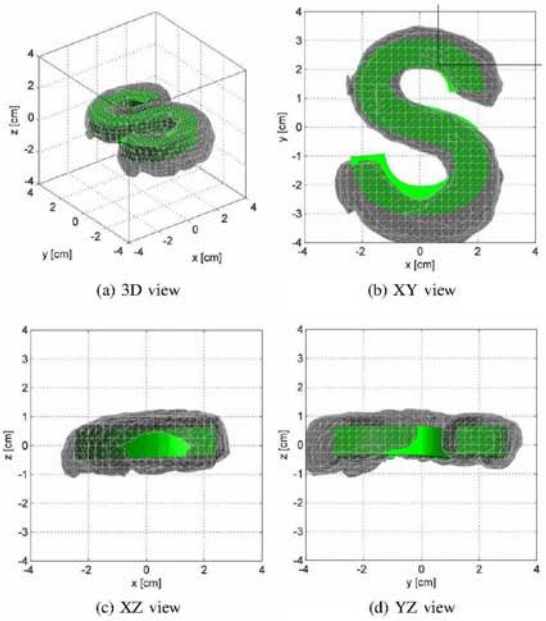

(a) 3D view (b) XY view (c) XZ view (d) YZ view

Figure 12. True profile for 'S'-shaped geometry (solid green surface) and reconstructed reflectivity (light gray mesh: −10 dB amplitude isosurface).

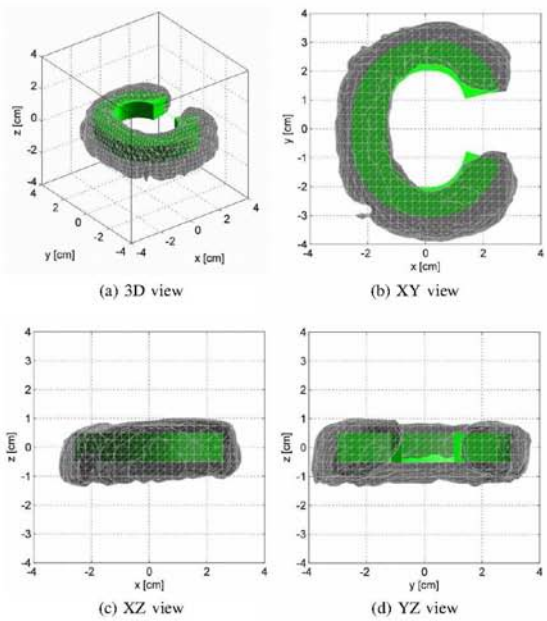

(a) 3D view (b) XY view (c) XZ view (d) YZ view

Figure 13. True profile for 'C'-shaped geometry (solid green surface) and reconstructed reflectivity (light gray mesh: −10 dB amplitude isosurface).

VII

inspect objects behind penetrable materials.

V. Conclusions

A novel design for phaseless and broadband *synthetic aperture radar* is presented in this paper. The monostatic element comprising the transmitter-receiver pair relies on *amplitude-only* acquisition and it only requires a minimum number of components to accomplish the full field retrieval. Computationally efficient algorithms inspired by conventional off-axis holography are used to compute the phase of the scattered field. In addition, this phase retrieval is accomplished at each acquisition point and, therefore, conventional *techniques to reduce the number of acquisition points* can be applied with minor (if any) changes.

In contrast to previous works, the phase retrieval is accomplished at all working frequencies *without the need to resort to phase shifters* [38]. In addition, the scanning system can work in the near-field with only minor restrictions regarding the distance to the OUT [36]. Furthermore, the non-iterative nature of the technique provides a good framework to work with *non-collaborative targets* as it avoids the acquisition at multiple surfaces, which usually requires a mechanical movement of the sensor array (e.g., [13]).

The performance of the approach is validated by raster scanning with a single element working in the K_a band. This demonstrator is implemented by means of standard components (e.g., directional couplers, variable attenuators boards, generic antennas, etc.) available in the market. Although the path of the reference signal is much longer than the one that

Figure 14. Open box containing a staple remover.

can be achieved with an ad-hoc design, *good time-domain dispersion characteristics* has been observed, which enables an accurate retrieval of the scattered field. This point is expected to be considerably improved in case of implementing the entire element as a single component enabling a lower dispersion as well as a closer minimum distance to the objects.

The performance of standard algorithms for profile reconstructions in case of using retrieved data is checked by means of simulated and experimental data. Both cases confirm the

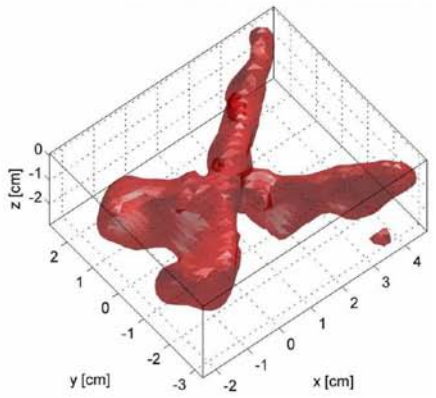

Figure 15. Staple remover profile reconstruction.

good quality of the retrieved field to be employed in inverse scattering algorithms.

REFERENCES

[1] D. M. Sheen, D. L. McMakin, and T. E. Hall, "Three-dimensional millimeter-wave imaging for concealed weapon detection," *IEEE Transactions on Microwave Theory and Techniques*, vol. 49, no. 9, pp. 1581–1592, Sep. 2001.

[2] S. Ahmed, A. Schiessl, F. Gumbmann, M. Tiebout, S. Methfessel, and L. Schmidt, "Advanced microwave imaging," *IEEE Microwave Magazine*, vol. 13, no. 6, pp. 26–43, 2012.

[3] S. Oka, H. Togo, N. Kukutsu, and T. Nagatsuma, "Latest trends in millimeter-wave imaging technology," *Progress In Electromagnetics Research Letters*, vol. 1, pp. 197–204, 2008.

[4] J. E. Peabody, G. L. Charvat, J. Goodwin, and M. Tobias, "Through-wall imaging radar," *Lincoln Laboratory Journal*, vol. 19, no. 1, pp. 62–72, 2012.

[5] M. Aamna, S. Ammar, T. Rameez, S. Shabeeb, N. Rao, and I. Safwat, "2d beamforming for through-the-wall microwave imaging applications," in *International Conference on Information and Emerging Technologies (ICIET)*, June 2010.

[6] L. Duchesne, L. Durand, and P. Garreau, "Development of a compact ms-gpr radar based on multi-sensors technology," in *2nd International Workshop on Advanced GPR*, Delft, Netherlands, 14-16 May 2003, pp. 36–44.

[7] G. P. Kniffin, L. M. Zurk, S. Schecklman, and S. C. Henry, "3d terahertz synthetic aperture imaging of objects with arbitrary boundaries," pp. 88 460T–88 460T–10, 2013.

[8] R. Pierri, G. D'Elia, and F. Soldovieri, "A two probes scanning phaseless near-field far-field transformation technique," *IEEE Trans. Antennas Propag.*, vol. 47, no. 5, pp. 792–802, May 1999.

[9] G. Junkin, "Planar near-field phase retrieval using GPUs for accurate THz far-field prediction," *IEEE Trans. Antennas Propagat.*, vol. 61, no. 4, pp. 1763–1776, 2013.

[10] C. H. Schmidt, S. F. Razavi, T. F. Eibert, and Y. Rahmat-Samii, "Phaseless spherical near-field antenna measurements for low and medium gain antennas," *Adv. Radio Sci.*, vol. 8, pp. 43–48, 2010.

[11] A. Tennant, G. Junkin, and A. P. Anderson, "Antenna far-field predictions from two phaseless cylindrical near-field measurements," *Electronics Letters*, vol. 28, no. 23, pp. 2120–2122, Nov 1992.

[12] S. F. Razavi and Y. Rahmat-Samii, "Phaseless planar near field measurements for scanned beams: Difficulties, a hybrid solution and measured results," in *Proc. IEEE Antennas Propaga. Society Int. Symp*, vol. 9-14, 2006, pp. 429–432.

[13] G. Hislop, L. Li, and A. Hellicar, "Phase retrieval for millimeter- and submillimeter-wave imaging," *IEEE Trans. Antennas Propagat.*, vol. 57, no. 1, pp. 286–289, Jan. 2009.

[14] A. Capozzoli, C. Curcio, G. D'Elia, and A. Liseno, "Phaseless antenna characterization by effective aperture field and data representations," *IEEE Trans. Antennas Propagat.*, vol. 57, no. 1, pp. 215–230, 2009.

[15] T. Isernia, G. Leone, and R. Pierri, "Phase retrieval of radiated fields," *Inverse Problems*, vol. 11, pp. 183–203, 1995.

[16] S. S. Caorsi, A. Massa, M. Pastorino, and A. Randazzo, "Electromagnetic detection of dielectric scatterers using phaseless synthetic and real data and the memetic algorithm," *IEEE Transactions on Geoscience and Remote Sensing*, vol. 41, no. 12, pp. 2745–2753, Dec. 2003.

[17] L. Crocco, M. D'Urso, and T. Isernia, "Inverse scattering from phaseless measurements of the total field on a closed curve," *J. Opt. Soc. Am. A*, vol. 21, no. 4, pp. 622–631, Apr. 2004.

[18] O. M. Bucci, L. Crocco, M. D'Urso, and T. Isernia, "Inverse scattering from phaseless measurements of the total field on open lines," *Journal of Optical Society of America*, vol. 23, no. 10, pp. 2566–2577, Oct. 2006.

[19] L. Crocco, M. D'Urso, and T. Isernia, "Faithful phaseless nonlinear imaging from only-amplitude measurements of incident and total field," *Optics Express*, vol. 15, no. 7, pp. 3804–3815, Apr. 2007.

[20] J. Tuovinen, A. Lehto, and A. Räisänen, "Accurate millimeter wave antenna phase pattern measurements using the differential phase method with three power meters," *Phase measurements of millimetre wave antennas at 105-190 GHz with a novel differential phase method*, vol. 138, pt. H, pp. 114–120, Apr. 1991.

[21] S. Costanzo, G. D. Massa, and M. D. Migliore, "Integrated microstrip probe for phaseless near-field measurements on plane-polar geometry," *Electronics letters*, vol. 37, no. 16, pp. 1018–1020, 2001.

[22] A. Lehto, J. Tuovinen, O. Boric, and A. Ra¨isa¨nen, "Antenna phase pattern measurements using three power meters," in *Microwave Conference, 1992. 22nd European*, vol. 1, Sep. 1992, pp. 515–520.

[23] A. Lehto, J. Tuovinen, O. Boric, and A. Räisänen, "Accurate millimeter wave antenna phase pattern measurements using the differential phase method with three power meters," *IEEE Transactions on Antennas and Propagation*, vol. 40, no. 7, pp. 851–853, Jul. 1992.

[24] S. Costanzo, G. D. Massa, and M. D. Migliore, "A novel hybrid approach for far-field characterization from near-field amplitude-only measurements on arbitrary scanning surfaces," *IEEE Trans. Antennas Propagat.*, vol. 53, no. 6, pp. 1866–1874, 2005.

[25] O. M. Bucci, C. Gennarelli, and C. Savarese, "Representation of electromagnetic fields over arbitrary surfaces by a finite and nonredundant number of samples," *IEEE Trans. Antennas Propagat.*, vol. 46, no. 3, pp. 351–359, Mar. 1998.

[26] S. Costanzo and G. D. Massa, "Wideband phase retrieval technique from amplitude-only near-field data," *Radioengineering*, vol. 17, pp. 8–12, 2008.

[27] S. Costanzo, A. Borgia, G. D. Massa, M. Pastorino, and A. Randazzo, "Phaseless imaging of dielectric scatterers - preliminary experimental results," in *Antennas and Propagation (EuCAP), 2013 7th European Conference on*, Apr. 2013, pp. 3852–3855.

[28] S. Costanzo, G. D. Massa, M. Pastorino, and A. Randazzo, "An inverse scattering approach for inspecting dielectric scatterers at microwave frequencies without phase information," in *IEEE International Conference on Imaging Systems and Techniques (IST)*, Oct 2013, pp. 392–397.

[29] ——, "Hybrid microwave approach for phaseless imaging of dielectric targets," *to appear in IEEE Geoscience and Remote Sensing Letters*.

[30] E. N. Leith and J. Upatnieks, "Reconstructed wavefronts and communication theory," *J. Opt. Soc. Amer.*, vol. 52, pp. 1123–1128, 1962.

[31] A. Tamminen, J. Ala-Laurinaho, and A. V. Räisänen, "Imaging with indirect holographic method at 310 GHz," in *Proc. XXXI Finnish URSI convention on radio science and electromagnetics*, 2008, pp. 31–32.

[32] G. Junkin, T. Huang, and J. Bennett, "Holographic testing of terahertz antennas," *IEEE Trans. Antennas Propagat.*, vol. 48, no. 3, pp. 409 –417, Mar. 2000.

[33] D. Smith, M. Leach, and A. Sambell, "Microwave indirect holographic imaging using an adaptation of optical techniques," *IEEE Microwave and Wireless Component Letters*, vol. 13, no. 9, pp. 379–381, Sep. 2003.

[34] D. Smith, M. Leach, M. Elsdon, and S. J. Foti, "Indirect holographic techniques for determining antenna radiation characteristics and imaging aperture fields," *IEEE Antennas Propagat. Mag.*, vol. 49, no. 1, pp. 54 –67, Feb. 2007.

[35] M. Schnell, P. S. Carney, and R. Hillenbrand, "Synthetic optical holography for rapid nanoimaging," *Nature communications*, vol. 5, 2014.

[36] J. Laviada, Y. Álvarez López, C. García-González, A. Arboleya, and F. Las-Heras, "A modified phaseless inverse scattering setup based on indirect holography implemented at submillimeter-wave band," *IEEE Trans. Antennas Propagat.*, vol. 61, no. 9, pp. 4876–4881, Sep. 2013.

[37] ——, "Inverse scattering with phase retrieval based on indirect holography via synthetic plane-waves," *IET Microwave, Antennas and Propagation*, vol. 6, no. 12, pp. 1389–1398, 2012.

[38] J. Laviada, Y. Álvarez López, A. Arboleya-Arboleya, C. García-González, and F. Las-Heras, "Interferometric technique with non-redundant sampling for phaseless inverse scattering," *IEEE Transactions on Antennas and Propagation*, vol. 62, no. 2, pp. 223–230, 2014.
[39] J. Laviada, Y. Álvarez López C. García-González, C. Vázquez-Antuña, S. Ver-Hoeye, M. Fernández-García, G. Hotopan, R. Camblor, and F. Las-Heras, "A novel phaseless frequency scanning based on indirect holography," *Journal of Electromagnetic Waves and Applications*, vol. 27, no. 4, pp. 275–296, 2013.
[40] J. Laviada and F. Las-Heras, "Phaseless antenna measurement on non-redundant sample points via leith-upatnieks holography," *IEEE Transactions on Antennas and Propagation*, vol. 61, no. 8, pp. 4036–4044, Aug. 2013.
[41] J. Laviada, Y. Álvarez López, R. Camblor-Díaz, C. García-González, C. Vázquez-Antuña, A. Arboleya-Arboleya, M. Fernández-García, G. Hotopan, S. V. Hoeye, and F. Las-Heras, "Phase retrieval technique for submm-wave frequency scanning-based radar system," *IET Microwave, Antennas and Propagation*, vol. 8, no. 14, pp. 1170–1178, 2014.
[42] Y. Álvarez, C. García-González, C. Vazquez-Antuña, S. Ver-Hoeye, and F. Las-Heras, "Frequency scanning based radar system," *Progress in Electromagnetic Research*, pp. 275–296, 2012.
[43] Y. Alvarez, J. Laviada, L. Tirado, C. Garcia, J. Martinez, F. Las-Heras, and C. Rappaport, "Inverse fast multipole method for monostatic imaging applications," *IEEE Geoscience and Remote Sensing Letters*, vol. 10, no. 5, pp. 1239–1243, 2013.
[44] O. M. Bucci and G. D'Elia, "Advanced sampling techniques in electromagnetics," in *Review of Radio Science 1993-1995*. London: Oxford University Press, 1996, pp. 177–204.
[45] O. M. Bucci and C. Gennarelli, "Application of nonredundant sampling representations of electromagnetic fields to NF-FF transformation techniques," *International Journal of Antennas and Propagation*, vol. 2012, p. 14.
[46] V. Krozer, T. Löffler, J. Dall, A. Kusk, F. Eichhorn, R. K. Olsson, J. D. Buron, P. U. Jepsen, V. Zhurbenko, and T. Jensen, "Terahertz imaging systems with aperture synthesis techniques," *IEEE Trans. Microwave theory and techniques*, vol. 58, no. 7, pp. 2027–2039, Jul. 2010.
[47] S. Ahmed, A. Schiessl, and L. Schmidt, "A novel fully electronic active real-time imager based on a planar multistatic sparse array," *IEEE Transactions on Microwave Theory and Techniques*, vol. 59, no. 12, pp. 3567–3576, 2011.
[48] *FEKO User Manual, Suite 6.1*. Stellenbosch, South Africa: EM Softw. Syst. S.A. (Pty) Ltd., 2011.

VII

Jaime Laviada was born in Gijón, Spain. He received the M.S. degree in telecommunication engineering and the Ph.D. degree from the University of Oviedo, Gijón, Spain, in 2005 and 2010, respectively.
In 2006, he joined the research group Signal Theory and Communications, Department of Electrical Engineering, University of Oviedo. He was a Visiting Scholar in the Electromagnetics and Communications Lab, Pennsylvania State University, during 2007 and 2008.
He has been involved in multiple national and European projects as well as contracts with multiple companies. His main research interests are in numerical efficient techniques applied to antenna measurements, method of moments, and antenna pattern synthesis.

Yuri Alvarez (S'06–M'09) was born in Langreo, Spain, in 1983. He received the M.S. and Ph.D. degrees in telecommunication engineering in 2006 and 2009, respectively.
He was a Visiting Scholar in the Department of Electrical Engineering and Computer Science, Syracuse University, Syracuse, NY, USA, in 2006 and 2008; and a Visiting Postdoc at the Gordon Center for Subsurface Sensing and Imaging Systems (CenSSIS)—ALERT Center of Excellence, Northeastern University, Boston, MA, USA, in 2011, 2012, and 2013. He is currently an Assistant Professor at the Signal Theory and Communications of the University of Oviedo, Gijón, Spain.
Dr. Alvarez received the 2011 Regional and National Awards to the Best Ph.D. Thesis on Telecommunication Engineering (category: security and defense). His interests and research studies have been focused on antenna diagnostics, antenna measurement techniques, RF techniques for indoor location, and inverse scattering and imaging techniques.

Ana Arboleya Arboleya received de M.Sc. degree in telecommunication engineering from the University of Oviedo, Spain, in 2009, where she is currently working toward the Ph.D. degree. Since 2008, she has been working as a Research Assistant with the Signal Theory and Communications Area at the University of Oviedo. Her major research interests comprise antenna and RCS measurement systems and high frequency scattering measurement techniques.

Cebrián García González (S'10) was born in Pola de Laviana (Spain) in 1983. He received the M.Sc. degree in telecommunication engineering from the University of Oviedo, Gijón, Spain, in 2010, where he is currently working toward the Ph.D. degree. Since 2010, he has been working as a Research Assistant with the Signal Theory and Communications Area, University of Oviedo. His research efforts are focused on the reconstruction of electromagnetic sources from field measurements, inverse scattering problem and imaging techniques.

Fernando Las-Heras (M'86, SM'08) received the M.S. in 1987 and the Ph.D. in 1990, both in Telecommunication Engineering, from the Technical University of Madrid (UPM). From 1988 to 1990, he was a National Graduate Research Fellow. From 1991 to 2000 he held a position of Associate Professor at the Department of Signal, Systems and Radiocommunications of the UPM. From December 2003 he holds a Full-Professor position at the University of Oviedo where he was the Vice-dean for Telecommunication Engineering at the Technical School of Engineering at Gijón from 2004 to 2008. As of 2001 he heads the research group Signal Theory and Communications TSC-UNIOVI at the Dept. of Electrical Engineering of the University of Oviedo. He was a Visiting Lecturer at the National University of Engineering in Peru in 1996, a Visiting Researcher at Syracuse University, New York, in 2000, and a short term Visiting Lecturer at ESIGELEC in France from 2005 to 2011. From 2005 he holds the Telefónica Chair ICTs Applied to Environment and Climate Change at the University of Oviedo and from 2010 he is a member of the Science, Technology and Innovation Council of Asturias, and member of the board of directors of the IEEE Spain Section. He has authored over 300 articles published in academic journals and proceedings of international conferences, mainly in the areas of antenna design and the inverse electromagnetic problem with applications in diagnostic, measurement and synthesis of antennas, phaseless techniques, propagation, and microwave to THz imaging and localization, as well as in engineering education. .

Publication VIII

J. Laviada, **. Arboleya**, F. López-Gayarre and F. Las-Heras **"Broadband synthetic aperture scanning system for threee-dimensional through-the-wall inspection,"** *IEEE Geoscience and Remote Sensing Letters,* vol. 13, no. 1, pp. 97–101, Jan. 2016.

Broadband Synthetic Aperture Scanning System for Three-Dimensional Through-the-Wall Inspection

Jaime Laviada, Ana Arboleya, Fernando López-Gayarre, and Fernando Las-Heras, *Senior Member, IEEE*

***Abstract*—This letter presents a cost-effective technique for through-the-wall imaging of objects beyond a wall. The approach relies on an amplitude-only multi-monostatic radar that operates as a synthetic aperture radar. In contrast to conventional approaches, the system employs recent broadband techniques for phase retrieval. Thus, the complexity of the scanner is reduced whereas it preserves the capacities of a conventional broadband system to retrieve the three-dimensional profile of objects. Moreover, the system is compatible with state-of-the art techniques that require full (i.e., amplitude and phase) acquisitions. Results at different frequency bands are shown to illustrate how the system can provide accurate estimation of the profile of metallic objects behind building materials such as plywood, plasterboard or hollow bricks and mortar.**

***Index Terms*—Through-the-wall imaging; synthetic aperture radar; monostatic; phase retrieval.**

I. Introduction

THROUGH-the-wall imaging has been mainly employed to detect the presence of people behind walls [1], [2]. In general, it has been achieved by means of electromagnetic waves up to 10GHz [1]. Nevertheless, the recent advances in higher frequency components, mainly at millimeter and submillimeter-wave bands, have enabled higher resolution capabilities at the expense of a shorter range. These new characteristics have opened up new possibilities involving *through-the-wall inspection* to detect hidden and illegal materials such as explosives, contraband or listening devices, which could be hidden behind and close to building materials [3].

In general, imaging based on electromagnetic waves can be accomplished by either using an antenna with a small spot (usually by means of lenses, e.g., [3]) or by using non-directive antennas with a large spot and processing the information by means of *synthetic aperture imaging*. This latter technique is widely used (e.g.,[1], [4], [5], [6]) and its major advantage is the capacity to focus at an arbitrary distance in contrast to the lenses which are usually optimized to focus at a fixed distance.

In through-the-wall inspection, it is advantageous to provide not only lateral resolution, which is given by the working frequency, but also depth resolution to find the distance to the hidden object. Nevertheless, depth resolution is proportional to the bandwidth of the signal [7] and, therefore, it is advisable to resort to a system based on broadband components to achieve the best resolution possible. In general, *power detectors*, which are only able to measure the amplitude of the received signal, enable a wider bandwidth compared to standard I/Q mixers, which are able to measure the amplitude as well as the phase of the received signal. Nevertheless, *synthetic aperture imaging* requires phase information [7].

Although the use of amplitude-only radar is convenient for a three-dimensional wall-inspection, an appropriate *phase retrieval* technique is required. Despite a large collection of techniques is available in the literature (e.g., [8], [9]), the work of approaches compatible with *phaseless and broadband* imaging has been very limited to the best knowledge of the authors. Nonetheless, a novel technique, which can operate with multifrequency monostatic imaging based on amplitude-only data, has been recently proposed [10].

The main *contribution* of this work is the demonstration of the capability of amplitude-only scanners to accurately compute the three-dimensional reconstruction of objects behind a wall. For this purpose, the model proposed in [10] is implemented by a microstrip circuit as well as by off-the-shelf components. In addition, the phase retrieval algorithm is modified so that the system does not require a variable attenuator in contrast to [10].

II. Scanning system

A. Modified quasi-monostatic scanning setup

The *synthetic aperture* approach employed in this paper is detailed in Fig. 1. A transmitter and receiver, which are connected by a reference signal, are moved along a plane parallel to the wall. This plane is referred to as *scanning surface*. A distance d has been intentionally left between the scanning surface and the wall in case reflections could affect the correct operation of the antennas. Otherwise, this safety distance can be reduced to zero.

In this system, the transmitter and receiver antennas are close to each other in a *quasi-monostatic* arrangement. An interferometric signal is obtained by combining the received signal, which is the result of the waves reflected by the wall and the objects behind, with a fraction of the transmitted signal. The latter signal is usually known as *reference signal*. The scheme of the circuit employed to combine both signals, which is based on standard microwave components, as detailed in [10], is shown in the inset of Fig.1. Thus, a directional coupler and a power combiner are the main components that are required.

In addition, a variable attenuator is usually included in the reference signal branch [10]. The goal of this component

This work has been supported by the Ministerio de Ciencia e Innovación of Spain /FEDER under projects TEC2014-55290-JIN; by the Gobierno del Principado de Asturias (PCTI)/FEDER-FSE under project GRUPIN14-114 and Grant BP11-169.

Jaime Laviada, Ana Arboleya and Fernando Las Heras are with the Departamento de Ingeniería Eléctrica, Universidad de Oviedo, Spain. Fernando López-Gayarre is with the Departamento de Construcción e Ingeniería de Fabricación, Universidad de Oviedo, Spain.

VIII

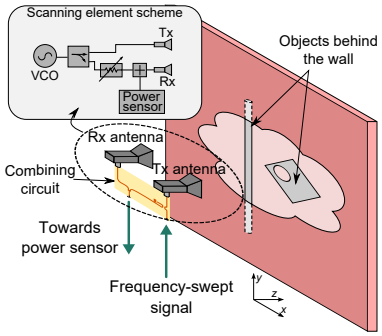

Figure 1. Synthetic aperture radar for through-the-wall imaging.

is twofold. First, it enables to balance the power between the scattered signal and the reference signal. Second, when operating at maximum level of attenuation, it enables to acquire only the intensity of the scattered signal, which is required in the phase retrieval approach originally proposed in [10]. However, in the next section, it will be described how a modified version of the phase retrieval, which does not resort to a variable attenuator, is also effective for the through-the-wall problem under consideration.

B. Phase retrieval

The system described in Fig. 1 enables the acquisition of the power of a signal composed of two components, one corresponding to the monostatic scattered field, which is the signal whose amplitude and phase must be retrieved, and the other one corresponding to the reference signal. Hence, the received power can be assumed to be given by [10]:

$$I\left(\vec{r},\omega\right)=\left|E_S\left(\vec{r},\omega\right)+E_R\left(\omega\right)\right|^2, \tag{1}$$

wherein E_S is the scattered field, E_R is the reference field at the (coupled) output port of the directional coupler, ω is the angular frequency and $\vec{r}$ is the position of the scanning element. In the original phase retrieval approach of [10], the value of the variable attenuator is changed for each position of the scanning element to improve the balance between both branches and, consequently, to improve the dynamic range. Nevertheless, the power of the scattered field in through-the-wall inspection is dominated by the field reflected by the wall and, consequently, it is mainly constant along the scanning surface. Thus, the variable attenuator voltage is set at the beginning of the acquisition and it remains fixed along the acquisition. Although the dynamic range is expected to be lower than in the case of considering the variable attenuator, it will be demonstrated that the system is still able to successfully identify objects behind a wall with good resolution at distances of several tens of centimeters for the considered frequencies (K_u and K_a bands).

Since the value of the reference signal does not change along the measurement, it would be of interest to consider a system without a variable attenuator. In this setup, the balance between the power from both branches would be directly controlled by the coupling coefficient (a fixed value) of the directional coupler.

Nevertheless, this setup entails some challenges because there is no possibility of measuring the amplitude of the scattered field independently from the reference signal in a single scan and, therefore, the algorithm detailed in [10] cannot be applied. To bypass this problem, we will resort to the technique proposed in [11], which takes advantage of the effective time-limited property of the scattered signal. Thus, the modified hologram is computed as:

$$\begin{aligned} I_m\left(\vec{r},\omega\right) &= I\left(\vec{r},\omega\right)-\left|E_R\left(\omega\right)\right|^2 \\ &= E_S\left(\vec{r},\omega\right)\bar{E}_R\left(\vec{r},\omega\right)+\bar{E}_S\left(\vec{r},\omega\right)E_R\left(\vec{r},\omega\right)+ \\ &+ \left|E_S\left(\vec{r},\omega\right)\right|^2, \end{aligned} \tag{2}$$

where the upper bar denotes complex conjugate. The square amplitude of the reference signal $\left|E_R\left(\omega\right)\right|^2$ can be easily characterized when there is not any scatterer nor the wall in front of the scanning element.

If the components of the reference branch have a low dispersive behavior, i.e., the ripple in the amplitude frequency response is moderated and their phase response has a linear dependency on the frequency, then the reference branch contribution can be modeled as:

$$E_R\left(\omega\right)=Ae^{-j\omega t_d}, \tag{3}$$

wherein A is the amplitude of the frequency response and t_d accounts for the delay of the signal to propagate from the VCO to the power sensor. Thus, the inverse Fourier transform of (2) is given by three terms:

$$\begin{aligned} i_m\left(\vec{r},t\right) &= Ae_S\left(\vec{r},t-t_d\right) \\ &+ Ae_S\left(\vec{r},-t+t_d\right)+e_S\left(\vec{r},t\right)*e_S\left(\vec{r},-t\right), \end{aligned} \tag{4}$$

where the operator $*$ denotes convolution. In the previous equation, it has been assumed, without loss of generality, that the complex amplitude A has zero phase.

Fig. 2 depicts these terms, where $\Delta\tau$ is the length of the signal corresponding to the scattered field in the time-domain. In this picture, the same notation as in [10] is used. Thus, the time delay of the reference signal is denoted by t_d and the minimum propagation delay due to the wave traveling from the transmitter to the object and from the object to the receiver, is denoted by t_{min} (see [10] for further details). It is clear that, as long as the central term does not overlap with the other two symmetric terms, the scattered field can be retrieved by means of time gating. This condition can be expressed as $t_d < t_{min} - \Delta\tau$.

In the particular case of through-the-wall inspection with the quasi-monostatic element depicted in Fig. 1, the time delay of the reference signal t_d is expected to be low due to the short distance between the transmitter and receiver antennas and, consequently, the previous condition is met in practice.

If the reference branch has been characterized in a first stage by means of either a network analyzer or a scalar calibration algorithm [12], then, after time gating the modified hologram, it is possible to retrieve the amplitude and phase of the scattered signal by dividing the right term of the signal by the reference signal as detailed in [10].

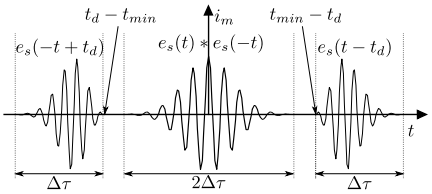

Figure 2. Modified hologram in the time-domain.

C. Interferometry circuit

In order to implement the microwave circuit detailed in Fig. 1, two options are considered. In the case of the K$_a$-band, a microstrip circuit, consisting of two coupled lines and a Wilkinson divider, is built. The employed substrate is Arlon 25N with a thickness of $203\,\mu$m. The circuit is designed to provide a coupling factor between -40 dB and -50 dB since it has been observed that the reflected signal suffers a similar loss in the considered walls and distances. Two low-directivity horn antennas separated by 5.5 cm have been used. The complete scanning element is shown in Fig. 3.

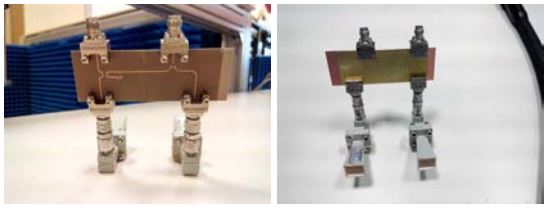

(a) Rear view. (b) Front view.

Figure 3. Implementation of the scanning element at the Ka-band .

In the case of the K$_u$-band, an alternative solution based on off-the-shelf components has been considered. In this case, the variable attenuator has been included. Two possible values of the variable attenuator have been considered. The first one enables to balance the reference and scattered signal branches. The second one corresponds to the maximum attenuation level so that the scattered signal power can be acquired, enabling the processing described in [10]. The employed components are a directional coupler Agilent 87301D, a power combiner Narda Microwave 4456-2 and two variable attenuators Hittite HMC985LP4KE. Components are connected by means of standard flexible coaxial cables. It is relevant to observe that a long delay line (a 1.5 m coaxial cable) has been introduced between the variable attenuator and the power combiner so that the two components $e_S(t-t_d)$ and $e_S(-t+t_d)$ of the modified hologram are swapped. This choice has been selected because due to the arrangement of the chosen off-the-shelf components a short delay for the reference signal could not be guaranteed and, consequently, it could result in the overlap of the terms in (4). The only effect of this long delay line in the postprocessing is that the time-gating must be applied to the left term of the time-domain modified hologram depicted in Fig. 2 as discussed in [13]. In this implementation, the separation between the antennas is 14.5 cm. A picture illustrating this setup is shown in Fig. 4.

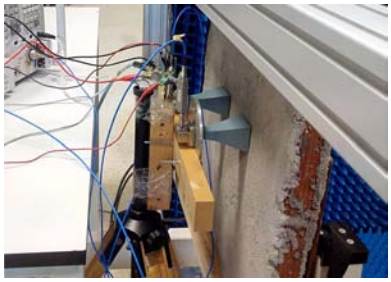

Figure 4. Implemented setup at the Ku-band with off-the-shelf components.

D. Postprocessing

In order to retrieve the amplitude and phase of the scattered field, a *calibration* is firstly required to characterize the reference signal. This calibration can be carried out by either measuring $E_R(\omega)$ with a vector network analyzer (VNA) or by means of the scalar measurement of a reference object under test (OUT) as detailed in [12]. It is important to note that the calibration is required only once.

Once the reference signal has been characterized, the phase can be retrieved *at each spatial point* by means of the next steps:

1) Measure the power of the hologram given by (1).
2) Compute the modified hologram given by (2).
3) Calculate the inverse Fourier transform of the modified hologram to translate the signal to the time domain.
4) Apply a time gating to retain the term $e_s(t) * e_r(-t)$.
5) Compute E_s by calculating the Fourier transform of the term from the previous step and dividing the result by $E_R^*(\omega)$.

After retrieving the phase, the imaging is carried out by using standard synthetic aperture imaging techniques as described in [7]. Since imaging algorithms do not demand *frequency sampling rates* as high as the one considered for the phase retrieval [7], [10], the data can be subsampled in the frequency domain to speed up the creation of the image. It is important to remark that the previous algorithm relies on considering free space and it does not take into account propagation through other mediums. Although it provides good results as shown in the next section, several algorithms can be applied to achieve further improvements by compensating the wall propagation [14], spatial filtering [15] or the possibility to include two different ray propagation constants in the formulation [16]. Differential SAR [5] has also shown good results to remove the approximately constant reflection due to the field scattered by the wall.

Since standard synthetic aperture imaging is used, depth and lateral resolutions are given by well-known formulas [7]. According to this, the radar will be able to detect objects as long as they are behind the wall at a distance larger than the depth resolution $\Delta z = c/2B$ [7], being c the speed of

light and B the bandwidth of the measurement. On the other hand, lateral resolution is mainly a function of wavelength and the raster scan surface [7] and, therefore, imaging capabilities are not expected to be degraded due to moving away some centimeters the objects under test from the wall.

III. Results

In this section, two demonstrators are presented to validate the system previously described. The first demonstrator operates at the K_a band that exhibits good penetration capabilities for 'weak' scattering materials such as plasterboard or wood. However, the high propagation losses make it not recommendable to analyze other kind of walls (see [17] for further details on the constitutive parameters of conventional building materials). In this demonstrator, the previously described microstrip circuit is used as combining circuit.

A second demonstrator is implemented at the K_u band, which exhibits better penetration capabilities. However, since the resolution of the system is proportional to the center wavelength, worse resolution is expected. In this case, the setup is completely implemented by means of off-the-shelf components. Both frequency bands have been sampled with 201 frequency points that have been observed to provide a correct phase retrieval in both cases.

Although a final system would perform raster scanning by moving the antennas along the wall, in these demonstrators, the antennas remain static and the object is moved along a plane. This approach is equivalent to move the antennas while the object remains static if the wall is (effectively) homogenous such as in the case of wood or plasterboard. In the case of non-homogenous materials such as building material containing bricks, it results in a fair approximation.

In both demonstrators, the spatial sampling rate is set at $\Delta x = \Delta y = \lambda_{min}/4$ wherein λ_{min} is the shortest wavelength, i.e., the wavelength at the maximum frequency. The object under test consists, in all the cases of study, on a square plate of 10 cm with a hole of diameter equals to 4 cm together with a cylinder of radius 1.6 cm. Both objects are fastened to a piece of cardboard by means of masking tape as shown in Fig. 5. The input and output of the scanning element are connected to a VNA. Nevertheless, the phase is discarded to emulate the data acquired by a power detector.

For the sake of completeness, the statistical parameters of the background reflectivity, measured in the volume at a minimum distance of 10 cm from the object in the x-axis and 5 cm from the wall are shown in Table I.

Table I
STATISTICAL BACKGROUND REFLECTIVITY.

Material	Mean	Stand. deviation	Max.
Plasterboard	-32.56 dB	5.20 dB	-19.40 dB
Plywood	-26.96 dB	5.71 dB	-15.39 dB
Hollow bricks and mortar	-19.89 dB	7.88 dB	-4.32 dB

A. K_a band results

This first demonstrator is implemented at the K_a band that ranges from 26.5 GHz to 40 GHz (see Fig. 5). The aperture of the antennas is placed at 6 cm from the wall whereas the objects are placed 10 cm behind the wall. The gain of each antenna is 10 dB and the beamwidth is 55° for the E and H planes. The scanning surface, i.e., the surface along which the object is moved, is a rectangular plane with dimensions of 16.5 cm and 64 cm for the x and y coordinates, respectively.

(a) Front view (b) Rear view

Figure 5. Setup implemented at the K_a band without the building walls.

The materials of the walls considered in this demonstrator are plasterboard and plywood. In both cases, the thickness is 1.3 cm. In this frequency range, the measured mean attenuation for each material is 1.17 dB and 7.93 dB, respectively. Fig. 6 shows the setup after including the materials between the antennas and the object.

(a) (b)

Figure 6. Setup implemented at the K_a including the walls: a) plasterboard; b) plywood.

After the phase retrieval, the first and last eleven frequencies are discarded since they are expected to be contaminated by some error [10]. Next, the reflectivity is calculated by using only 90 frequencies. The results for both materials are shown in Fig. 7 with a very good agreement with the real OUT.

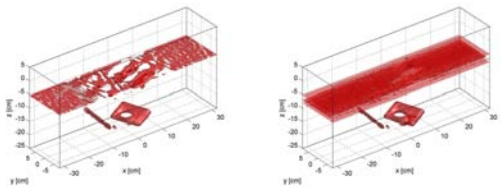

(a) (b)

Figure 7. Computed reflectivity the OUT placed behind a wall of: a) plasterboard; b) plywood. Reconstructed profiles correspond to the isosurface at -8 dB.

B. K_u band results

In this demonstrator, the setup has been implemented at the K_u band to analyze materials exhibiting poor penetration. In

particular, a hollow bricks and mortar wall is considered. The bricks contain a single air chamber and their thickness is 4 cm. The total thickness of the wall, including the concrete layers, is 7 cm. The measured mean attenuation of the wall is 16.46 dB in the K_u band. Antennas are placed so that the aperture of the horns is on the wall surface and the separation between both antennas is 14.5 cm. The typical gain and beamwidth of each antenna are 16.5 dB and 28.5° for the E and H planes. The object under test is placed at 18.5 cm behind the wall.

In this case, the variable attenuators have been introduced and, therefore, it is possible to resort to the original postprocessing scheme detailed in [10] as previously discussed. Fig. 4 shows the implemented setup at this working band.

In this example, the scanning dimensions are 21.84 cm and 59.64 cm for the x and y directions. The frequency band ranges from 12.4 GHz to 18 GHz. After the phase retrieval, the first and last five frequencies are discarded and the resulting field is subsampled again by a factor of two in frequency. Hence, the number of frequencies for the profile reconstruction is 96.

Fig. 8 depicts the computed reflectivity. Despite resolution is poorer than at the K_a band due to the lower available power and shorter wavelength, the square plate and the cylinder bar can still be clearly identified.

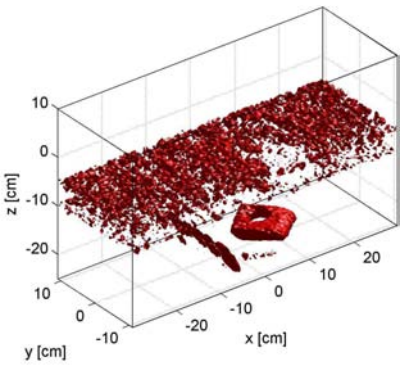

Figure 8. Reflectivity at -6 dB for the bricks and mortar wall.

IV. Conclusions

A simple scheme for non-destructive inspection of objects behind a building wall has been presented in this paper. The approach avoids the use of I/Q mixers and it only relies on power detection. On the one hand, the phase retrieval and profile computation algorithms are based on efficient Fourier transforms and, therefore, they involve a low computational burden. On the other hand, the system can be physically implemented by means of either simple microwave circuitry, which can be manufactured with widespread milling machines, or off-the-shelf components.

The approach has been validated at the K_u and K_a bands employing *ad-hoc* microwave circuitry as well as commercial components. The performance of the system reveals a good capability to detect the shape of metallic objects (as pipes) close to walls of conventional materials such as plywood, plasterboard or hollow bricks and mortar. Thus, the system is expected to be compatible with advance postprocessing to compensate the propagation through the walls that could be required in other environments such as the analysis of embedded or buried objects.

Although dielectric objects (e.g., PVC pipes) have not been considered in this work, the setup would remain unchanged. Nevertheless, special care must be paid in the postprocessing since internal reflections and weak reflectivity could result in artifacts degrading the quality of the image.

Acknowledgment

The authors would like to thank Dr. Carlos Vazquez-Antuña, Mr. George Hotopan and Mr. Cebrián García-González for their help in fabricating the microstrip circuit and setting up the components and construction walls.

References

[1] N. Maaref et al., "A study of UWB FM-CW radar for the detection of human beings in motion inside a building," *IEEE Trans. Geosci. Remote Sens.*, vol. 47, no. 5, pp. 1297–1300, May 2009.
[2] F. Adib and D. Katabi, "See through wall with Wi-fi!" in *ACM SIGCOMM'13*, Hong Kong, China, August 12-16 2013, pp. 75–86.
[3] C. Adams, D. Holbrook, and R. Sengsten, "A handheld active millimeter wave camera," in *IEEE International Conference on Technologies for Homeland Security (HST)*, Nov 2010, pp. 283–286.
[4] M. Dehmollaian and K. Sarabandi, "Refocusing through building walls using synthetic aperture radar," *IEEE Trans. Geosci. Remote Sens.*, vol. 46, no. 6, pp. 1589–1599, Jun. 2008.
[5] M. M. Dehmollaian, M. Thiel, and K. Sarabandi, "Through-the-wall imaging using differential SAR," *IEEE Trans. Geosci. Remote Sens.*, vol. 47, no. 5, pp. 1289–1296, May 2009.
[6] T. S. Ralston, G. L. Charvat, and J. E. Peabody, "Real-time through-wall imaging using an ultrawideband multiple-input multiple-output (MIMO) phased array radar system," in *IEEE International Symposium on Phased Array Systems and Technology (ARRAY)*, Oct 2010, pp. 551–558.
[7] J. M. Lopez-Sanchez and J. Fortuny-Guasch, "3-D radar imaging using range migration techniques," *IEEE Trans. Antennas Propagat.*, vol. 48, no. 5, pp. 728–737, May 2000.
[8] L. Crocco, M. D'Urso, and T. Isernia, "Inverse scattering from phaseless measurements of the total field on a closed curve," *J. Opt. Soc. America*, vol. 21, no. 4, pp. 622–631, Apr. 2004.
[9] G. Hislop, L. Li, and A. Hellicar, "Phase retrieval for millimeter- and submillimeter-wave imaging," *IEEE Trans. Antennas Propagat.*, vol. 57, no. 1, pp. 286–289, Jan. 2009.
[10] J. Laviada et al., "Phaseless synthetic aperture radar with efficient sampling for broadband near-field imaging: Theory and validation," *IEEE Trans. Antennas Propagat.*, vol. 63, no. 2, pp. 573–584, 2015.
[11] ——, "Phase retrieval technique for submillimetre-wave frequency scanning-based radar system," *IET Microwave, Antennas, Propag.*, vol. 8, no. 14, pp. 1170–1178, Nov. 2014.
[12] J. Laviada and F. Las-Heras, "Scalar calibration for broadband synthetic aperture radar operating with amplitude-only data," *IEEE Antennas Wireless Propag. Lett*, no. 14, pp. 1714–1717, 2015.
[13] J. Laviada et al., "A novel phaseless frequency scanning based on indirect holography," *J. Electromagn. Waves Appl.*, vol. 27, no. 4, pp. 275–296, 2013.
[14] F. Fioranelli, S. Salous, and X. Raimundo, "Frequency-modulated interrupted continuous wave as wall removal technique in through-the-wall imaging," *IEEE Trans. Geosci. Remote Sens.*, vol. 52, no. 10, pp. 6272–6283, Oct 2014.
[15] Y.-S. Yoon and M. G. Amin, "Spatial filtering for wall-clutter mitigation in through-the-wall radar imaging," *IEEE Trans. Geosci. Remote Sens.*, vol. 47, no. 9, pp. 3192–3208, Sept 2009.
[16] S. C. Henry et al., "Three-dimensional broadband terahertz synthetic aperture imaging," *Optical Engineering*, vol. 51, no. 9, pp. 091 603–1–091 603–9, 2012.
[17] I. Cuiñas and M. G. Sanchez, "Measuring, modeling, and characterizing of indoor radio channel at 5.8 ghz," *IEEE Trans. Veh. Technol.*, vol. 50, no. 2, pp. 526–535, Mar. 2001.

VIII

Publication AI

A. Arboleya Arboleya, C. García González, Y. Álvarez López, J.Laviada Martínez and F. Las-Heras Andrés **"Millimeter and submillimeter planar measurement setup,"** in *IEEE international Symposium on Antennas and Propagation and USNC-URSI National Radio Science Meeting (APS / USNC-URSI),* Florida (USA), pp. 1–2, 7–13 Jul. 2013.

AI

Millimeter and Submillimeter Planar Measurement Setup

Ana Arboleya, Yuri Álvarez, Fernando Las-Heras
Área de Teoría de la Señal y Comunicaciones, Department of Electrical Engineering
Universidad de Oviedo
Edificio Polivalente, Módulo 8, Campus Universitario de Gijón. E-33203, Gijón (Asturias). Spain.
aarboleya@tsc.uniovi.es ; yalopez@tsc.uniovi.es ; flasheras@tsc.uniovi.es

***Abstract*— A three-axes planar measurement setup for antenna characterization and inverse scattering applications is described. The need for a new measurement facility capable of working at millimeter and sub millimeter frequency bands is the main motivation of this work. The system can be divided into two main blocks devoted to mechanical and radiofrequency control respectively. Frequency band is extended up to 330 GHz by means of mixing heads, and a working surface of 1450x1500x1100 mm, with 0.01 mm positioning accuracy is achieved. Measurement setup is provided with an easy-to-use graphical user interface allowing configuration of mechanical and radiofrequency devices, as well as graphical representation of the results and post processing tasks.**

I. MOTIVATION

The main motivation for the implementation of a planar measurement range is mostly related to the development of novel submillimetric and terahertz circuit designs [1] and inverse scattering and imaging applications on this frequency band [2]. Due to free-space propagation, cable and connectors losses and rotary joint, an existing measurement setup at spherical range in anechoic chamber is limited in frequency up to 40 GHz.

These drawbacks have encouraged the development of a new measurement system to allow field measurements at mm- and sub-mm frequency bands. The implemented setup is based on a modular design, so it can be modified, for example, by adding rotary positioners which increase its functionality, allowing cylindrical scanning. In addition to antenna measurement and diagnostics applications, scattered field acquisitions for inverse scattering problems are also possible.

II. SYSTEM DESCRIPTION

The system can be divided into two separate subsystems working together: i) mechanical control subsystem, including elements such as the axes controllers, actuators, chassis, etc. and ii) radio frequency subsystem which comprises the measurement devices, probes, cables, etc. An overview of the implemented system is pictured in Fig. 1.

A. Mechanical control

Main components of the mechanical subsystem are the X-SEL-P IAI controller [3] and the multi-axis Cartesian positioner consisting of: i) two actuators for the X-axis working in a master/slave configuration, ii) one actuator for the Y-axis and, iii) another for the Z-axis with a holding accessory for the probe. Those actuators are remotely controlled from the PC interface via the IAI controller. They can reach 150 mm/s speed with 0.01 mm precision.

The multi-axis positioner is placed parallel to the floor on an aluminum chassis so the AUT (Antenna Under Test) can be mounted on the floor below the probe, avoiding floor reflection. The chassis also performs the function of giving strength to the whole structure preventing it from torsion and buckling during field acquisition and works as a lean structure for the absorber panels (see Fig. 1). The framework made with the chassis, the actuators and the absorber panels is called XYZ-board and performs a working surface of 1450x1500x1100 mm. Absorber sheets are fixed over aluminum plates all over the floor and lateral sides of the chassis to provide the system with anechoic behavior.

Thanks to the multi-axis actuator, it is possible to do sampling sweeps in three different planes (XY, XZ and YZ). Generally, antenna measurement setups employ XY surface sampling, because the probe and the AUT are placed parallel to this plane with their central axis in the Z direction. XZ and YZ planes are usually used in scattering measurement setups where a quasi-monostatic configuration is employed. In those cases, the position of the antennas is fixed and the objects are moved across different paths. It is also possible for the multi-axis positioner to describe cylindrical, spiral and any kind of arbitrary trajectories apart from planar surfaces.

B. Radiofrequency (RF) equipment

Measurement devices can be classified depending on the type of measurement they are used in. The main block is formed by the vector network analyzer (Agilent PNA-X N5247A [4]) with a working range from 10 MHz to 67 GHz that can be extended by two sets of mixing heads to the W band between 75 GHz and 110 GHz and from 220 GHz to 330 GHz. This vector network analyzer is used with two different sets of probes in the form of horns and open-ended waveguides.

Cable motion is one of the main sources of error due to the phase deviation of the measured transmission coefficient. Those phase uncertainties become more significant with the increase of the working frequency. To reduce the uncertainty, a method to evaluate and correct cable phase deviations [5] has been implemented.

The implemented setup supports phaseless measurements. To recover phase information, sampling in two surfaces can be

AI

used as described in [6]. When working under this configuration, an amplitude detector (Agilent E4416A, EPM-Series [4]) can be used. Frequency range depends on the amplitude sensors connected to it. Available sensors cover frequency bands from 50 MHz to 110 GHz. Connection between the sensor and the amplitude detector is made through an AC cable at the frequency of 440 MHz, avoiding high frequency cable losses, which are a critical factor in the mm- and sub-mm frequency bands.

Finally, to provide users an easy operation mode, a complete graphical user interface, depicted in Fig. 2, has been developed. This graphical interface allows sending orders to the positioner controller, remote configuration of the measurement devices, measurement sampling path creation, and graphical visualization of measurements results. In addition, post processing capabilities for antenna measurement and inverse scattering problems are also enabled.

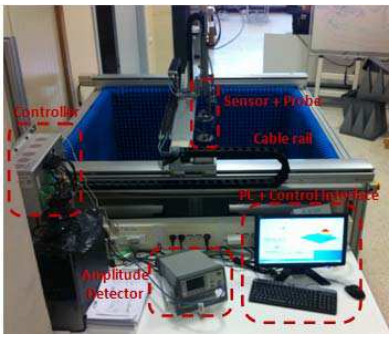

Figure 1. Planar range measurement setup

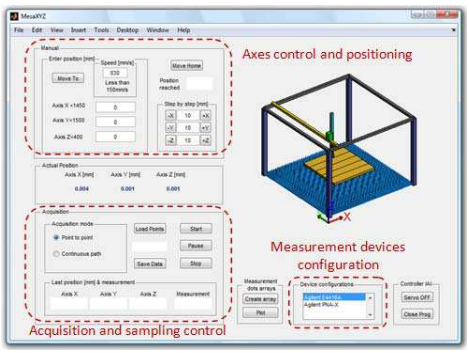

Figure 2. Graphical user interface for system control.

III. Application Example

To evaluate the measurement system functionality, a simple test case has been chosen. The problem-under-test consists on a 4-element antenna array working at 10 GHz, with a U-shaped metallic object blocking the array aperture (Fig. 3, left). First, the radiated field is acquired in a planar domain of 300x300 mm, placed 15 cm above the U-shaped object, as depicted in Fig. 3 (right). Next, an antenna diagnostics method [7] is applied to recover the field on the plane which contains the metallic object. As shown in Fig. 4, the blockage introduced by the object fits the U-shaped geometry. More similar diagnostics tests are actually in progress at higher frequency bands (W band and 300 GHz band).

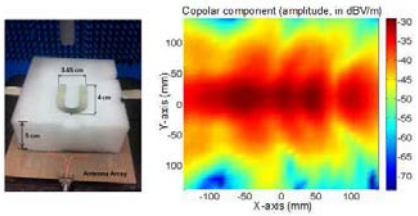

Figure 3. Antenna with metallic obstacle (left). Measured copolar field 15 cm above the object.

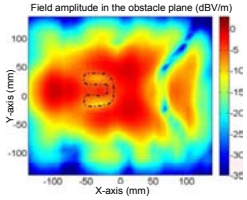

Figure 4. Backpropagated field on the metallic object plane.

Acknowledgement

This work has been supported by the European Union under COST IC1102 ("VISTA") action; by the "Ministerio de Ciencia e Innovación" of Spain/FEDER under projects IPT-2011-0951-390000, CSD2008-00068, TEC2011-24492/TEC; by the "Gobierno del Principado de Asturias" (PCTI)/FEDER-FSE under projects EQUIP10-31 and PC10-06; grants BP-11-169 and BES-2009-024060.

References

[1] R. Camblor, S. Ver-Hoeye, C. Vazquez, G. R. Hotopan, M. Fernandez, and F. Las-Heras, "Sub-millimeter wave frequency scanning 8 x 1 antenna array," *PIER*, Vol. 132, 215-232, 2012.

[2] K. B. Cooper, R. J. Dengler, N. Llombart, B. Thomas, G. Chattopadhyay, P. H. Siegel, "THz Imaging Radar for Standoff Personnel Screening," *IEEE Transactions on Terahertz Science and Technology*, Vol.1, pp.169-182, Sept. 2011.

[3] IAI Intelligent Actuators, http://www.eu.iai-gmbh.de/

[4] Agilent Technologies, http://www.home.agilent.com/

[5] J. Vancl, P. Čêrní, Z. Skvor, M. Mazánek, "Evaluation and Correction of Cable Phase Stability in High Frequency Near-Field Measurement", *IEEE 14th Conference on Microwave Techn.*. 23-24 April, 2008. pp. 1-4.

[6] S. Farhad Razavi, Yahya Rahmat-Samii, "A New Look at Phaseless Planar Near-Field Measurements: Limitations, Simulations, Measurements, and a Hybrid Solution," *IEEE Antennas and Propagation Magazine*, Vol. 49, No. 2, April 2007, pp. 170-178.

[7] Y. Álvarez, F. Las-Heras, M. R. Pino, "Reconstruction of Equivalent Currents Distribution Over Arbitrary Three-Dimensional Surfaces Based on Integral Equation Algorithms", *IEEE Transactions on Antennas and Propagation*, Vol. 54, pp. 3460-3468, December 2007.

Publication BI

A. Arboleya, J. Laviada, Y. Álvarez-López and F. Las-Heras **"Error characterization tool for planar near-field antenna measurement and diagnostics applications,"** *1st Conference on Antenna Measurements and Applications (2014 IEEE CAMA),* Antibes (France), 26–29 Nov. 2014.

BI

This is the author's version of an article that has been published in this journal. Changes were made to this version by the publisher prior to publication.
The final version of record is available at http://dx.doi.org/10.1109/CAMA.2014.7003425

Error Characterization Tool for Planar Near-Field Antenna Measurement and Diagnostics Applications

Ana Arboleya-Arboleya*, Yuri Álvarez-López, Cebrián García-González, Jaime Laviada, Fernando Las-Heras
Área de Teoría de la Señal y Comunicaciones, Dpto. Ingeniería Eléctrica, Universidad de Oviedo
Edif. Polivalente, Mod. 8, Campus Universitario de Gijón. E-33203, Gijón (Asturias), Spain
Email: $\{aarboleya, yalopez, cgarciag, jlaviada, flasheras\}@tsc.uniovi.es$

***Abstract*—An error characterization tool is presented in this contribution to study the effect of mechanical and positioning errors in the near-field to far-field transformation and the computation of the aperture field processes in different planar measurement setups. Validation of the error simulation tool is made by comparison of the results with a set of measurements in a planar near-field range.**

I. Introduction

Over the years, Planar Near-Field (PNF) ranges have become one of the most used systems for directive antenna characterization. These systems rely on mechanical positioners that can introduce errors in the acquisition process. Assessment of error and correction of its effects, when possible, has become an essential part of the measurement method.

Mechanical and alignment errors of the positioners and the holding accessories for the antennas can be easily identified and quantified by means of simulation [1].

By having knowledge of the effect that each of the considered error introduces in the acquisition results, an uncertainty analysis of the measurement setup can be made to correctly characterize it. Also by defining the error bounds, the tolerance of the measurement system for each setup can be established.

This paper will describe the implementation of a simulation tool, to evaluate the effect of the majority of mechanical and alignment errors that can affect the planar measurement range. A graphical interface has also been added to make its use easier not only for scientific but also for educational purposes.

The paper is divided as follows; Section II will describe the use and the configurations of the implemented tool. Also, the basis of the methods for evaluating the radiated field distortion due to the probe pattern and mechanical errors, as well as the near field to far field transformation, are explained.

Outcomes of the comparison between the simulations and the measurements performed in the actual system are presented in Section III.

Finally, main conclusions will be drawn in Section IV within some proposed future work.

II. Implementation and use of the simulation tool

The tool has been implemented in Matlab and it includes a graphical user interface to make the data input and results representation easier. It can be used for the simulation of antenna measurement and diagnostics from amplitude and phase data, although the authors are also implementing an extended version for phaseless antenna measurement and diagnostics setups.

Calculations will be made in four steps: i) selection of the Antenna Under Test (AUT), probe antenna and the working frequency; ii) definition of the measurement parameters; iii) computation of the tangential electric field in the acquisition points; iv) Near-Field to Far-Field (NF-FF) transformation or the aperture fields of the AUT calculation.

A. AUT and probe antenna selection

The software tool has implemented several predefined types of antennas, such as pyramidal horns, Open-Ended WaveGuide (OEWG), as well as an ideal isotropic source, that can be selected as both Antenna Under Test (AUT) or probe antenna. Also, the user can select a user-defined antenna by loading a file with the characterization of the antenna in terms of its equivalent magnetic currents located in the aperture.

B. Measurement parameters and error definition

Once the AUT and the probe antenna are selected, the user can define the rest of the measurement parameters. Dimensions of the scanner are coincident with the dimensions of the XYZ scanner available in the TSC-Uniovi Research Group [2].

The working area of the scanner is 1450 x 1500 x 1100mm. The probe is mounted in a holding accessory fixed to the Z-axis positioner and can travel from 0 to 400 mm being the Z-axis increasing direction defined from the top of the positioners towards the floor. The AUT antenna is placed in a variable height platform over the floor. A scheme of the setup, which is integrated in the upper right corner of the user interface, can be seen in Fig.1.

The AUT and probe antenna alignment can be modified at any time by changing the coordinates of the positioners and the holding platform of the AUT.

After determining the AUT and the probe antenna positions, the user has to define the measurement plane by selecting the number of points of each of the plane dimensions and the step size. By default, the acquisition planes are defined in the XY plane (with the probe's Z coordinate fixed and pointing towards the floor), however, it is also possible to perform the acquisition of the field samples either in the YZ or XZ planes.

At this point, users can select and define the mechanical errors affecting the measurement process. The errors can be classified within deterministic or statistical.

1) *Deterministic errors definition*

This kind of errors are used to emulate mechanical errors of the positioners and the probe antenna and AUT holding accessories.

The following errors regarding the movement of the positioners and the acquisition plane can be simulated:

- *Z-axis deviation*: simulates errors in the planarity of the acquisition plane. The deviations are defined as a sine function whose amplitude can be selected by the user (Fig.2(a)).
- *XY- plane deviation*: this error adds a constant distance to each of the columns defining the position of the measurement points in the acquisition plane, in order to simulate the effect of an offset error in the movement of the positioners (Fig.2(b)).
- *X-axis tilt*: defines a tilt of the measurement plane with respect to the X-axis.
- *Y-axis tilt*: same as X-axis tilt but performs the tilt in the Y-axis (Fig.2(c)).

Errors associated to the AUT and the probe antenna positioners and holding accessories are:

- *Z-axis rotation*: this parameter produces a rotation of the probe antenna or the AUT with respect to the Z-axis introducing a change on the polarization of the antennas.
- *X-axis tilt and Y-axis tilt*: as in the previous case, these parameters define a tilt of the probe or AUT aperture with respect to the selected axis.

2) *Statistical errors definition*

Error statistical modelling can also be performed, allowing the user to set up other four different parameters:

- *SNR*: with this parameter, white Gaussian noise is added to the acquired field in the planar surface according to a certain SNR value specified by the user.
- *Scanner planarity*: this parameter allows the user to consider a random Gaussian distribution, defined by its standard deviation, to model the errors in the planarity of the acquisition plane. The statistical modelling of the scanner planarity can substitute, or add up, to the effect of the deterministic *Z-axis deviation* parameter.
- *X-axis and Y-axis accuracy*: those parameters produce errors in the XY plane by means of random Gaussian distributions also defined by their standard deviation. As the previous parameter, those ones can either substitute or complement the error modeled with the deterministic *XY-axis deviation parameter*.

C. Simulation parameters selection

Last step before starting the simulation process is the configuration of the simulation parameters. By setting up these parameters, the user can choose between the following options associated with using error correction techniques or plotting the results:

- Apply the probe correction algorithm.
- Apply the geometrical errors correction algorithm.
- Do not apply probe distortion during the computation of the radiated fields.

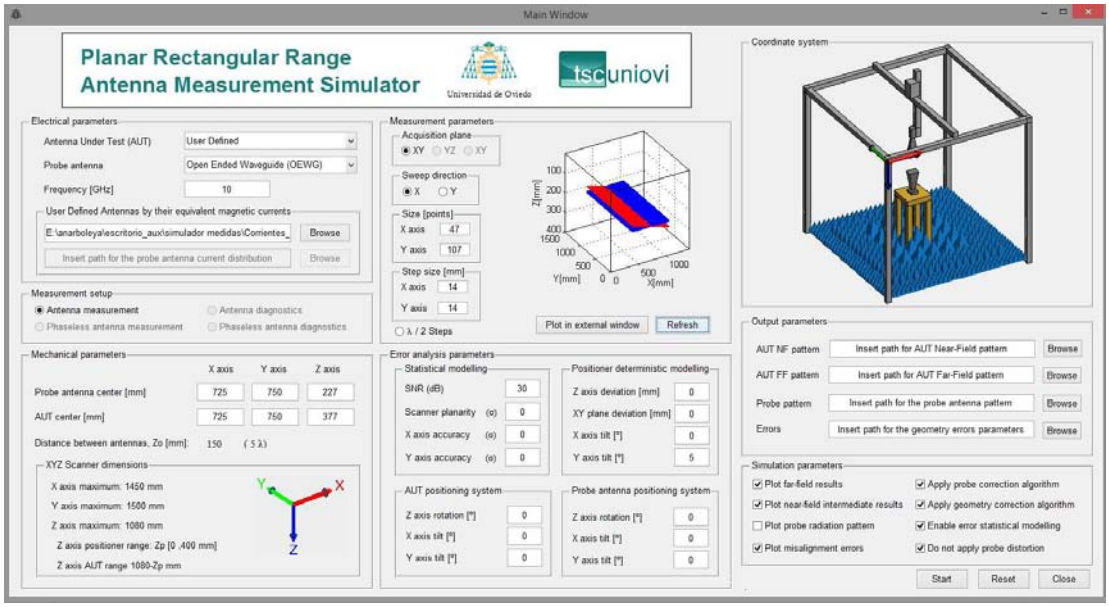

Fig. 1: Simulation tool graphical interface.

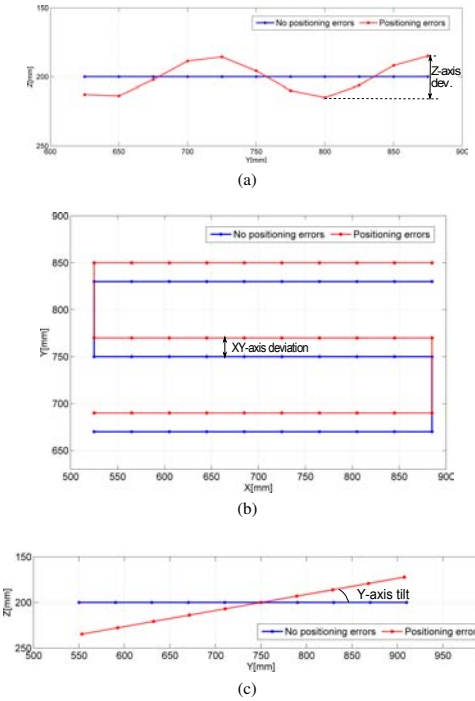

Fig. 2: Deterministic errors affecting the probe antenna positioning system. (a) Z-axis deviation; (b) XY-axis deviation; (c) 20° tilt with respect to the Y-axis

- Enable statistical modelling of errors.
- Plot the simulated misalignment errors.
- Plot the intermediate Near-Field results.
- Plot the simulated Far-Field or Aperture-Fields results.

D. Computation of the fields in the acquisition plane

An integral equation-based formulation is used to evaluate the radiated field in the acquisition plane given the equivalent magnetic currents on the aperture of the AUT. The effect of the probe antenna pattern is introduced inthese equations (1) following the formulation described in [3].

$$\vec{E}_{1,2}(\vec{r}) = \int_S \vec{M}(\vec{r}) G_M(\vec{r},\vec{r}') \vec{E}_{p_{1,2}}(\vec{r})\, dS \tag{1}$$

Being $\vec{E}_{1,2}(\vec{r})$ the tangential fields in the observation domain, S. Probe antenna polarization, $\vec{E}_{p_{1,2}}(\vec{r},\vec{r}')$, is calculated from its equivalent magnetic currents as indicated in (2). $\vec{M}(\vec{r})$ are the equivalent currents defining the AUT and $G_M(\vec{r},\vec{r}')$ is the Green function defined by (4).

$$\vec{E_p} = \int_{S'} G_M(\vec{r},\vec{r}')(\bar{d}_g(\vec{r},\vec{r}') \cdot \vec{M}_p(\vec{r}'))\, dS' \tag{2}$$

With $\bar{d}_g(\vec{r},\vec{r}')$ defined as indicated in (3), reflecting the effect of the mechanical errors, which can be deterministic or statistical.

$$\bar{d}_g(\vec{r},\vec{r}') = \begin{bmatrix} 0 & (z-z') & -(y-y') \\ -(z-z') & 0 & (x-x') \\ (y-y') & -(x-x') & 0 \end{bmatrix} \tag{3}$$

$$G_M(\vec{r},\vec{r}') = \frac{1}{4\pi}\frac{1+jkR}{R^3} e^{-jkR} \tag{4}$$

R is the position vector as indicated in (5) and k is the wave propagation constant defined in (6).

$$R = |\vec{r}-\vec{r}'| = \sqrt{(x-x')^2+(y-y')^2+(z-z')^2} \tag{5}$$

$$k = \sqrt{k_x^2+k_y^2+k_z^2} = \frac{2\pi}{\lambda} \tag{6}$$

E. NF-FF transformation or backpropagation to the AUT aperture

After computation of the radiated fields considering all the mechanical and statistical errors, the calculation of the plane wave spectrum (PWS) of the AUT (7) is made with the modal expansion formulation as follows [1]:

$$\vec{T}_t(k_x,k_y) = \frac{e^{-jk_z z_0}}{2\pi} \iint_{-\infty}^{+\infty} \vec{E}_t(x,y,z_0) e^{-j(k_x x + k_y y)}\, dxdy \tag{7}$$

Once the PWS of the field is obtained the far-field pattern of the AUT can be easily calculated by asymptotic evaluation of the expression as indicated in (8). The aperture fields of the AUT can also be obtained by back propagating the fields towards the aperture as it is shown in (9).

$$\vec{E}(r) = \frac{-je^{-jkr}k_z}{r} \vec{T}_t(k_x,k_y) \tag{8}$$

$$\vec{E}_t(x,y,z) = \frac{1}{2\pi} \iint_{-\infty}^{+\infty} \vec{T}_t(k_x,k_y) e^{-jk_z z} e^{-j(k_x x + k_y y)}\, dk_x dk_y \tag{9}$$

III. Validation

Validation of the proper working of the simulation tool has been made by comparison of several simulations with a set of measurements, with the same predefined errors, acquired at the planar measurement range of the TSC-Uniovi Research Group facilities. Some of the performed tests were:

- Reference measurement free of positioning and mechanical errors. The AUT aperture fields computed from this reference measurement will be the input for the simulation of the rest of measurements with errors.
- Measurements and simulations with a tilt of 20° with respect to the positioner Y-axis.

BI

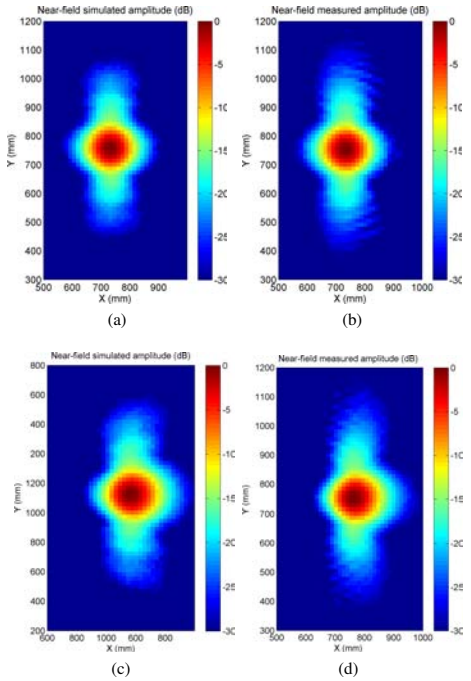

Fig. 3: Near-field simulations and measurements. (a) Simulated with no errors; (b) measured with no errors; (c) simulated with a tilt of 20° in the Y axis; (d) measured with a tilt of 20° in the Y axis.

- Measurements and simulations with a deterministic error in the acquisition plane planarity of ±5 mm.
- Measurements and simulations with a Z-axis rotation of the probe antenna of 45°.
- Measurements and simulations with a tilt in the pointing of the AUT of -20° with respect to the Y-axis.

Comparison were conducted in the three stages of the simulation process: calculated near field from the aperture currents, far field radiation pattern and back propagated aperture fields, obtaining a very good agreement between simulations and measurements.

To illustrate the process, the results for the near-field and the radiation pattern without errors and with a tilt of 20° in the Y-axis of the positioner are compared. The AUT is an X-band pyramidal horn and the probe antenna is an OEWG. Results for the near-field acquisition plane are shown in Fig.3 for the simulated and the measured fields and the calculated far-field radiation pattern of the Copolar component is shown in Fig.4.

IV. Conclusions

Error assessment is an essential part of antenna measurement and diagnostics systems. In this contribution, a simulation tool to study the effect of mechanical and positioning errors is developed to accurately know how each type of error is going to affect the measurement process. Validation of the tool is made by comparing the results with measurements. A graphical interface is implemented to make the use of the tool simpler and to easily visualize the results. Some of the future work in this field will include the simulation of errors in phaseless setups and the use of the simulation tool to automate part of the error assessment process in the uncertainty analysis of measurements

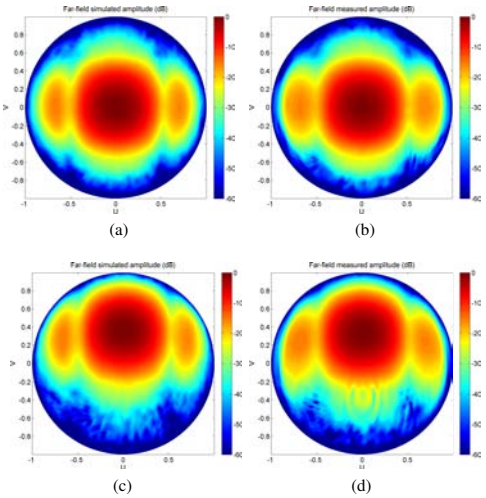

Fig. 4: Far-field simulations and measurements, Copolar component. (a) Simulated with no errors; (b) measured with no errors; (c) simulated with a tilt of 20° in the Y-axis; (d) measured with a tilt of 20° in the Y-axis

Acknowledgement

This work has been supported by the Ministerio de Ciencia e Innovacin of Spain/FEDER under projects TEC2011-24492, CSD2008-00068 and MICINN-11-IPT-2011-0951-390000, by the Gobierno de Asturias (PCTI)/FEDER-FSE under projects PC10-06, EQUIP08-06, FC09-C0F09-12, EQUIP10-31 and by grant BP11-169.

References

[1] A. Newell, "Error Analysis Techniques for Planar Near-Field Measurements," *IEEE Trasnactions on Antennas and Propagation*, AP-36, p.581, 1988

[2] Arboleya, A.; Alvarez, Y.; Las-Heras, F., "Millimeter and submillimeter planar measurement setup," *Antennas and Propagation Society International Symposium (APSURSI)*, 2013 IEEE, pp.1,2, 7-13 July 2013

[3] Alvarez, Y.; Las-Heras, F.; Pino, M.R., "Analysis and correction of the influence of probe distortion in near field-far field transformations," *Antennas and Propagation Society International Symposium*, 2006, IEEE, vol., no., pp.441,444, 9-14 July 2006

[4] Arthur D. Yaghjian, "An Overview of Near-Field Antenna Measurements," *IEEE Transactions on Antennas and Propagation*, Vol. AP-34, No. 1, 1986

BI

BI

Publication BII

A. Arboleya, J. Laviada, Y. Álvarez-López and F. Las-Heras **"Study of the influence of mechanical errors in diagnostics applications by means of statistical analysis,"** in *9th European Conference on Antennas and Propagation (EUCAP'15),* pp. 1–5 (Convened sessions), Lisbon (Portugal), 12–17 Apr. 2015.

Study of the Influence of Mechanical Errors in Diagnostics Applications by Means of Statistical Analysis

Ana Arboleya[1], Jaime Laviada[2], Yuri Álvarez[1], Fernando Las-Heras[1]
[1]Área de Teoría de la Señal y Comunicaciones, Universidad de Oviedo
Edif. Polivalente Mod. 8, Campus Universitario de Viesques. E-33202, Gijón (Asturias), Spain
Email: aarboleya@tsc.uniovi.es, yalopez@tsc.uniovi.es, flasheras@tsc.uniovi.es
[2]Grupo de Antenas, Universidad Pública de Navarra
Edif. de los Tejos, Sala de asociados, Planta 2, Campus Arrosadía, E-31006, Pamplona (Navarra), Spain
Email: jaime.laviada@unavarra.es

***Abstract*—Mechanical errors introduced by a planar measurement range and their effect on diagnostics applications are analyzed in this contribution. The study is based on Monte Carlo statistical analysis by means of an error simulation tool for antenna measurements and diagnostics applications. The effect of each type of error and its contribution to the final uncertainty of the system can be used to establish the error bounds and tolerance of the measurement system to mechanical inaccuracies for the implemented setups. Measurement and diagnostics of a W-band horn antenna with partial aperture blockage is considered for experimental testing.**

***Index Terms*—antenna, measurement, diagnostics, error analysis, uncertainty, statistical, Monte Carlo.**

I. Introduction

Planar Near-Field (PNF) ranges rely on mechanical positioners that can introduce errors in the acquisition procedure. Assessment and correction of error is an essential part of the measurement process in order to obtain an accurate analysis. Different approaches to characterize the error can be made depending of its nature. Mechanical and alingnments errors for PNF systems can be effectively identified and quantified by means of simulation [1]. Once the error bounds are determined, it is possible to know if the accuracy requirements can be fulfilled for each type of setup.

In this paper, the use of an error simulation tool [2] is extended to perform an statistical analysis to determine how the mechanical errors introduced by the PNF measurement system [3] developed at the TSC-Uniovi research group, influence the outcomes in diagnostics applications.

The paper is divided as follows: in Section II, the use of the simulation tool for the statistical analysis of the errors produced by the mechanical inaccuracies of the system is described. Section III describes an application example for the analysis of the influence of error in the determination of the aperture size of a horn antenna, and the size of an object blocking its aperture. Finally, main conclusions are drawn in Section IV.

II. Error Simulation and Characterization Based on Statistical Analysis

The developed simulation tool can be used for the simulation of different types of errors for antenna measurement and diagnostics applications, from both amplitude and phase data and phaseless setups. The software tool can be used for several predefined types of antennas, such as pyramidal horns or open-ended waveguide antennas. It is also possible to employ user-defined antennas, defined in terms of their equivalent magnetic currents located in the aperture, so data for actual measurements can be analyzed.

The user needs to completely define the measurement setup by specifying the following data: position of the Antenna Under Test (AUT) and probe antenna, size of the acquisition plane, step size and frequency. Once the setup is defined, the computation of the tangential electric field in the acquisition points, considering error-free scenario, is performed. The result will be used as a reference for the comparison with the data affected with errors.

At this point, mechanical errors affecting the measurement process can be introduced. The acquisition planes are defined in the XY plane at a constant distance ($z = z_0$). Inaccuracies are used to emulate mechanical errors introduced by the positioners and the AUT and probe antenna holding systems, and can be defined either in a deterministic form, in a statistic way or as a combination of both. The following types of inaccuracies are defined:

- *Z-axis deviation in the acquisition plane*: errors in the planarity of the acquisition plane.
- *XY-plane deviation on the acquisition plane*: errors in the distribution of the acquisition points on the XY plane
- *X-axis and Y-axis tilts in the acquisition plane*: definition of tilts in the acquisition plane with respect to the X-axis or the Y-axis.
- *Z-axis rotation in the probe or AUT positioning systems*: this parameter emulates changes in the polarization of the antennas by means of a rotation of their reference system

- *X-axis and Y-axis tilts in the probe or AUT positioning systems*: tilts of the probe or AUT aperture with respect to the selected axis.
- *Signal to Noise Ratio (SNR)*: addition of White Gaussian Noise to the acquired field according to a certain SNR specified value.

Given the equivalent magnetic currents of the probe antenna and the AUT, an integral equation-based formulation is used to evaluate the radiated field in the acquisition plane, according to the defined mechanical errors [2]. After computation of the radiated fields, the calculation of the Plane Wave Spectrum (PWS) of the AUT is made by means of modal expansions [1]. Once the PWS of the field is obtained the far-field pattern of the AUT can be calculated. Aperture fields of the AUT can be obtained by backpropagating the acquired field towards the aperture.

Generally, calculation and characterization of errors for antenna measurement applications are based on the estimation of the standard deviation of each error term and the calculation of its contribution to the total uncertainty of the system by the application of the central limit theorem [4].

To this end, the tool has been extended to perform statistical analysis of the effect of the considered errors in the final outcome of the simulations. A Monte Carlo method has been developed to characterize the variation of the error terms for a certain number of iterations. The Monte Carlo method randomly generates a number of trials from different realizations of the input variables (for which their probability functions are a-priori known), and numerically fits the empirical output distribution data to a normal distribution function defined by its mean and standard deviation [5].

Some conditions of validity have to be fulfilled in order to obtain accurate results with the Monte Carlo Method [6]. To be able to estimate a 95% confidence interval, it is recommended to use a number of trials of at least 10^6. Nevertheless, the number of trials can be reduced depending on the complexity of the simulated model.

The studied parameters in case of diagnostics applications are the size of the aperture and/or the size of possible objects blocking that antenna aperture [7]. Also directivity, beamwidth, Secondary Lobe Level (SLL) or antenna pointing can be characterized in antenna measurement applications.

III. Diagnostics application example

A study on the influence of the inaccuracies introduced in the acquisition process regarding aperture diagnostics, is developed for a horn antenna in the W-band at 110 GHz. The effect of three different error terms is simulated and statistically characterized by applying the Monte Carlo method.

In order to simulate the real performance of the measurement system, whose relative precision for the three Cartesian axes positioners is $\pm 10\,\mu m$, Probability Density Distributions (PDF) for the input studied parameters are defined as follows:

- *Scanner planarity*: an error defined by a Gaussian PDF with a standard deviation of $10\,\mu m$ ($N(0, 10.10^{-6}\,m)$) is considered.
- *Scanner XY plane accuracy*: an error defined by a Gaussian PDF with a standard deviation of $10\,\mu m$ ($N(0, 10.10^{-6}\,m)$) is considered.
- *Tilt in the acquisition plane*: a tilt defined by a Gaussian PDF with a standard deviation of 1° ($N(0, 1^\circ)$) with respect to the X and Y axis are respectively considered.

Independent simulations with 250 trials for each of the error terms are performed. 30 dB Gaussian noise, is added.

The antenna is defined by means of the equivalent magnetic currents on its aperture (22 mm $\times$ 28 mm), calculated from actual measurements using an OEWG antenna as a probe. The measurement setup can be seen in Figure 1. The characterization has been made at 110 GHz. The acquisition plane is placed at $z_0 = 5\,\lambda$ of the antenna aperture and its dimensions are $10\,\lambda \times 10\,\lambda$ with a step size of $\Delta x = \Delta y = \lambda/4$.

After characterizing the antenna, a metallic plate of $12\,\text{mm} \times 22\,\text{mm} \times 0.5\,\text{mm}$ is placed over the aperture of the antenna (see Figure 1) repeating the characterization process in order to study the influence of the errors in the determination of the size of the metallic plate.

For the determination of the aperture size without blocking objects, the width at -18 dB of the aperture field level is obtained for the main cuts in $x = 0$ and $y = 0$. In case of having the metallic plate blocking the antenna aperture, the following methodology is used to determine the size of the plate along X-axis (figure 2): i) determination of the size of the aperture using -18 dB level position and considering symmetry in the aperture field with respect to the Y-axis. ii) determination of -5 dB level position in the side of the antenna where the aperture is blocked, iii) the object size is defined by the difference between the previous calculated values.

In Figure 3 a comparison between the measured data for the case with and without a 12 mm metallic plate blocking the antenna aperture, and the simulated data used as reference in the Monte Carlo method, is depicted. It is worth noting that in order to decrease the simulation time, no probe correction algorithms were applied, and so, some discrepancies between the real dimensions of the antenna and the object, and the obtained dimensions are present. These discrepancies are larger for the X-axis dimension.

A. Results for the antenna aperture characterization

Results on how the mechanical errors in the positioner influence the determination of the aperture size are shown next. Figure 4 (a) shows the simulation results for the aperture field cut in $y = 0$ for 250 Monte Carlo trials considering errors in the planarity of the scanner, Figure 4 (b) shows the results for 250 iterations taking into account the effect of the errors in the XY plane accuracy. Finally, in Figure 4 (c) results for the cut in $x = 0$ are depicted when tilts in the acquisition plane in the X and Y axes are considered.

The histograms of the previous data are shown in Figure 5. Statistical data, mean (μ) and standard deviation (σ), after

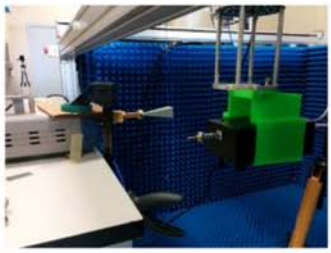

(a)

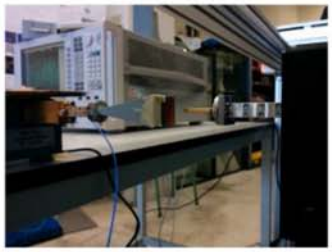

(b)

Fig. 1. Measurement setup: a) General view for the antenna characterization process; b) Detail of the metallic plate blocking the antenna aperture.

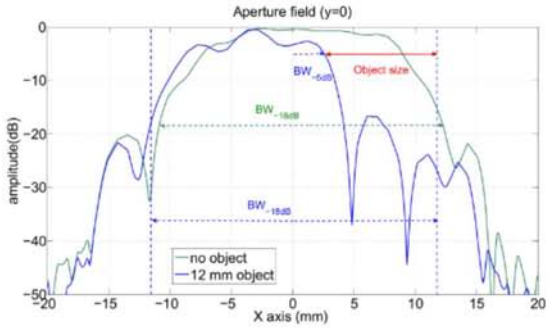

Fig. 2. Methodology for antenna and object size determination

fitting the output data by a normal distribution for each of the considered error terms, are tabulated in Table I.

TABLE I
STATISTICAL VARIATION OF THE OUTPUT DENSITY FUNCTION FOR THE THREE ERROR TERM IN CASE OF HAVING NO OBJECT BLOCKING THE APERTURE. APERTURE UNITS IN MILLIMETERS.

	XY accuracy		Z planarity		acquisition plane tilts	
Axis	μ	σ	μ	σ	μ	σ
X	28,1284	0,2123	28,1400	0,1931	28,0778	0,2508
Y	22,5720	0,0744	22,5629	0,0951	22,5042	0,2233

According to the aforementioned error distributions for each parameter, the three error terms have similar effect in the estimation of the size of the aperture. The mean (μ) of the output variables obtained, differ in less than 0.22% and 0.30%

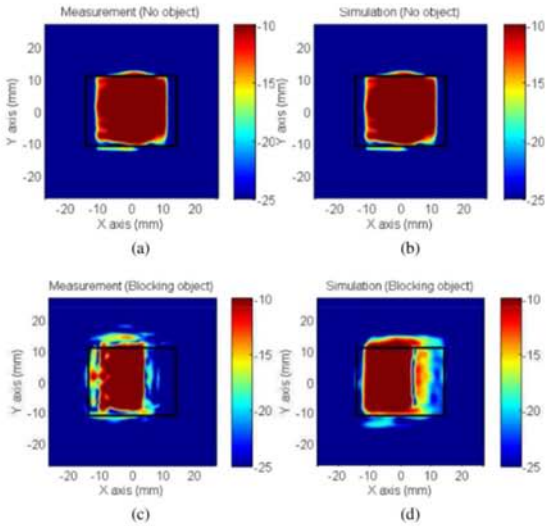

Fig. 3. Comparison of measurement data and simulation reference data for both cases: (a) Measurement with no blocking object, (b) Simulation with no blocking object, (c) Measurement with blocking object, (d) Simulation with blocking object

for the X and Y axes respectively. Maximum variability of data is obtained when analyzing the effect of the tilts in the X and Y axes, being the standard deviation (σ) 0.2508 and 0.2333 for each of them respectively.

Accurate results are obtained in the estimation of the aperture size in both axes. Estimation of the X-axis size is 28 mm approximately for the three analyzed error terms. For the case of the Y-axis dimension, the estimated size is about 22.5 mm versus the 22 mm of the actual dimension of the measured antenna.

B. Results for the antenna aperture characterization with the blocking metallic plate

The same study is performed for the case of having the metallic plate blocking the aperture. The goal is the evaluation of the metallic plate size. Figure 6 (a) shows the outcome of the Monte Carlo trials for the case of planarity error simulation. Figure 6 (b) shows the results in case of considering errors in the accuracy of the XY plane points. And Figure 6 (c) shows the results in case of considering tilts of the acquisition plane.

The probability distributions of the output variables are depicted in Figure 7. The estimated size of the object for each of the cases is around 10.2 mm, slightly lower than the real size of the object which is 12 mm.

Table II shows all the statistical data obtained for the analysis of the three error terms. The outcome of the simulations, shows an object size varying between approximately 8 mm and 9.8 mm versus the 12 mm size of the metallic plate used in the measurements.

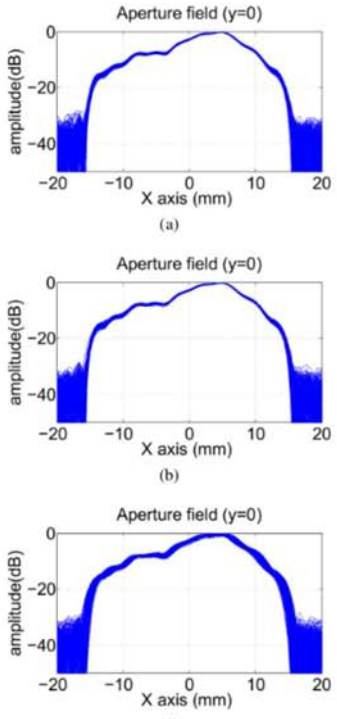

Fig. 4. Results for the Monte Carlo trials: a) errors affecting the planarity of the scanner; b) errors affecting the accuracy in the XY plane; c) errors affecting the tilt of the acquisition plane.

TABLE II
STATISTICAL VARIATION OF THE OUTPUT DENSITY FUNCTION FOR THE THREE ERROR TERM IN CASE OF HAVING A METALLIC PLATE BLOCKING THE APERTURE. APERTURE UNITS IN MILLIMETERS.

	XY accuracy		Z planarity		acquisition plane tilts	
Axis						
X	10,2400	0,1628	10,2734	0,2561	10,2656	0,6331

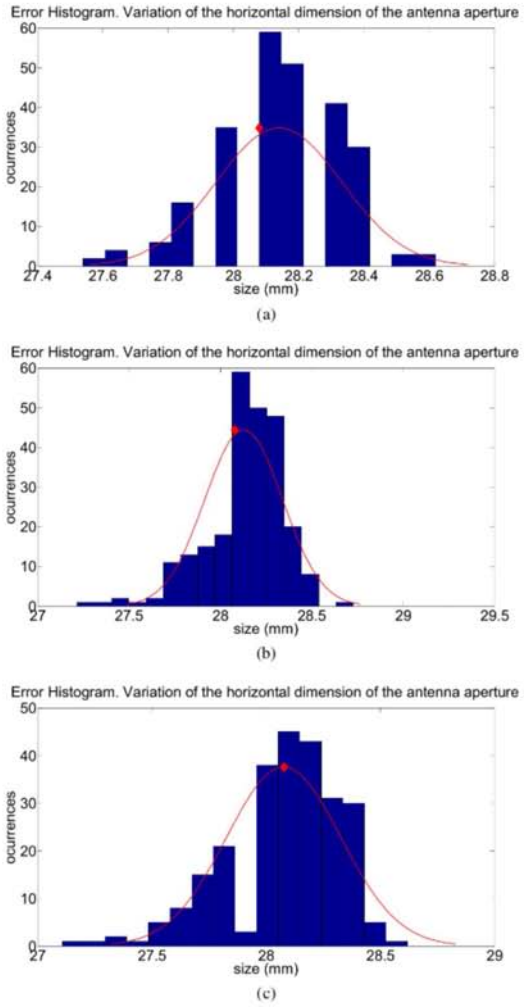

Fig. 5. Histograms for the output data distribution: a) errors affecting the planarity of the scanner; b) errors affecting the accuracy in the XY plane; c) errors affecting the tilt of the acquisition plane. The red diamond shows the reference value for every case

IV. CONCLUSION

An error simulation tool for the analysis of the influence of mechanical inaccuracies in antenna measurement acquisition process has been modified to perform a statistical analysis of data by means of a Monte Carlo method. By statistically modeling the output data, it is possible to a-priori predict the influence of each error term and being able to determine if the precision requirements are fulfilled for each setup or application. Validation of the method has been made for an antenna diagnostics case in which the effects of the mechanical errors in determining the size of an object blocking the antenna aperture are analyzed.

ACKNOWLEDGMENT

This work has been supported by Ministerio de Ciencia e Innovación of Spain/FEDER under projects TEC2011-24492, CSD2008-00068 and MICINN-11-IPT-2011-0951-390000, by Ministerio de Economía y Competitividad of Spain under postdoctoral fellowship FPDI-2013-16278, by Gobierno del Principado de Asturias (PCTI)/FEDER-FSE under projects PC10-06, EQUIP08-06, FC09-C0F09-12, EQUIP10-31 and by grant BP11-169 and by the European Union under COST IC1102 (VISTA) action.

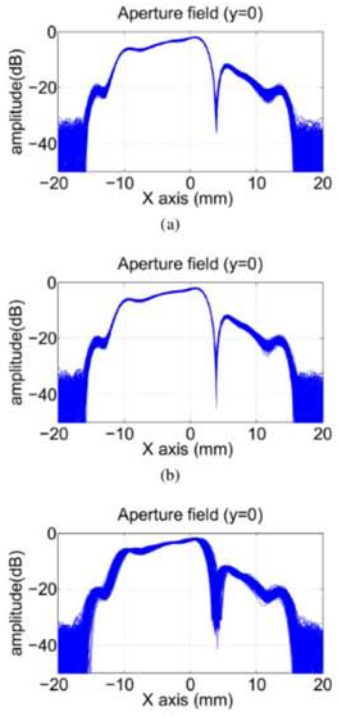

Fig. 6. Results for the Monte Carlo trials: a) errors affecting the planarity of the scanner; b) errors affecting the accuracy in the XY plane; c) errors affecting the tilt of the acquisition plane.

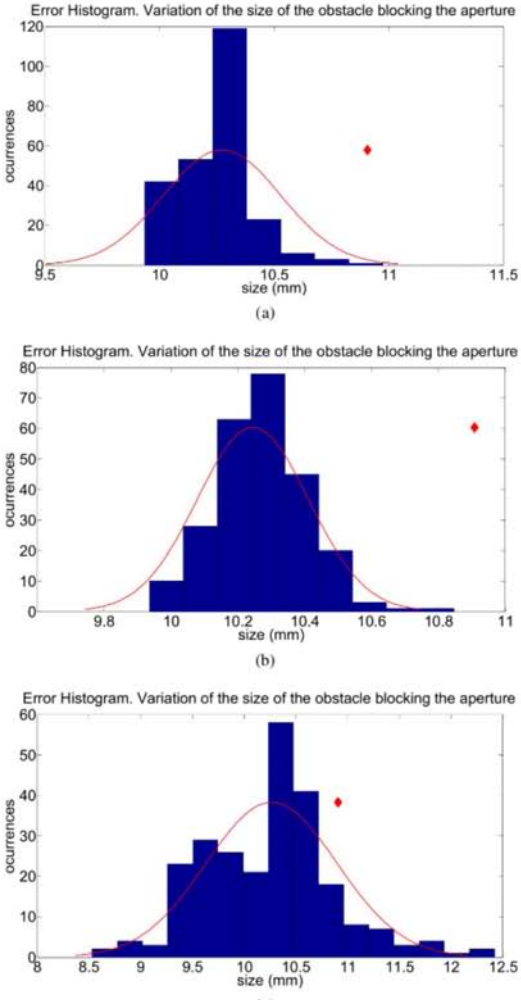

Fig. 7. Histograms for the output data distribution: a) errors affecting the planarity of the scanner; b) errors affecting the accuracy in the XY plane; c) errors affecting the tilt of the acquisition plane. The red diamond shows the reference value for every case

REFERENCES

[1] A. Newell, "Error analysis techniques for planar near-field measurements," *IEEE Transactions on Antennas and Propagation*, vol. 36, no. 6, pp. 754–768, Jun 1988.

[2] A. Arboleya-Arboleya, Y. Alvarez-Lopez, C. Garcia-Gonzalez, J. Laviada, and F. Las-Heras, "Error characterization tool for planar near-field antenna measurement and diagnostics applications," in *2014 IEEE Conf. on Antenna Meas. Applicat. (CAMA)*, Nov 2014, pp. 1–4.

[3] A. Arboleya, Y. Alvarez, and F. Las-Heras, "Millimeter and submillimeter planar measurement setup," in *2013 IEEE Antennas and Propag. Soc. Int. Symp. (APSURSI)*, July 2013, pp. 1–2.

[4] S. Burgos, M. Sierra-Castañer, F. Martin, and J. Besada, "Uncertainty evaluation through simulations of virtual acquisitions modified with mechanical and electrical errors in a cylindrical near-field antenna measurement system," in *30th Annu. Symp. of Antenna Meas. Techniques Assoc. (AMTA 2008)*, November 2008, pp. 1–7.

[5] M. Azpurua and E. Paez, "Monte carlo approach for the far-field uncertainty estimation due to errors in near-field measurements transformed using spherical wave expansion," in *Int. Symp. on Electromag. Compat. (EMC 2013)*, September 2013, pp. 1–6.

[6] "J. c. for guides in metrology, evaluation of measurement data - supplement 1 to the guide to the expression of uncertainty in measurement. propagation of distributions using a monte carlo method," Bureau International des Poids et Mesures, Tech. Rep., 2008.

[7] J. Laviada Martinez, A. Arboleya-Arboleya, Y. Alvarez-Lopez, C. Garcia-Gonzalez, and F. Las-Heras, "Phaseless antenna diagnostics based on off-axis holography with synthetic reference wave," *IEEE Antennas Wireless Propag. Lett.*, vol. 13, pp. 43–46, 2014.